University of Southampton

Faculty of Engineering and the Environment

Fluid Structure Interactions Group

Numerical Investigation of Wave Structure Interaction with Application to Wave Energy Devices

by

Linghan LI

Supervisors:

Mingyi Tan

James I R Blake

A thesis for the degree of Doctor of Philosophy

September 2015

Declaration of Authorship

I, Linghan LI, declare that the thesis entitled “Numerical Investigation of Wave Structure Interaction with Application to Wave Energy Devices " and the work presented in the thesis are both my own, and have been generated by myself as the result of my own original research. I confirm that:

- this work was done wholly or mainly while in candidature for a research degree at this University;
- where any part of this thesis has previously been submitted for a degree or any other qualification at this University or any other institution, this has been clearly stated;
- where I have consulted the published work of others, this is always clearly attributed;
- where I have quoted from the work of others, the source is always given. With the exception of such quotations, this thesis is entirely my own work;
- I have acknowledged all main sources of help;
- where the thesis is based on work done by myself jointly with others, I have made clear exactly what was done by others and what I have contributed myself;

Signed:

Date:

Abstract

Wave energy has become one of the most promising energy resources and hence has attracted more attention from the governments and energy companies. In order to meet the growing demands on global energy, the next generation of energy extracting device needs to be more efficient with less operation cost, and as an offshore structure, the survivability also needs to be taken into consideration. Therefore, it is vital that the hydrodynamic behaviour of the energy device can be predicted accurately at the initial design stage.

In this research, the wave structure interaction with application to wave energy device is studied numerically through an open source CFD library: OpenFOAM. The computational fluid dynamic (CFD) analysis based on the Reynolds Average Navier Stokes (RANS) equations is used to investigate the interaction between wave and structure, and array effects among devices. The numerical method with a reasonable computational cost can be an alternative to physical experimental test in offshore engineering. The background to this research is firstly introduced, including methodologies adopted in this study, followed by a series of case study to demonstrate the applicability of the numerical model. These include wave generation validation, hydrodynamic behaviour determination, and the predication of the performance of wave point absorber and wave point absorbers array.

It has been shown that the numerical model is capable of modelling wave propagation and interaction with structure including nonlinear effect with a reasonable degree of accuracy. The wave point absorber energy device has been chosen as the object to study. The RANS approach in time domain improves the accuracy when compared with the potential theory based method. The influence of wave point absorber devices array on their performance is then investigated under the irregular wave conditions in order to improve the overall performance. The influence factors include array configuration, separation distance and wave direction.

The study yields an improved understanding of wave-structure problem and has extended the range of RANS model used in wave energy research.

Acknowledgements

I would like to express my gratitude to all those people who gave me help during my PhD study. Particular, I would like to thank my supervisor, Dr Mingyi Tan and Dr. James Blake for their supervision and guidance. And I would also like to thank Dr. Alexander Phillips, as an examiner, for his suggestions and comments that largely improve this thesis.

I am very much thankful for Dr. Kamal Djidjeli and Dr. Narakorn Srinil from Newcastle University. They kindly served as my examiner for my PhD viva.

At last, a particular thank to my family for their unconditional love and support in the last three years.

Contents

List of Figures

List of Tables

1. Introduction

Global energy is the key to the progress of mankind and energy demands will become greater over the coming years. Currently, nearly 80% of the world's energy is supplied by conventional fossil fuels, which accounts for 70% of the total energy-related carbon/sulphur dioxide and other hazardous substance emissions. By 2050, the population of urban society will grow to be approximately 66% of the total population, and for that reason, the current energy demands will increase by 70% (IEA, 2016). It is obvious that the current primary energy supplements are not sustainable and they are not under strategic development for each country. As part of the drive to meet these increasingly strict requirements, there is now a heavy focus on the development of technologies to accelerate the transition to a clean renewable energy system.

It is a well-known fact that the ocean covers 71% of the Earth's surface, and that the ocean is rich in resources and energy. The ocean's energy includes the energy carried by the waves, tidal range, tidal currents, ocean currents, thermal energy, and salinity gradient (Uihlein, 2016), and the full use of the ocean's energy is the best way to solve the problem of the energy crisis. Currently, only the tidal range can be considered in the early stages of development from conceptual up to the demonstration stage. Among all of the energies under conceptual study, the ocean wave is the most advanced and is expected to contribute significantly to the supply of energy in future. However, since wave energy technology is still in the initial stages of research, the costs and performance of the device and the rest of the installation would be difficult to be estimate, and most of the current numerical studies are oversimplified. This PhD project focuses on CFD simulation to quantify the hydrodynamic behaviour of the wave energy device. This chapter introduces the main goals of this PhD project and the unique contributions to knowledge that it will provide.

1.1 Research background

By year's end of 2015, renewables comprised an estimated 28.9% of the world's power generating capacity enough to supply an estimated 23.7% of the global electricity total, with hydropower providing about 16.6%, see Figure 1-1. Renewable energy resources such as wind and solar have been developed and utilized over years and they account for up to 20% of the total energy demands in some countries (IEA, 2016). Other than solar and wind energy, it is necessary to increase resource diversity by investigating other forms of sustainable energy, which has been less developed at present but with a huge potential (Arent et al., 2011). Many policies have encouraged investors to use

renewable energy. It could be of great potential to meet national and global low-carbon ambitions in the future.

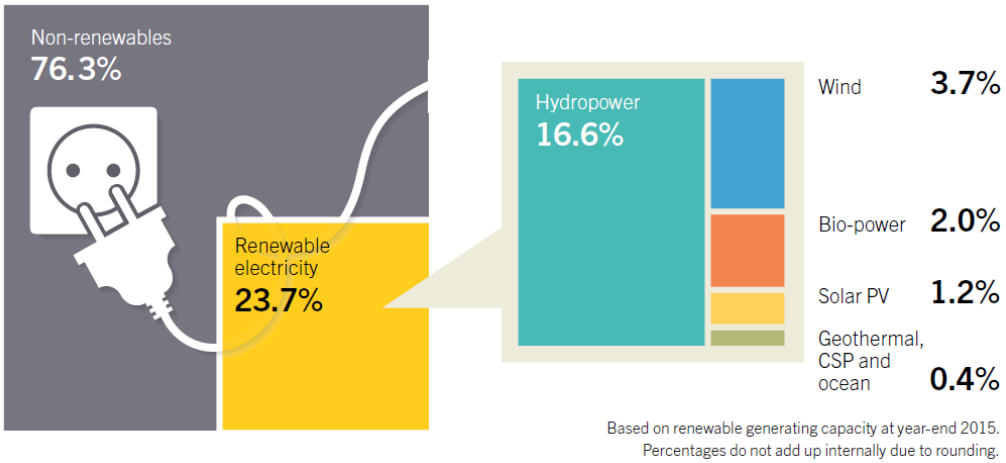

Figure 1-1 Estimated Renewable Energy Share of Global Electricity Production, End–2015 (REN21, 2016)

In 2015, the capacity of global ocean energy reached to approximately 530 Mw. Most of the marine energy technologies developed focus on tidal barrages across bays and wave energy devices in remote areas. The study of wave energy started to progress in this year, and many projects were launched around the world. Most of them were based in Europe (EMEC Ltd, 2015). According to Andres, there is a global deployment potential for ocean energy of up to 337 GW, which could result in the generation of over 885 TW h/year (Andres et al., 2017). So far, only tidal ranges can be considered in the early stage of development from conceptual up to the demonstration stage.

The ocean wave is recently regarded as one of the most promising sources of renewable energy on the planet. It is predicted that the energy in the ocean waves around the world has great potential, which has been roughly estimated up to 10 TW (Galarraga et al., 2011) and, more importantly, the highest energy density around (Clement et al, 2002). The power density of wave energy is much higher than that of wind or solar energy. The magnitude and periodic characteristics of wave changes along with the variations of the sea's surface, weather conditions, shore structure, time and the location on Earth. During twenty-four-hours, wave energy converters can produce power up to 90% of the time, whereas wind and solar power systems produce power 20–30% of the time. Compared to most of the other alternative energy sources, wave power is easily predictable and this quality can be used to calculate the amount that it can produce.

The first wave-power patent was obtained by Girard and his son in 1799 (Lawrence et al., 2013). Since then, the interest in wave energy keeps increasing, and many device concepts have been

proposed and developed with the resources of wave power ranging from 3 kW/m to 50 kW/m. According to López, more than 1000 WEC projects (both conceptual and operational are included) have been reported at a global scale (López, 2013), and 256 concepts are known by European Marine Equipment Council (EMEC, 2016). Among these, nearly half of WECs were developed in Europe (especially in the United Kingdom), with point absorber devices being the most studied systems. Outside Europe, the US reports the most intense activity (with 98 concepts).

Figure 1-2 presents a map of the mean wave power density (in kW/m) corresponding to the 15-year interval from January 2000 to December 2014.

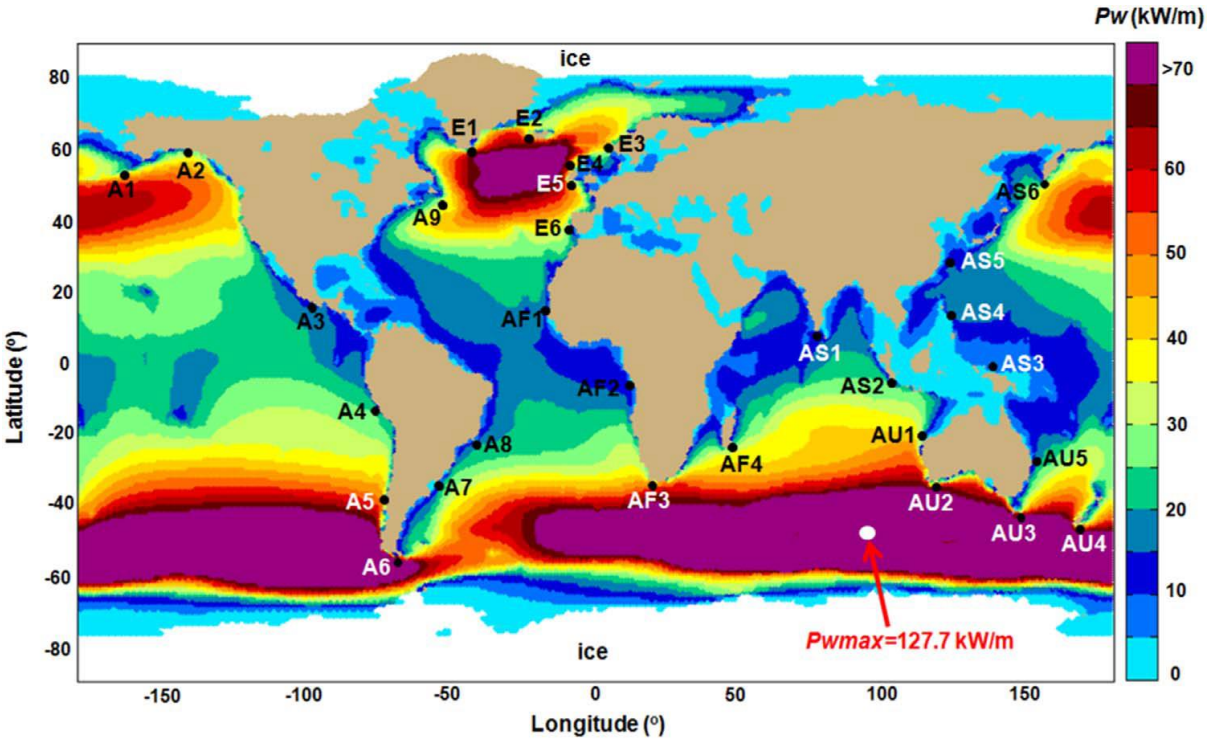

Figure 1-2 Map of the mean wave power density (in kW/m) corresponding to the 15-year interval from January 2000 to December 2014; the positions of 30 reference points, distributed along the coastal environments of: America (A1–A9), Europe (E1–E6), Africa (AF1–AF4), Asia (AS1–AS6) and Australia (AU1–AU5), are also indicated (Rusu et al.,2017)

As shown in the figure above, the most consistent wave power potential is encountered in the areas located between the 40° and 60° latitude lines (north and south), with the maximum of 127.7 kW/m located in the Indian Ocean region. According to the literature, the capacity of wave power potential in Europe is approximately 320 GW in 2011 (Ghosh et al., 2011). The capacity of wave power in Ireland is 21 GW (Vicinanzaa et al., 2013) and the exploitable wave energy resource is approximately 21 TWh, which would full fill 60% of the total national electrical demand in 2012 (Sharkey et al., 2013). In the United Kingdom, up to approximately 25% of electricity demand could be covered by

wave energy in 2008 (Drew et al., 2009). There are about twenty-five countries involved in such developments since 2010 (REN21, 2016) and the number will be becoming larger.

In 2012, the terms of a “theoretical” and “technical” resource was proposed by Gunn (Gunn et al., 2012). The technical part refers to the actually extractable energy from the total theoretical resource by applying the calculations related to the currently available wave energy devices. The main results of assessment include the estimation of total wave power (P), the extractable energy by current available wave energy devices (Ψ), and the extraction efficiency (η). According to the report, the estimated extraction efficiency of global incident wave power is only 4.6%. The annual mean statistics for selected countries are given in Table 1-1.

Table 1-1Annual mean statistics for selected countries

Country	*P (GW)*	*ψ (GW)*	*η (%)*
Australia	280 ± 13	8.3 ± 0.20	3.0
United States	233 ± 12	3.59 ± 0.17	1.6
Chile	194 ± 11	4.62 ± 0.17	2.4
New Zealand	89 ± 16	3.51 ± 0.16	4.0
Canada	83 ± 7	5.31 ± 0.19	6.2
South Africa	69 ± 4	2.17 ± 0.08	3.1
United Kingdom	43 ± 4	2.44 ± 0.14	5.7
Ireland	29 ± 4	1.13 ± 0.09	3.8
Norway	29 ± 4	1.67 ± 0.12	5.7
Spain	20 ± 3	0.65 ± 0.05	3.3
Portugal	15 ± 13	0.49 ± 0.04	3.2
France	14 ± 3	0.57 ± 0.06	3.9

The table has listed the countries with an inherent advantage in wave energy resources, such as Australia, US and some European countries.

Currently, only the coastal environments that have expressed high interest for wave energy extraction includes the southern part of Australia and some regions from Europe, presenting potential wave power in the range of 70–80 kW/m, from which we can mention DanWEC (Denmark) and EMEC (Scotland). Among the most notable success stories in wave energy conversion has been the 296 kW Mutriku plant in the Basque Country of Spain, the first commercial wave energy plant in Europe. Since its installation in 2011, the plant has operated continuously and, as of early 2016, it has

generated more than 1 GWh of electricity by harnessing wave-driven compressed air (by way of an oscillating water column).

Although there have been great contributions and there is a giant potential in using wave power, only a few full scale model remains at sea. There are still no commercial wave farms in operation due to the high cost of wave energy in comparison with other renewable energy sources. Besides, it is difficult to utilize the highly random, slow but large force wave oscillating motions used to drive a generator with an acceptable quality output to the utility grid (Clement et al., 2002; Drew et al., 2009 and Czech and Bauer, 2012). Moreover, saltwater is a hostile environment for wave energy devices, and the maintenance operations become much more difficult than those on land (Czech and Bauer 2012). Lastly, the deployment of a wave energy device or multiple devices requires a higher level of funding as well as comprehensive planning. Much work is still required to achieve economically-competitive energy from wave power.

Currently, wave energy utilisation has lagged far behind as a renewable energy source and there is no existing commercial scale wave power plant. It is noted that there are a number of technical challenges that need to be overcome for wave energy to become commercially competitive in the global energy market:

- The most significant challenge is to design wave energy device array, which maximises the wave energy dissipation and to take up a minimum amount of space at the same time.
- In offshore locations, wave direction, height and frequency are highly variable. Therefore, in order to improve the capture efficiency, the devices have to align themselves accordingly with the wave direction (Drew, Plummer et al. 2009).
- The irregular behaviour of ocean waves makes it difficult to obtain the maximum efficiency of a device over the entire range of excitation frequency and structural loading under extreme conditions may be as high as 100 times the average (Linkopin, 2011), which leads to difficult structural engineering challenges. Furthermore, the average power absorbed is much smaller than the power peaks.

1.2 Problem statement

The power captured by WEC can be analyzed numerically by using the frequency domain approach. The hydrodynamic behaviors of the body in motion under regular or irregular waves can be obtained by the frequency domain method. It is widely used due to its low computational cost, but the major assumption is the linear theory, which is not suitable for the floater under steep waves, large

displacements or rotations and nonlinear effect such as wave break and forces related to the power take-off system and turbulent drag. In this work, a computational fluid dynamics (CFD) analysis based on Reynolds Averaged Navier Stokes (RANS) solver has been developed to investigate the wave-structure coupled field around WEC structures. When compared to existing methods, the CFD approach improves the accuracy of wave-structure simulation so that a better solution to the prediction of power output for a given set of conditions can be more readily achieved. This thesis intends to investigate the performance of isolated wave energy device in irregular wave site and provide an insight into how the deployment of devices within an array affects the total power output.

To date, many studies are focusing on harvesting technology to maximize the potential to extract the renewable source of energy available from the ocean. Regardless of which concept or technology is in use, the commercial exploitation of wave energy requires the installation of large numbers of Wave Energy Converters (WEC) in order to provide enough power and to convert the variable input into a smooth electrical output. Similarly, deployment, such as an isolated converter with multiple bodies, is also encountered as a device array. Wave farms of these kinds, on the other hand, bring a considerable saving in terms of the cost of a mooring system, power transfer system, maintenance and other requirements. The key issues in this field are to improve WEC design and to optimize the geometrical layout based on the understanding of the interactions between the bodies involved. In contrast to the large number of numerical simulations of isolated WECs and several experimental works concerning WEC arrays, there is only a small proportion of work in investigating numerical wave energy farms, especially in the time domain and 3D conditions. The hydrodynamic interactions between the converter body and irregular waves including waves that are reflected or radiated from other converters, are very complex to consider. The hydrodynamic behaviour between the devices may have a positive or negative effect on the individual power output compared with isolated installations; hence the total power output from the array cannot be simply calculated by multiplying the number of devices by the power captured from isolated device. Additionally, there are many factors that can influence the nature of this interaction, such as wave conditions, the shape of the device, power take-off system parameters etc.

1.3 Scope of thesis

The overall purpose of this work is to examine the interaction between the wave energy converter and irregular ocean wave and to improve the power efficiency of an isolated device and the devices array. To achieve this, the numerical method based on Reynolds averaged Navier stokes equation

(RANS) is presented to be able to cover all nonlinear effect on the wave energy device during the energy extraction process.

A number of objectives are identified regarding the capabilities of the model. More specifically, the model should:

- be able to represent the wave environment accurately that overcome the drawback of potential wave theory.
- be able to determine the hydrodynamic derivatives of the wave energy device with considering the nonlinear effect of waves on the device correctly
- improve the design of an isolated device in an irregular sea-sates
- improve the design of the devices array with different configurations in an irregular sea-states

In order to demonstrate the characteristics of the numerical methods adopted in this work, a series of case studies, ranging from determining hydrodynamic derivatives acting different capture devices with different shape to optimizing the performance of a small wave farm, have been undertaken. The studies described in this work yield an improved understanding of wave energy converters, drawing guidelines to optimize power production in an array, and extending the range of the application of open source software in wave research.

1.4 Novel contribution

This is a novel investigation on the design of wave energy point absorber and point absorbers array. In this investigation, a more accurate numerical model based on RANS method is adopted, with the consideration of nonlinear wave effects on the point absorber structure. This approach improves the accuracy of wave-structure simulation so that a better solution to the prediction of power output for a given set of conditions can be achieved. The novel contributions presented in this thesis are summarized as:

- The investigation of the hydrodynamic behaviour of a wave energy device in a full viscous solver is conducted. The characteristics hydrodynamic coefficients of point absorbers are studied and discussed. This thesis provides results and discussion of the parameters regarding of the buoy shape, draft, oscillating amplitude and frequency. This is relevant to the field of wave energy device reacting in the waves.
- The performance of different wave energy devices are quantified at a given sea state. The optimal configuration is studied and discussed. Moreover, the dimensions of an isolated

point absorber and the wave parameters could vary with ease which further increases the numerical model availability for future studies.

- In the study of two-body point absorber, some key finding are summarized. The choice of numerical scheme has a great impact on wave environments. Different choices will lead to a large discrepancy in the results regarding of power efficiency, thus the numerical scheme that adopted in this study are discussed and their strengths and weakness are highlighted.
- In the study of wave energy arrays, the optimal configurations with up to four devices are studied and discussed. The star and square layouts are further investigated to deliver a better extraction efficiency.

1.5 Thesis outline

The present thesis has been organised into nine Chapters. Each of the following Chapters are briey summarised below:

Chapter 2 firstly presented the background of the point absorber. It introduced the development of point absorber concepts, the working principles and their corresponding mooring systems. Then, the recent literature about point absorber wave energy converters has been reviewed. The primary approaches adopted in the mentioned work includes the analytical method, the frequency and time domain boundary element method (BEM) and the Navier-stokes (NS) based computational fluid dynamic (CFD) method. For a different research emphasis, each method has its own advantages and drawbacks

In Chapter 3, the procedures to solve the wave-structure interaction problem was introduced. The implementation that adopted in OpenFOAM was presented in order to solve the RANS equation. Three different turbulent models were provided to close the NS equation. The spatial and transient discretisation approach was then introduced. Moreover, the brief introduction about the boundary condition and pressure-velocity coupling method has also been provided. The dynamic mesh strategy that was used to simulate the point absorber motion under waves has been discussed.

The wave generation and absorption method in a 3D wave tank have been investigated in Chapter 4 and a validation of hydrodynamic parameters against experimental and analytical results was conducted in Chapter 5. These two chapters built up the confidence in modelling wave-structure interaction problem.

Later on, a parametric study about the heaving point absorber was carried out to investigate the wave energy potential that can be captured at a given sea site in Chapter 6. It can be found that the wave energy has a great potential and this amount of wave energy can be extracted by employing proper wave energy converters. In this study, the hydrodynamic behaviour of four different heaving point absorbers together with PTO system has been examined in irregular wave conditions by way of the CFD method.

In Chapter 7, a particular two-body PowerBuoy model has been chosen as the test model. The numerical simulation was carried out to compare the results with the ones from the experimental measurements to demonstrate that the CFD model is able to represent the energy harvest processes accurately.

In Chapter 8, the point absorber array with five configurations is investigated in terms of separation distance and wave climate to quantify the performance in power extraction efficiency. The presented numerical approach is based on the RANS equation with the consideration of the fully nonlinear effect. Finally, Chapter 9 conclusions from the present numerical investigation were given and it also extended the discussion to possible future study to be conducted on the subject.

2. Background and literature review

In the last few years, many researchers have been focusing on wave energy. Hundreds of Wave Energy Converters (WECs) have been studied and developed. Full-scale prototypes have been tested, and technology review papers have been published by the pioneers, such as McCormick ME (2013), Lopez et al. (2013) and Guedes Soares et al. (2014)

The concepts of the point absorber wave energy system, including heave, pitch and surge type, has been developing since 1975 (Budar et al., 1975). The point absorber WEC is a device with small dimensions compared to the incoming wave lengths. The attracting device oscillates in one or more degrees of freedom and the energy is captured and absorbed by dampening the oscillating motion. The wave energy is converted into electricity and finally stored in the national grid.

The point absorber is a simple but robust wave energy device. A point absorber can be equipped with a direct drive power take-off (PTO) system which is designed for a long wave length and periodic ocean waves (Falcao, 2007). Alamian et al (2014) investigated the different types of WEC system and found that the point absorber is the most suitable device for the given sea site that was selected. Some multiple-body heaving absorber systems are currently being developed such as the FO^3 and Wave Star, see Figure 2-1.

Figure 2-1 Seewec FO^3 (left, http://www.seewec.org/) and Wavestar (right, http://wavestarenergy.com/) prototypes

Other than installing vulnerable control mechanisms, the point absorber WEC system can be equipped with an additional body to shift the optimal oscillating frequency. The additional body can increase the system inertia to tune the point absorber to the resonance of a given sea site (Candido, et al., 2011). The WEC is modelled as two coaxial axisymmetric bodies with the optimal mechanical damping and spring coefficients under different wave conditions being mathematically analysed.

Zabihian and Fung (2011), Carballo et al. (2012), Rusu and Onea (2013) and Veigas et al. (2014) investigated the optimal power production of given coastal locations using numerical methods. Their work characterized the local wave resource and assessed the optimal location for the largest energy production based on yearly wave patterns. The future of wave energy is not clear since the cost of energy from this resource is high (Neary et al., 2014). However, wave energy continues to attract interest and investment, with new concepts being continually developed. (European Ocean Energy Association, 2012).

2.1 Background about Point Absorber

A Point absorber is provides a large amount of power in a relatively small device; the dimensions of point absorbers are much smaller than the wavelength of the waves (López, 2013). The use of a point absorber is one of the most commonly used approaches to utilize wave energy at or near to the water's surface. The main concept of point absorbers is to use the movement of floats to produce energy. They can collect the energy in all directions through its range of movements, like bobbing or pitching actions, depending on the mechanism used. The produced energy can be converted to electrical energy in shoreline or offshore facilities; or direct electricity.

Point absorbers are known as a third generation of wave energy devices, and it has the following advantages:

- The capture device contacts with the waves directly, which reduces the energy conversion numbers, leading to less energy dissipation and a higher converging efficiency;
- The device dimensions are smaller than other devices, and the influence of them on the wave field are negligible;
- The installation of point absorbers is comparable flexible, the configuration of point absorber arrays can be designed according to the power capacity and the wave energy distribution.

Currently, most of point absorber research has been conducted in Europe, the United States and Japan, etc. Hundreds of point absorbers have been developed in the past decade. Single-degree-of-motion

types, multi-degree-of-motion types and multi-floating-bodies types make up the majority of the point absorber category.

2.1.1 Single-Degree-of-Motion Type

One of the earliest attempts of using point absorbers was conducted in the Trondheim Fjord with the N2-power-buoy model in 1983, and a video clip from the test is shown in Figure 2-2

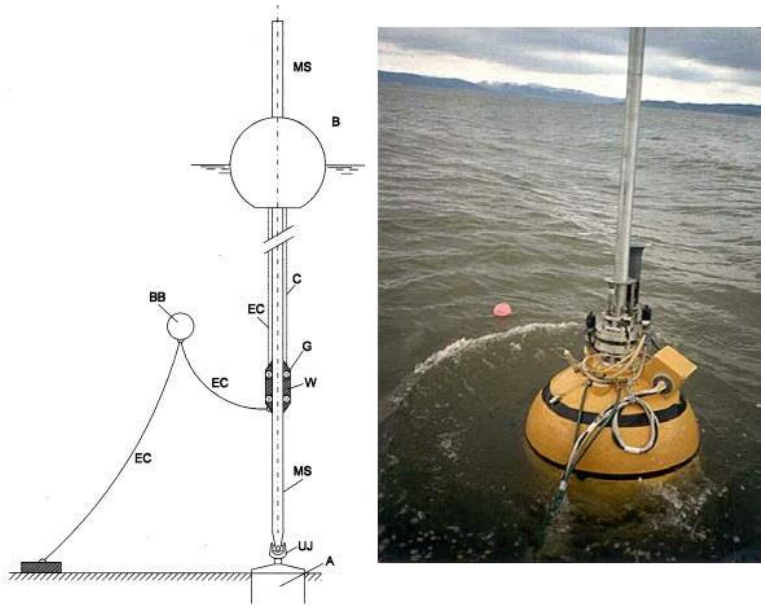

Figure 2-2 Power buoy of "type N2" (Falnes, 2003)

The N2-power-buoy model consists of a spherically shaped buoy hull with a diameter of 1 m and a strut connected to a universal joint on an anchor on the sea bed. The buoy is arranged to slide up and down along the mooring strut with little friction. A particularly flexible electric cable connects the weight and the seabed, which is carried partly by a submerged buoyant body. The ball shape buoy oscillates along the strut within the range of 4 to 7m. As the bottom of the hull is open, the water's surface works like the piston of an air pump.

Another idea related to point absorber design is to submerge both the floater and the basement in water, which gives a better chance for the device to survive from storms. As shown in Figure 2-3, a sufficient high air pressure is stored inside the piston chamber to keep water out of the device, and the waves passing over the piston cause it swing along the basement. The oscillating movement of the floater drives the linear PTO in order to produce electricity. This concept was firstly proposed in 1993, after a few years of theoretical and modelling study, and overcoming financial constraints and technical difficulties with the submersion operation. The submersion of the Archimedes Wave Swing

(AWS) pilot plant was successfully tested offshore Portugal in May 2004. The AWS is the first wave energy device using a liner generator, which has a power capacity of 2MW.

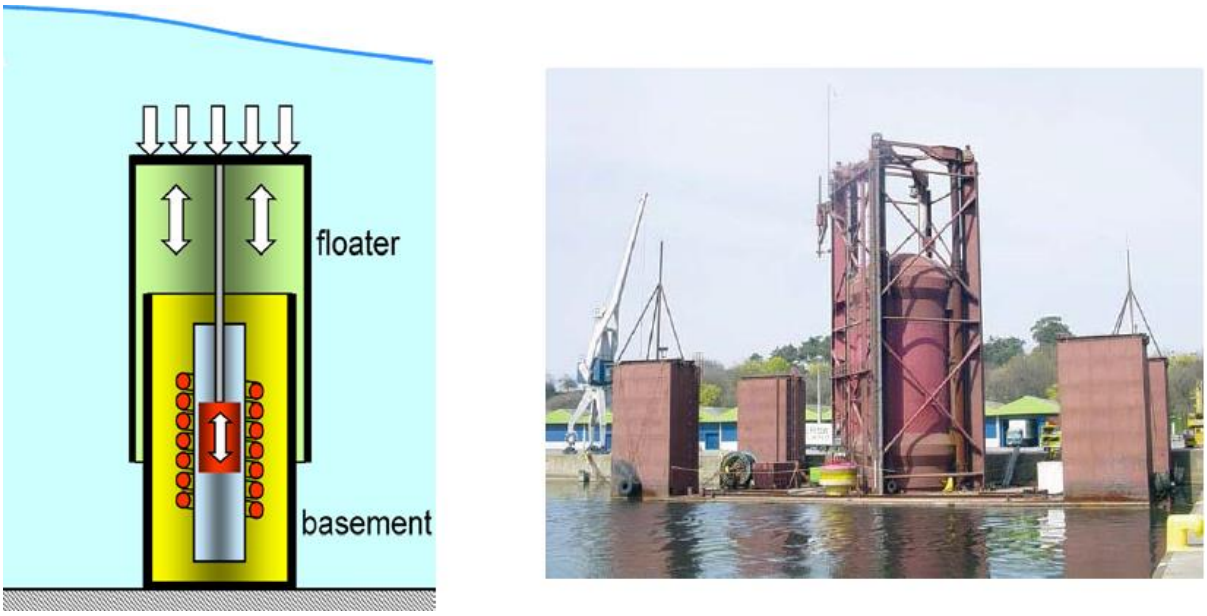

(a) (b)

Figure 2-3 Archimedes Wave Swing Scheme (a) (Antonio, 2010) and its Prototype (b) (Cruz, 2007)

In 2009, the concept of directly driving a linear generator for power production was deployed at the Lysekil research site (Sweden). As shown in, the L9 wave energy converter consists of a torus buoy on the surface and a linear generator placed on the seabed. The two components are connected through a steel wire. The result confirms that the buoy size and translator weight has a large impact on the power absorption from the generator. By optimizing the buoy size and translator weight, the WEC is believed to produce power more evenly over the upward and downward cycle. Apart from that, to predict the maximum power limit during normal operations, a simulation model has been derived. The results correlate well with the experimental data gathered during normal operation.

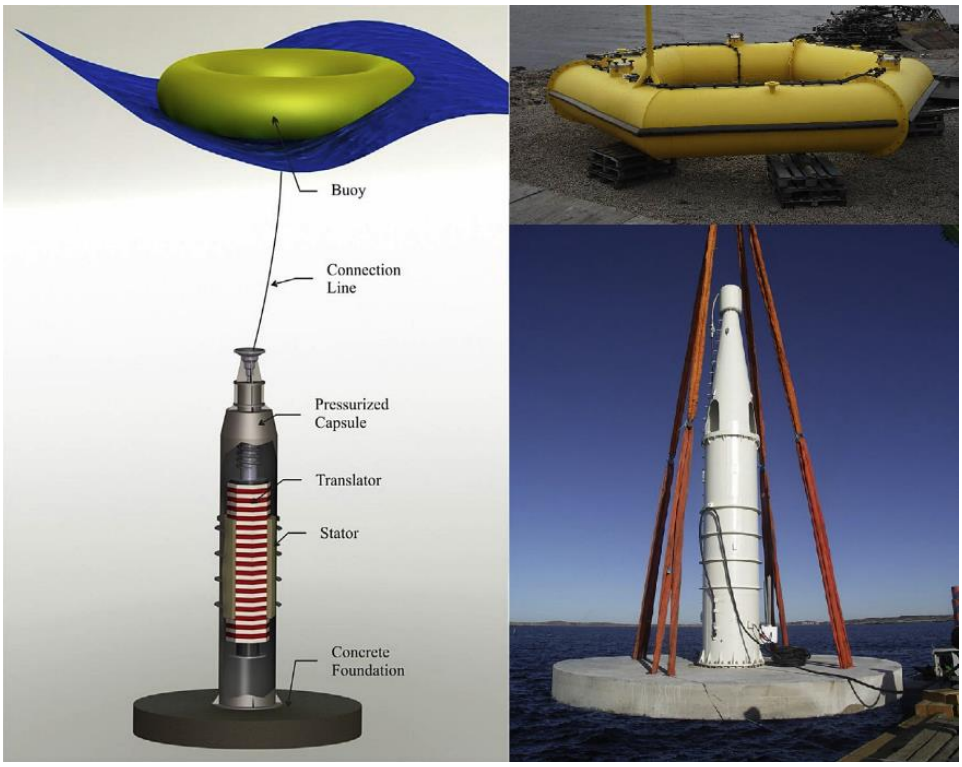

(a) (b)

Figure 2-4 Illustration of the WEC developed at Uppsala University (a); picture of L9 during deployment (b) (Lejerskog, 2015)

Despite the slight difference in design principles, all of the above samples can be summarised as a single body system oscillating in heave, which is the first generation of point absorber. According to the research, it was found that a point absorber WEC in resonance with the incident wave achieves higher relative heave motion amplitude and velocity, thereby transferring more wave energy to where it needs to go. Accordingly, many researchers in the renewable wave energy field have been searching for ways to adequately tune the WEC system to oscillate in resonance with the incoming wave, and the concept of a two-body floating point absorber system has been developed.

Take a recently developed two body floating absorber developed by Ocean Power Technologies (OPT) for example, as shown in Figure 2-5. The two-body system includes a float section and reaction section. By utilizing the relative motion between the two sections, the system converts wave energy into electricity. The first 40-kW utility-scale system was tested offshore in Santona, Spain in 2008, and is currently in-use or in-planning at nine locations around the world.

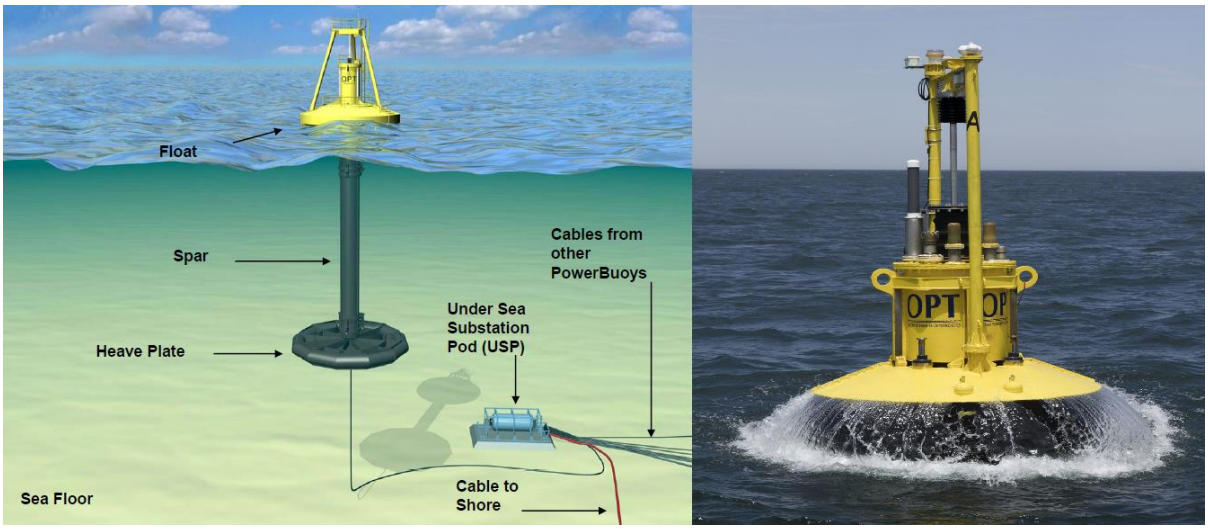

Figure 2-5 Power-buoy developed by Ocean Power Technologies (Energy without carbon, 2015)

Apart from the heave motion wave energy absorber, wave energy can also be transferred through pitch motion. The nodding duck, or by its official name, the Edinburgh duck, is a device that converts wave power into electricity through the rotation of gyroscopes located inside a pear-shaped "duck", and according to the calculations, up to 90% of the rotating energy can be converted by an electrical generator converts.

Figure 2-6 Conceptual sketch of Edinburgh Duck Wave structure interaction (Edinburgh Wave Power Group, 2009)

The Edinburgh duck was invented by Stephen Salter in the 1970's. However, since the prototype test, no wave-power devices have ever gone into large-scale production due to the cost and complexity involved.

Theoretically, waves can be described using basic hydrodynamic equations. The water surface motion, water particle velocities and wave-induced pressure in the water can be theoretically estimated by

models (Kinsman, 1965). But the exact descriptions of real ocean wave behaviours are still not available (McCormick, 2013). Some of the theories that ignore the effects of wave height and current were employed to calculate wave characteristics, for example, the linear wave theory (or airy theory) (Airy, 1845), Eckart's approximation (Eckart, 1952), Olson's approximation (Olson, 1973), Hunt's approximation (Hunt, 1979), Nielsen's approximations (Nielsen, 1984), Vanezian's approximation (Vanezian, 1980), and Wu and Thornton's approximation (Wu and Thornton, 1986). Hedges's approximations (Hedges, 1987), and Stoke's higher order theories (Fenton, 1985) considers wave heights. Stoke's higher order theories derived by Fenton includes both the wave height and wave currents in the calculations (Fenton, 1985).

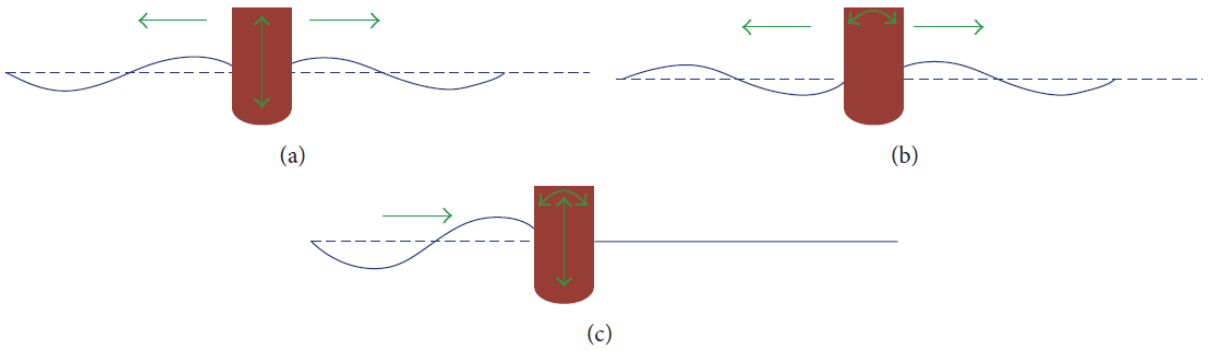

Figure 2-7 (a) Wave radiation by heaving (b) wave radiation by pitching (c) superposition of incident wave, heaving, and pitching motions (McCormick, 2013, Le-Ngoc, 2010 and Rahm, 2010)

The basic principles of how a point absorber extract energy from incident wave are present in Figure 2-7. When the point absorber is in resonance and oscillates in a heaving motion only, as shown in Figure 2-7 (a), a symmetric reduced height wave radiates from the point absorber with the same frequency as the incident wave. Ideally, up to 50% of the energy can be absorbed from the heaving motion alone. When the point absorber is in pitching motion only (see Figure 2-7 (b)), antisymmetric waves generated around the device, and more than half of the wave energy can be taken from the incident wave. Figure 2-7 shows the accumulation of the heaving motion, pitching motion, and the incident wave. It is ideally possible to extract all of the energy from the incident wave through this combination (McCormick, 2013, Le-Ngoc, 2010 and Rahm, 2010).

According to Farley (Farley, 2012), the power captured by the WEC is equal to the power subtracted from the incident waves by interference, minus the power spreading out in all directions. He also derived the relationship between capture width and the angular distribution of the combined total of all waves generated by the WEC, where the optimization can be done in most cases by adjusting the resonant frequency and internal damping the system (Farley, 2012). Also, the steepness of the wave

is another important factor for considering the power output, which should be taken into consideration during the optimization.

2.1.2 Natural frequency

The natural frequency of a point absorber is determined by the mass and elastic characteristics of the structure and the mooring system. Damping is to dissipate energy by resistance. For large damping, the device may not oscillate at all before coming to rest at its equilibrium position, and no appreciable vibration is expected to occur. For small damping, it will take a long time for the device to come back to rest after being displaced. Without damping, a device will keep moving continuously once excited (Chakrabarti, 2002), which is impractical, since every motion extinguishes with time. The calculation of the decay rate of the motion can be made with damping included (Hooft, 1982).

Vibration is harmful for most physical systems, except for the system which extracts energy from vibration (Chakrabarti, 2002). When an oscillator is displaced, the structure will return to its equilibrium position if no more external forces are applied to the system, and this is named 'free oscillation'. If a force is continually or repeatedly applied to keep the oscillation going, it is called 'force oscillation'. For point absorbers, their response depends on the frequency of the waves. The cyclic motions of the point absorber are more pronounced when the waver frequencies correspond to the natural frequency of the waves themselves, and the maximum power generated under suitable harvested situations (Payne, 2008a). For a linear system, the excitation force and resulting motion are both sinusoidal, as shown in Figure 2-8 (Hooft, 1982).

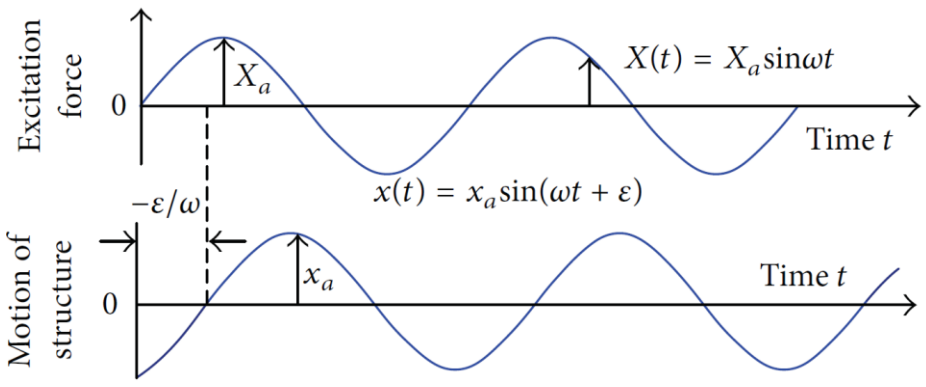

Figure 2-8 Schematic diagram showing harmonic excitation and the resulting motion (Xa is amplitude of excitation force, Xa is amplitude of motion, ε is phase, and ω is excitation frequency) (Hooft, 1982)

The differential equation of motion that represents vibration for a device for a single degree of freedom can be obtained from the inertia, restoring force, damping force arising from fluid viscosity effects, and harmonic excitation force (Berteaux, 1976. Hooft, 1982, Patel, 2013).

$$M\frac{d^2x}{dt^2} + b\frac{dx}{dt} + cx = X_a sin\omega t \tag{2-1}$$

M is the virtual mass ($m + m_a$), m is the mass of the device, m_a is the added mass, b is the damping coefficient, and c is the spring coefficient. The added mass relates to the shape of device, and is a result of the disturbance of the flow field (Dean and Dalrymple, 1991). For a system with multi degrees of freedom, the equation of motion is given as:

$$M_{ij}\frac{d^2x}{dt^2} + b_{ij}\frac{dx}{dt} + c_{ij}x = F_{ij} \tag{2-2}$$

Where subscript *i* and *j* stand for the parameter in *i* direction due to a motion in *j* direction and F_{ij} is a linear reaction force.

For a multi-degree freedom system, the behaviour of each degree of freedom affects the other. The restoring spring coefficient for a floating system in heave is given as (Berteaux, 1976. Hooft, 1982):

$$c_z = \rho g A_{wet} \tag{2-3}$$

Where ρ is seawater density, g is gravity, and AWP is the area of the water plane. The natural frequency of a floating body in heave motion is thus calculated as (McCormick, 2013):

$$f_z = \frac{1}{2\pi}\sqrt{\frac{\rho g A_{wet}}{m + m_a}} \tag{2-4}$$

The natural frequency of a point absorber can be tuned by varying its mass and spring constant (Eriksson, 2007). The resonance can be achieved by tuning the natural frequency of the device to coincide with the incident wave frequency (Eriksson, 2007). However, the band of point absorbers is mostly narrow, and the resonance frequency bandwidth then does not usually coincide with the spectrum of the incident ocean waves, Also, the incident wave heights have a large variating range.

To be equipped with phase control of the oscillation, and the amplitude control of the point absorber are two main factors should be taken into consideration in designing (Falnes, 2012).

2.1.3 Mooring

Mooring systems are designed to keep the device at the desired location and to ensure its safety (Harris, 2004). For the wave energy conversion system, the mooring system are required to limit the excursions and orientation of the device under the action of environmental forces due to waves, currents and the wind. In the offshore oil and gas industry, design codes for mooring systems already exist, such as DNV OS-E301 (DNV, 2004), API RP-2SK (API, 2005) and ISO 19901-7 (ISO, 2005). These technologies can be used as a basis to design the mooring systems for floating WECs, but cannot be directly applied. Different from the offshore oil and gas industry, the mooring system can influence the wave energy extraction of a point absorber by interacting with its oscillations (Karmakar et al., 2012, Wang and Sun, 2010). Thus, the mooring system for WEC is required to have minimal force in relation to the WEC to guarantee the efficiency of the device (Babarit et al., 2005, McCormick, 2013).

The primary mooring components include the mooring lines, anchor, connecting elements, and floats. The choice of mooring configuration depends on the location, environmental conditions, and operating principles of the floating WEC. McCormick has given a few suggestions on the mooring system's chose according to the WEC's position (McCormick, 2013), that both slack the mooring and tension mooring, which is suitable for deep water situations. But tension mooring is not recommended for shallow water, due to impact of the relatively large tidal amplitude.

Possible mooring configurations mainly consist of three categories: single point, spread, and dynamic positioning configurations. For single point mooring, the floating device is moored to a mooring point in the ocean. The floating device can align itself to the waves, winds, and currents, and *Table 1* describes the types of single point mooring configurations in use (Faizal, 2014).

Table 2-1 Types of single point mooring configurations (Faizal, 2014)

Single point mooring

Turret mooring	A turret is a device that is directly built into the floating device and attached to the seabed mostly using catenary anchor lines. A bearing arrangement on the turret allows for weathervaning of the floating point absorber
Fixed tower mooring	A tower is installed with a turntable to carry the mooring line to allow weathervaning of the point absorber. A fixed tower will work well if the water depth and wave heights are not so high.
Catenary anchor leg mooring (CALM)	In this system, a catenary moored buoy is used instead of a fixed tower. The device can weathervane and CALM system can be applied to deeper waters.
Single anchor leg mooring (SALM)	In this system a single vertical tensioned mooring leg is installed instead of multiple catenary anchor lines used in CALM.
Articulated loading COLUMN (ALC)	The ALC system is more of a combination of the fixed tower and the SLAM system. The swivels are located above the water which allows for weathervaning of the point absorber. This system may five rise to a lot of difficulties during maintenance.
single point mooring and reservoir (SPAR)	The SPAR system can be part of a large CALM buoy. This system can also be used for storage purposes (e.g., oil).

For spread mooring, the floating device is anchored to the seabed using a set of mooring lines and is not allowed to revolve in any direction. Spread moorings are suitable for use in deep water and in applications which are not very sensitive to the direction of the incident waves (Barltrop, 2004). On such occasions, due to the weathervaning restrictions, the wave and current forces on the floating device as well as the mooring system will be really high (Chakrabarti, 1994, Harris, 2004, Paik. Et al. 2007).

Dynamic positioning is a computer-controlled mooring system. By using thrusters or propulsion on the device or the mooring line, the floating device is maintained at the desired positon (Eriksson, 2007, Kelly, 2007). An analysis of system performance is required to optimise the design, and a robust and efficient dynamic positioning or mooring system is essential for improving the efficiency of the WECs using this.

2.2 State of the art

In process of wave energy extraction, complex wave diffraction, radiation together vorticity formation and wave over-topping may also take place (Falcao, 2010). It is considerably difficult to represent such phenomena theoretically. Most of previous research studies have been conducted to investigate wave energy device by physical tests or numerically under some assumptions. Some of the studies have been reviewed as follows.

2.2.1 In terms of single device

Candido et al. (2011) investigated a wave energy device with two coaxial axisymmetric bodies in both frequency and time domain. The amplitude restrictions have been taken into consideration. The power take-off system has been further developed into a non-linear hydraulic model. The characteristic mechanism parameter is optimized to maximize the averaged power absorption. The study indicates that the damping coefficient should be tuned to match the wave energy period to maximize the absorbed power in any irregular waves. The frequency domain approach is shown to be suitable in the modification concerning the power take-off coefficient of a device under specific frequencies of the spectrum. But the drawback is that the non-linear effect cannot be captured.

The true behaviour of ocean waves is highly nonlinear, thus the time-domain model of a WEC system is essential to observe the effects on the performance of a WEC. A frequency-based model is not suitable to model the system's characteristics (Yavuz et al., 2011). The linear model of the WEC system could be used in simulations in which the wave frequency is assumed to be stable. However, the linear model approximation becomes insufficient when put under variable conditions. Thus, Pierson–Moskowitz's or the JOWNSWAP spectrum is preferred to model the behaviour of real sea waves (Rodriguez and Soares, 2001). In general, the prediction of long-term wave energy production is based on the significant wave height and energy period at the given sea site. Saulnier et al. (2011) looked at this problem from the other aspects; the wave group and spectral bandwidth of sea states. The wave energy converter is simulated with a realistic power take-off device in real sea states. A conclusion can be drawn that the performance of an isolated WEC is not sensitive to wave direction, and the bandwidth is therefore characterized for the purpose of estimating wave energy production.

For many previous studies, they are often assessed with reference to the linear assumption for incoming waves. Tedeschi et al. (2011) found linear techniques are not suitable since the wave energy device performance is quite different when irregular waves are considered. Thus they analysed the influence of irregular waves on the power absorption with different control techniques in the case of a point absorber in heave motion. Truong and Ahn (2012) also investigated the control of a WEC

device in irregular waves. They focused on real-time control and developed a model to forecast the incoming random waves with high adaptability and accuracy. As a result, the proposed model can be applied to predicting ocean waves at a given site in advance without requiring old time-series data.

Flocard and Finnigan (2012) performed an experimental study on the performance of a pitching type point absorber in intermediate depth water under both regular and irregular wave conditions. The device was tuned to match the dominant wave periods during the year. The power capture efficiency was improved by modifying the device inertia to switch the wave energy converter to a natural frequency. The results show a capture which could be improved by 70–100% under larger regular waves and 35-55% for irregular waves. A common finding can be drawn from this study is that the power capture will achieve its peak value when the incoming wave frequency is close to the natural frequency of the device. The natural frequency can be shifted by added inertia without an extra control unit being required.

Falcao et al. (2012b) developed a frequency domain model when studying a particular WEC device, where the power was derived from an unsteady flow inside a non-uniform body, in both regular and irregular waves. The device had a cylindrical buoy. The numerical investigation included the optimization of the acceleration tube, geometry and a PTO damping coefficient for several wave periods. The results showed that a longer tube and longer piston stroke with a small damping coefficient had the largest energy absorption. However, the study was based on a mathematical model with several simplified assumptions - some of them may not be suitable, such as the geometry of practical prototype. The model should be improved to present an analysis if complemented by a more rigorous numerical approach based on the finite volume method.

Chen and Duan (2012) studied the dissipation forces of a heaving point absorber. The wave diffraction and radiation around the point absorber bodies were considered based on the linear potential theory. The velocity potential was described by using the boundary integral method involving green functions and a multi-domain boundary element method used to study the resonant motion of a water column. The results indicated that this method had a good order of accuracy in characterizing the additional damping effect for the floating body at resonance. The coefficient of the dissipation term came from experiments or CFD computations.

Heikkinen et al. (2013) studied an oscillating wave energy converter with two degrees of freedom motion. The model was a horizontally placed cylinder submerged below the free surface. The interaction between the wave and the converter was studied by way of the potential flow theory. The force on the converter was calculated by integrating the surface pressure, which was derived from potential flow and Euler’s equations. This highlighted that the phase shift is a vital parameter for the

power capture ratio, thus the phase should be tuned for each wave period to improve the power efficiency in this thesis.

Vicente et al. (2013) studied the nonlinear dynamic of a floating point absorber with a tight mooring line. The numerical model consisted of a hemispherical buoy in regular and irregular waves and a tight mooring cable, which was modelled as a spring. The power take-off was modelled by a simplified system of a linear spring and damper. A proper time-domain model was used due to the nonlinear behaviour caused by restoring the forces in both a gravitational and horizontal direction.

Chaplin (2013) examined a new concept, Seaweaver; a surging type of wave point absorber from an economic point of view. The concept was a floating body whose central area moves in resonance with the swell motion of an ocean wave. The performance of the point absorber was investigated in both physical tests and numerical simulations by Flow 3D solver, which uses a fractional areas/volumes approach to define problematic geometry, and a free-gridding technique for mesh generation.

Zurkinden et al. (2014) conducted a time domain model to investigate a wave point absorber's hydrodynamic behaviour in a 3D condition. The point absorber was a semi-submerged hemisphere oscillating around a pivot point. The results indicated the linear potential theory had a good agreement with the experimental results when the waves were less steep. The non-linear hydrostatic restoring force included viscous drag which was essential to predicting the dynamics of the wave energy converter under steep waves.

Cordonnier et al. (2015) reviewed a particular wave pint absorber SEAREV. The development process regards of economy in the last two decades has been reviewed. A developed economic model has been used to estimate the cost of energy of twenty full-scale prototypes within an array

Barbarit has made a great contribution to wave energy research in terms of control strategy and device arrays. Barbarit et al. (2004) started to investigate control strategies for wave energy devices. In this work, the equation of the motion of a device was solved in a semi-analytical method. The equation of the motion of the mechanical oscillator was restricted to a single degree of freedom motion. The result showed that the latching control is able to improve the amplitude of the motion under different wave frequency. In 2015, Barbarit (2015) established a database in terms of the hydrodynamic performance of the different types of Wave Energy Converters (WECs). The database relies on the collection of WECs under operation and a mathematical analysis of the data available in the previous literature. The database summarizes the annual average capture width ratio (CWR) of the different prototypes and this data is used to derive what the relationship is between CWR and the different WEC operational principles.

Other than the literatures listed in this section, most of the state of the art tools, as indicated in Emre and Ismail (2017), estimate the performance of the wave energy converter by boundary element method (BEM) codes with the potential theory or a linear radiation-diffraction model with additional correction terms for any non-linear effects. These include the non-linear Froude–Krylov force as in Retes et al. (2015), or the parameterised viscous drag forces as in Bhinder et al. (2015) and Nematbakhsh et al. (2015). In order to account for the viscous effects prior to force calculation, the viscous damping term, which relies on a coefficient C_d, needs to be considered in the Morison equation. Bhinder et al. (2015) developed a viscous model in the potential time domain for use in evaluations of the performance of a surging type point absorber. The modified drag term in the radiation force had great improvement since the radiation force from frequency domain is found to be under estimated when compared with the CFD results. However, the correction terms are based on a parameterization of the non-linearity of the system, and therefore there are cases where a more complete and rigorous model approach is needed.

2.2.2 In terms of array

The study of wave energy farming was first studied by Evans (1979). In his work, a theoretical model for the mean power absorption in the array was developed assuming that the hydrodynamic coefficients of each isolated device within the array are known. In wave energy farming, the performance is normally calculated through the interaction factor (q), which is the ratio of the total power absorbed by the array divided by the number of devices and additionally, the power absorbed by an isolated device. A q factor larger than one indicates a positive effect on the power production from the array. A literature on the q factor of point absorbers in irregular sea-states has been reviewed by Babarit and Hals (2011) recently. The use of factor q is widely applied in the studies with an array problem involved.

On the other hand, the power generated by a single point absorber within a linear PTO system will fluctuate with irregular waves. The wave energy farm can reduce the power fluctuations with multiple point absorbers to smooth the power output to the grid (Vicente et al, 2013; Babarit, 2013). Rahm et al. (2012) conducted two physical tests with three WECs with linear PTO in operation with 19.7 days in real sea conditions. The results showed that the standard deviation of the power output is reduced with the number of WECs in a given array.

Moreover, wave energy converters should be designed to achieve maximum efficiency. The device is normally equipped with a large buoy to resonate with the incoming wave at the peak frequency of the given sea site. With one or few degrees of freedom, the resonance is usually band-limited. Garnaud and Mei (2010) examined the theoretical power extraction by a compact array of small buoys

using the linear theory based method. They found that in practical terms, only a large buoy with a size 1/6 of a wavelength can be resonated without the control device of the power take-off system, while the bandwidth increases as the size of the buoy decreases. A wave energy converter array with many degrees of freedom has a broader bandwidth with a higher efficiency. Thus, a compact array of wave energy devices built with the same amount of material as a large device is potentially more efficient in natural seas. Additionally, a conclusion was drawn; the extraction rate of the power take-off system should be equal to the rate of radiation damping as such that a peak power absorption can be achieved.

Borgarino et al. (2012) presented a parametric study on the array of wave energy converters. The wave energy converter was modelled as a heaving cylinder and surging barge. They focused on the influence of interactions between bodies (9-25 devices) on the overall yearly energy production of the array. An important guide for the design of WECs array that can be drawn from this study is that the power take-off system bandwidth should be tuned for a large harvest range rather than the optimal value for a resonant frequency. This is such that the overall power production can be increased.

Babarit et al. (2012) investigated the annual mean power absorption of eight full-scale point-absorber devices installed on the Swedish west coast. In their study, different working principles were considered, and their characteristic mass, including CWR and the power take-off (PTO) load at five locations. The power matrices of each WEC were computed in the frequency domain at different wave conditions so that the annual power production energy could be found. An additional time domain model was used to characterize the non-linear effects. However the estimation of the power loss in the absence of this additional viscous term was omitted while the drag coefficient was taken from the existing experimental data. The incorporation of the viscous force in a BEM solver demonstrates that their technique was successful in achieving the additional damping for the floating body while the coefficient of the viscous term relied on the experimental measurements or CFD calculations. The existing useable data, mostly from the experimental test, had a difference of 30–40% in the value of the coefficients. Therefore the prediction of the drag coefficient for a complex geometrical structure with random motion remains a major issue (Bhinder et al. 2012). The CFD can be employed for dealing with this problem.

Later on, Barbarit (2013) provided a guideline for designing the layout of arrays of oscillating point absorbers with analysis by BEM. The results show that the park effect ($q<1$) appears to be negligible for small arrays of devices, but the park effect becomes more important with the increasing number in rows in the WECs. Therefore, the number of rows should be kept minimal.

Renzi and Dias (2013) and Renzi et al. (2014) developed a semi-analytical model to investigate the dynamic behaviour of flap-type wave energy converter and applied a numerical model to analyse the configurations of WECs in the array. The near-resonant mechanism was accountable for the occurrence of a constructive effect in the array ($q > 1$). A parametric study was conducted to identify the near-resonant phenomenon which has the potential to increase the power efficiency of the array. The results also highlighted that non-symmetric layouts of WECs can be less effective.

Stratigaki et al. (2014) performed an experimental test with twenty-five scaled heaving point absorbers under both short and long-crested waves. Different geometric configurations and wave conditions were considered. A numerical model was developed based on the linear theory and the power take-off (PTO) was modelled to dampen out the WEC's motion. The results indicated that significant wave height in the downstream of the WEC array was reduced by 16.3% to 18.1% for long-crested waves and 11.2% to 18.1% for short-crested waves.

Göteman et al. (2014) investigated the hydrodynamic interaction between devices using a boundary element potential flow solver to reduce the power fluctuations and to improve the power output. In their work, the impact factor of an array included the number of devices, the separating distance between the units, the global and local geometries of the array and wave conditions was considered. But the hydrodynamic interaction due to scattered waves was neglected. Later on, Göteman et al. (2015) investigated the wave energy parks using an analytical method. The array of point-absorber WEC was studied and the results validated against a numerical method based on potential flow theory. The benefit of such a method was the low computational cost and the model included up to and over a thousand interacting devices. The irregular wave data was collected from the Swedish west coast. This study focused on park geometry and reducing the power fluctuations.

Cordonnier et al. (2015) reviewed a particular wave pint absorber called SEAREV. The development process regarding the economy in the last two decades was reviewed. A developed economic model was used to estimate the cost of the energy of twenty full-scale prototypes within an array.

It can be seen that most of the literatures that they adopted the potential-theory based model to address the array problem. Their advantages and disadvantages were reviewed by Folley et al. (2012), see Table *2-2*. It shows that there is no universal numerical technique that can be applied to a WEC array. Some physical experimental tests of WEC arrays have been published recently by Lamont-Kane et al. (2013) and Stratigaki et al. (2014). However, these physical tests only use scaled small point absorbers and the point absorbers with full scales are still lacking in investigation.

Table 2-2Numerical modelling techniques for WECs array (Folley et al., 2012)

	Potential flow models				Spectral wave models				
	Linear BIEM	**Semi-analytical techniques**	**Time-domain formulation**	**Nonlinear BIEM**	**Boussinesq**	**Mild-slope**	**Supra-grid**	**Sub-grid**	**CFD**
Fundamental									
Definition of hydrodynamics	Implicit body surfaces	Explicit coefficients	Implicit body surfaces		Explicit absorption layers		Explicit absorption layer	Explicit source strength	Implicit fluid flow
Nonlinear wave dynamics	Not capable			Implicitly capable	Implicitly capable	Not capable	Implicitly capable for phase-averaged dynamics		Implicitly capable
Nonlinear dynamics	Not capable		Implicit solver		Explicit absorption layers		Explicit absorption layer	Explicit source strength	Implicit solver
Vortex shedding	Explicit inclusion by linearisation		Explicit inclusion		Explicit inclusion		Explicit inclusion		Implicit inclusion
WEC radiation	Implicitly capable				Explicitly capable		Not capable	Explicitly capable	Implicitly capable
Diffraction	Implicitly capable				Explicitly capable		Approximated by phase-decoupled refraction-diffraction		Implicitly capable
Variable bathymetry and marine currents	Not capable				Implicitly capable	Implicitly capable	Implicitly capable		Implicitly capable
Computational									
Primary dependent	Number of panels	Complexity of function	Number of panels and complexity of equations	Number of panels	Number of cells		Number of cells		Number of cells
Secondary dependent	Number of frequencies and directions		Number of time-steps		Number of time-steps		Number of frequencies and directions		Number of time-steps
Determinate of array size	Quadratic increase with number of WECs				Linear increase with spatial area		Linear increase with spatial area		Linear inc. with spatial volume
Solver	Simple and stable		Simple and poss. unstable	Complex and stable	Simple and poss. unstable	Simple and stable	Simple and stable		Complex and poss. unstable
Usability									
Required skill	Low	High	Medium	High	Medium	Low	Low	Medium	High
Software availability in 2012	Commercial code available	Research code only	Commercial code available	Research code only	Commercial code available, WEC model required		Open-source code available, WEC model required		Commercial and open-source code available
Suitability (**—highly suitable, ***—moderately suitable, **—poorly suitable, *—not suitable)**									
Localised effects	***	* to ***	***	***	**	**	*	*	****
Dynamic control	*	*	****	****	*	*	*	*	**
AEP (small WEC array)	***	***	**	**	***	***	**	***	**
AEP (large WEC array)	**	***	**	**	***	***	**	***	**
Environmental impact	*	*	*	*	***	***	****	****	**

2.2.3 In terms of methodology

In the early stage of studies about WECs in array, the computing resources are limited. The methods used at that time were mainly based on the mathematical analysis of the WECs with axis-symmetrical bodies (Budal, 1977). Only regular and unidirectional waves were considered and linear potential flow theory was used. The analytical approaches are numerically efficient but they cannot be applied in the cases with complex WEC geometry, multiple Degrees of Freedom (DoF) or irregular waves.

For the linear theory based method, Renzi and Dias (2012) developed a linear inviscid potential-flow model to study the resonance effects encountered during experiments. But they only successfully applied this to waves that were small in amplitude. Heikkinen et al. (2013) adopted the potential flow theory to investigate the effect of wave height and period together with wave energy converter size on the performance of a submerged wave energy converter. In terms of device development, this type of numerical model can estimate the performance of a particular capture device and gain great insight into the behaviour of some novel devices (Farley et al., 2011 and Alam, 2012). These numerical models can be adopted to optimize some of the key factors before experimental tests are done (Oskamp and Ozkan-Haller, 2012 and Falcao et al., 2012a).

Davis (1990) indicated that the linear theory-based solution on the performance of wave energy absorbers under steep waves was highly unreliable. The linear theory-based method assumes the flow to be linear, irrotational and inviscid. Payne et al. (2008b) carried out several studies and showed that the numerical solution matched well with the experimental results for wave conditions with moderate wave steepness (< 0.03). But for steeper waves, including wave conditions with the resonance phenomena, large inconsistencies were observed due to both non-linear and viscous effects. However, the effects of the nonlinear interaction between the waves and the WEC, particularly wave overtopping, was and remains crucial to the dynamic response and the power generation performance of the system.

A popular solution to reducing the discrepancy is considering the effect of viscosity. A damping/drag term was added into the Morrison equation to describe viscous drag. The empirical parameter employed in this method is determined through experimental data, and it may lead to significant uncertainty in numerical predictions (Babarit et al., 2012). A constant drag coefficient is not suitable for the non-uniform motion of point absorber in irregular waves. The wave-induced force is thus wrongly calculated, which will affect the prediction of the performance of the wave point absorber.

WEC with complicated geometry in non-steep wave conditions are normally studied in the frequency domain. The hydrodynamic loads, due to radiation and diffraction, are calculated by boundary

element method and the dynamic response of the WEC and can be obtained by solving the equation of motion in the frequency domain (Babarit et al., 2012). This approach has often been used in the study of optimal control strategies.

BEM-based numerical codes, such as WAMIT and ANSYS Aqwa, are able to deal with the cases of array with a restriction of the small amplitude of motions and wave steepness (with linear potential theory). Borgarino et al. (2011) investigated an array of eight floating Oscillating Surge Converters (OSWCs). The numerical models are restricted by CPU performance, hence they are limited to relatively small arrays. Another important limitation with this method is that it assumes a uniform water depth whereas, in the case of a large array of WECs, bathymetry might vary significantly (Babarit, 2013).

In order to predict the power performance more accurately, a study of a WEC device that considers nonlinear interactions using Computational Fluid Dynamics (CFD) methods is needed. CFD methods have been widely used to model complex nonlinear hydrodynamic waves and floating body interaction problems, including the analysis of several types of WEC systems by such as that by Bhinder et al. (2009), Westphalen (2010) and Paixão et al. (2011).

Schmitt et al. (2012a) used different numerical solvers to calculate the pressure distribution on an oscillating wave surge converter. The results of the fully viscous CFD codes showed a better agreement with the experimental data than the potential-based solver like WAMIT.

In the same year, Bhinder et al. (2012) employed a CFD code to quantify the drag coefficients for an oscillating wave converter with the cubic geometry in translational mode. His work indicated that the importance of viscosity for the devices with such geometry; the results showed that performance was reduced by 60% when compared to non-viscous solutions.

Rafiee et al. (2013) investigated the oscillating type wave energy converter using the smoothed particle hydrodynamics (SPH) method in 2D and 3D respectively. In their simulation, the wave over-topping phenomena was observed in extreme wave conditions. The wave was modelled based on the moving piston theory and the viscosity was modelled by a $k-\epsilon$ turbulence. The results showed that performing 3D simulations is essential since the flow at the sides of the capture body has a great impact on the performance of the device.

Yu and Li (2013) and Eskilsson et al. (2015) conducted several studies with CFD tools to model floating WECs with one or two degrees of freedom (DoF). The results compared with results from faster methods with a lower fidelity. In some CFD studies with moored WECs, a linear spring was

the simplified equivalence to modelling the mooring dynamics (Verduzco-Zapata and Ocampo-Torres, 2015).

The general conclusion is that for non-linear effects such as viscous drag and non-linear wave loading, a large impact will be on the power production estimates, thus the CFD approach should be capable of dealing with these effects for estimating power production.

2.3 Methodology review

2.3.1 Frequency domain analysis

The wave energy study was started in 1970's (Budak and Falnes, 1975a and 1975b). They focused on the maximum capture efficiency of simple geometry. The governing equation and power take-off were all assumed to be linear. The energy was captured by the oscillating motion of the point absorber. The total force on the point absorber included the wave exciting force, radiation force and hydrodynamic restoring force. The hydrodynamic parameters were obtained from a mathematical derivation (for simple geometry), experimental data or a computational code, normally based on the Boundary Elemental Method (BEM). This method has been widely used in the ship hydrodynamic research field. For a point absorber in heave motion:

$$(m + m_a)\ddot{z} = f_{ex} - C\dot{z} - \rho g V_{wet} + F_{pto} \tag{2-5}$$

m is the mass of the point absorber, m_a is the added mass, z is the displacement in gravity direction, f_{ex} is the wave exciting force, C is the radiation damping coefficient, $\rho g V_{wet}$ is the hydrodynamic restoring force, and F_{pto} is the load from power take-off system. Normally the power take-off load can be described by:

$$F_{pto} = -B\dot{z} - Kz \tag{2-6}$$

B and K are the linear damping coefficient and the stiffness strength of the power take-off system respectively. In such cases, the whole system is linear. In the frequency domain, the equation (2-5) is then:

$$Z = \frac{F_{ex}}{-\omega^2(m + m_a) + i\omega(C + B) + \rho g S + K} \tag{2-7}$$

Z and F_{ex} are the complex modulus of z and f_{ex}, {z, f_{ex}} =Re ({Z, F_{ex}}$e^{-i\omega t}$), ω is the wave frequency and S is the wetted area of the point absorber. Thus, the mean power absorption can be described by:

$$P_{mean} = \frac{1}{8C}F_{ex}^2 - \frac{C}{2}\left(A - \frac{F_{ex}}{2C}\right)^2 \tag{2-8}$$

Where A= $i\omega Z$ is the complex amplitude of the $\dot{z}$. For a given wave condtion, the P_{mean} is decided by Z which is dominated by power take-off parameter B and K. When $A = \frac{F_{ex}}{2C}$, the maximum power absorption can be achieved:

$$P_{max} = \frac{1}{8C}F_{ex}^2 \tag{2-9}$$

$$\omega = \sqrt{\frac{\rho g S + K}{m + m_a(\omega)}} \tag{2-10}$$

$$B = C(\omega) \tag{2-11}$$

Equation (2-9) to (2-11) stand for the optimal conditions for the point absorber resonant under a curtain wave frequency.

This points out that the power take-off damping coefficient should be tuned to match the hydrodynamic coefficient in order to maximise power extraction.

2.3.2 Time domain analysis

It can be seen that linear theory is the most basic assumption in terms of frequency domain analysis. However, most of the wave-structure interactions are non-linear and the frequency domain is not suitable to capture the hydrodynamic behaviour between the waves and wave energy device. Thus in 1980, a time domain analysis based on Fourier transmission was developed by Jefferys (1980) to study the performance of an oscillating wave energy device. The governing equation can be described by:

$$(m + m_a)\ddot{Z}(t) + \rho g V_{wet}(t) + \int_{-\infty}^{t} L(T - \tau)\ddot{Z}(\tau)d\tau = f_{ex}(t) + F_{pto} \tag{2-12}$$

$$L(t) = \frac{2}{\pi}\int_0^{\infty} \frac{C(\omega)}{\omega} sin\omega t d\omega \tag{2-13}$$

The time analysis has the advantage of introducing the time term into the equation to consider nonlinear effects, such as controlling the power take-off system when the waves are irregular. The drawback, on the other hand, is that time analysis requires much more computing resources compared to frequency analysis. One of the solutions is to consider the distribution of probability density instead of the full time series (Falcao, 2004).

2.3.3 Analytic method

The hydrodynamic response of the wave energy device can be calculated from the frequency or time domain analysis and theoretically, the hydrodynamic effect can be calculated through the analytical method, empirical method and numerical method.

In the analytic method, the hydrodynamic force is assumed to be made up of radiant force and diffraction force. The diffraction force includes the F_{DF} due to the floating body and Froude-Krylove force F_{FK}

$$F_{dynamic} = F_r + F_d \tag{2-14}$$

$$F_r = m_a\ddot{z} + C\dot{Z} \tag{2-15}$$

$$F_d = \int_S \frac{\partial\phi}{\partial t} nds = \int_S \frac{\partial(\phi_l + \phi_D)}{\partial t} nds = F_{FK} + F_{DF} \tag{2-16}$$

F_r and F_d are the radiant force and diffraction force respectively, and ϕ_l and ϕ_D stands for the velocity potentials of incident and diffraction wave respectively.

The velocity potential function can be obtained by the analytical method and most of the analytical method is based on linear wave theory. In reality, the viscous effect is crucial in some cases. The performance of the wave energy converter, especially at the resonance, will be overestimated without considering the effect produced by the viscosity as mentioned in the work by Babarit (2012). Thus in his work, the viscous effect was described by one or two damping terms in the equation of motion. During the last couple of decade, the analytical method has been used in the analysis of wave energy devices (Ekrsson et al., 2005, Garnaud and Mei, 2010 and Babarit, 2012). This method can effectively estimate the performance of a simple wave energy device but the drawback is that it cannot be used on a device with complex geometry.

2.3.4 Boundary Element Method (BEM)

The Boundary Element Method (BEM), also named the Boundary Integral Element Method (BIEM), is a strategy to deal with structures with complex geometry. The governing equation is:

$$\nabla^2\phi=0 \tag{2-17}$$

In the BEM method, the potential function (ϕ) is derived from the Green function G (p,q) and p and q stand for the filed point and source point respectively.

$$\alpha(p)\phi(p)+\int_{s_b}\left(\phi(p)G_n(p,q)-\phi_n(p)G(p,q)\right)ds_b=0 \tag{2-18}$$

$$G_n=\nabla G\cdot n,\phi_n=\nabla\phi\cdot n \tag{2-19}$$

Where s_b the boundary of flow field, $\alpha(p)$ stands for boundary inner corner, n is the normal factor pointing out of the surface. With the Dirichelet and Neumann boundary condition, the linear equations can be derived by discretizing the boundaries and thus can be used to obtain the potential function.

With the potential function, the pressure can be derived from the Bernoulli equation to calculate the hydrodynamic force and subsequent momentum:

$$p=-\rho(\phi_t+\frac{1}{2}\nabla\phi\cdot\nabla\phi+gz) \tag{2-20}$$

$$F=\int_s pnds;M=\int_s pn\times rds \tag{2-21}$$

r is the length vector to the rotating centre. The extra viscous damping term can be added to the force and the damping coefficient is obtained in the same way as the analytical approach. It should be noted that this method is based on the potential theory. For the interaction between the small point absorber and the infinite flow field, the key assumptions are as follows:

- The flow is incompressible, inviscid and irrotational.
- Coriolis forces and Surface tension are neglected.
- Pressure at the free surface is uniform and constant.
- Incident wave is harmonic wave with small amplitude, the wave length is much longer than the wave height.
- The fluid field is infinite with even bottom.
- The point absorber has simple harmonic oscillating motion.

The frequency domain BEM method is widely used to build up the hydrodynamic model to estimate the performance of the wave energy device.

2.3.5 Potential theory with viscous effect

In offshore engineering, a semi-empirical equation, the Morison equation, can be used to estimate the hydrodynamic force on a structure with relatively small dimensions. In the Morison equation, the viscous damping term is described by the drag force:

$$F_{drag} = -\frac{1}{2}\rho C_d A(\Delta u)|\Delta u| \tag{2-22}$$

Where C_d is the drag coefficient, A is the characterize length of the point absorber, Δu is the relative speed between flow and the point absorber. The value of C_d is decided by many factors such as Re number, the size of the point absorber and Keulegan-Carpenter (KC) number. It should be noted that the C_d is restricted by the geometry of the point absorber and the empirical data for the point absorber is still lacking. It is common to use computational fluid dynamic (CFD) to calculate this parameter.

2.3.6 Navier-stokes equation method

In the design of the point absorber, it is more suitable to adopt an NS equation-based CFD method to consider the full non-linear problem. In some cases, the point absorber will suffer a huge wave incident force and it always comes with situations such as wave breaking and overtopping. In such cases, the nonlinear interaction between the wave and the point absorber is quite remarkable. The time domain BEM cannot capture such phenomena which will affect the performance and survivability of the point absorber device. Amongst all of the available methods, the NS approach can handle all complex nonlinearities in the hydrodynamic behaviour of the system. This method will be discussed in the next chapter.

2.4 Chapter closure

In this chapter, the recent literature about point absorber wave energy converters has been reviewed. The primary approaches adopted in the mentioned work includes the analytical method, the frequency and time domain boundary element method (BEM) and the Navier-stokes (NS) based computational fluid dynamic (CFD) method.

Table 2-3 summary of each method in studying point absorber WEC

<table>
<tr><th>Method</th><th>Viscous effect</th><th>Complexity</th><th>Wave-structure interaction</th><th>Accuracy</th><th>Wave condition</th></tr>
<tr><td>Analytical</td><td rowspan="3">Empirical/ CFD</td><td rowspan="2">Wave radiation and diffraction theory</td><td>Linear</td><td rowspan="3">Based on hydrodynamic coefficient</td><td rowspan="2">Small amplitude</td></tr>
<tr><td>Frequency domain BEM</td><td rowspan="2">Partial nonlinear</td></tr>
<tr><td>Time domain BEM</td><td rowspan="2">Full interaction in time domain</td><td rowspan="3">Fully nonlinear</td></tr>
<tr><td>CFD</td><td>NS equation</td><td>Fully nonlinear</td><td>Good</td></tr>
</table>

For a different research emphasis, each method has its own advantages and drawbacks, see Table 2-3. More specifically:

- The analytical method can effectively estimate the performance of a simple wave energy device but the drawback is that it cannot be used on a device with complex geometry.
- Frequency and time domain BEM can handle more complex and realistic models. The frequency domain approach uses the same strategy as the analytical method to solve the radiation and diffraction problems in order to estimate the hydrodynamic force. This approach is limited to wave structure interaction problems with small motion amplitude. The time domain BEM considers the solution of motion equation at every step thus it can be used to study the non-linearity of the whole system. But time domain BEM cannot capture phenomena such as viscous flow separation, wave plunging, breaking, and overtopping.
- The NS based CFD method is a solution that considers all of the problems in the wave structure interaction. The major drawback is that it requires huge computational resources and the time cost is much more than the others. The time cost relies on the computer CPU, numerical algorithm, convergence control, mesh quality and the complexity of the wave-point absorber system. Thus the accuracy and efficiency of this method should be balanced.

3 Methodology

3.1 CFD approach

As discussed in the previous chapter, the potential flow models resolve simplified versions of the Navier–Stokes equations which is averaged in the gravity direction with the assumption of continuous fluid. They are suitable for simulating wave propagation, refraction, diffraction and shoaling problem. They are ideal to simulate large domains up to hundreds of km and time series due to the relative simple equations involved. However, the potential flow models present limitations derived from their initial assumption such as considering a uniform velocity profile along the water column. Since vertical velocities are not accounted for, it is not possible to fully characterize regions where there are dominant dynamics such wave impacts on a highly reflective structure. The models are also unable to consider complex free surface such as plunging waves. Moreover, wave breaking itself cannot be simulated.

This is why and when the CFD approach comes into play. There are three main methods adopted in the Computational Fluid Dynamic (CFD):

1. Panel methods. The method is ordinarily progressed from a closed-form solutions by a potential flow. This method discretizes the surfaces of complex shapes with panels. The panel methods is still being used, both on its own and in combination with other methods. The major benefits are that the panels only discretise the surface of the fluid domain, which brings a huge reduction in computational cost when compared to the other methods below.
2. Euler equations. This equation promised to provide a more accurate solution with regard to transonic flows. The Euler model is also simplified by removing the terms describing viscous effect. Other than panel methods, the whole fluid domain has to be discretised.
3. Navier-Stokes equations. The Navier-Stokes model includes viscous terms and it provides the most faithful representation of realistic fluid behaviour. This method requires an increased computational resource due to the discretisation of viscous terms.

The advanced approach to modelling highly non-linear system of floating point absorbers is to use Navier–Stokes simulations. This family of computational fluid dynamic (CFD) methods inherently includes non-linear waves, viscous flow and large amplitude motion effects. A fluid flow with physical properties such as velocity, pressure and temperature is usually described by a mathematical model which is defined as a system of Partial Differential Equations (PDEs). The governing equations needs to be discretised into a numerical analogue before it can solved by computer. In CFD, the

equation discretisation is usually performed by three main schemes: The Finite Difference Method (FDM), Finite Element Method (FEM) and Finite Volume Method (FVM).

The FDM employs the idea of Taylor expansion to solve the second-order PDEs in the governing equations of flow. In this method, the derivatives of PDE are transformed into discrete quantities of variables in a series of algebraic equations whose variables are stored at the nodes of the mesh. This method is straightforward and has a higher order of discretisation accuracy. The FDM is simple but it can only employ structured mesh for simple geometry. When considering complicated geometry, unstructured mesh can be used in FEM. The computational domain is then subdivided into a finite number of elements. In each element, the unknown variables are determined and defined at the nodes. The discretisation is based on the integral formulation obtained by different interpolation functions. FEM is famous and has an ease in application around complex structures while this is offset by the increased computational requirements compared to FDM.

In the Finite Volume scheme, the methodology is mathematically similar to FEM in some cases and it can be used for both structured and unstructured meshes. In FVM, the computational domain is separated into a finite number of cells known as control volumes. It transforms the PDEs into discretized algebraic equation over the finite cells. The algebraic equation is integrated over each volume element and the unknown parameters are solved based on the conservation laws for control volume. The discretisation process is achieved at points within the control volumes using a direct and efficient integration method, thus it requires less computer cost compared to FDM, thus it is more widely used in common CFD packages.

3.2 Numerical implementation in OpenFOAM

Traditionally, the design of the wave energy converter and other offshore structures has been carried out by applying potential-based formulations and proper physical experimental tests. These two approaches have been proven to be both operable and reliable. The numerical wave-structure interaction involves studying all of the processes including local wave propagation and deformation due to the impact on the structures. Primarily, the model for wave-structure interaction needs to be able to simulate the all of the processes of wave transformation at a local scale such as reflection, diffraction, and non-linear behaviour in realistic waves, to ensure that the waves that reach the structure are represented correctly.

Thus it is essential that a comprehensive study should be done to accurately evaluate the power production of a single wave energy converter or wave energy farm before deployment of WECs in real sea.

In the present study, the wave structure interaction was performed by using the solver built upon the open source code OpenFOAM (Weller et al, 1998), which is a collection of C++ libraries that are developed for the purpose of solving continuum problems with the finite volume discretisation procedure. OpenFOAM has an extensive range of features to solve problems ranging from complex fluid flows involving chemical reactions, turbulence and heat transfer, to solid dynamics. It also features applications for pre- and post-process cases, including mesh generation tools (blockMesh, snappyHexMesh), functions to set and modify field values, libraries for mesh decomposition and sampling data. OpenFOAM is an open source platform, which means that the user can modify the source code to deal with any specific problem. For a more detailed explanation of OpenFOAM, the reader is referred to the paper by Weller et al. (1998).

Among all of the codes in libraries of OpenFOAM, a RANS based multiple phase solver together with Volume of Fluid (VoF) methodology, named interFoam, has been selected to investigate free surface waves. There are some examples of studies related to interFoam solver with the particular application of interest by the following respective authors: Liu and Garcia (2008) adopted interFoam solver to calculate velocity profiles for a flow around a partially submerged cylinder and the results are validated against the experimental. data; Berberovic et al. (2009) simulated droplet impact and crater formation and compared the results with their experiments; Ishimoto et al. (2010) modified the solver of interFoam to simulated atomization caused by cavitation in the gasoline injection system. Deshpande et al. (2012) simulated plunging jet flow and compared the velocity and liquid fraction profiles with their experiments.

In terms of the numerical simulation of wave structure interaction, the interFoam solver based Navier stokes method with volume of fluid method has also been adopted by:

1. Dalzell (1999) specified the inlet boundary to represent extreme wave formulation;

2. Ning et al. (2008, 2009) studied the propagation of focused wave groups by different wave heights summed up and the results of the numerical study and physical experiment tests were found to be in good agreement;

3. Gerald et al. (2010) adopted Reynolds averaged Navier Stokes (RANS) solver based interFoam to simulate the interaction between water fluid and a cylinder;

4. Li et al. (2012a, 2012b) represented ship motion in a tank sloshing in the numerical way and they compared the results in terms of ship motion and wave forces on both the tank and the

ship's hull with the ones from the experimental test. It can be seen that RANS solver is capable of modelling the nonlinear fluid structure interaction accurately;

5. Schmitt et al. (2012b) compared the solution from the fully viscous CFD solvers to experimental tank tests. This paper lists the examples of applications of CFD tools in the design of an oscillating surge wave energy converter and highlights the necessity of physical experiments in wave energy research. The results also show that the OpenFOAM solution agreed well with the cases using experimental data;

6. Chen et al. (2014) focused on the interactions between regular waves and a vertical cylinder. The results were confirmed by a physical test;

7. Higuera et al. (2014) modified the interFoam solver to simulate a porous coastal structure on breakwater under irregular waves;

8. Schmitt and Elsaesser (2015) used interFoam based solver to assess the applicability of the simulation of oscillating wave surge converters (OWSC) under irregular wave conditions. The simulation used a linear equation to represent the wave energy converter power take-off system in surge motion. It is found that the RANS solver based model reproduced the experiment with high accuracy.

The following sections are devoted to implementation of the features stated so far in the OpenFOAM solver. The purpose of the section below is to describe the Finite Volume discretization method used for solving Navier-Stokes equations. Firstly, the Reynolds-averaged Navier-stokes equation and volume of fluid (VoF) approach will be described. This is followed by a discussion of the discretization approaches of the general transport equation, time marching, boundary conditions and the PIMPLE algorithm. Finally, the linear algebraic equations and the moving grid method will be brief introduced.

3.2.1 RANS modelling

This section gives an overview of the implementations used in OpenFOAM. Firstly the equation of motion for a full viscous fluid is introduced here. The governing equation was first introduced by Navier and Pisson, and corrected by Saint-Venant and Stokes. The equation can be described as:

$$\frac{\partial u_i}{\partial x_j} = 0 \tag{3-1}$$

$$\frac{\partial u_i}{\partial t} + \frac{\partial u_i u_j}{\partial x_j} = -\frac{1}{\rho}\frac{\partial p}{\partial x_i} + \frac{\partial}{\partial x_j}\left(v\left(\frac{\partial u_i}{\partial x_j} + \frac{\partial u_j}{\partial x_i}\right)\right) \tag{3-2}$$

i,*j*=1, 2, 3 stands for the streamwise, crossflow and stream normal direction, respectively. p and v are the pressure and kinematic viscosity of the fluid involved.

The benefit of utilizing the NS equation is introducing the damping effect through the viscous stress within the fluid flow. In practical cases, flows are usually turbulent with fluctuations in fluid properties over a small amount of space and time. Turbulence flow is the flow region characterized by the formation of eddies. Flow properties can vary rapidly in both space and time. Chaotic turbulence flow is still a challenge for the description of fluid particles. Direct Numerical Simulation (DNS) solves NS equations for the whole range of spatial and temporal scales; the computational cost is extremely high at even a low Reynolds number. Large Eddy Simulation (LES) deals with large scale eddies by resolving them spatially through a finer computational grid than the Reynolds-averaged Navier-stokes (RANS) model. In terms of computational costs and efficiency, LES is more time consuming, but more accurate and reliable than RANS, especially for flows in which large scale unsteadiness is significant (Pope, 2000). Detached Eddy Simulation (DES) is a hybrid method that combines the RANS and LES methods. This model switches automatically between RANS and LES model depending on the ratio of the turbulence length scale and the largest cell size at the near wall region. This saves on computational cost by using a RANS formulation in the areas with low levels of separation. For a more in-depth discussion of turbulence modelling, the reader is suggested to the relevant literature, such as that by Wilcox (1998), Pope (2000), and Lesieur (2008).

The principal character is to distinguish the RANS model rather than the LES or DNS models as the desired strategy to deal with turbulence effects. Directly solving these fluctuated properties requires an ultra-fine mesh in which the cells are designed to be the same size as the viscous eddies. The resolution is too high to be practical for most problems. Because of this, turbulence is only simulated with a simplified model when the turbulence effects are significant. For this purpose, the flow properties are decomposed into time-average and time-varying components:

$$u_i = \bar{u_i} + u_i' \tag{3-3}$$

$$p = \bar{p} + p' \tag{3-4}$$

The Equation (3-3) and Equation (3-4) are the Reynolds decomposition. The Reynolds averaged approach defines the averaging component by assuming steady turbulence with a series of key simplifications due to the nature of the averaging operator. Thus the Reynolds-Averaged Navier-Stokes (RANS) equations can be obtained from Equation (3-1) to Equation (3-4).

$$\frac{\partial \overline{u_\iota}}{\partial t} + \frac{\partial \overline{u_\iota u_J}}{\partial x_j} = -\frac{1}{\rho}\frac{\partial \bar{p}}{\partial x_i} + \frac{\partial}{\partial x_j}\left(v\left(\frac{\partial \overline{u_\iota}}{\partial x_j} + \frac{\partial \overline{u_j}}{\partial x_i}\right)\right) - \overline{u'_\iota u'_J} \tag{3-5}$$

$$\frac{\partial \overline{u_\iota}}{\partial x_j} = 0 \tag{3-6}$$

The nonlinear term $\overline{u'_\iota u'_J}$ represents the fluctuation in turbulent stress. These stresses, namely Reynolds stresses, are normally written as $\tau_{ij} = \overline{u'_\iota u'_J}$. With this notation, the stresses stemming from all the averaged components are combined into one that represents the effects of the turbulent variations. It can be seen that the number of unknown variables is increased therefore the equation set is not closed. To close the RANS equations, a turbulence model for the Reynolds stress is required. A common method is to employ the Boussinesq approximation to relate the Reynolds stresses to the mean velocity gradients (Boussinesq, 1877).

$$\tau_{ij} = v_T\left(\frac{\partial \overline{u_\iota}}{\partial x_j} + \frac{\partial \overline{u_j}}{\partial x_i}\right) - \frac{2}{3}\delta_{ij}k \tag{3-7}$$

When k is defined as the kinetic energy for turbulent variations, δ_{ij}=1,$if\ i = j$ and δ_{ij}=0 $if\ i \neq j$.

There are several turbulence closure models that have been proposed to provide solutions to the stress term. Each turbulence is developed for predicting a certain type of flows and there is no unique turbulence model that satisfies all of the turbulent flows that may be required. Therefore, it is vital to select the most applicable model for the case study.

A brief description of the turbulence models used in this work has been given below.

- **$k - \epsilon$ Model**

The $k - \epsilon$ model is one of the most widely used models in the CFD approach. It was developed to solve the problem of free shear flow under the assumption of isotropic turbulent viscosity (v_T). It is specially designed for flows with relatively small pressure gradients. The $k - \epsilon$ model is not suitable for cases where a large adverse pressure gradient exists such as a flow with curved boundary layers and flow separation.

The standard $k-\epsilon$ model is a two transport equation model with a turbulence kinetic k and dissipation rate ϵ (Lauder and Sharma, 1974). It is a semi-empirical model and the transport equation for k is derived from the exact equation, while the coefficients of the transport equation for ϵ are empirically derived. In the derivation of the $k-\epsilon$ model, it assumed that the flow is fully turbulent without considering the effects of molecular viscosity.

$$v_T = \frac{C_\mu k^2}{\epsilon} \tag{3-8}$$

$$\frac{\partial \mathrm{k}}{\partial t} + \frac{u_i \partial k}{\partial x_i} = \frac{\tau_{ij} \partial u_i}{\partial u_j} - \epsilon + \frac{\partial}{\partial x_i}\left(\left(v + \frac{v_T}{\sigma_k}\right)\frac{\partial k}{\partial x_i}\right) \tag{3-9}$$

$$\frac{\partial \epsilon}{\partial t} + \frac{u_i \partial \epsilon}{\partial x_i} = C_{\epsilon 1}\frac{\epsilon}{\mathrm{k}}\tau_{ij}\frac{\partial u_i}{\partial u_j} - \rho C_{\epsilon 2}\frac{\epsilon^2}{k} + \frac{\partial}{\partial x_i}\left(\left(v + \frac{v_T}{\sigma_\epsilon}\right)\frac{\partial \epsilon}{\partial x_i}\right) \tag{3-10}$$

Where $C_{\epsilon 1} = 1.44$, $C_{\epsilon 2} = 1.92$, $C_\mu = 0.09$, $\sigma_k = 1.0$, and $\sigma_\epsilon = 1.3$

- **$k-\omega$ Model**

The standard k–ω model (Wilcox, 1988) is also a two transport equation model with turbulence kinetic k and turbulent frequency ω. This model improves on the accuracy of the model for predicting free shear flows and low Reynolds number flows. The model is expressed as:

$$v_T = \frac{k}{\omega} \tag{3-11}$$

$$\frac{\partial \mathrm{k}}{\partial t} + \frac{u_i \partial k}{\partial x_i} = \frac{\tau_{ij} \partial u_i}{\partial u_j} - \beta^* k\omega + \frac{\partial}{\partial x_i}\left((v + \sigma^* v_T)\frac{\partial k}{\partial x_i}\right) \tag{3-12}$$

$$\frac{\partial \omega}{\partial t} + \frac{u_i \partial \omega}{\partial x_i} = \frac{\alpha\omega\tau_{ij} \partial u_i}{k\partial u_j} - \beta^* \omega^2 + \frac{\partial}{\partial x_i}\left((v + \sigma v_T)\frac{\partial \omega}{\partial x_i}\right) \tag{3-13}$$

Where $\alpha = 0.52, \beta = 0.075, \beta^* = 0.09, and\ \sigma = \sigma^* = 0.5$

In the study of interactions between waves and a floating structure, the $k-\epsilon$ turbulence model shows that the turbulence in the near-wall boundary layer is not simulated well due to poor separation prediction. The $k-\omega$ model, on the other hand, takes the near-wall cell space into account. This model improves on the accuracy of predicting the turbulence in the near-wall boundary. So does the viscous wake and the transport of turbulent kinetic energy within it. In the recent years, a mix of these two models has been developed by a weighted function to switch between the $k-\epsilon$ and $k-\omega$ model based on the wall distance (Menter et al., 2003). This is the most suitable approach for modelling a point absorber in waves.

- **$k-\omega$ *SST* Model**

The $k-\omega$ *SST* model looks very much alike the $k-\epsilon$ and $k-\omega$ model with the common equation for the k equation. An expression that link ϵ and ω can be described by:

$$\epsilon = \beta^* k\omega \tag{3-14}$$

The turbulent kinematic viscosity v_T that stands for turbulent energy dissipation in RANS equations, is now calculated as:

$$v_T = \frac{ak}{\max(a\omega, SF_2)} \tag{3-15}$$

$$S = \sqrt{2S_{ij}S_{ij}} \tag{3-16}$$

$$S_{ij} = \frac{1}{2}\left(\frac{\partial u_i}{\partial x_j} + \frac{\partial u_j}{\partial x_i}\right) \tag{3-17}$$

$$F_2 = \tanh\left(\left(max\left(\frac{2\sqrt{k}}{\beta^*}, \frac{500v}{y^2\omega}\right)\right)^2\right) \tag{3-18}$$

Thus the $k-\omega$ *SST* model is represented as follow:

$$\frac{\partial k}{\partial t} + \frac{\partial u_i k}{\partial x_i} = p_k + \beta * kw + \frac{\partial}{\partial x_i}\left((v + \sigma_k v_T)\frac{\partial k}{\partial x_i}\right) \tag{3-19}$$

$$\begin{aligned}\frac{\partial \omega}{\partial t} + \frac{\partial u_i \omega}{\partial x_i} = \frac{\gamma}{v_T}p_k - \beta\omega^2 + \frac{\partial}{\partial x_i}\left((v + \sigma_\omega v_T)\frac{\partial \omega}{\partial x_i}\right) \\ + 2(1 - F_1)\sigma_{\omega 2}\frac{1}{\omega}\frac{\partial k}{\partial x_j}\frac{\partial \omega}{\partial x_j}\end{aligned} \tag{3-20}$$

$$F_1 = \tanh\left(\left(min\left(max\left(\frac{\sqrt{k}}{\beta^*\omega y}, \frac{500v}{y^2\omega}\right), \frac{4\sigma_{\omega 2}\, k}{CD_{k\omega}y^2}\right)\right)^4\right) \tag{3-21}$$

$$p_k = \min\left(\frac{\tau_{ij}\partial u_i}{x_j}, 10\beta^* k\omega\right) \tag{3-22}$$

$$CD_{k\omega} = \max\left(2\rho\sigma_{\omega 2}\frac{1}{\omega}\frac{\partial k}{\partial x_i}\frac{\partial \omega}{\partial xi}, 10^{-10}\right) \tag{3-23}$$

Where the y is the distance from a given point to the nearest wall, F_1 and F_2 are weighted functions varying from 0 to 1. The major difference that distinguishes the $k-\epsilon$ and $k-\omega$ model is the cross-diffusion term ($CD_{k\omega}$) which helps to switch turbulence models in the boundary layer zone ($k-\omega$)

into the free flow region ($k-\epsilon$) smoothly. The coefficients in the previous equations can be calculated through:

$$\gamma = F_1\gamma_1 + (1-F_2)\gamma_2 \tag{3-24}$$

$$\beta = F_1\beta_1 + (1-F_2)\beta_2 \tag{3-25}$$

$$\sigma_k = F_1\sigma k_1 + (1-F_2)\sigma_{k2} \tag{3-26}$$

$$\sigma_\omega = F_1\sigma_{\omega 1} + (1-F_2)\sigma_{\omega 2} \tag{3-27}$$

In OpenFOAM, the default values of these coefficients are similar to the ones provided by Menter et al. (2003), see Table 3-1.

Table 3-1 Coefficients for The $k-\omega\ SST$ model:

$\gamma_1 = 0.5532$	$\beta_1 = 0.075$	$a = 0.31$
$\gamma_2 = 0.075$	$\beta_2 = 0.0828$	$\beta^* = 0.09$
$\sigma_{k1} = 0.85$	$\sigma_{\omega 1} = 0.5$	
$\sigma_{k2} = 1$	$\sigma_{\omega 2} = 0.85616$	

3.2.2 Free surface

For all of the wave-structure interaction problem, the calculation for a free surface must be involved. Basically, there are several methods to capture the fluid interface. The Marker and Cell (MAC) method is the earliest numerical method used for solving time-dependent, free-surface problems (Harlow and Welch, 1965). It adopts a fixed, Eulerian grid of control volume. The location of the fluid in the grid is determined by a set of marker particles that move with the fluid without the influence of the fluid's properties (volume, mass etc.) and any change therein. Grid cells containing markers are treated as liquid, while those without markers are considered as air. The interface between the grid cells with marker particles and their adjacent cells which are air is defined as free surface. The marker particles track the fluid volumes instead of tracking the interface directly. Therefore, the boundaries of each fluid volume then build up the free-surface between air and fluid. Most of the relatively early publications adopted the MAC method to simulate free-surface flow and some modifications have been made to improve the accuracy of this method. Normally, the large number of marker particles limits the MAC method to be only suitable for 2D simulations due to the high computational cost. Another drawback for the MAC method is that the marker particles are not good at tracking flow processes, especially for converging and diverging flows.

The method adopted in OpenFOAM to capture the free surface is the Volume of Fraction (VoF) technique (Hirt and Nichols 1981), which is widely used in modern commercial and open source CFD codes (see the book by Ferziger and Peric (2002) for more applications). The main advantage of the VoF approach is that it can easily represent complex free surface profiles without mesh motion. It is used to capture the interface between air and water with a higher resolution (see Figure *3-1*). The VoF equation is expressed as:

$$\frac{\partial \alpha}{\partial t} + \frac{\partial (\alpha u_i)}{\partial x_j} + \frac{\partial (\alpha(1-\alpha)u_r)}{\partial x_j} = 0 \tag{3-28}$$

where $u_r$the velocity field is suitable to compress the interface, u_r is computed at each cell face through the direction and magnitude of max velocity at the interface region; a is the fluid fraction in each cell. The value of a in a cell ranges from 0 to 1. If the cell is completely filled with liquid then a =1 and if the cell is empty (air), then its value is 0. At the interface, the value of a is between 0 and 1.

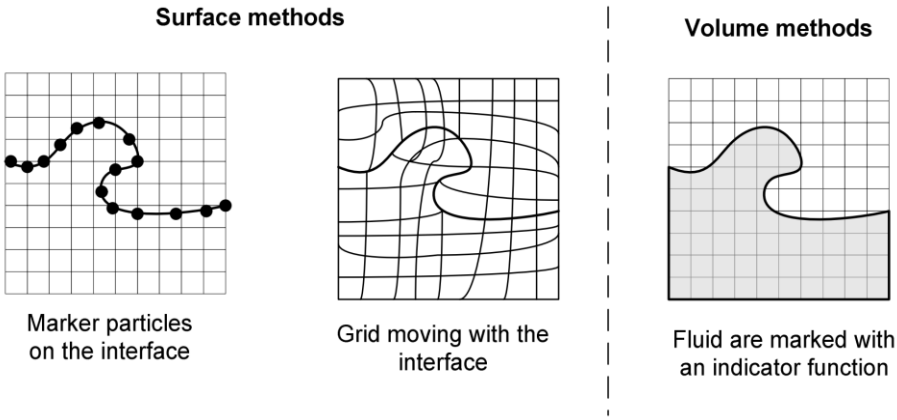

Figure 3-1 Typical methods for free surface tracking

The artificial term in Equation (3-28) is active only in the interface region due to the extra term $a(1- a)$. The density r and dynamic viscosity n at any point in the computational domain are defined as weighted averaged of the volume fraction of two phases:

$$\begin{aligned} \rho &= \alpha \rho_{air} + (1-\alpha)\rho_{water} \\ \mu &= \alpha \mu_{air} + (1-\alpha)\mu_{water} \end{aligned} \tag{3-29}$$

The surface tension in the source term will be defined as:

$$f_\sigma = \frac{\sigma k(x) \nabla \alpha}{|\nabla \alpha|} \tag{3-30}$$

Where S is the surface tension coefficient, $k(x)$, which is expressed as follows, is the curvature of the surface interface calculated at cell faces.

$$k(x) = \nabla \cdot \frac{\nabla \alpha}{|\nabla \alpha|} \tag{3-31}$$

In the multiple phase model resolving loop, the flux limit technique can provide a highly accurate and explicit solution for the given system. A high resolution scheme, such as the VanLeer scheme, is used to avoid solution fluctuation caused by exhibit shock, large gradients or discontinuities in the computational zone. The Monotonic Upstream Centered Scheme for Conservation Laws (MUSCL) scheme is the first high-order, total variation diminishing (TVD) scheme with second order accuracy, introduced by van Leer (1979).

In this study, the VanLeer Scheme is used to ensure the advection of the VoF function that the alpha solution is bound between zero and one. The VanLeer scheme semi-discretizes the VoF equation into the following form:

$$\frac{\partial \alpha}{\partial t} + \sum_b \phi_{low} + \sum_b \lambda_r \phi_{high} = 0 \tag{3-32}$$

Where ϕ_{low} and ϕ_{high} are the explicit flux of α with low and high order scheme respectively at the cell boundary (b). The flux limiter (λ_r) performs a switch between the two schemes depending on the gradient close to the cell. In this theory, having shared flux limiters between adjacent cells ensures the conservation of any mass. The gradient of the adjacent cells (owner cell, i, with neighbouring cell i-1and i+1) is represented by

$$r = \frac{\phi_i - \phi_{i-1}}{\phi_{i+1} - \phi_i} \tag{3-33}$$

The VanLeer flux limiter is defined as:

$$\lambda_r = \frac{r + |r|}{1 + |r|} \tag{3-34}$$

For more details, the reader is referred to the original paper by VanLeer (1974). In this study, the α value at the inlet boundary is calculated through wave elevation based on the different stokes theory.

3.2.3 Solving the RANS equation

The Reynolds-Averaged Navier-Stokes (RANS) equations in this study are solved in OpenFOAM. OpenFOAM, as with most CFD codes, uses a finite volume method for the discretization of the governing equations. The Finite Volume Method (FVM) is a numerical technique to transform RANS equations into a discretized algebraic equation over finite cells. The algebraic equation is integrated over each volume element and the dependent fluid properties are then calculated. In the finite volume method, the conservation equation is strictly fulfilled by turning some of the terms into face fluxes at the cell boundary and matching the face fluxes entering the cell to the ones leaving the neighboring volumes, as stated by Ferziger and Peric (2002), In OpenFOAM, the RANS equations are integrated over a controlled volume to derive the transport equation, as described below

$$\int_{CV} \frac{\partial \bar{u}_i}{\partial x_j} dV = \int_S \bar{u}_i \cdot n dS \tag{3-35}$$

$$\int_{t-\Delta t}^{t} \left(\frac{d}{dt} \int_{CV} \frac{\partial \bar{u}_i}{\partial t} dV + \int_{CV} \frac{\partial \overline{u_i u_j}}{\partial x_j} dV - \int_{CV} \frac{\partial}{\partial x_j} \left(\nu \left(\frac{\partial \bar{u}_i}{\partial x_j} + \frac{\partial \bar{u}_j}{\partial x_i} \right) \right) dV - \int_{CV} \tau_{ij} dV \right) dt = \int_{t-\Delta t}^{t} \left(\frac{1}{\rho} \int_{CV} \frac{\partial \bar{p}}{\partial x_i} dV \right) dt \tag{3-36}$$

where S is the border enclosing a control volume CV, n is the unit normal vector pointing outward of the surface f, which is shown in Figure 3-2. This discretisation scheme ensures that the exact same physical quantity leaving one control volume enters the adjacent control volume.

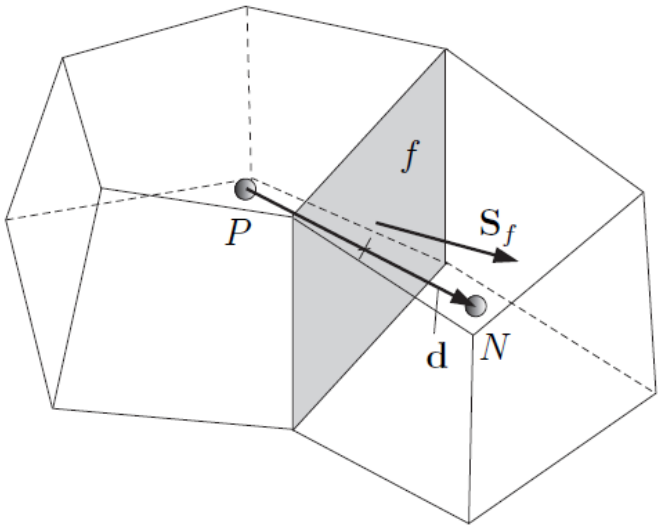

Figure 3-2 Two adjacent finite control volume

3.2.3.1 Spatial discretisation

Throughout this study, the computational domain has been discretized into an unstructured mesh with hexahedra and tetrahedral cells. In the unsteady wave structure interaction problem, the time domain was divided into a finite number of time steps (t) and the solution was obtained by marching Δt from its initial condition. The terms in the momentum Equation (3-36) from left to right are: temporal term, convective term, diffusive terms (3rd and 4th terms) and source term, respectively. Each term describes a physical process that changes the dependent variable ϕ in a different way. Since the diffusion term includes a second order derivative, the order of the numerical scheme to discretize each term is suggested to be equal to or higher than the second order to reach the second order of accuracy. All of the variables are assumed vary linearly around the calculated control volume and time.

In OpenFOAM control volume, the pressure (p), velocities (u_i) and other scalar variables are stored at the centre (P and N in Figure 3-2) of the control volume (CV). Each term in the momentum Equation (3-36) needs to be discretised into the whole domain. For a transport variable ϕ in the CV:

$$\frac{\partial \phi_i}{\partial x_i} = \lim_{\Delta V \to 0} \left(\frac{1}{\Delta V} \int_V \frac{\partial \phi_i}{\partial x_i} dV\right) \approx \frac{1}{\Delta V} \int_V \frac{\partial \phi_i}{\partial x_i} dV \tag{3-37}$$

The Equation (3-37) indicates that the control volume size has a great impact on the $\frac{\partial \phi}{\partial x_i}$ within the control volume. A large gradient of $\frac{\partial \phi}{\partial x_i}$ requires a sufficient small control volume to achieve an accurate result. Throughout the cases in his study, a mesh independent study was carried out to discuss the influence of the mesh on the results.

From Equation (3-37), the variable related to the flux through the boundary of each cell can be calculated as:

$$\frac{1}{\Delta V} \int_V \frac{\partial \phi_i}{\partial x_i} dV = \frac{1}{\Delta V} \int_S \phi_i \cdot n dS \approx \frac{1}{\Delta V} \sum_{i=1}^{n} \phi_i \cdot n S_i \tag{3-38}$$

n is the number of the faces surrounding the cell.

There are many interpolation methods available in OpenFOAM. The most basic interpolation scheme is the linear interpolation option, namely Central Differencing Scheme (CDS). Equation (3-39) introduces the CDS with two adjacent cells, P and N:

$$\phi_i = f_x \phi_i^P + (1 - f_x) \phi_i^N \tag{3-39}$$

where f_x is the linear coefficient which is computed from the cell geometry; and vector **f**N and **P**N are shown in Figure 3-2. The locations of cell centers P, and N and face center, f are determined by the shape of each cell, as shown in Figure 3-2.

$$f_x = \left\| \frac{\boldsymbol{f}N}{\boldsymbol{P}N} \right\| \tag{3-40}$$

Equation (3-40) shows that the geometries of the adjacent cells strongly affects the linear coefficient f_x therefore it in turn affects accuracy and stability of the numerical method. This can conclude that for the two adjacent control volumes, there will be more errors during the face interpolation when there is a large difference in geometry between two cells; and the errors will be therefore accumulated in the entire system.

For second order of the derivative $\frac{\partial^2 \phi_i}{\partial x_i^2}$:

$$\frac{\partial^2 \phi_i}{\partial x_i^2} \approx \frac{1}{\Delta V} \int_V \frac{\partial^2 \phi_i}{\partial x_i^2} dV \approx \frac{1}{\Delta V} \sum_{i=1}^{n} \frac{\partial \phi_i}{\partial x_i} \cdot nS_i \tag{3-41}$$

This second order scheme shows that for face f, the derivate of ϕ needs to be calculated, which can be achieved by assuming that there is a linear variation of the gradient between the cell centres:

$$\left(\frac{\partial \phi_i}{\partial x_i} \right)_f = \frac{\phi_i^P - \phi_i^N}{PN} \tag{3-42}$$

Where PN is the distance between cell P and N centres in the direction of x_i

Other interpolation schemes commonly include upwind, in which the variable field at cell face center ϕ_f is also calculated from the adjacent cell before cell P or N (based on the local flow direction). An alternative for the interpolation with 1st and 2nd order of accuracy is to use the Total Variation Diminishing (TVD) schemes (Versteeg and Malalasekera, 2007) where the weighting function is used to shift the scheme between upwind and 2nd order central differencing.

3.2.3.2 Transient discretisation

Transient problems require governing equations that are discretized in both space and time. For the temporal term of a discrete equation, the Euler first-order temporal discretization scheme is the basic technique for transient problems. It can be seen that Equation (3-36) also has a time derivative term that needs to be discretized in order to obtain the discrete model. Therefore, the integration of the time derivative term in Equation (3-36) can be approximated as

$$\int_{t-\Delta t}^{t} \frac{\partial}{\partial t} \int_{CV} \frac{\partial \bar{u}_i \phi}{\partial t} dV dt = \int_{t-\Delta t}^{t} \frac{\partial \phi_i}{\partial t} V dt \approx V(\phi_i^n - \phi_i^{n-1}) \quad (3\text{-}43)$$

where superscript ^{n} and $^{n-1}$ denote the function values at the current and previous time steps of the simulation, respectively, and Δt denotes the time step itself.

In this study, the backward time discretization scheme, which uses the property values from the current and the two previous time steps, has been adopted to create a second order accuracy temporal derivative. The derivative is calculated using a Taylor series expansion with the current time and two time steps as before:

$$\phi_i{}^{n-1} = \phi_i{}^n(t - \Delta t) = \phi_i{}^n(t) - \phi_i{}^{n\prime}(t)\Delta t + \frac{1}{2}\phi_i{}^{n\prime\prime}\Delta t^2 - \frac{1}{6}\phi_i{}^{n\prime\prime\prime}\Delta t^3 + \cdots \quad (3\text{-}44)$$

$$\phi_i{}^{n-2} = \phi_i{}^n(t - 2\Delta t) = \phi_i{}^n(t) - 2\phi_i{}^{n\prime}(t)\Delta t + \frac{1}{2}\phi_i{}^{n\prime\prime}4\Delta t^2 + \cdots \quad (3\text{-}45)$$

Combining Equation (3-44) with (3-45), results in the backward temporal discretization of a cell-centered field ϕ_c:

$$\frac{\partial \phi_i}{\partial t} \approx \frac{\frac{3}{2}\phi_i^n - 2\phi_i^{n-1} + \frac{1}{2}\phi_i^{n-2}}{\Delta t} \quad (3\text{-}46)$$

The temporal derivative by backward scheme is calculated explicitly from the known (n-1) and (n-2) time step and it has a second order accuracy. All of the cell and face centered fields in the previous (n-1) and the one before (n-2) time step have been stored to be extracted for calculating the current variable field.

3.2.3.3 Time marching

For a steady problem, the time step is not always that important. Whereas for an unsteady problem, the time marching of the simulation is crucial since the convergence of the fluid fields must be achieved based on a reasonable residual control. The RANS equations represents an unsteady process since they contain the transient derivative of the velocity field. The time marching is an outer time loop after the convergence has been accomplished within each time step (inner loop). To keep the stability throughout the simulation and for the temporal derivative to be accurately represented, the cell face Courant Number, also referred to as the Courant-Friedrichs-Lewy (CFL) condition, should be set below 1. It indicates that the flow cannot travel through several cells in one time step's passing:

$$N_C = \frac{u_i}{\Delta x_i}\Delta t \leq 1 \tag{3-47}$$

3.2.3.4 Boundary condition

The boundary condition is very important to solve the system of RANS equations. For general boundaries:

• **Inlet**

The boundary condition at inlet is normally of the Dirichet type where the inflow velocity field and turbulence of the fluids (air and water in this study) are supplied. For consistency, the boundary condition on pressure is zero gradient. The turbulence quantities, such as k and omega, are not easy to specify. In this study, initial assumptions are made based on the turbulence intensity.

• **Outlet**

The outlet boundary condition is normally of the Neumann type. The outlet boundary should be placed far away from interest zone to ensure that the fluid quantities are fully developed.

Jasak (1996) indicated that the outlet boundary condition should specify the overall mass balance for the computational domain. At the outlet boundaries, the Dirichet boundary condition is specified for pressure and a zero gradient boundary condition for velocity is also applied. Overall mass conservation is guaranteed by the pressure equation. It should be noted that the pressure field defined here is dynamic pressure instead of total pressure.

• **No-slip impermeable wall**

The velocity of the fluid at the non-slip wall specifies that there is no tangential fluid velocity at the wall surface. A fixed value condition for velocity can be specified. The pressure gradient at wall boundary for two phase flow is assumed to equal the static pressure gradient ($-\nabla\rho gh$).

3.2.3.5 Pressure-velocity coupling in OpenFOAM

After the discretisation of the RANS equation, it can be seen that there are still four unknown quantities; the pressure p and the three velocity components u_i. The mass conservation equation does not have the pressure term and therefore numerical techniques are required to solve the momentum equation. The idea here is to use the mass conservation equation by applying the divergence operator onto the momentum equation. This is achieved within the pressure-momentum coupling algorithms PISO, SIMPLE and PIMPLE which are:

- SIMPLE, Semi-Implicit-Method-Of-Pressure-Linked-Equations, is used for steady-state analysis.
- PISO, Pressure-Implicit-Split-Operator, is used for transient calculation.
- PIMPLE, combination of PISO and SIMPLE, is used for transient calculation with bigger time steps than PISO algorithm.

The PIMPLE algorithm can be widely used in transient problems. For simple fluid flow, the PIMPLE method does not provide too many advantages. For more complex geometries and flow patterns, the PIMPLE algorithm will provide more advantages and can stabilize the simulation. In the PISO algorithm, the time step need to be small for fast changing flow otherwise the calculations will diverge. This will lead to a long simulation time for some cases. The PIMPLE adopts the SIMPLE steady-state scheme within each time step and use PISO for time marching. Under the SIMPLE loop created by Patankar and Spalding (1972):

1. An initial pressure field with a guessed value is used to solve the momentum equations. This will result in a discrepancy from the continuity equation.
2. The velocities from the continuity equation are then used to correct the pressure gradients. This pressure-velocity coupling sequentially changes the other to reduce the residual mass until the pressure and velocity fields are considered to be converged

Within each time step, the multi-phase model is solved in the SIMPLE loop and the turbulence models will be solved using the updated velocities and mass fluxes at the cell faces. The models presented in this research will use the transient PIMPLE algorithm, which is a mixture of PISO and SIMPLE algorithms. The structure is improved from PISO and the difference is that: the equation is under-relaxed in order to guarantee that all equations under a large time step are converged. This scheme can be explained as:

1. Discretize the momentum equation and assemble the coefficient. The momentum equation can be represented as follows, where M is the coefficient matrix that represent the implicit term, S_{u_i} represents the source term that depends on the velocity and S represents the velocity-independent source term; u_i* and p* are the unknown velocity and pressure respectively. Apply under-relaxation to help improve the stability when solving discretized momentum equation.

$$Mu_i^* = -\nabla p^* + S_U + S \tag{3-48}$$

2. Predict the momentum with pressure and velocity from previous time step (n-1) to obtain a pseudo-velocity, which does not fulfil the mass conservation equation.

$$Mu_i' = -\frac{\partial p^{n-1}}{\partial x_i} + S_{u_i}^{n-1} + \mathrm{S} \tag{3-49}$$

3. Calculate the pressure field. The coefficient matrix M is decomposed into two parts: a diagonal term, A, and an off-diagonal term, H, then the equation above becomes:

$$\mathrm{A}u_i^n = -\frac{\partial p^n}{\partial x_i} + S_{u_i'} + S - Hu_i' \tag{3-50}$$

Additionally, the velocity must fulfil the mass conversation equation

$$\frac{\partial u_i^n}{\partial x_i} = 0 \tag{3-51}$$

Combining two equations above yield:

$$\frac{\partial^2 \mathrm{p}}{\partial x_i^2} = \frac{\partial}{\partial x_i}(S_{u_i'} + S - Hu_i') \tag{3-52}$$

4. Solve process 3 iteratively until convergence has been achieved

The PIMPLE scheme is an extension of the SIMPLE and PISO scheme with further corrections to enhance on the convergence. The desired level of convergence is set by the user to balance the accuracy and computational time.

3.2.3.6 Dynamic mesh strategy

In this study, dynamic mesh actions are taken into consideration to investigate the interaction between a wave and floating wave energy device. Therefore, the wave-structure interaction involves another field (mesh) coupling problem. The Arbitrary Lagrangian Eulerian (ALE) approach has been adopted to allow the cells to move inside the fluid domain, following the motion of the device boundary. The wave energy device is assumed to be rigid so that the boundaries are not deformed.

The dynamic mesh technique can be divided into two categories:

- **Mesh deformation and displacement**, where the mesh is deformed and moved according to the moving boundary motion within one time step;

- **Topology**, when the mesh cell is compressed (enlarged) to minimum (max) level, and that cell will be removed and new one will be added between the time steps.

It should be noted that the topology may lead to conservation errors during a local re-mesh. For this reason, mesh deformation technique has less of a computational cost, fewer numerical errors and it is easier to implement.

In this study, the displacement of the points on the point absorber surface satisfies the moving boundary condition. The mesh deforms during the computations according to the motion of the object and there is no need to change the topology of the mesh itself. The positions of cell point is solved by a Laplace equation

$$\frac{\partial}{\partial x_i} \cdot \left(\gamma \frac{\partial \mathrm{U_i}}{\partial x_i} \right) = 0 \tag{3-53}$$

$$U_i = \frac{(X_i^n - X_i^{n-1})}{\Delta t} \tag{3-54}$$

Where, **U** is the point velocity that calculated by the point position X_i. In order to maintain the internal mesh quality near the cylinder wall region, four different diffusivity parameters γ are adopted in OpenFOAM based on distance between the cell node and the moving boundary:

$$\text{Uniform: } \gamma = r \tag{3-55}$$

$$\text{Linear inverse r: } \gamma = \frac{1}{r} \tag{3-56}$$

$$\text{Quadratic inverse: } \gamma = \frac{1}{r^2} \tag{3-57}$$

$$\text{Exponential inverse: : } \gamma = \frac{1}{\exp(r)} \tag{3-58}$$

Where r is the distance of the cell node to its nearest moving boundary. The mesh motion with the displacement = 0.75 diameter of the cylinder is shown in Figure *3-3* to Figure *3-6*. It can be seen that the inverse scheme performs better than the uniform setting, in which the boundary layer is going to break during the mesh motion. Within the inverse scheme, the exponential setting has the problem of non-orthogonality with 3 faces > 70 degrees and has 4 highly skewness faces with a max skewness >4.32. The linear inverse scheme and quadratic inverse scheme has similar results. But the quadratic one has a slight superiority in that the max non-orthogonality is 39.9 whereas the linear inverse scheme is 37. Thus throughout this study, the quadratic inverse scheme has been adopted.

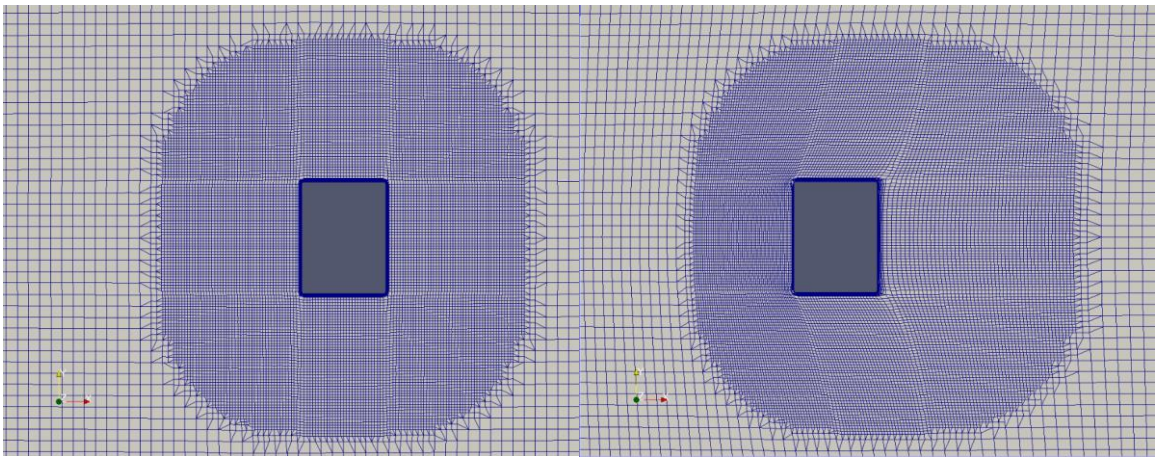

Figure 3-3 Mesh motion with uniform setting $\gamma = r$

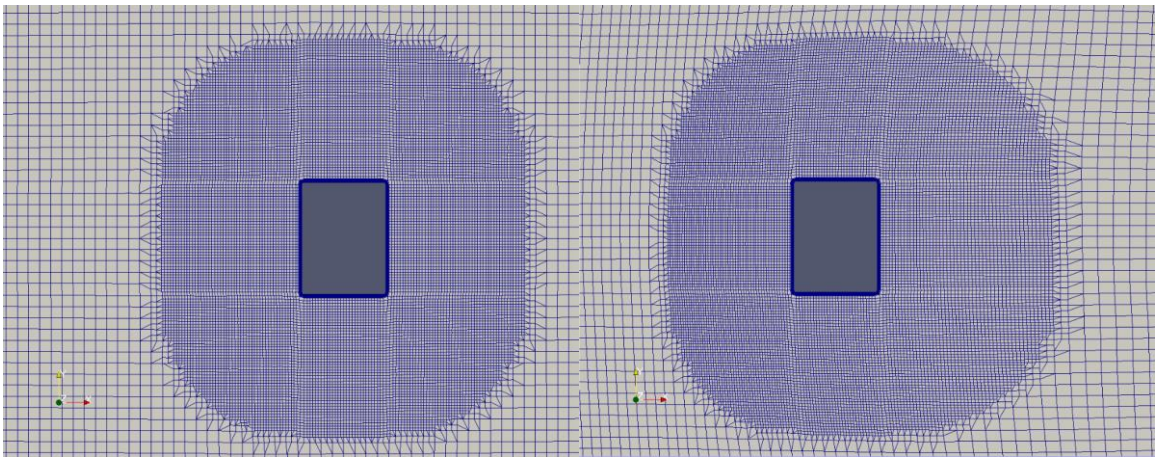

Figure 3-4 Mesh motion with linear setting $\gamma = \frac{1}{r}$

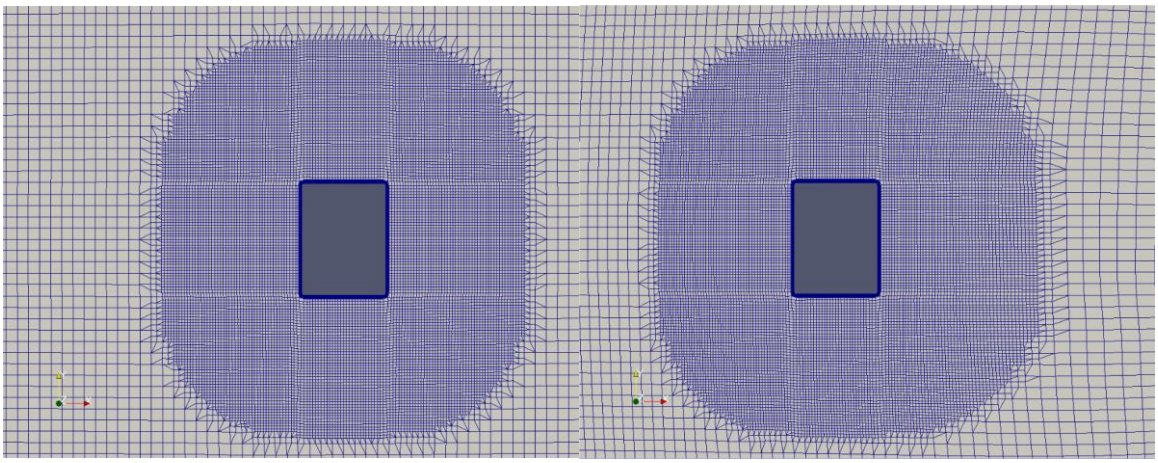

Figure 3-5 Mesh motion with quadratic setting $\gamma = \frac{1}{r^2}$

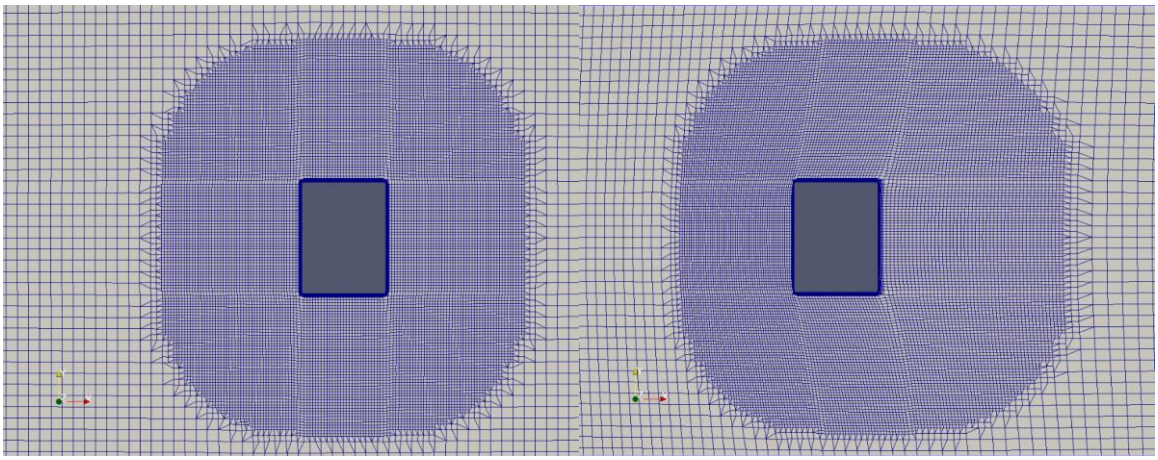

Figure 3-6 Mesh motion with Exponential setting $\gamma = \frac{1}{exp(r)}$

3.2.3.7 Solving the algebraic equations

In the last part of this chapter, the methods for solving the system of discrete equations are generally classified as either direct or iterative, and have been briefly summarized below.

- **Direct Methods**

The first technique is the direct method which adopts Gauss elimination to solve the Equation (3-59) in a direct manner, by rearranging the coefficient matrix.

$$\boldsymbol{A} \cdot \boldsymbol{x} = \boldsymbol{B} \tag{3-59}$$

Where $\boldsymbol{A}$ is the coefficient matrix, $\boldsymbol{x}$ represents unknowns of the system and $\boldsymbol{B}$ denotes the source term of the system. Ferizer and Peric (2002) indicated that the number of rearrangements is proportional to n^3, with n being the size of the matrix. This type of method requires a huge computational cost so it is not feasible to generate large matrices in current CFD models.

- **Iterative Methods**

The second type of method is vital for non-linear problems and is different from the direct method. The solving procedure starts with an initial estimation and the final solution is achieved by an iteration process. The solving procedure of the system of discrete equations can be simplified as:

$$\begin{aligned} \boldsymbol{A} \cdot \boldsymbol{x^n} &= \boldsymbol{B} - \boldsymbol{r^n} \\ \boldsymbol{e^n} &= \boldsymbol{x} - \boldsymbol{x^n} \\ \boldsymbol{A} \cdot \boldsymbol{e^n} &= \boldsymbol{r^n} \end{aligned} \tag{3-60}$$

In contrast to direction methods, the approximate solution $\boldsymbol{x}^n$ after n iterations has a residual r^n. The residual represents the absolute error $\boldsymbol{e}^n$ in the solution of a particular variable. The aim of this method is to reduce the residual to zero in the iteration process. The convergence criteria is decided from the magnitude of the residual. It is important to find an efficient iterative solver for the particular application in order to improve the convergence speed. There are several iterative solvers available in the OpenFOAM package, such as the preconditioned conjugate gradient (PCG) method and generalized geometric-algebraic multi grid (GAMG) method. For more details, the reader is referred to work by Ferizger and Peric (2002) and Saad (2003).

Another common method to improve the convergence and to stabilize the iterative solution process to employ under-relaxation. Under-relaxation slows down the changes in flow variable between iterations by introducing a blending factor. A blender factor of 1 means that no under-relaxation employed; the new solution accounts for entirely the results for this time step. A blender factor of 0 means that the solution is entirely composed from the previous solution. The blender factor within (0, 1) describes the solution of the system depending on both the new and old iterations. The optimum under-relaxation factor is different for each problem and there is no general rule for all problems. Normally, the blending factor is decided based on experience or previous calculations.

3.3 Chapter closure

In this chapter, the implementation that adopted in OpenFOAM was presented in order to solve the RANS equation. Three different turbulent models were provided to close the NS equation. The VoF method with MULES scheme was used to capture the sharp free surface. The spatial and transient discretisation approach was then introduced and the focuses are on the 2nd order scheme to achieve the results with a higher order of accuracy. The brief introduction about the boundary condition and pressure-velocity coupling method has also been provided. Moreover, the dynamic mesh strategy that was used to simulate the point absorber motion under waves has been discussed and the results show that the moving mesh with a quadratic inverse distance scheme is the most robust strategy.

Four types of error may occur during the process of OpenFOAM simulation and they can be summarized as:

- Discretization error: The results highly depend on the spatial and transient discretisation scheme. The use of cell size, geometry, time step and interpolation scheme may yield different orders of accuracy. So much so that a grid independent study is required for each study and the interpolation scheme should be discussed within the application;

- Initial input and Boundary condition: The geometry of the structure may not be exactly the same as the ones in the real world would be. The boundary conditions represent the flow behaviour in an approximate way. The whole computational domain will be contaminated if the boundary is not set properly;

- Modelling error: The complex wave-structure interaction cannot be fully represented by the NS equations (including turbulent model, free surface…);

- Numerical error: The solution to the algebraic equation requires a small residual guarantee the converge of each step, otherwise the error may grow and affect the results of the numerical study.

4. Wave generation

Numerical wave flumes are considered to be an effective tool to support the design and regulation of costal, ocean and offshore structures, since the size of any physical experimentation is limited by the size of the wave tank, which leads to scaling effect errors. Numerical wave generation is a basic, but important, requirement in coastal and ocean engineering studies. If the simulation is not accurate, all of the errors will accumulate to affect the final simulation results. There are now various options available in the literature and, according to the wave implementation methods, they can be divided into two categories (Figure 4-1): waves generated by piston-type maker and artificial waves. The waves in the first category are generated by simulating the motion of a laboratory wave maker by way of a moving mesh; while the method relating to the second category cannot be achieved in a physical wave tank experiment. An artificial wave is generated at the inlet boundary of the computation domain based on the analytical solution of wave theory; this can also be achieved by, for example, adding a source function term into the fluid momentum equation in the wave-generating region. Both of these methods need an effective absorbing technique to prevent the reflected wave from affecting incident waves in the whole domain.

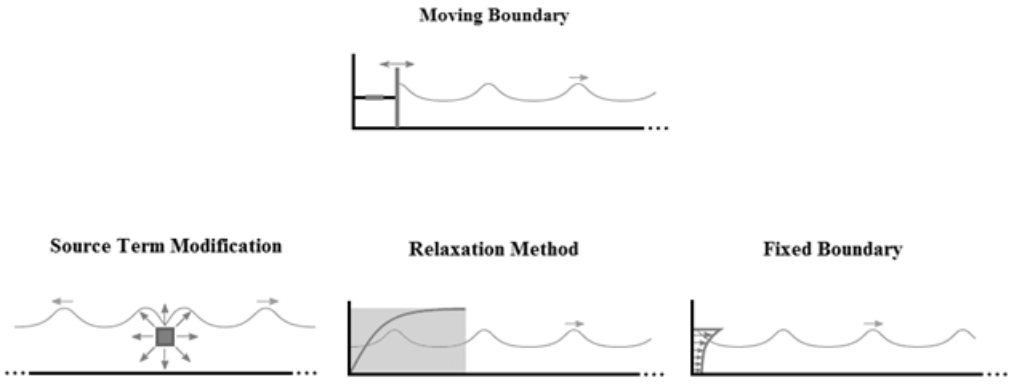

Figure 4-1 Two types of wave generation methods

The most common method used in a physical wave tank to generate waves is through the movement of a paddle, which can be a flap or piston. The classical wave maker theory was first developed by Havelock (1929), and he derived an analytical solution for the surface waves produced by the piston and flap wave -maker based on the linear theory in a water basin. The theory was further verified experimentally through a piston-type wave maker by Ursell et al. (1960) and Flick and Guza (1980). Later on, the linear wave maker theory was extended to a three-dimensional condition (Newman

2010). However, the solutions above are based on the small wave amplitude assumption; a higher wave amplitude field is governed by the nonlinear theory. The second-order wave maker theory has a long history. Some investigators use the Stokes expansion technique to keep the terms up to the second order in wave maker motions. At the early stage, the second order solutions were only applied in the two-dimensional wave tank. Ottesen-Hansen et al. (1980), Sand (1982) and Sand and Donslund (1985) derived the second-order long wave generation theory for use with physical experimental models. Hudspeth and Sulisz (1991) developed a complete second order mathematical model for both the flap and piston type wave-paddle pattern and the theory was later amended by Schaffer (1996). In that paper, the homogeneous wave field is successfully generated by a wave paddle with second order motion. Numerical wave models based on the Boussinesq equation and shallow water equations are validated against the physical test by Zhang (2005) and Hu et al. (2000) respectively. Li and Williams (2000) developed a second order theory in a three-dimensional wave basin.

As the models in the previous literature do not show detailed information in the vertical direction, advanced numerical wave flumes should be based on the Navier-Stokes (NS) equations. The flow is discretized in all three directions, as opposed to as in the shallow water and Boussinesq equations. In ocean wave research, the main challenge for wave generation based on NS equation is how to locate the free surface. The free surface can be tracked either by the mesh-based approach or meshless method. For the purpose of this thesis, the focus is on simulations using the mesh-based approach: which is the volume of fluid (VOF) method to capture the free surface together with a NS equation solver. It is assumed that the volume fraction α (air or water), velocity and pressure exist as variables in this simulation.

In the potential flow solver, wave absorption can be achieved by a relaxation method following work by Larsen and Dancy (1983). In this method, a desired target solution is implemented to cancel out incoming waves over a certain zone in space, normally referred to as a relaxation or damping zone.

4.1 Fixed boundary Wave Generation

Artificial wave generation is carried out through a customized boundary field to impose constraints on the variables such as pressure, velocity and volume fraction with a two-phase flow solver, originally proposed by Mayer et al. (1999). The customized boundary condition is implemented in many wave generating models, since the analytical expressions for free surface and the velocity distribution throughout the gravity direction are given. The new boundary condition as an input is added to the solver for regular and random wave generation. To take a wave based on 2nd order wave theory as an example:

$$U_{horz}(z,t) = \alpha \cdot \left[\frac{Hgd \cdot \cosh\big(k(z+d)\big)\cos(kx-\omega t)}{2\omega\cosh(kd)} + \frac{3H^2\omega k \cdot cosh\big(2k(z+d)\big)\cos(2(kx-\omega t))}{16\sinh^4(kd)}\right] \quad (4\text{-}1)$$

$$U_{vert}(z,t) = \alpha \cdot \left[\frac{Hgd \cdot \sinh\big(k(z+d)\big)\sin(kx-\omega t)}{2\omega\cosh(kd)} + \frac{3H^2\omega k \cdot sinh\big(2k(z+d)\big)\sin(2(kx-\omega t))}{16\sinh^4(kd)}\right] \quad (4\text{-}2)$$

$$\alpha_{VoF}(z,t) = \begin{cases} 0, air\ z > \eta \\ 1, water\ z \le \eta \end{cases} \quad (4\text{-}3)$$

Where U_{horz} and U_{vert} are the horizontal and vertical velocity on the inlet boundary respectively, H is the wave height, d is the water depth, η is the wave elevation, z is the vertical coordinate to describe wave motion (z=0 for still water level) and α_{VoF} is the volume of fraction. The velocity is only calculated when the cell face is below the free surface.

Again, with further increase of wave height, the 2nd order wave can no longer represent the wave surface. Another theory is needed to characterize the waves with a larger amplitude. Therefore, the fifth order stoke waves are taken into consideration. There are several fifth order stokes wave theories available due to the research of pioneers, and the theory stated by Fenton (1985) is applied in this work. The expressions for the free surface are given below. For more details, the reader is referred to the original paper.

$$\begin{aligned} k\eta(x) = \mathrm{kd} &+ \epsilon\cos(kx) + \epsilon^2 B_{22}\cos(2kx) + \epsilon^3 B_{31}(\cos(kx) - \cos(3kx)) \\ &+ \epsilon^4(B_{42}\cos(2kx) + B_{44}\cos(4kx)) \\ &+ \epsilon^5(-(B_{53}+B_{55})\cos(kx) + B_{53}\cos(3kx) + B_{55}\cos(5kx)) \end{aligned} \quad (4\text{-}4)$$

The methodology was further developed by the Morgan et al. (2010) and Afshar (2010) in OpenFOAM; a numerical wave solver was developed to generate and absorb through the relaxation method by Jacobsen et al. (2012). In this method, the velocity and volume fraction are relaxed to the numerical solution with the utilization of a weighting average operation, which is applied in the domains adjacent to the inlet boundaries. Additionally, the relaxation technique is capable of wave

generation and absorption at the same time. It also guarantees that the incident wave is unaffected by reflected waves from both the inlet and outlet boundary. The relaxation technique is described as:

$$\phi = \beta_R \phi_{calculated} + (1 - \beta_R)\phi_{analtical} \tag{4-5}$$

$$\beta_R(x) = 1 - \frac{exp((x - x_s)^{3.5}) - 1}{exp(x_e - x_s) - 1} \tag{4-6}$$

Where β_R is the relaxation coefficient, and x_s and x_e are start and end positon of relaxation zone respectively. $\phi_{analtical}$ is the variation of velocity, pressure and elevation as the function of space and time, and it can be combined with different wave theory. The β_R is zero at the inlet and outlet boundary and it is one at the end of relaxation zone. The exponential constant "3.5" can be modified to fulfil different requirements.

In addition to the relaxation method, the following boundary was adopted before the simulation. The numerical wave tank bottom is defined as a solid wall condition which is:

$$\begin{aligned} u_n &= 0 \\ \frac{\partial p}{\partial \vec{n}} &= 0 \\ \frac{\partial \alpha}{\partial \vec{n}} &= 0 \end{aligned} \tag{4-7}$$

Where $\vec{n}$ is the unit normal vector to the boundary.

The outlet is set to be the Dirichlet type (with a fixed value of the dependent flux variable) when the velocity vector points out of the domain. This is done to increase the stability of the outlet. The inlet boundary condition is set so then the ϕ function follows those of the waves being generated in the adjacent relaxation region to ensure that all of the gradients over the inlet boundary equal zero. At the top of the computational domain, an atmosphere boundary is set so that the atmosphere pressure equals zero; and the inlet/out condition is imposed by a Neumann type to force zero gradient condition for the outflow (as defined by the flux); and for the inflow, the velocity is obtained from the patch-face normal component of the internal-cell value.

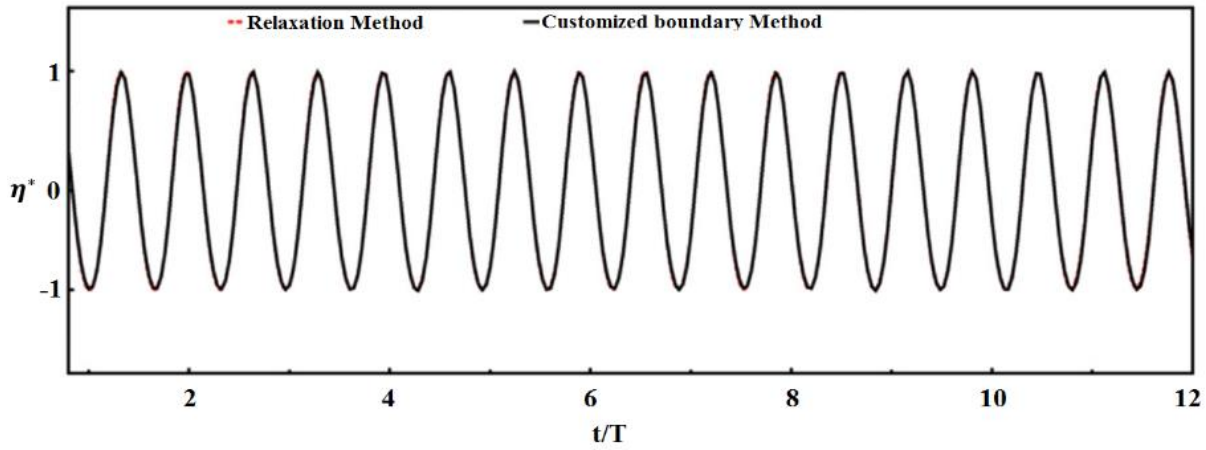

Figure 4-2 Time series of dimensionless wave elevation η^* for two wave generation methods

The time series of wave elevation* (η^*) recorded at two wavelength away from inlet is plotted in **Error! Reference source not found.**2 for the two wave generation methods. It can be seen that there is no discrepancy between the two methods; and the results are further validated below.

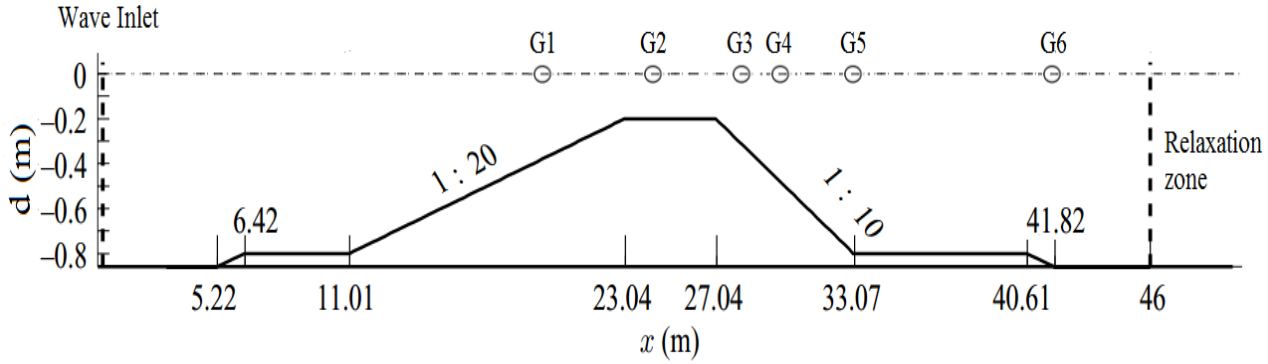

Figure 4-3 Sketch of the wave tank to verify wave elevation against numerical results by Luth et al. (1994)

Error! Reference source not found.3 shows a physical wave tank for a wave propagation test with different water depths and steepness (Luth et al., 1994 and Dingermans, 1994). The experiment results have been discussed by other researchers such as Janseen et al. (2006), Morgan (2011) and Engsig-Karup et al. (2006). The wave tank was 46m long and 0.86m deep; and the details of the submerged obstacle are shown in the figure above. The waves were generated at the left boundary and a wave absorber was installed to eliminate any reflected waves; the markers (G1-G6) were at the free surface stand for wave gauges. The incident waves are regular waves with a period of 2.86s and 0.04m in height. The courant number was set to be 0.5 and the results were recorded after twenty wave cycles when the wave profiles became steady. Figure 4-4 Comparison of wave elevation between OpenFOAM simulation and Physical Experimental results at different wave probes

4 shows the comparison between the OpenFOAM and physical experimental results. The free surface elevation was calculated at each location above the obstacle. Both the numerical and experimental results indicate that the wave profiles deformed into a higher wave crest and relatively shallow trough, especially at the top of the shoal when the wave crest height was almost twice the trough depth. During the propagation over the obstacle, the wave height will increase due to the reduced water depth and it reaches the maximum at the end of flat top of the obstacle. The wave profile becomes unstable with the appearance of a secondary crest after the primary. This can be seen from G1 and G2 in Figure 4-4 Comparison of wave elevation between OpenFOAM simulation and Physical Experimental results at different wave probes

4. The secondary crest is well developed when the incident wave approaching the rear slope of the obstacle; and from this position afterward, the wave height begins to reduce as the wave travels from shallow water to deep water region with appearance of a third crest. In general, the comparison shows a good agreement of the surface elevations between the numerical results and experimental results, except for a minor difference of the wave peaks. This may be caused by wave dissipation and dispersion in the numerical calculation.

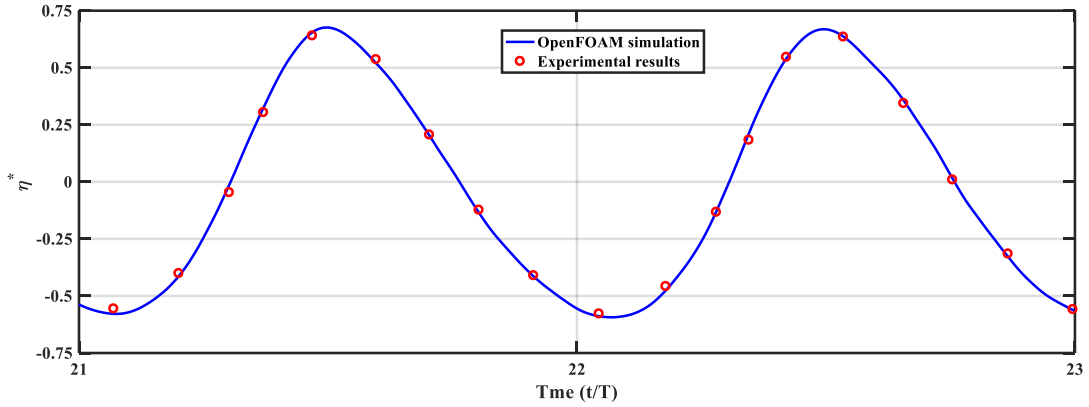
OpenFOAM simulation
Experimental results
0.75
0.5
0.25
0
-0.25
-0.5
-0.75
21
22
23
Tme (t/T)

G1

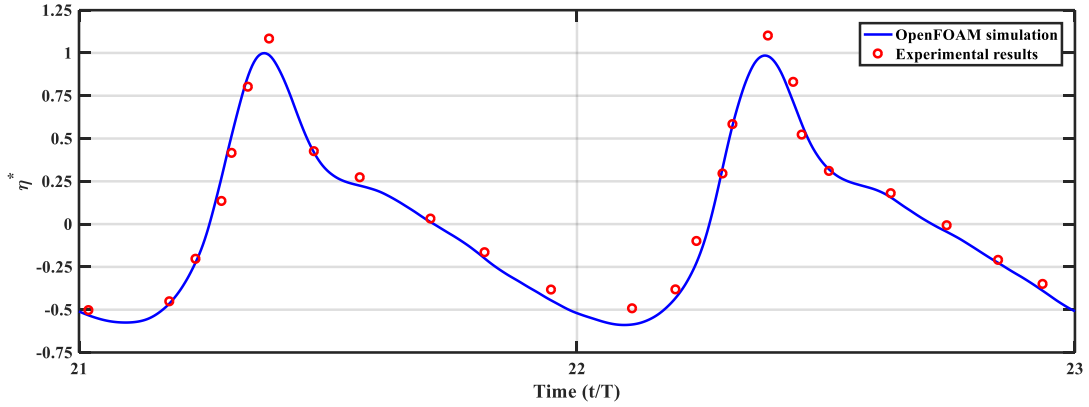
OpenFOAM simulation
Experimental results
1.25
1
0.75
0.5
0.25
0
-0.25
-0.5
-0.75
21
22
23
Time (t/T)

G2

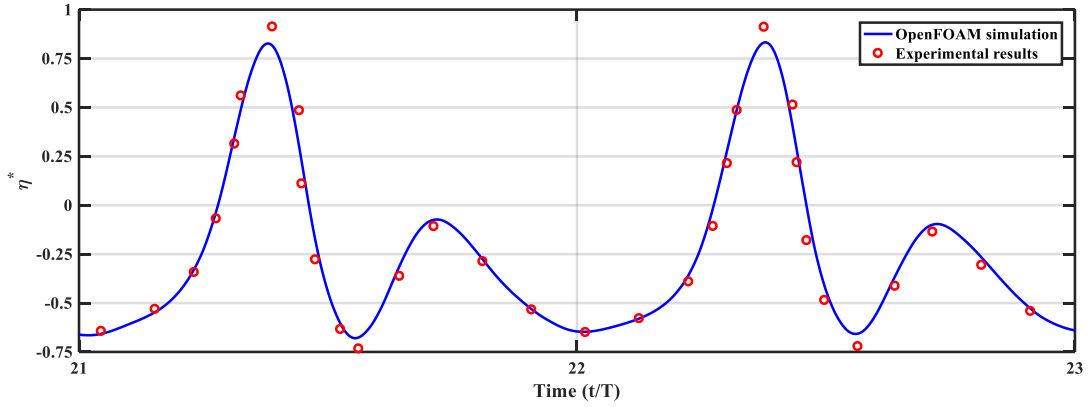
OpenFOAM simulation
Experimental results
1
0.75
0.5
0.25
0
-0.25
-0.5
-0.75
21
22
23
Time (t/T)

G3

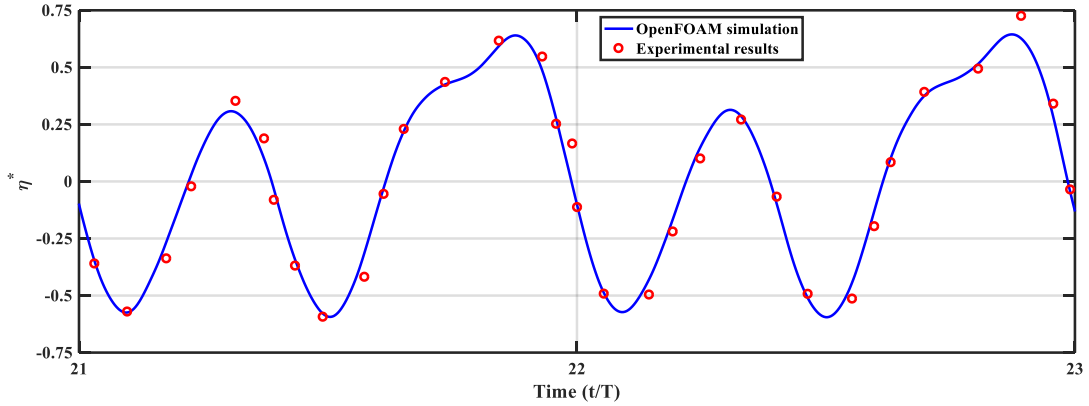

G4

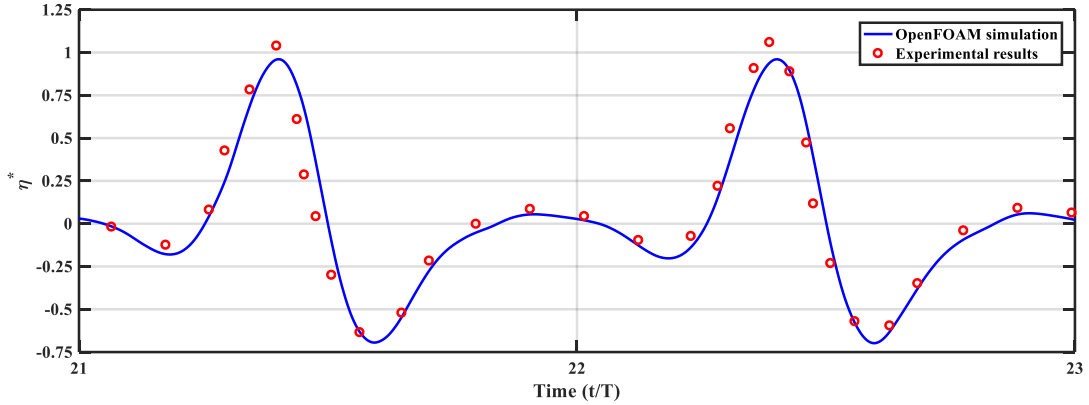

G5

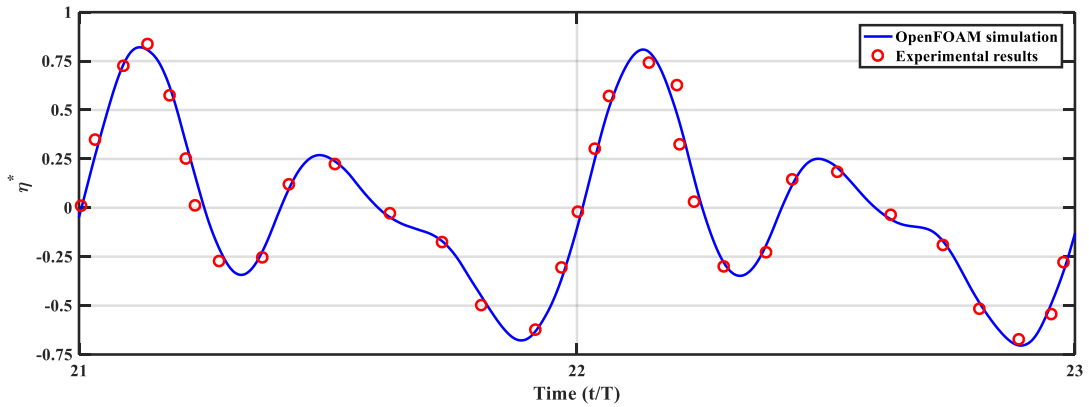

G6

Figure 4-4 Comparison of wave elevation between OpenFOAM simulation and Physical Experimental results at different wave probes

4.2 Conclusion

In this chapter, the current OpenFOAM solver has been developed to deal with the application in relation to ocean engineering. To validate the wave generation and damping method, a 3-D numerical wave flume was created and a series of tests conducted.

Two types of wave generation method have been confirmed, by simulating 1^{st}, 2^{nd} and 5^{th} -order stroke waves and irregular waves that are able to work well at the inlet of the numerical tank. The results show that the hydrodynamic parameters in each numerical wave model matches well with the ones in the theoretical predication and physical experiment. Compared with the moving boundary method, the purely numerical generation technique does not need the movement of inlet boundary which means that it will avoid the error caused by mesh motion and also reduce the computational cost. The wave absorption technique was also investigated through the parameter of the damping factor and the damping zone length. It has proven to be applicable to various types of waves.

The wave generation and absorption method in a 3D wave tank have been investigated in this chapter. It can be concluded that these approaches can be successfully used to generate waves as well as to absorb wave reflection for the studies involving wave propagation.

5. Validation of hydrodynamic parameters

This chapter will firstly conduct the validation of the CFD model. From the perspective of the intended users of this model, validation is the key process to determine to what degree the model represents the real world accurately. This includes confirmation of the consistency and convergence of a CFD solution, the study of the space and time discretisation independence, the examination of the effects of the turbulence and multiphase models, and finally, the comparison with the experimental and analytical solution. For the validation of the method used in this study, the added mass and damping coefficient of three objects with different cross-sections on a calm free surface was determined and compared to the experimental and analytical potential flow results. The three types of model were forced to do harmonic oscillations with several amplitudes and different draft ratios.

The estimation of the structure's reaction in the waves relies on an accurate estimation of hydrodynamic behaviour. For linear motion theory, the hydrodynamic forces calculation can be divided into two parts: the added mass and damping coefficients dominating radiation forces; and the force made up of Froude-Krylov and diffraction forces. Most of the previous studies were found to have adopted the linear potential flow theory for the purpose of simplification. They showed good agreement between added mass and damping coefficients calculated using the potential flow theory and experimental results. But the viscous effect is also vital in some cases. Thus, in this section, the RANS method has been employed to calculate the hydrodynamic coefficients and the outcomes have been compared with the experimental (Vugts, 1968) and analytical results. The test models with three different cross-sections have been oscillated in heave, sway and roll conditions and the calculated hydrodynamic coefficients have been compared with the results from the physical experiments and those computed by way of the potential theory.

5.1 Hydrodynamic coefficient calculation

The equation of motion for a solid body can be described by Newton's second law of motion:

$$F_{dynamic} + F_{static} = M\ddot{Z} \tag{5-1}$$

Where M is the mass of the solid body and $\ddot{Z}$ is the second derivative of body displacement. $F_{dynamic}$ is the hydrodynamic force and F_{static} is the hydrostatic restoring force. The restoring force is calculated through the body geometry and position to the mean water level over time.

$$F_{static} = \rho g V_{wet} \tag{5-2}$$

Where c is the hydrostatic restoring coefficient and V_{wet} is the instantaneously immersed body volume.

Then the hydrodynamic coefficients can be calculated from the harmonic function of the oscillating body and the hydrodynamic force in that direction of motion. Take the heave motion as an example; the harmonic sinusoidal motion with the form, Eqation (5-3), is considered

$$\mathrm{z} = \mathrm{A}\sin(\omega \mathrm{t}) \tag{5-3}$$

Where A and ω are the harmonic sinusoidal motion amplitude and frequency respectively and t is elapsed time.

In this study, the total force can be obtained by the integration of the pressure field and friction from the water phase around the solid body of the surface. The pressure p and viscous friction τ can be derived by solving the governing equations without extra computational power. By removing the component of the hydrostatic force from the total force involved, the hydrodynamic force can be described as:

$$F_{total} = \iint_S (p + \tau)\vec{n}dS \tag{5-4}$$

$$F_{dynamic} = F_{total} - F_{static} = -(m_a\ddot{z} + C\dot{z}) \tag{5-5}$$

Where, $\vec{n}$ is the normal vector point out the body surface, m_a and C are the frequency dependant added mass and damping coefficient respectively.

The first term in right-hand side is in-phase with the heaving motion and the second one is in-quadrature. These two terms can be transformed by Fourier analysis, thus the hydrodynamic

coefficients in the heave motion can be obtained from the force response and the period of sinusoidal motion

$$m_a = \frac{\int_{t-\frac{T}{2}}^{t+\frac{T}{2}} F_{dynamic} \sin(\omega t)\, dt}{\pi \omega A} \tag{5-6}$$

$$C = \frac{\int_{t-\frac{T}{2}}^{t+\frac{T}{2}} F_{dynamic} \cos(\omega t)\, dt}{\pi A} \tag{5-7}$$

Where T is harmonic period, the coefficients in surge and roll motion can be calculated through the similar function.

5.2 The environmental set-up

The laboratory water tank used in the experiment is 142m in length, 4.2 m in width with 2.25m as the maximum depth. The test models are located in the centre of the tank. The dimension of the numerical water tank is 40m long. There are two numerical beaches to damp out waves generated by an oscillating cylinder at both ends of the basin. An initial set of simulations showed that 40m is long enough to get rid of the effect by reflected waves. The outgoing waves are measured at a distance of 10m away from the centre of the test model and their heights are validated against the analytical and physical experimental results. Normally, free elevation is measured in a distance of 2λ (wave length) away from the oscillating center. The free surface will be affected by the non-linear process of interaction between the model body and the wave if it is measured too close. A short wave cannot be captured due to gradual decay if measured too far away. The test models are summarized in Table 5-1 and Figure 5-1.

Table 5-1 Parameters for test models

	Models		
	Rectangle	Circle	triangle
Draft (m)	0.05, 0.1 and 0.20	0.15	0.3
Draft/Height	1/8, 1/4 and 1/2	1/2	1/1.115

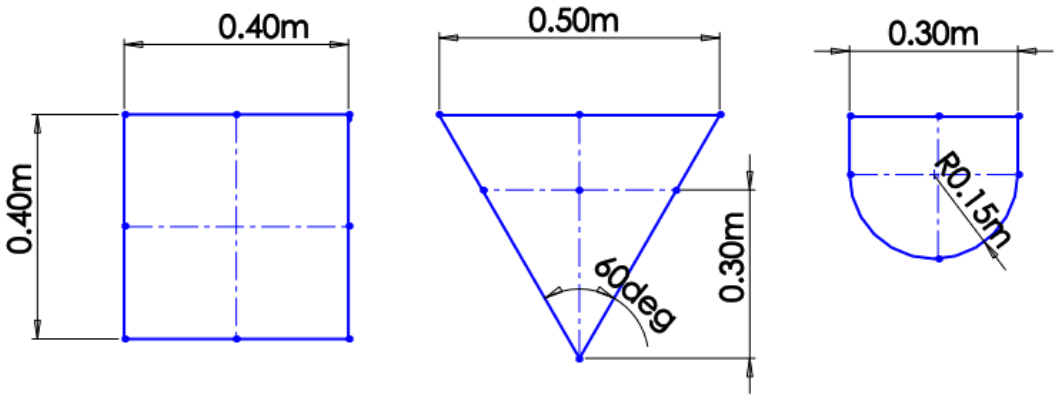

Figure 5-1 Cross-section of the test models

The hydrodynamic coefficients are calculated for the model with rectangular cross-sections in heave, sway and roll motion at different drafts and with a different oscillating amplitude over a series of frequencies.

5.2.1 Mesh

The grid resolution has a dramatic effect on the accuracy of the solution. Thus, a mesh dependency study was needed. The stability and accuracy of the computational calculation can be compromised if the mesh is not designed properly. The mesh structures are developed to keep the mesh dependency to a minimum without increasing the computing cost. It is crucial to identify the region where the highest resolution is required. In the case of the oscillating structure presented here, the refined mesh is where the vorticity and wave will form and develop. Therefore, the dependency study will focus on the area around the model body and the free surface. Added layers are used to grow cell layers, with growth rate of 1.1, from the structure wall with the ability to capture near wall phenomena such as turbulence.

The simulations are performed with three different grid resolutions (coarse, medium and fine) using unstructured cells. The time step of CFL number ≤ 1 is used to maintain numerical stability. The flow data was gathered after the wave gauge received 20 wave cycles. Table 5-2 and Table 5-3 summarizes the y^+ values together with the non-dimensional added mass and damping. The non-dimensional oscillating frequencies used for mesh sensitive study are 0.36 and 1.17 under the highest 0.03m oscillating amplitude, respectively. Turbulence was modelled using a SST $k-omega$ approach. It is recommended that the y^+ value should be less than 1. However, with the enhanced wall function, the numerical results should perform relatively well.

It is found that the difference between the added mass and damping coefficient for medium and fine grid is less than 5%. Therefore, the medium mesh has been used for all subsequent simulations.

Table 5-2 Grid sensitivity study of hydrodynamic coefficients under heave motion, draught =1/2 model height, $\omega^* = 0.36$, amplitude=0.03m

Mesh	Coarse	Medium	Fine
No. of cells	0.8M	1.3M	1.7M
y^+ maxx	15.05	1.07	1.02
y^+ average	2.61	0.85	0.28
m_a^*	1.12	0.98	0.98
C^*	0.31	0.41	0.42

Table 5-3 Grid sensitivity study of hydrodynamic coefficients under heave motion, draught =1/2 model height, $\omega^* = 1.17$, Amplitude=0.03m

Mesh	Coarse	Medium	Fine
No. of cells	0.8M	1.3M	1.7M
y^+ maxx	31.61	6.41	2.81
y^+ average	9.81	4.11	1.05
m_a^*	1.12	1.01	1.05
C^*	0.23	0.11	0.11

5.3 Results

5.3.1 Heave motion

The test models with rectangular cross section are forced to heave with the draft (D) = 1/2, 1/4 and 1/8 model height (H_{model}) under non-dimensional frequency ($\omega^* = \omega\sqrt{\frac{H_{model}}{2g}}$) ranging from 0.2 to 1.71 with the amplitude = 0.01m, 0.02m and 0.03m. The examples of the results for added mass of rectangular cross section with semi-submerged body and amplitude 0.01m to 0.03m are shown in Figure 5-2 and Figure 5-4 and the rest of the numerical results as shown in Appendix F. These results were then compared with the experimental data and analytical solution by Vugts (1968).

Figure 5-2 and Figure 5-4 show the added mass coefficient as a function of the oscillating frequency. It can be seen that the RANS solver, experimental test and potential flow theory show good agreement in terms of the calculation of the added mass. For the cases of all low frequencies, the RANS and experimental results for added mass are lower than those of the potential flow theory. The results by RANS solver slightly over-predicted the added mass coefficient than the ones from the experimental test before $\omega^* = 0.8$. This may be caused by the water tank bottom effects in the experimental tests. In the cases with 0.03m amplitude and high frequencies of oscillation motion, the hydrodynamic force became nonlinear with a deviation from sinusoidal form. The added mass and damping coefficient derived from the Fourier transformation broke down in this circumstance, thus the results from the RANS solver, as well as experimental test, are higher than the ones from the potential theory.

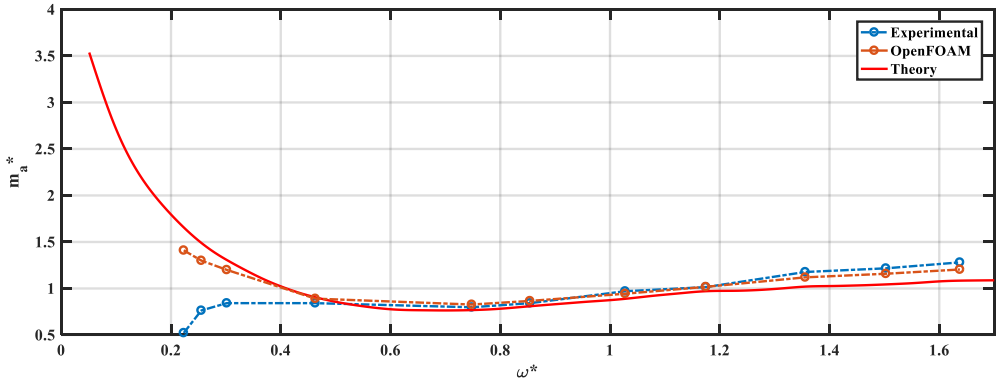

Figure 5-2 Non-dimensional added mass coefficients vs non-dimensional frequency under heave motion, draft =0.5 cylinder height, amplitude =0.01m

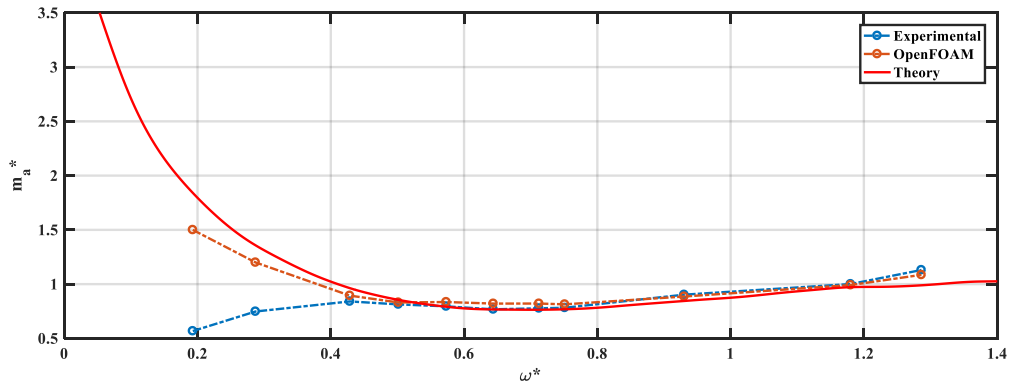

Figure 5-3 Non-dimensional added mass coefficients vs non-dimensional frequency under heave motion, draft =0.5 cylinder height, amplitude =0.02m

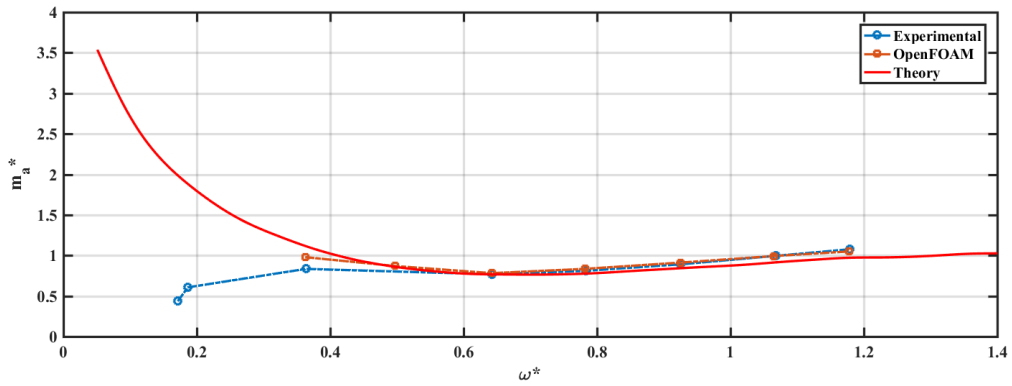

Figure 5-4 Non-dimensional added mass coefficient vs non-dimensional frequency under heave motion, draft =0.5 cylinder height, amplitude =0.03m

In the case of high frequencies, the non-linear effects are detected, and both the RANS and experimental results for the damping coefficients are higher than those from the potential theory. This can be explained in Figure 5-8 and Figure 5-9 by the increment of eddy strength and the damping coefficients representing the dissipation energy. The results also show that dissipation energy increases with the oscillating amplitude.

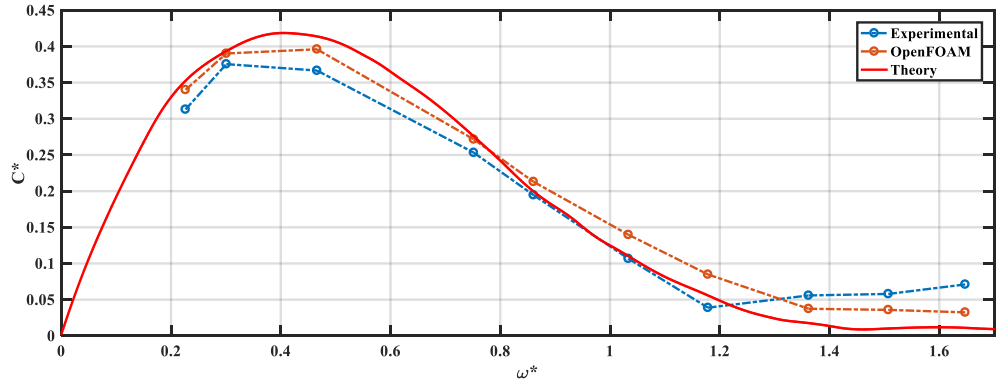

Figure 5-5 Non-dimensional damping vs non-dimensional frequency under heave motion, draft =0.5 cylinder height, amplitude =0.01m

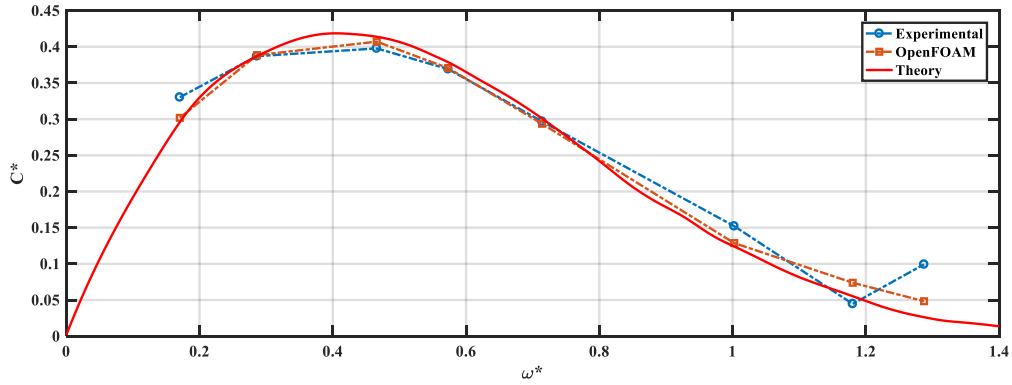

Figure 5-6 Non-dimensional damping vs non-dimensional frequency under heave motion, draft =0.5 cylinder height, amplitude =0.02m

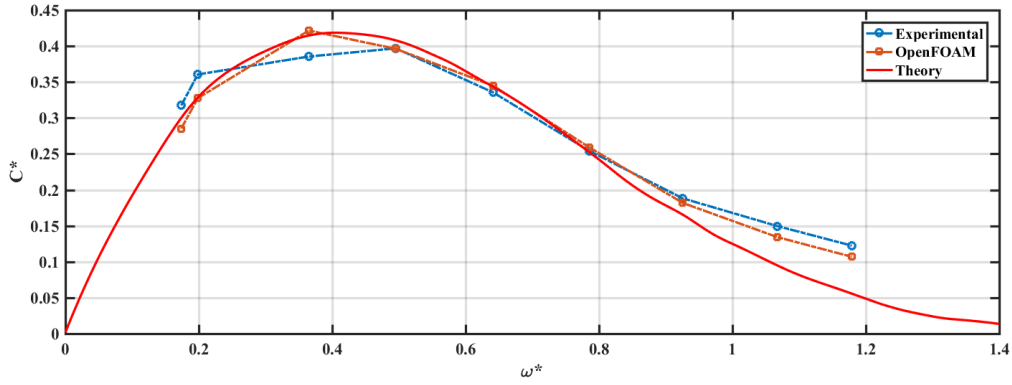

Figure 5-7 Non-dimensional damping vs non-dimensional frequency under heave motion, draft =0.5 cylinder height, amplitude =0.03m

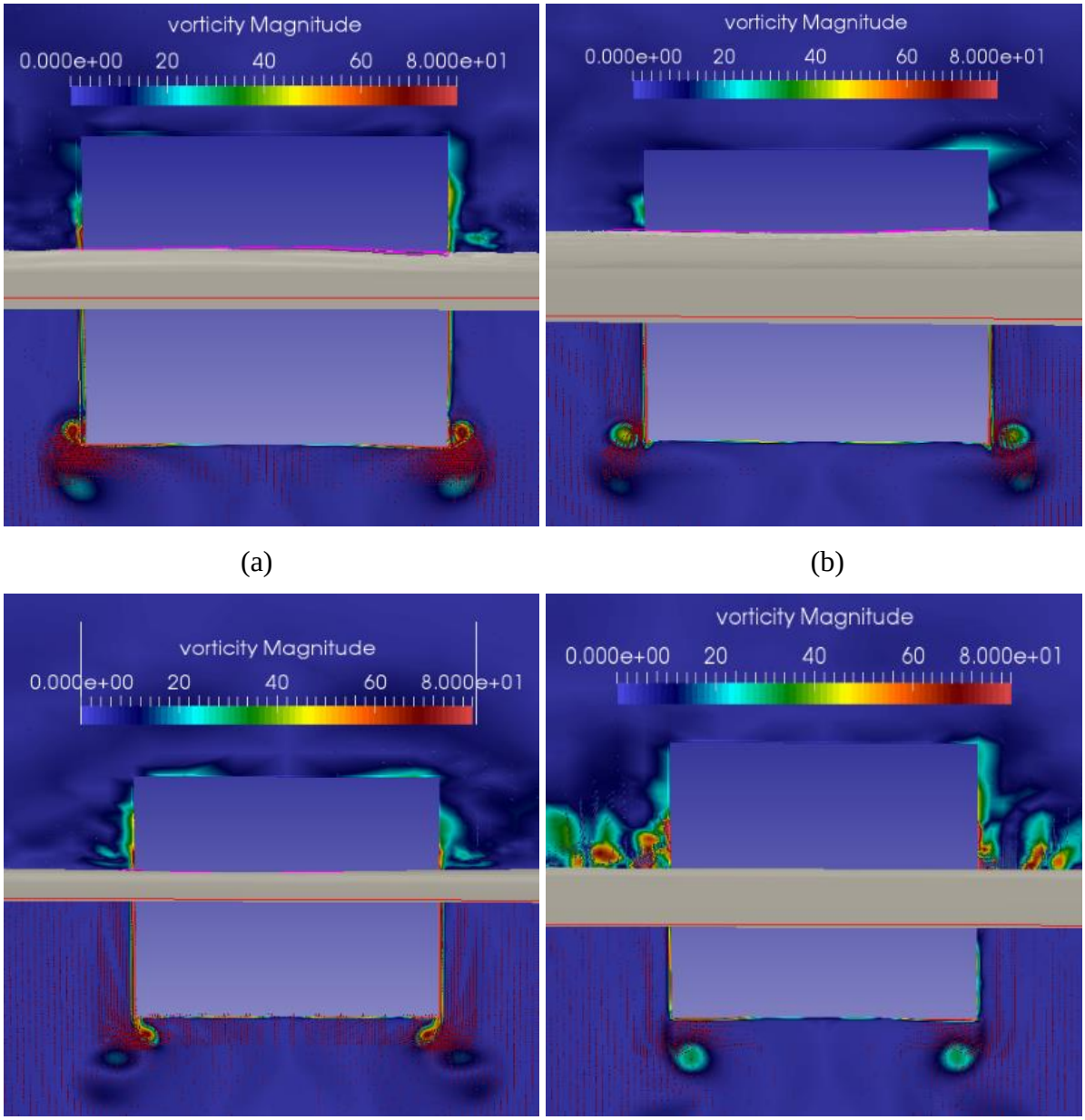

Figure 5-8: Vortices contours and free surface in heave motion at t/T = 0.25(a), 0.5(b), 0.75(c) and 1(d) for cylinder with rectangular cross-section

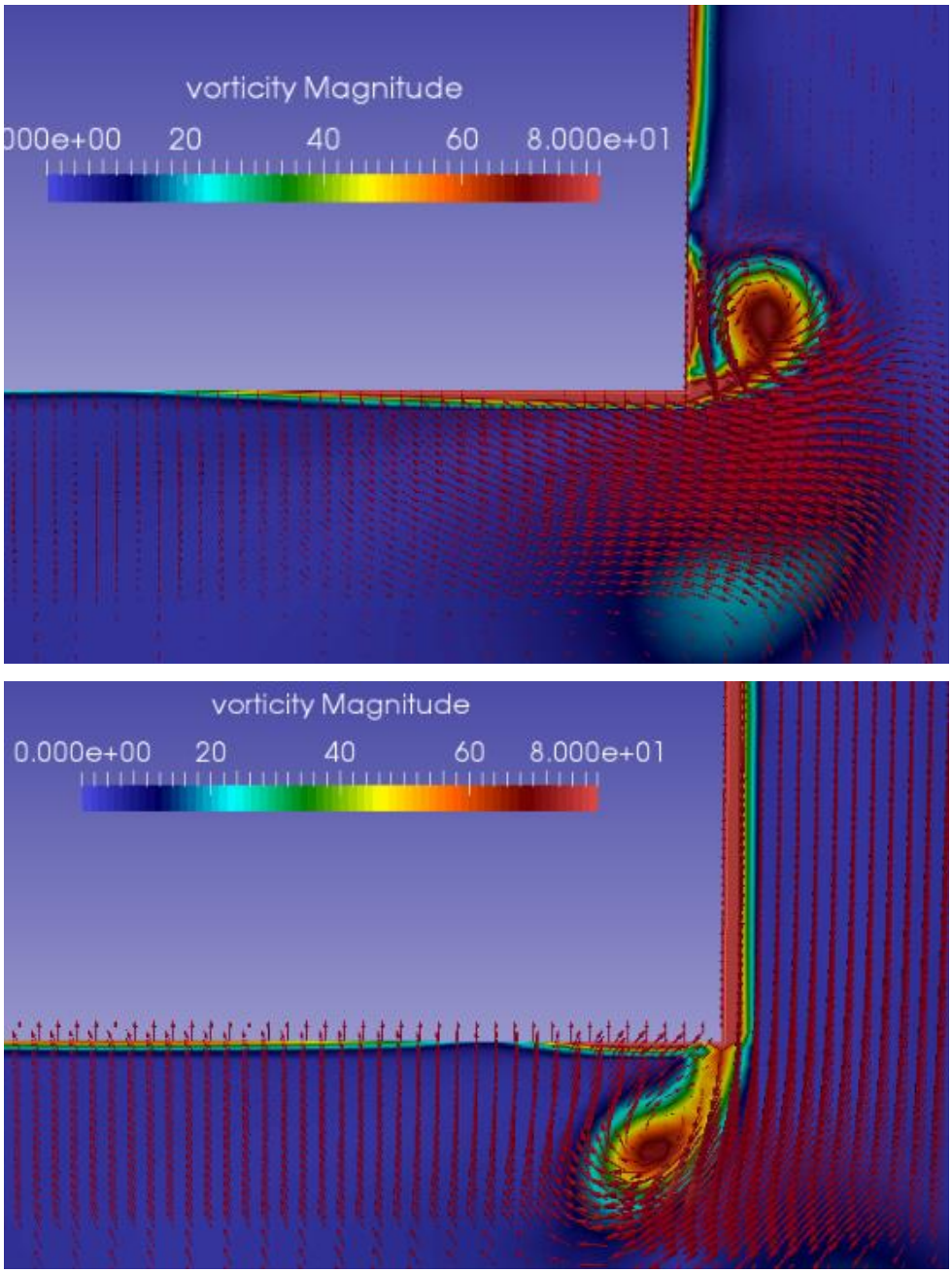

Figure 5-9: Velocity vectors in heave motion at t/T = 0.25(up) and 0.75(down) for cylinder with rectangular cross-section

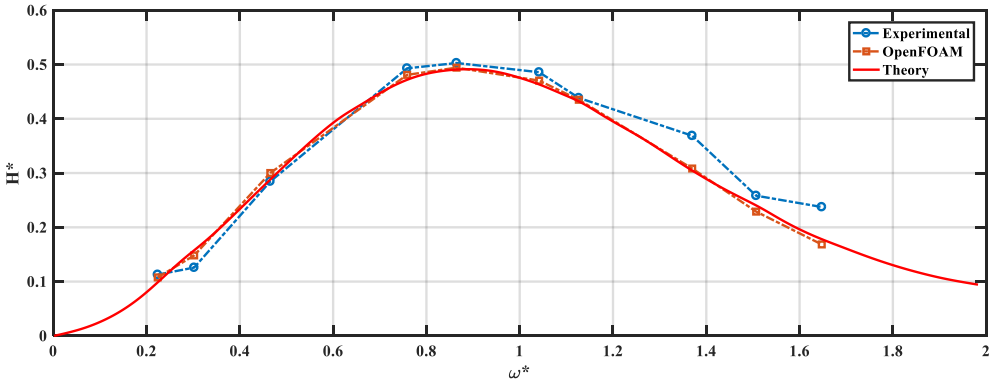

Figure 5-10 Non-dimensional wave height vs non-dimensional frequency under heave motion, draft =0.5 cylinder height, amplitude =0.01m

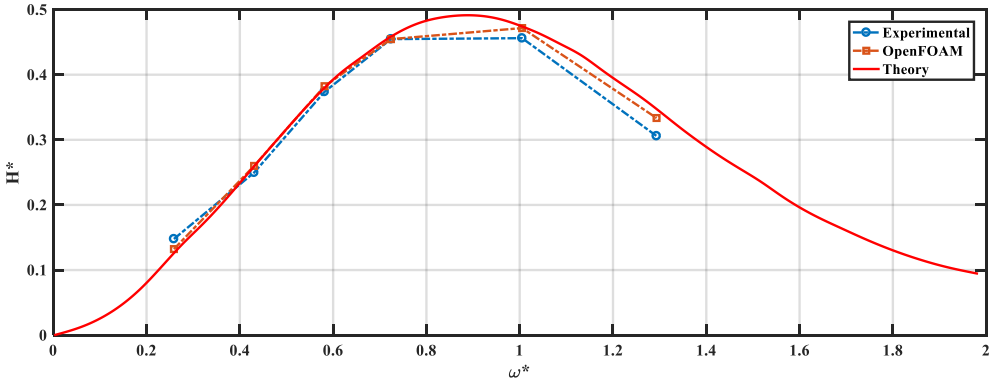

Figure 5-11 Non-dimensional wave height vs non-dimensional frequency under heave motion, draft =0.5 cylinder height, amplitude =0.02m

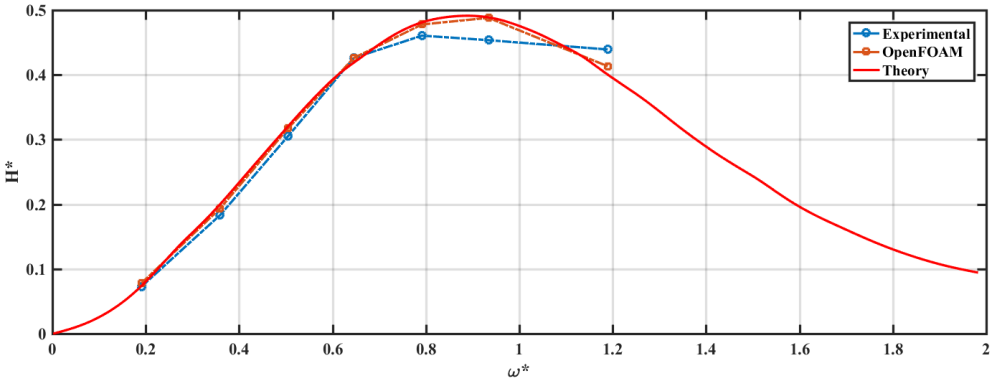

Figure 5-12 Non-dimensional wave height vs non-dimensional frequency under heave motion, draft =0.5 cylinder height, amplitude =0.03m

In general, the added mass and damping coefficients under the middle range of frequencies shows the best match. The generated wave height (Figure 5-10 to Figure 5-12) was also monitored and it shows that the energy decays faster in waves with a short period. In the high frequency range, the wave height simulated by RANS solver is lower than the one from the potential theory due to viscous dissipation.

In terms of the effect by the draft, it can be seen, from Figure 5-13 and Figure 5-14, that the submerged depth for the heaving motion is a crucial parameter. It is shown that a smaller draft is associated with a large exciting force, thus larger added mass and hydrodynamic damping coefficient are observed.

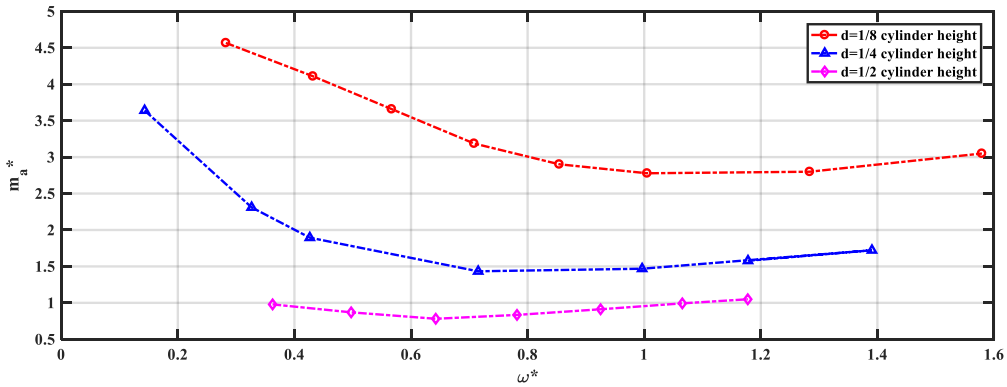

Figure 5-13 Non-dimensional added mass coefficient vs non-dimensional frequency under heave motion, amplitude =0.03m

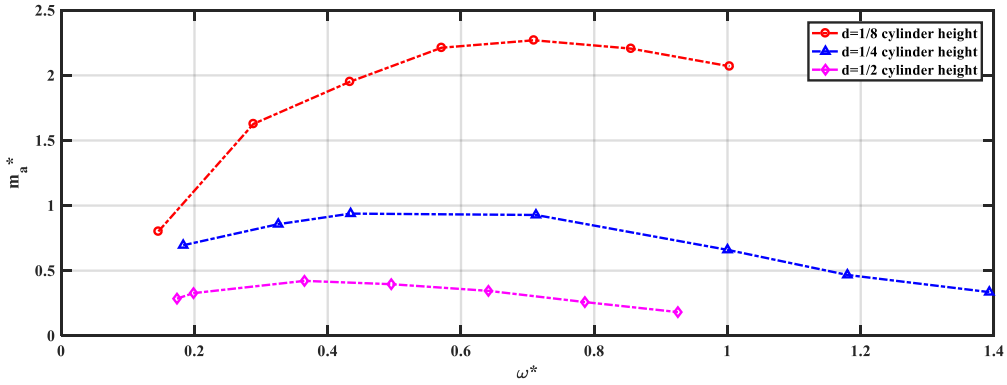

Figure 5-14 Non-dimensional damping coefficient vs non-dimensional frequency under heave motion, amplitude =0.03m

From the technique-based point of view, the hydrodynamic parameters of the oscillating body are affected by the nonlinearity of the oscillating system from two aspects and they can be concluded as:

- The nonlinear profile of the free surface around the oscillating body will lead to a variation in the added mass coefficient. The hydrostatic force is poorly addressed due to the linear assumption. The free surface at higher frequency cases is nonlinear thus the hydrostatic part in the total force will remain in the hydrodynamic force. As a result, the added mass calculated by linear theory and the RANS model will be different due to the discrepancy in wetted surface area prediction.

- Moreover, viscous eddies will form along the body surface and dissipate in the wake of the motion. The viscous force is an unsteady component of the total force which will affect the hydrodynamic coefficients since the damping coefficient is related to the dissipation of energy. The viscous eddies can be seen in *Figure 5-8* and Figure *5-9*. The flow separation at the sharp edges leads to an energy loss because of the formation of eddies. The strength of the eddies will increase with the frequency and amplitude of the oscillating motion. The nonlinearity has a great effect on the whole system when the draft is lower and the frequency and amplitude of motion are higher. This is such that the method used by many previous literatures that uses constant coefficients is not suitable and may lead to a greater discrepancy.

It is surmised that the RANS model can handle the free surface distribution, eddy formation and diffusion much better than the potential flow solutions, especially at a high frequency amplitude of motion.

5.3.2 Sway Motion

The cases of a rectangular cylinder oscillating in sway motion at a free surface are then studied with the same draft ratio and frequency range that was used in heave. The amplitudes of oscillation 0.01m are then simulated. The examples of added mass and damping coefficients are shown as given in Figure 5-15 to Figure 5-20. The damping coefficient from both the RANS model and the experiment was over-predicted except the one in the lower draft ratio when $\omega^* \leq 0.8$. The RANS solution agrees well with the linear potential flow theory and the experiment results are slightly greater than the ones from the RANS model. Overall, the RANS and potential flow solutions match very well with the experiment results and the RANS solution has a better agreement with the experiment results than with the potential flow theory. In general, the numerical results shows good agreement with the ones from the experiments and potential assumptions. The numerical and analytical solutions correspond better than the ones in heave motion in the low frequency range, especially for the added mass with a higher draft ratio (see Figure 5-5 to Figure 5-7 for added mass and Figure 5-18 and Figure 5-20 for

damping coefficients) . The results also show the influence of viscosity in the high frequency range. The formation of eddies is shown in Figure 5-21, which indicates that the eddy strength is smaller than the one in the heave motion and thus there is less discrepancy in the prediction of the hydrodynamic force.

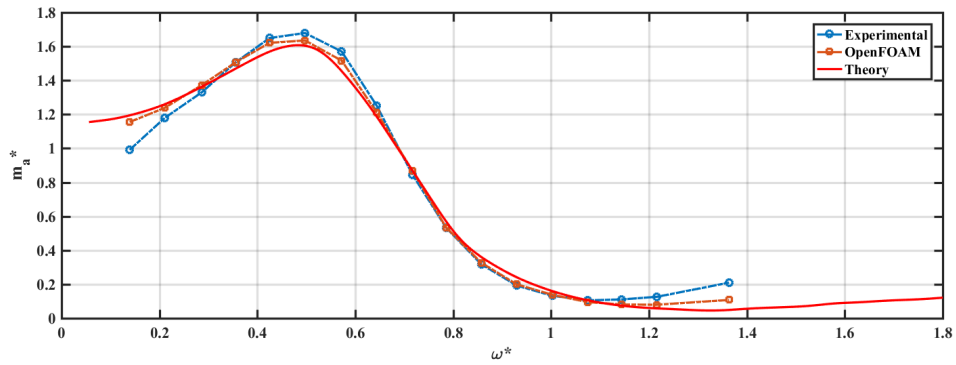

Figure 5-15 Non-dimensional added mass vs non-dimensional frequency under sway motion, Draft =1/2 cylinder height, Amplitude =0.01m

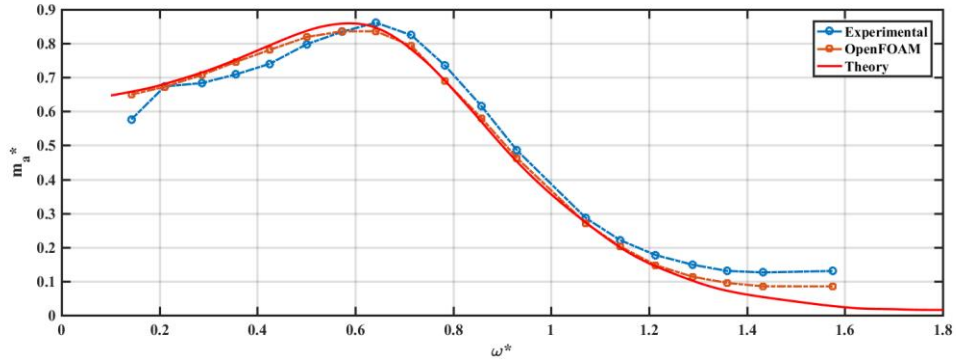

Figure 5-16 Non-dimensional added mass vs non-dimensional frequency under sway motion, Draft =1/4 cylinder height, Amplitude =0.01m

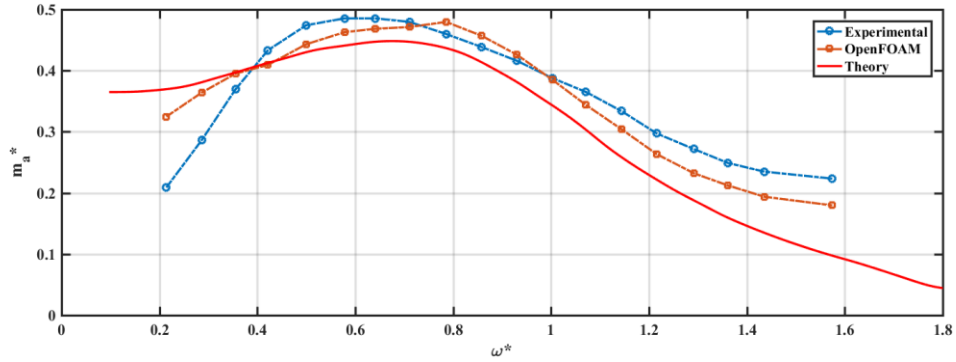

Figure 5-17 Non-dimensional added mass vs non-dimensional frequency under sway motion, Draft =1/8 cylinder height, Amplitude =0.01m

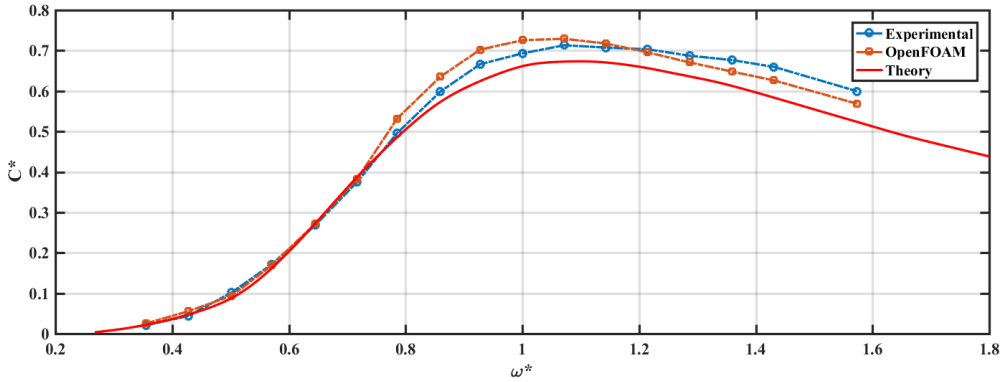

Figure 5-18 Non-dimensional damping vs non-dimensional frequency under sway motion, Draft =1/4 cylinder height, Amplitude =0.01m

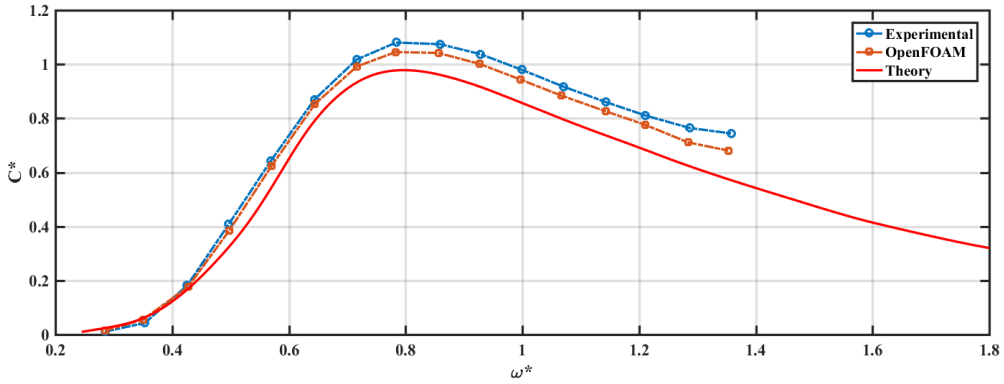

Figure 5-19 Non-dimensional damping vs non-dimensional frequency under sway motion, Draft =1/2 cylinder height, Amplitude =0.01m

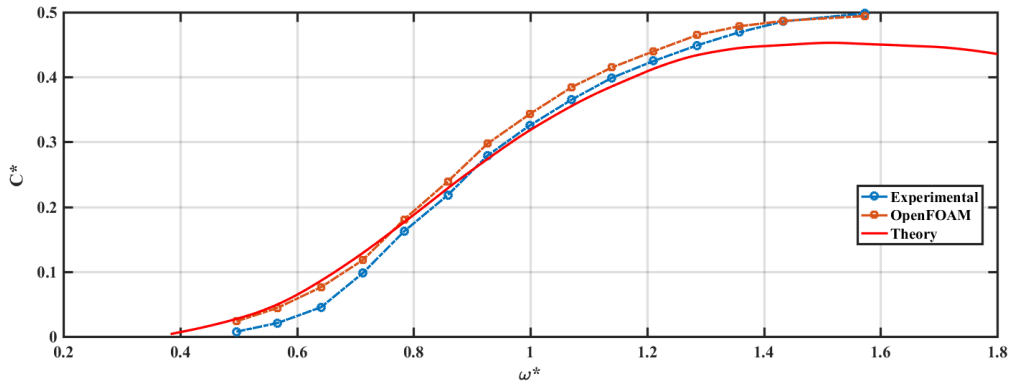

Figure 5-20 Non-dimensional damping vs non-dimensional frequency under sway motion, Draft =1/8 cylinder height, Amplitude =0.01m

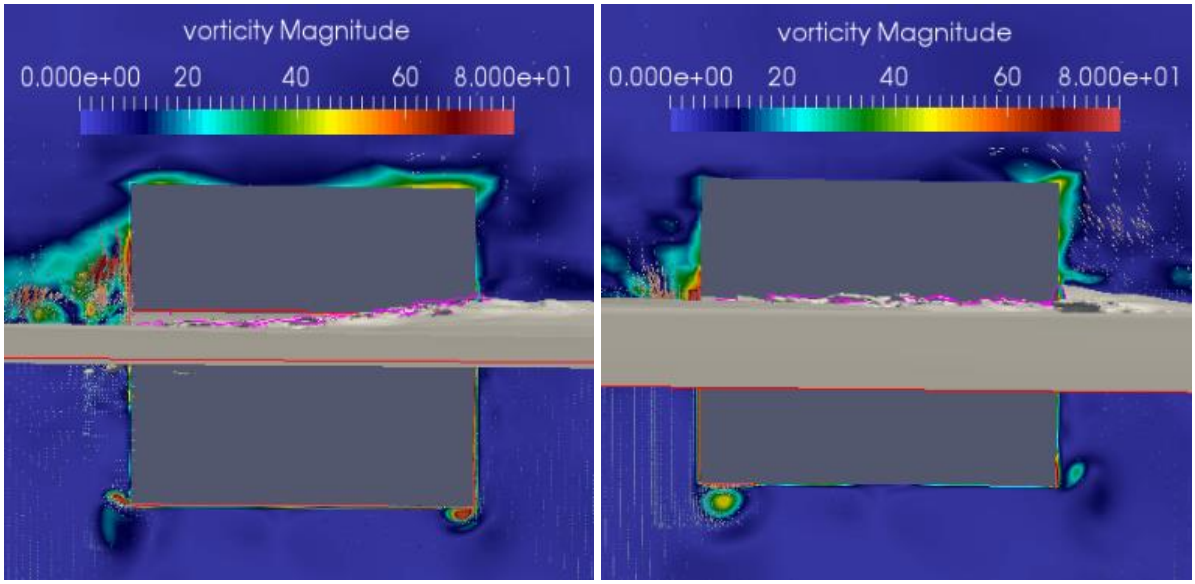

(a) (b)

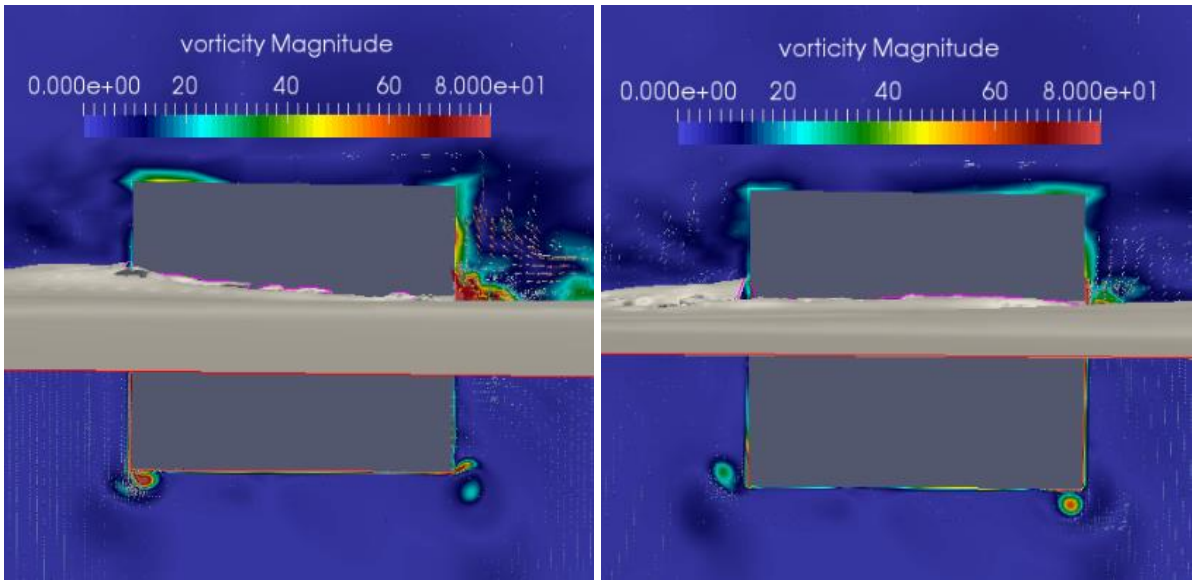

(c) (d)

Figure 5-21: Vortices contours and free surface in sway motion at t/T = 0.25(a), 0.5(b), 0.75(c) and 1(d) for cylinder with rectangular cross-section

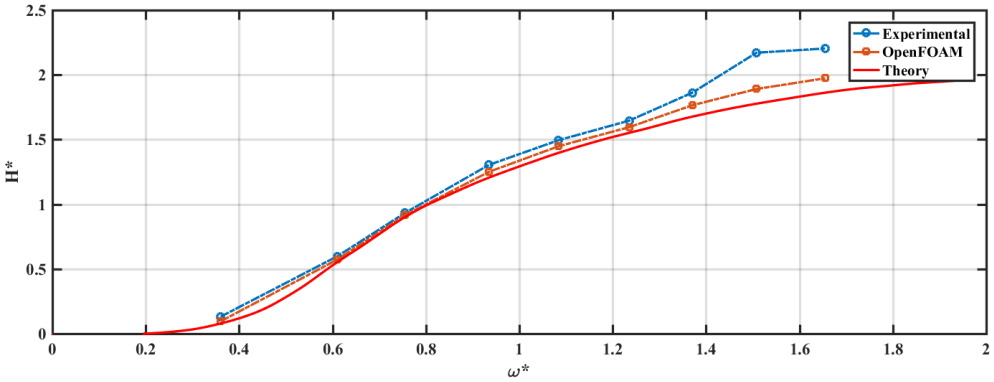

Figure 5-22 Non-dimensional wave height vs non-dimensional frequency under sway motion, Draft =1/2 cylinder height, Amplitude =0.01m

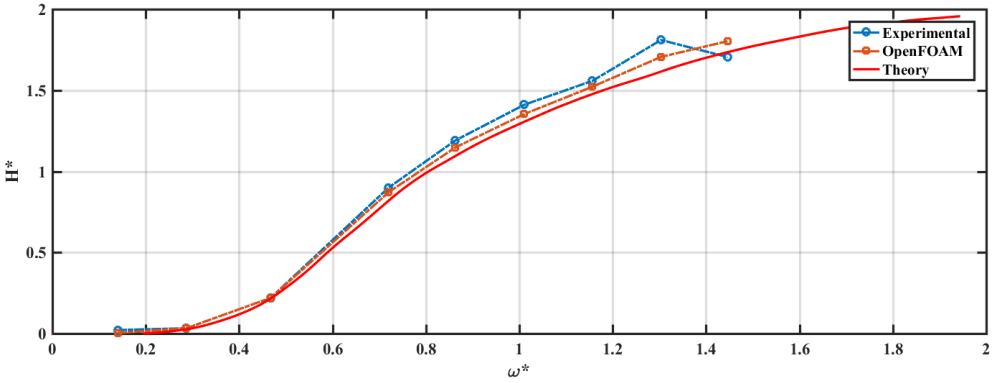

Figure 5-23 Non-dimensional wave height vs non-dimensional frequency under sway motion, Draft =1/2 cylinder height, Amplitude =0.02m

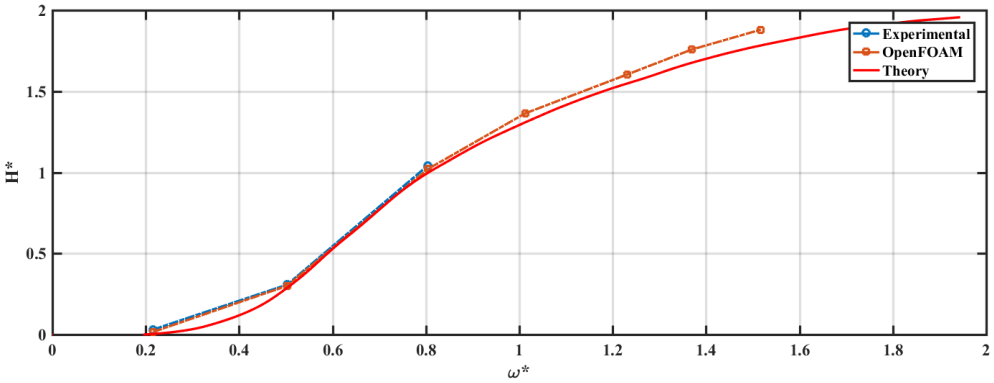

Figure 5-24 Non-dimensional wave height vs non-dimensional frequency under sway motion, Draft =1/2 cylinder height, Amplitude =0.03m

Like the flow pattern in heave mode, the sharp edges at the corners generate eddies that increase with the sway amplitude. The outgoing waves in sway motion are higher than the ones in heave motion in the middle and high frequency range. The predicted wave heights are closer to the ones measured by the experiments (Figure 5-22 to Figure 5-24)

A short conclusion that can be drawn is that the draft ratio proves to be a crucial parameter that affects hydrodynamic behaviours in sway mode and the amplitude has less impact on the results for all three methods. The three methods for the oscillating body with higher draft ratio coincide well with each other and the lower draft ratio results show some deviations. This may be caused by a stronger flow separation with smaller submerged body than the larger one, and the shallower immersed body leads to a bigger wave forming and an even wave breaking at the free surface under high frequency.

It is clear that the numerical outcomes in sway motion has the best agreement with the analytical solution and experiment results. The hydrodynamic behaviour is well predicted and more importantly, the generated waves height have been accurately simulated, which is important for wave energy estimation.

5.3.3 Roll Motion

The coefficients derived from the numerical simulation are shown in Figure 5-25 and Figure 5-26. The results with the deeper submerged body and low oscillating amplitude have a better agreement with the physical tests. The viscous effect in rolling is much larger than the ones in heave and sway. There is a relatively big difference compared to the experimental results in the whole frequency range under high oscillating amplitude. In tests with a shallower submerged depth, the damping coefficients are different for each method but they show the same trend. The viscosity effect is much larger than in the test with the semi-submerged model. The sharp edges lead to flow separation, and the energy loss in eddy formation, which increases with the roll speed and amplitude, is quite noticeable. In the practical sense, concerning the problem with roll motion in high frequency, motion could be avoided.

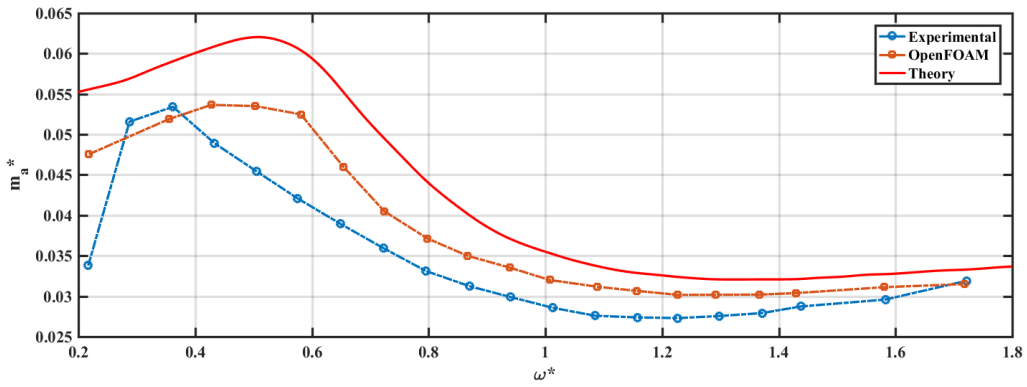

Figure 5-25 Non-dimensional added mass vs non-dimensional frequency under roll motion, draft =1/2 cylinder height, amplitude =0.05 rads

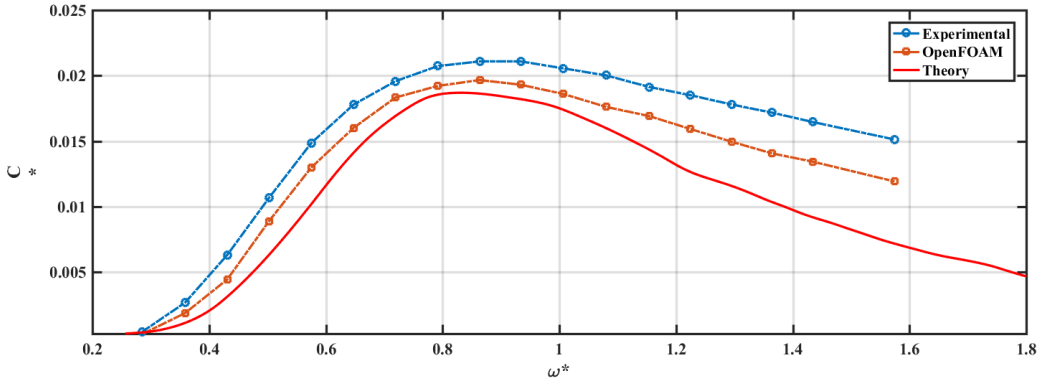

Figure 5-26 Non-dimensional damping vs non-dimensional frequency under roll motion, draft =1/2 cylinder height, amplitude =0.05 rads

The results for model with the hemisphere and triangle cross-section is shown in the Appendix G and Appendix H. Overall, the triangle model has a similar result to the rectangle model in sway and roll motion. The triangular has the smallest added mass and the hydrodynamic damping for the triangle shape appears to be larger than the hemisphere and rectangular shape as shown in Figure 5-27 and Figure 5-28. An example of the vortices contours for the triangular shape in heave motion is given in Figure 5-29. It can be seen that the eddy formation is much less than the one with the rectangular shape.

The circle model, other than rectangle and triangle models, shows the best agreement in terms of the roll motion.

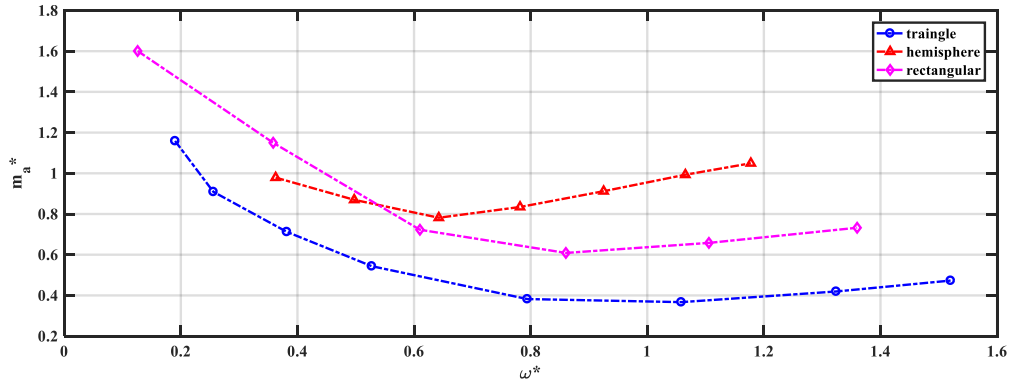

Figure 5-27: Non-dimensional added mass vs non-dimensional frequency under heave motion, draft =0.5 cylinder height, amplitude =0.03m

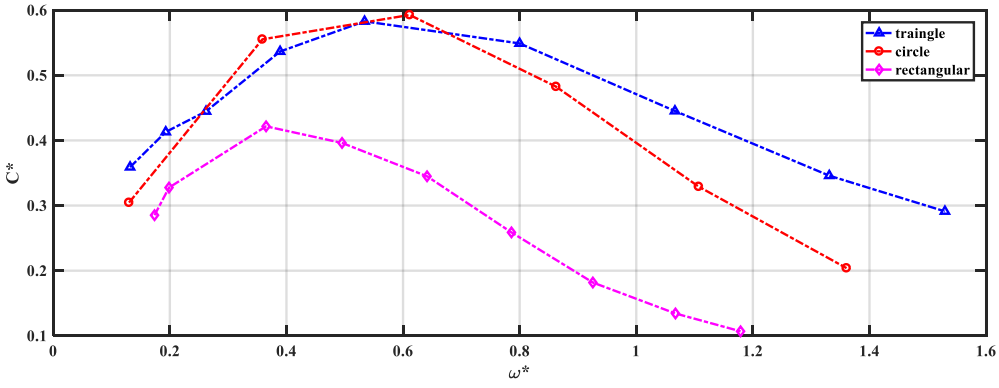

Figure 5-28: Non-dimensional damping vs non-dimensional frequency under heave motion, draft =0.5 cylinder height, amplitude =0.03m

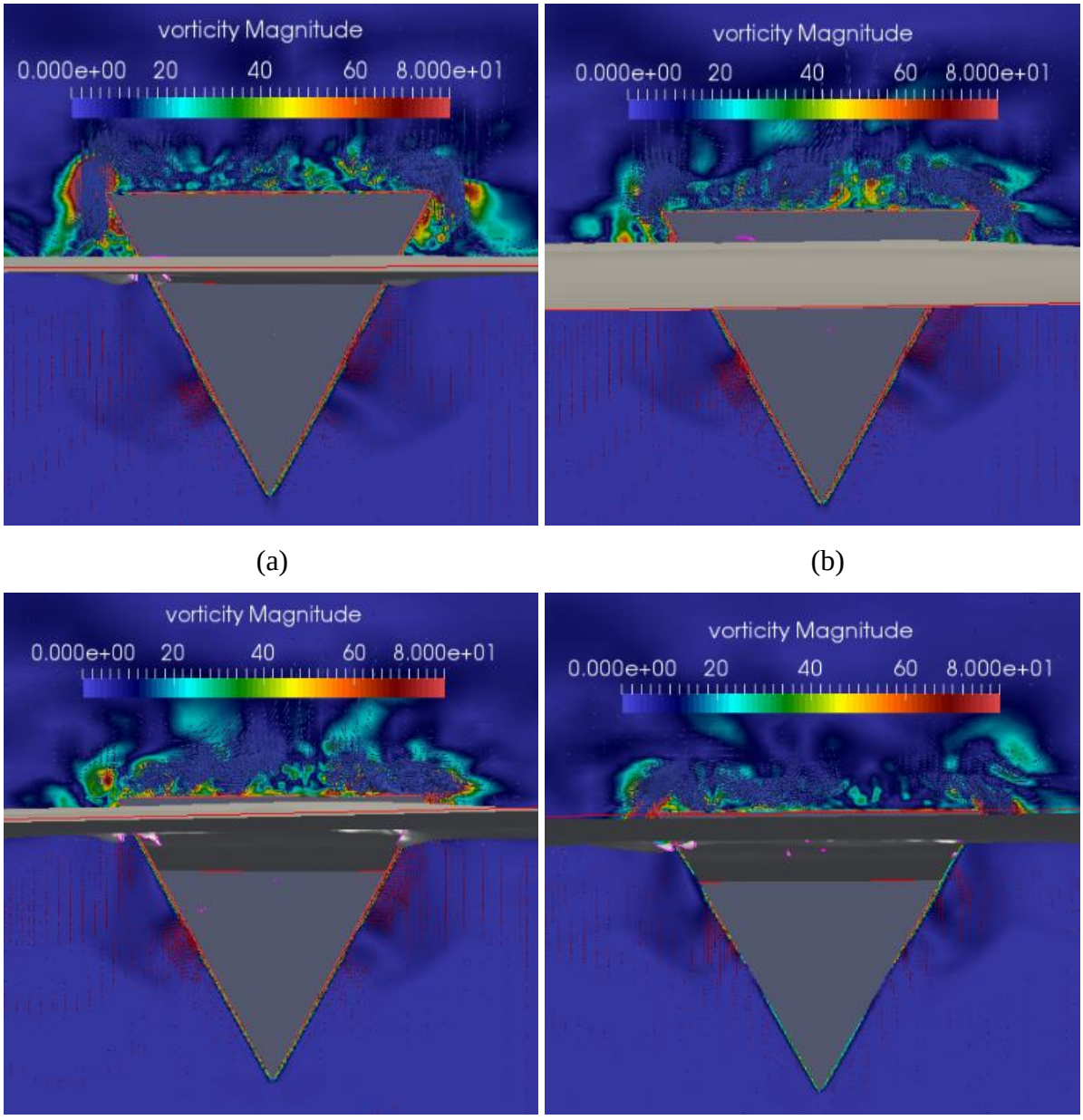

Figure 5-29: Vortices contours and free surface in heave motion for the triangle cross-section at t/T = 0.125 (a), 0.25(b), 0.375(c) and 0.5(d) for the cylinder with a rectangular cross-section

5.4 Conclusion

In this section, it can be proven that the hydrodynamic coefficient can be calculated accurately by RANS and that the influence of viscosity is not negligible. The approach of estimating hydrodynamic behaviour in a full viscous solver in time domain proved to be successful and some key findings can be summarized as:

- The differences in the hydrodynamic parameter predicted by the potential theory without considering non-linear effect and the RANS model can be significant and vary considerably depending on the draft, frequency and amplitude of the oscillation motion.

- The nonlinear profile of the free surface around the oscillating body will lead to a variation in the added mass coefficient. The hydrostatic force is poorly addressed due to the linear assumption. The free surface in the higher frequency cases are nonlinear thus the hydrostatic part in the total force will remain in the hydrodynamic force. As a result, the added mass calculated by the linear theory and RANS model will be different due to the discrepancy in the wetted surface area prediction. It also suggests that the added mass is becoming frequency independent (as well as frequency increasing) and the increase in the damping from the Fourier transmission produces the best match to the nonlinear hydrodynamic force.

- Moreover, the viscous eddies will form along the body surface and dissipate in the wake of any motion. The viscous force is an unsteady component of the total force which will affect the hydrodynamic coefficients since the damping coefficient is related to the dissipation of energy. The viscous eddies can be seen in Figure 5-8 and Figure 5-9. The flow separation at the sharp edges leads to an energy loss because of the formation of eddies. The strength of the eddies will increase with the frequency and amplitude of the oscillating motion. The nonlinearity has a great effect on the whole system when the draft is lower and the frequency and amplitude of motion is higher. The method used by many previous literatures using constant coefficients is not suitable and may lead to discrepancies. It can be surmised that the RANS model can handle the free surface distribution, eddy formation and diffusion much better than the potential flow solutions, especially at high frequency amplitudes of motion.

- The submerged depth for the heaving motion is a crucial parameter. It is shown that a smaller draft is associated with a large force and a larger added mass and hydrodynamic damping

coefficient are then observed. This suggests that a smaller draft will result in a larger power absorption from the wave energy device. The submerged depth also proves to be a crucial parameter that affects the hydrodynamic behaviours in sway mode and the amplitude has less of an impact on the results.

- The hydrodynamic damping coefficient for the cone shape appear to be slightly larger than the other two shapes. Therefore, it might be expected that the triangle-cylinder will be a better wave energy absorber.

- The results also indicate that eddy formation has less of an impact on the pressure distribution around the body since the added mass in all three modes has been predicted well. It proves that the added mass-related sinusoidal component of the force is accurately calculated, which is crucial to estimate the hydrodynamic loads on an offshore structure occurring in all wave conditions.

6. Application to Heaving Point Absorber WEC

The RANS model described in Chapter 3 will now be applied to the simulation of Point absorber WEC. As described in Chapter 2, a point absorber WECs is the most appropriate devices for most coastal and offshore areas. In this section, a parametric study about the floating type point absorber WEC with four different geometries of buoy will be employed to determine power production. Irregular waves with deep water conditions will also be applied.

A linear external PTO model was applied to dampen the wave energy, and a stiffness term will be introduced to tune the point absorber into the incoming waves. Various wave conditions, chosen from the EMEC report, was considered to find the effects of each different climate. The parameters included buoy shape, draft, size and the power take-off system which are required to optimize the power absorption. The RANS solver was used to simulate the hydrodynamic behaviour of the oscillating point absorber WECs and then the output was used to determine power production.

6.1 Equation of motion of the buoy

The motion of the point absorber WEC is considered to move in heave mode only. Each of the buoys with draft (d) and radius (r) are floating on the free surface. The equation of motion for the point absorber buoy can be described by the Newton's second law of motion:

$$F_{dynamic} + F_{static} + F_{pto} + F_{stiff} = M\ddot{z} \tag{6-1}$$

Where M is the mass of the point absorber buoy, z and $F_{dynamic}$ is the body displacement and total wave dynamic force in gravity direction respectively, F_{static} is the hydrostatic restoring force including gravity force, F_{pto} is the PTO damping force and F_{stiff} is the term that helps to shift the body natural period. The last two terms on the left-hand side can be simplified as:

$$F_{pto} = C\dot{z} \tag{6-2}$$

$$F_{stiff} = kz \tag{6-3}$$

Where C and k are the linear damping coefficient and stiffness for the power take-off system. The natural period of the buoy can be shifted by the strength of stiffness in the control mechanism.

6.2 Set up of the numerical wave tank

A numerical tank set-up is introduced here with the purpose of studying point absorber motion in waves. It can be summarised in Table 6-1 and Table 6-2.

Table 6-1 Main parameter within numerical wave tank

Parameter	*Setting*
Water	Incompressible fluid
Air	Ideal gas
Motion	Wave-induced heave motion
Inlet	JONSWAP spectrum
Turbulence model	$SST\ k-\omega$
Wall boundary	Non-slip
Spatial discretisation	Second-order Linear Upwind
Temporal discretisation	Second-order backward Euler
Multiple Phase model	VoF with MULES for sharp resolution
Timestep control	Courant number = 0.5
Convergence control	Residual 1e−6

Table 6-2 Boundary conditions for numerical wave tank

Boundary	*descriptions*
Inlet	p : Zero gradient
	k and ω: Fixed value
	u and α: Based on JONSWAP
Outlet	k and ω: Zero gradient
	p (dynamic): Fixed value = 0
	u: Zero gradient
WEC model	p and α: Zero gradient
	k and ω: Wall function
	u: Fixed value = 0
Sides and bottom	Slip wall

6.2.1 Wave environment

In this study, the Joint North Sea Wave Project (JONSWAP) spectra (Hasselmann et al., 1973) has been adopted to represent an irregular wave environment. The JONSWAP is an empirical relationship that describes the energy distribution vs frequency in the ocean. The JONSWAP spectrum is derived from the Pierson-Moskowitz (PM) spectrum. The waves described by the JONSWAP spectra are not fully developed due to the non-linear effect among the waves. Therefore, the waves continue to grow during propagation and the peak in the spectrum is specified by the enhancement factor (γ term).

$$S(f) = 0.205H_{1/3}^2 T_p^{-4} f^{-5} exp\left[-\frac{5}{4}\left(\frac{f_p}{f}\right)^4\right]\gamma^{\exp\left[-\frac{(f-f_p)^2}{2\sigma^2 f_p^2}\right]} \quad (6\text{-}4)$$

$$T_z = 0.7775T_p, \text{ if } \gamma = 3.3 \quad (6\text{-}5)$$

$$\sigma = \begin{cases} 0.07, f \le f_p \\ 0.09, f > f_p \end{cases} \quad (6\text{-}6)$$

$$H_{1/3} = \frac{1}{\frac{N}{3}} \sum_{i=1}^{\frac{N}{3}} H_i \quad (6\text{-}7)$$

where $H_{1/3}$ denotes a significant wave height. The significant wave height is defined as the mean wave height (trough to crest) of the highest one-third of the waves; similarly, the significant wave period is defined as the average wave period of the highest one-third of the waves. H_i is the wave height component; *i*=1 denotes the highest wave component and the lowest wave is for *i*=*N*. f is the frequency, γ is the peak enhancement factor whose default value is 3.3, T_p and f_p denotes the peak wave period and the frequency respectively. T_z is the mean zero-crossing period. In this numerical model, irregular waves are generated by superposition of the regular wave components and the elevation of each regular wave component, which can thus can be expressed as:

$$\eta_i = \sqrt{2S(f_i)\Delta f} \quad (6\text{-}8)$$

where f_i is a random frequency and Δf is the interval between the frequency components. Each wave component is generated by the inlet boundary of the computational domain.

In the presented study, Table 6-3 shows the significant wave height together with the zero-crossing wave period at Billia Croo Wave Site (Location: 59,00°N; 3,66°W). The parameter study of heaving point absorption was performed in 14 different wave conditions. The irregular wave conditions have

been selected from the EMEC report by picking up the zero-crossing wave periods with the highest occurrences in each significant wave height.

Table 6-3 The irregular wave conditions selected from EMEC report

Scenario	$H_{1/3}$ *(m)*	T_z *(s)*	*Occurrences (%)*
1	0.25	4.5	7.52
2	0.75	4.5	19.49
3	1.25	5.5	14.52
4	1.75	5.5	15.92
5	2.25	5.5	11.25
6	2.75	6.5	10.56
7	3.25	6.5	6.83
8	3.75	7.5	5.65
9	4.25	7.5	3.59
10	4.75	8.5	1.79
11	5.25	8.5	1.59
12	5.75	9.5	0.53
13	6.25	9.5	0.47
14	6.75	9.5	0.29

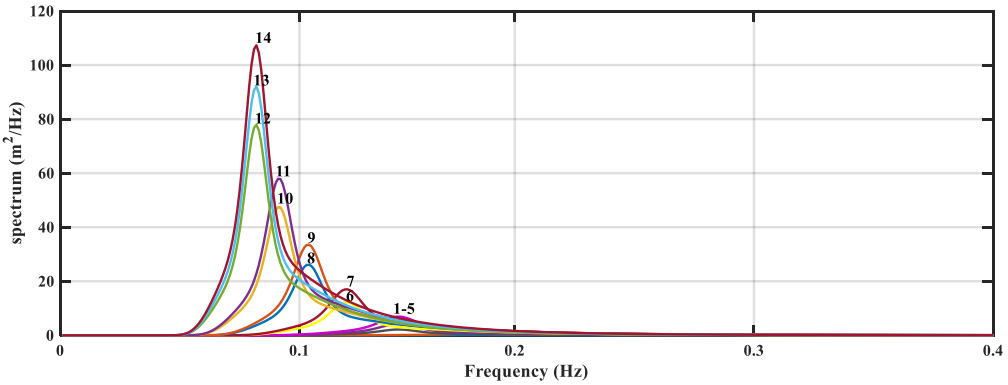

Figure 6-1 Wave spectrum generated by RANS solver for scenarios 1-14, $\Delta f = 0.01 Hz$

Based on the wave conditions in Table 6-3, the waves were simulated in the RANS solver and monitored at the distance of a two-peak wave length away from the inlet boundary, see Figure 6-1. The spectrum consisted of 40 frequency components ($\Delta f = 0.01\ Hz$), ranging up to 0.4 Hz. It has been proven that wave generation based on modified inlet boundary was simulated accurately.

6.2.2 Point absorber buoy parameters

Four different buoy shapes have been considered in this study. A buoy with cylinder shape bottom, a buoy with hemisphere shape bottom and two cone-shaped buoys with a bottom angle of 120° and 90° respectively. These models are shown in Figure 6-2.

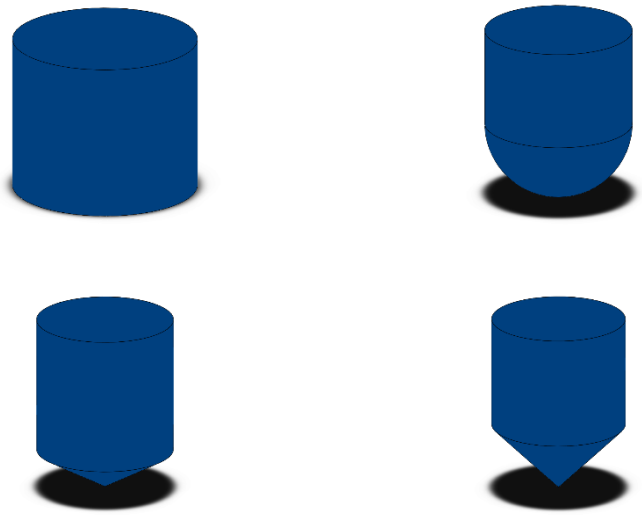

Figure 6-2 Four different models used in this study with bottom shapes: cylinder (top left) hemisphere (top right), 120° cone (bottom left) and 90° cone (bottom right)

A point absorber is an oscillating WEC with a dimension far less than the incident wave lengths. For linear wave theory, the wave length under deep water conditions is assumed to be

$$\lambda = \frac{gT^2}{2\pi}\tanh\left(\frac{2\pi d}{\lambda}\right) \approx \frac{gT^2}{2\pi} \tag{6-9}$$

Where λ is the wave length, T is the wave period and d is the water depth.

From Table 6-3, the scenarios with zero-crossing wave period of 4.5s had the shortest peak wave length of 52.3m, thus the largest diameter for each buoy is set to be 6m, which is about 10% of the typical incident wave length. For each buoy shape, the diameters of the top cylindrical part ranges from 2.5m to 6m and the drafts are set to be 2m, 3m and 4 m for each diameter.

In this study, the density and mass of each model were kept constant, thus the size of the extended cylindrical parts above the free surface were not equal.

6.3 PTO parameters

In order to improve the efficiency of any power absorption, the damping coefficient and stiffness term should be optimized to increase the absorbed power. In this study, the natural frequency of the oscillating body was shifted to coincide with the peak frequency of each wave condition, which resulted in a resonance phenomenon in that the system will oscillate with a greater amplitude. Take the cylinder-shape model with mass, m, as an example. The natural period can be described as:

$$T = 2\pi \sqrt{\frac{m + m_a}{\frac{1}{4}\rho g \pi D^2 + k}} \tag{6-10}$$

Where D is the diameter of the cylinder and k is the strength of stiffness in the control mechanism. In such a way, the harvest range of the cylinder-shape model can be shifted by controlling the strength of the stiffness. In this study, the value of k was kept constant. It should be noted that in the activate control mechanism, the stiffness varied according to the instantaneous incoming wave in order to maximize power absorption.

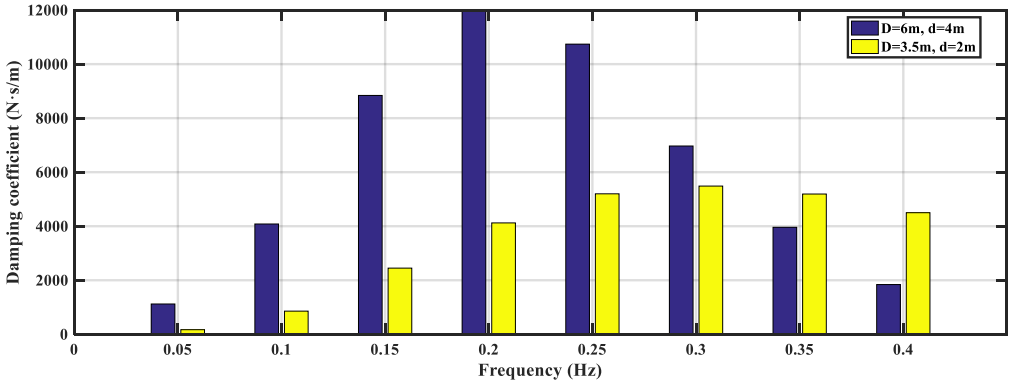

Figure 6-3: The optimal damping coefficient at each wave frequency for buoy with hemisphere shape bottom, different diameter and immersed depth

Furthermore, the amplitude of the heave response was also strongly affected by the PTO damping coefficient, and the damping coefficient had only a slight influence on the response frequency. Garnaud and Mei (2010) indicated that the PTO damping coefficient should match the hydrodynamic damping factor for the largest energy output. From the previous section, the hydrodynamic damping coefficients for heave mode can be accurately estimated. An example of the damping coefficient on the buoy with the hemisphere-shaped bottom is shown in Figure 6-3. It should be noted that larger

diameter of the capture device will not only increase the resonance period, but also improve the harvest bandwidth. The effect by diameter (D) and draft (d) will be discussed later.

6.4 Results

The use of the full wave spectrum is crucial for the estimation of wave energy potential over both deep and shallow ocean areas. Wave energy depends on the distribution of significant wave height and the wave energy period itself:

$$P_{resource} = \frac{\rho g^2}{64\pi} H_{1/3}^2 T_e \tag{6-11}$$

Where T_e is the wave energy period. The wave energy period is the variance-weighted mean period in the density spectrum. It is defined as:

$$T_e = \frac{m_{-1}}{m_0} \tag{6-12}$$

The frequency moments (m_n) of the variance spectrum can be calculated from the following equation:

$$m_n = \sum_{i=1}^{N} S(f_i) f_i^n \Delta f_i \tag{6-13}$$

In the present study, the frequency f_i varies from 0.01 to 0.4Hz and N=40. By applying the equations above, the wave energy potential for each scenario has been summarized in the Table 6-4.

Table 6-4: The energy potential for wave environment conditions 1-14

SCENARIO	*Power (kw/m)*
1	0.16
2	1.43
3	4.82
4	9.45
5	15.62
6	27.47
7	38.37
8	58.82
9	75.55
10	106.83
11	130.51
12	174.86
13	206.59
14	240.97

Additionally, the capture width (CW) was introduced to determine the power captured by the WEC (Falnes, 1975). It defines the ratio between the absorbed wave power (in kw) and the wave resource (in kw/m) as:

$$CW = \frac{P_{absorb}}{P_{resource}} \tag{6-14}$$

The capture width indicates the width of the generated wave crest, which could be completely captured and absorbed by the WEC. The performance of a given WEC was then measured by the capture width ratio (CWR), which was obtained by dividing the capture width by the characteristic dimension - diameter, in this study - of the WEC. The CWR reflects the efficiency of wave power absorbed by the device when flowing over the device:

$$CWR = \frac{P_{absorb}}{P_{resource} \cdot D} \tag{6-15}$$

It should be noted that CWR relates to ideal wave power energy absorption instead of the overall performance. Efficiency in the PTO system and the power transportation, and the manufacture or operation costs, has not been included. It may be such that the most efficient capture device could be the least efficient device from an economic perspective.

An example of a time series of wave elevation at the buoy location with a significant wave height of 1.25m and period of 5.5s, is shown in Figure 6-4. The waves have been measured after 20 significant waves from the wave power spectrum in Figure 6-1 .

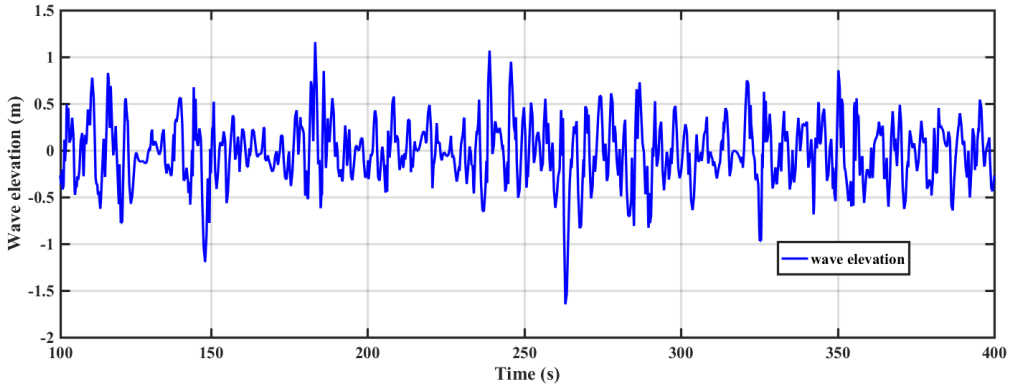

Figure 6-4 wave elevation for $H_{1/3}$ =1.25 and T_z=5.5s

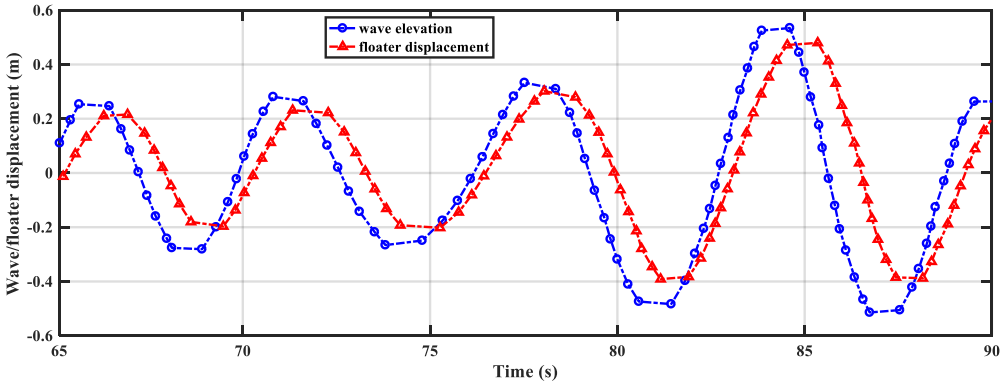

Figure 6-5 Comparison between floater displacement and wave elevation for buoy with cylinder-shape bottom

Figure 6-5 shows an example of a time series of wave elevation and floater displacement for a cylinder-shape buoy. The floater followed the wave movement with a phase shift. The oscillating amplitude is lower than half of the wave height. For each individual wave, the wave height is determined by the vertical distance from the wave trough to the crest.

6.4.1 Effect by buoy draft

At the beginning, the diameter of each buoy is kept constant and the results for different drafts of 2, 3, and 4 m are compared. The minimum 2m was selected in case of the buoy's lower parts moving beyond the free surface in extreme wave conditions.

The results for the different buoy shapes and immersed depth are shown in Figure 6-8 to Figure 6-6. It is quite clear that the results observed by different buoy shapes has a similar trend in terms of buoy draft. As shown, for wave conditions with a large amplitude, the buoy draft has a dramatic effect on power absorption. The results for the different buoy shapes under conditions with a small wave height are nearly the same. More specifically, the peak hydrodynamic damping coefficient are shifted to a higher wave frequency for smaller drafts. The buoy with diameter of 3.5m and draft of 2m absorbed 20% more power than the one with the draft of 4m. Overall, the capture device with a shallower immersed depth had the best performance, thus the models with 2m draft have been used for further simulations in this study.

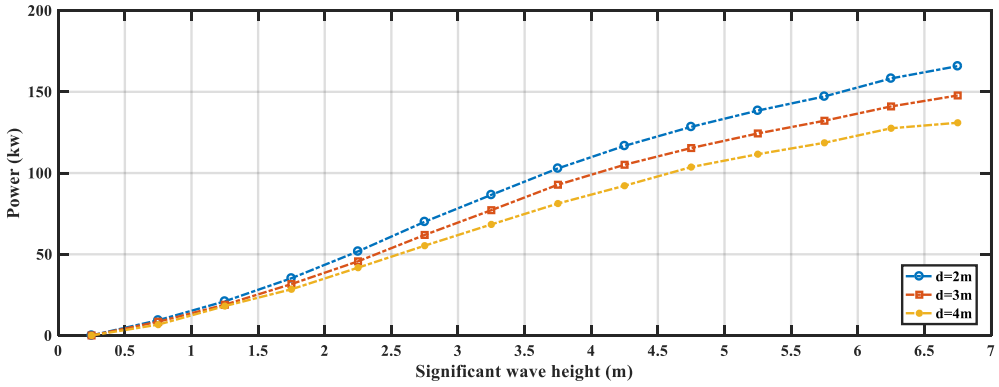

Figure 6-6: The power absorption by buoy with cylinder shape bottom for different draft

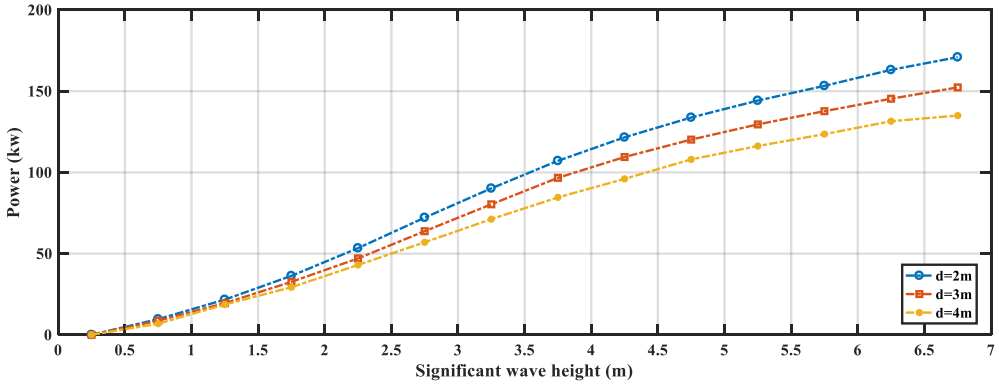

Figure 6-7: The power absorption by buoy with hemisphere shape bottom for different draft

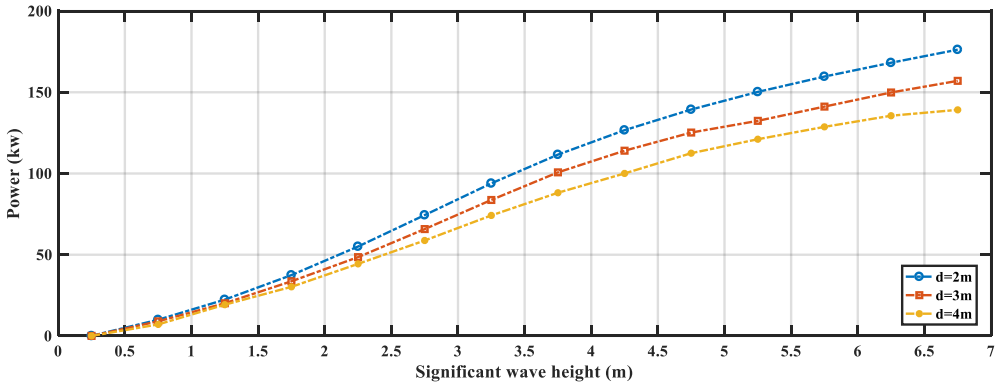

Figure 6-8: The power absorption by buoy with 120° cone shape bottom for different draft

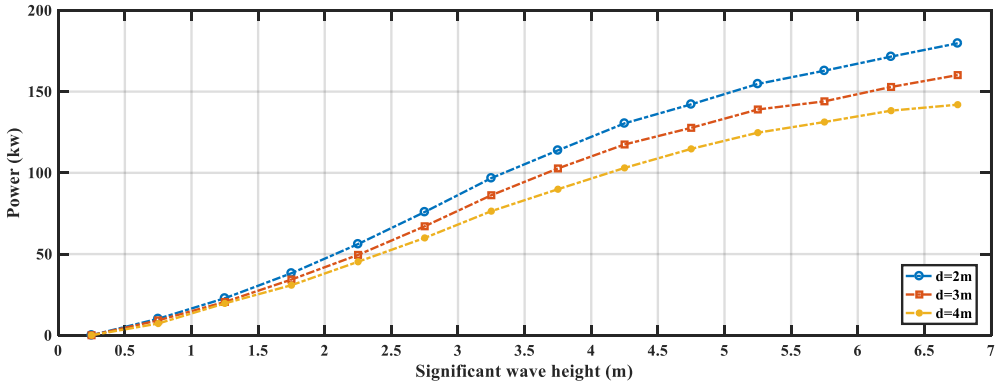

Figure 6-9: The power absorption by buoy with 90° cone shape bottom for different draft

6.4.2 Effect by buoy size and shape

The selection of the characteristic dimension D is critical to P_{absorb} and CWR between different buoys. The power potential and CWR are calculated as the function of the significant wave height ($H_{1/3}$) and the wave energy period (T_e).

With the tuned PTO parameters described in previous section, the power absorption of each buoy for five different diameters and 2m draft under wave conditions 1-14 have been calculated and shown in Figure 6-10 to Figure 6-13.

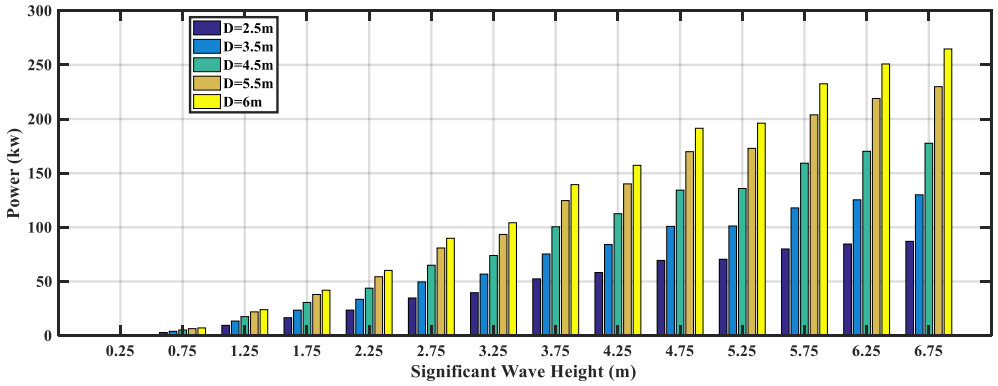

Figure 6-10: The power absorption under different buoy diameters for cylinder-shape bottom

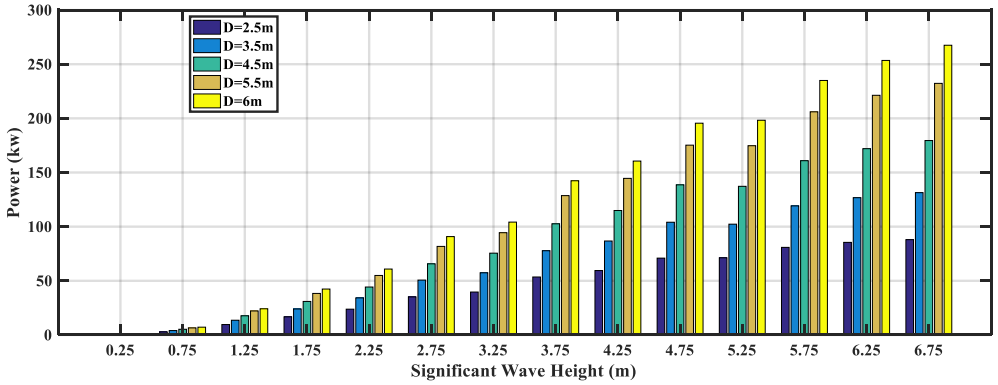

Figure 6-11: The power absorption under different buoy diameters for hemisphere-shape bottom

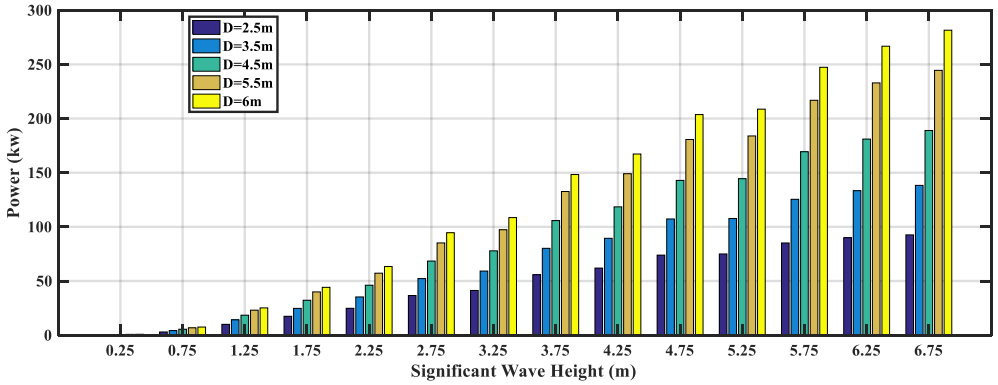

Figure 6-12: The power absorption under different buoy diameters for 120° cone-shape bottom

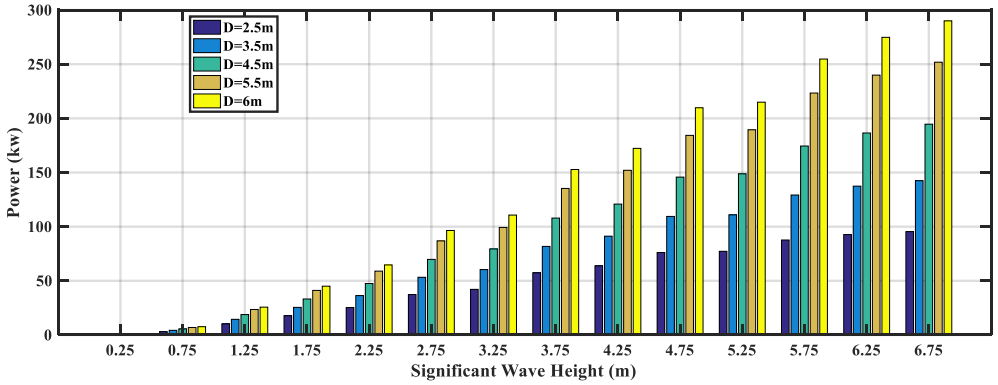

Figure 6-13: The power absorption under different buoy diameters for 90° cone-shape bottom

The results show that the power absorption increases dramatically with significant wave height but is not proportional to the square of the significant as indicated in the power potential calculation (Equation 1-11). This could be caused by the non-linear effect that occurs during the interaction between the buoy and the water's waves. As shown in Figure 6-14, the wave overtopping effect was observed and it has a direct impact on the behaviour of the oscillating motion of the wave point absorber.

It should be noted that the PTO parameters are only optimized for the peak wave frequency instead of each incoming wave frequency.

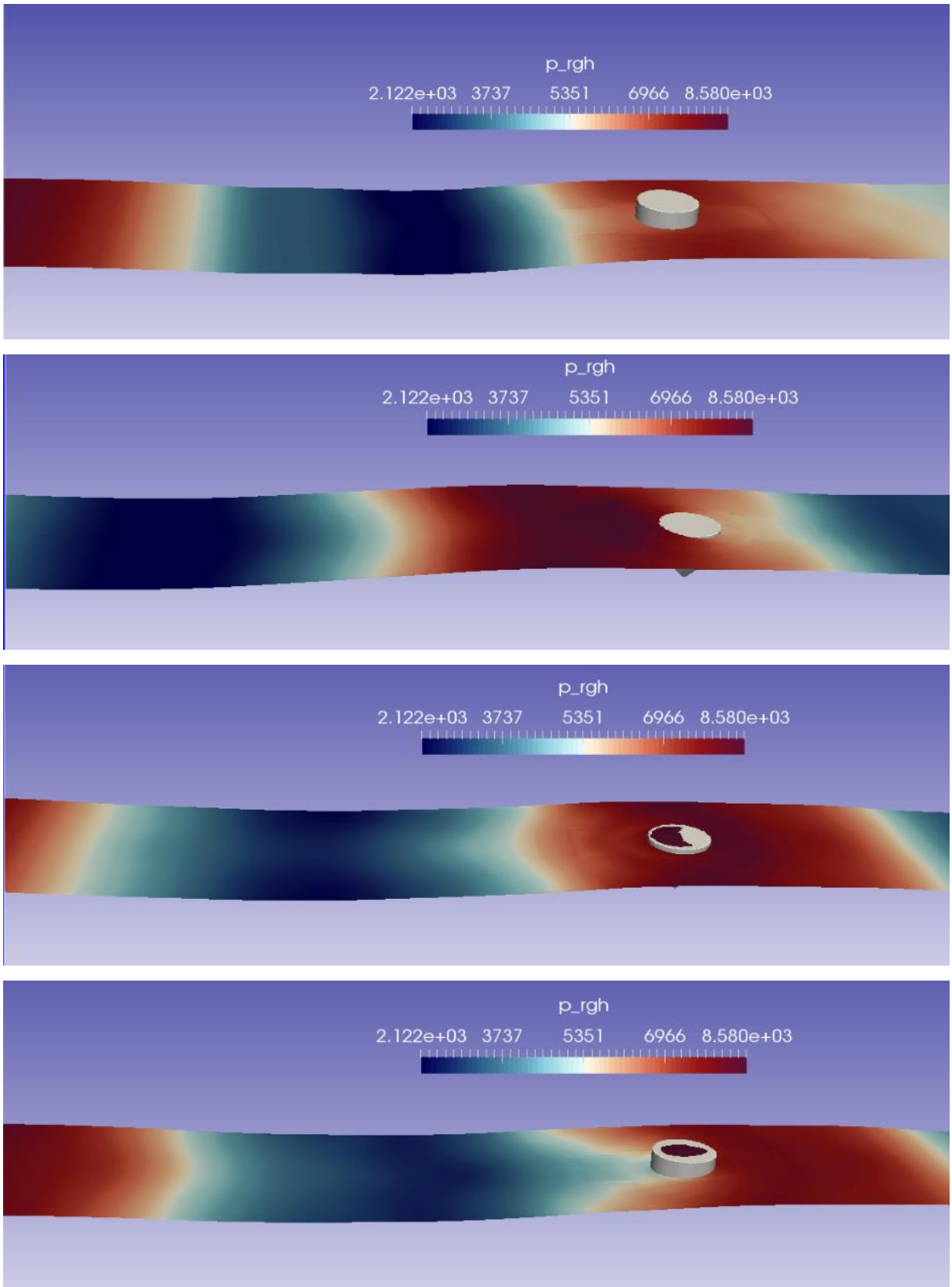

Figure 6-14 :Hydrodynamic pressure of the free surface (top) at t=25.13T_e and the wave overtopping effect at around t= 55.48T_e (bottom three)

The buoy diameter has a big effect on the captured power. When comparing the results of a buoy with the same draft of 2m, the diameter is increased by 1.4 times from 2.5m to 6m while the power production is more than doubled in the wave conditions with the highest significant wave height. There is a constructive effect with growth in relation to significant wave height.

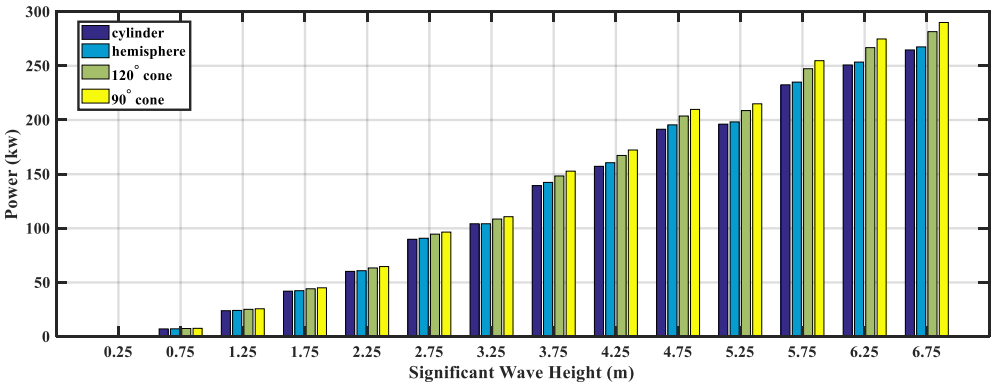

Figure 6-15: The power absorption for buoy bottom shape with D=6m

In Figure 6-15, the buoy with 90° cone shape bottom has the best performance in terms of wave power absorption. It captures about 9.5% more power than the cylinder shape buoy model in the waves with the largest wave height, but the difference at the small wave height range is too small to be noticed.

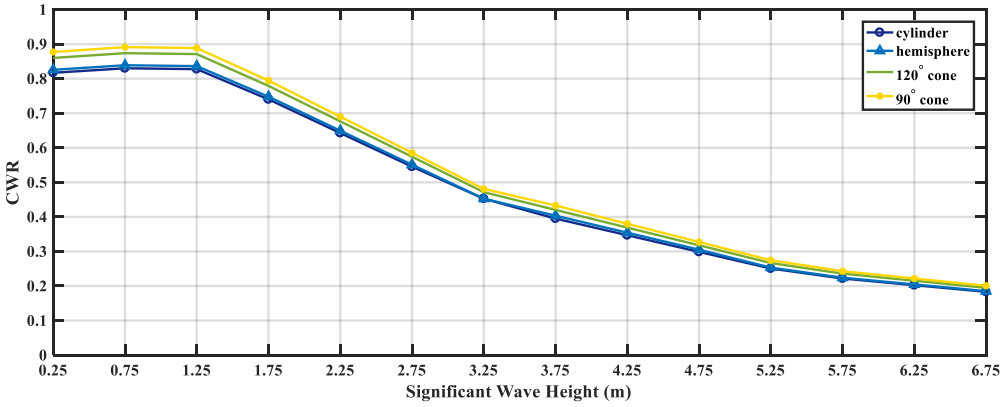

Figure 6-16 The CWR for different buoy shapes

Figure 6-16 shows a comparison for the CWR for the four buoy shapes in different wave conditions. It is can be seen that the capture efficiency decreases with the growth of the wave height. The buoy with 90° cone shape at the bottom has the largest CWR compared with other shapes and the differences between them are too small to be noticed at large wave height. It is obvious that the buoys

capture more wave energy at the sea site with higher wave heights but they are more efficient in a sea site with smaller wave heights.

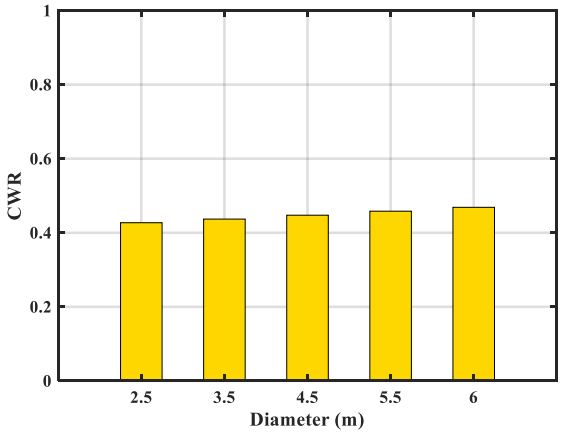

Figure 6-17 The overall CWR for 90° cone shape bottom buoy with different diameters.

The dominated wave heights at this specified sea site are between 0.75m and 2.75m. The overall CWR for the capture device with a 90° cone shape bottom at this sea site has been summarized in Figure 6-17.

It should be noted that the optimal stiffness strength and damping coefficient are set to match the wave conditions. The CWR calculated from scenarios 1-3 are almost the same due to the similar optimal stiffness strength. Thus, it can be concluded that CWR is dominated by the damping coefficient and wave periods.

6.5 Conclusion

In this section, a numerical model based on the RANS equation has been proposed to investigate the behaviour of point absorber WECs. For validating the model, free vibrations in various non-dimensional damping ratios and free decay tests of a heaving subject on the free surface have been firstly simulated. The numerical results have then been compared with those from the experiments and analytics where a good agreement was observed.

A parametric study about the heaving point absorber was carried out to investigate the wave energy potential that can be captured at a given sea site. It can be found that the wave energy has a great potential and this amount of wave energy can be extracted by employing proper wave energy converters. In this study, the hydrodynamic behaviour of four different heaving point absorbers together with PTO system has been examined in irregular wave conditions by way of the CFD method.

The effects by buoy draft, size, shape and PTO parameters on the performance of a point absorber at different sea conditions was investigated and can be concluded as follows:

- The power take-off (PTO) system should co-operate with an extra control mechanism to adjust the natural frequency of the device to match the frequency of the incoming waves. This results in a resonance phenomenon where the oscillating motion is so large so that the interaction between waves and PTO device cannot be accurately estimated by the analytical solution. Additionally, the capture width ratio (CWR) relies on the PTO damping coefficient and the incident wave period. For an irregular sea state, the PTO parameter, including the stiffness strength of the control mechanism, should be tuned for the largest overall power production.

- The capture device with the 90° cone shape at the bottom has the best performance in the investigated harvest range, especially in the one with a large wave height (Figure 6-15). This can be explained by the relatively large hydrodynamic parameters when compared with the other shapes. Also, the cone shape has a wider resonance range than the shapes. The hydrodynamic added mass and damping coefficient, which are force and energy related, has been examined and discussed in the previous section and the conclusions have been further proven within this study.

- The draft of the capture device has a dramatic effect on the power production (Figure 6-9). A lower draft results in a large hydrodynamic force, which will increase the power absorption potentially. The lower draft, on the other hand, changes the capture device's harvest range and

shifts the optimal PTO damping coefficient to suit the sea site with a higher wave frequency. The investigation about draft also indicates that the wave energy is highly concentrated in the region close to the free surface.

- Similarly, the size of capture device also has a great influence on the power absorption (Figure 6-13). The performance of each buoy in terms of power absorption is improved by using a larger capture device. By increasing the diameter of the capture device, the resonance period is increased and so does the bandwidth. The bandwidth is a crucial factor for WEC in irregular wave condition since the device cannot keep working in its optimal condition. While the larger size of point absorber WEC buoy results in a deeper draft for the devices made from the same material, the balance between buoy size and draft should be taken into consideration. It should be noted that the characteristic dimensions of the floating buoy should be kept within a reasonable range to get rid of the impact from wave direction.

- The sea site studied in this section is dominated by waves with significant heights from 0.75m to 2.75m. The benefit of using a cone shape buoy is rather limited from the manufacturing perspective, since the influence of buoy shape within this range is too small to be noticed. Moreover, the overall CWRs for a capture device with different sizes is slightly different (Figure 6-17), but a smaller device reduces the hydrodynamic damping effect. The device could be equipped with a compact PTO unit.

7. Validation to two-body PowerBuoy model

Validation is a mandatory process for the numerical models to prove their capabilities in simulating physical phenomena in an accurate way. This can be confirmed by the convergence and reliability of the CFD model, the independent study of the space and time discretisation method, the examination of the effects of the turbulence models, and a comparison with the experimental data.

In this section, a particular two-body PowerBuoy model, see Figure *7-1*, has been chosen as the test model. The current PowerBuoy (PB3) is under commercial use and can operate in any ocean depth from 20m to 1000m. The numerical simulation was carried out to compare the results with the ones from the experimental measurements to demonstrate that the CFD model is able to represent the energy harvest processes accurately. The validation work was conducted to represent the job done by Yu and Li (2013).

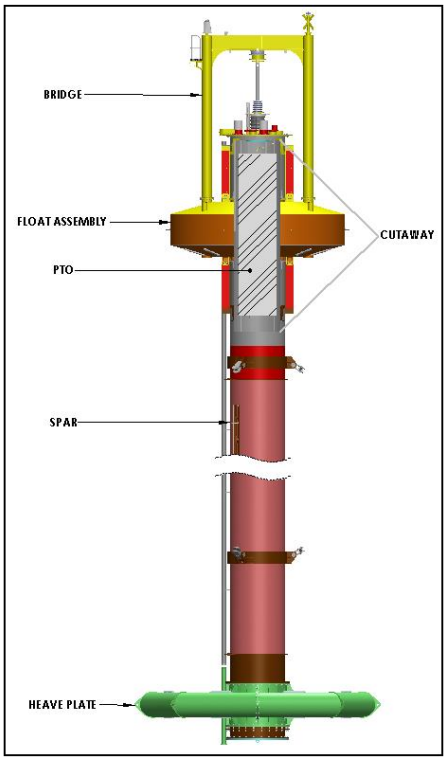

Figure 7-1: Two-body PowerBuoy point absorber WEC model, picture from PowerBuoy PB3 Project

7.1 Computational domain

The CFD model was validated with an experimental test carried out by Yu and Li (2013) in the UC Berkeley wave tank with a 1/100-scaled model. The experiments involved translated motion only and there was no angular motion. Thus, the validation of CFD model was restricted to translated movement only. The physical tank was 68 m long, 2.4 m wide and 1.5 m deep (Figure 7-2). The point absorber model motion was captured by a 2D motion-tracking system. The total weight of scaled point absorber was 313g including the measurement device.

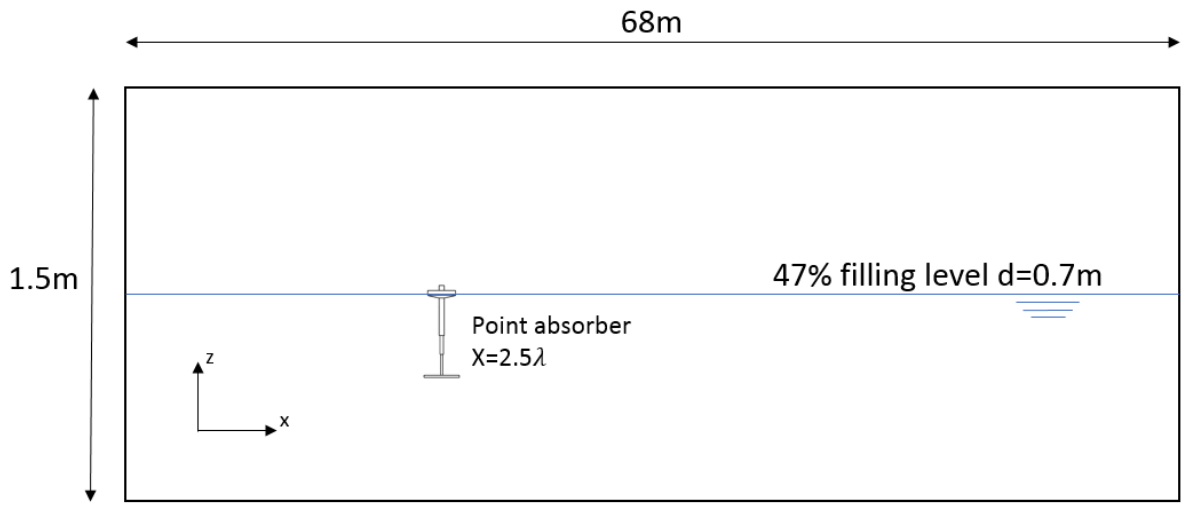

Figure 7-2 Experimental tank dimension and the location of point absorber

For validation purposes, the geometry of the computational domain was created to match the conditions in the experimental tests with a full-scale dimension (Figure *7-4*). One of the advantages of the CFD model was that a full-scale test and a lower blockage effect could be achieved compared to the water tank tests. The blockage effect was relatively small due to the concept of point absorber WEC and it is important to represent the wave environment as it has a dominant effect on the performance of the point absorber in this case.

The point absorber scaled model and its corresponding geometry used in the numerical simulation are shown in Figure 7-3 and Figure 7-4, respectively. The total weight of the full-scale model is about 249.5 tons and its centre of gravity is located 22.4 m below the calm water surface. In the design of the two-body point absorber, only the simplified structure with a spring and damper system, which is regarded as the PTO system, was considered.

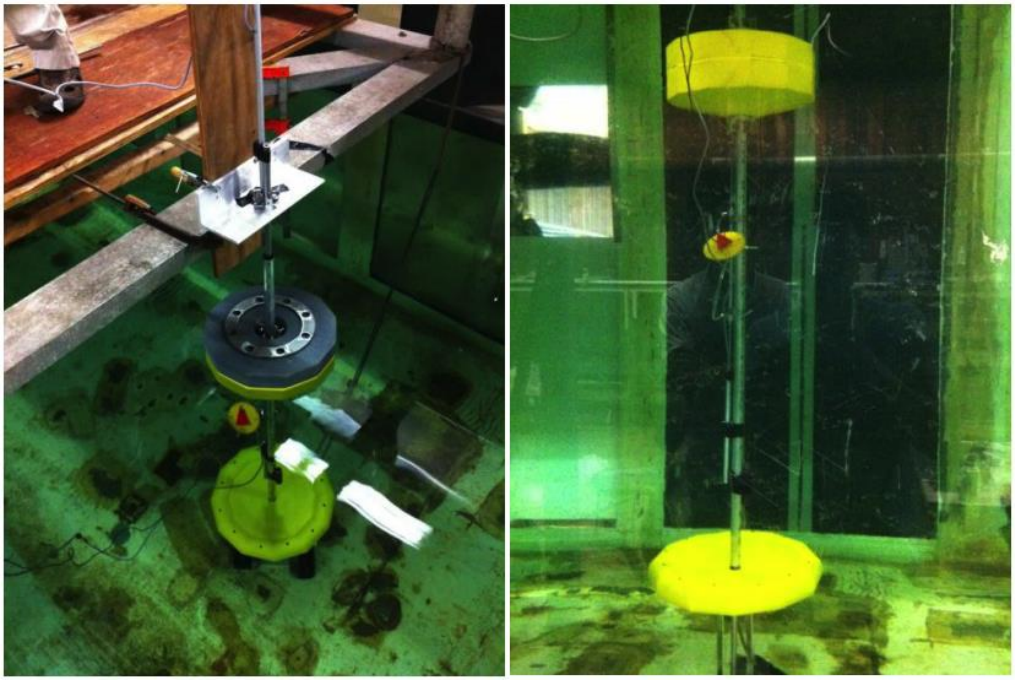

Figure 7-3 Physical experimental test of 1/100-scaled point absorber model (Yu and Li, 2013)

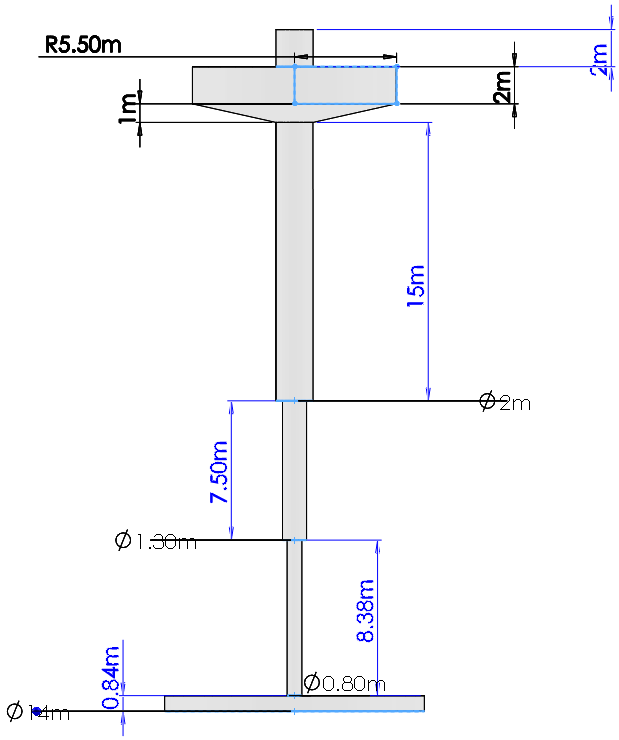

Figure 7-4 The computational model of two-body point absorber with its dimension

7.1.1 Mesh

The background mesh was generated by the OpenFOAM utility *blockmesh*. To snap the mesh and add boundary layer zones to the point absorber surface, the utility *snappyHexMesh* was used. There were several factors considered during the process to create the mesh before the numerical simulations were applied.

- Higher resolution in the point absorber model boundary layers.
- Higher resolution at the free surface to capture the wave profile and to eliminate numerical diffusion.
- Higher resolution around the point absorber to capture viscous, wave overtopping and slamming phenomena.
- Building up buffer layers to have a smooth transition between different levels.

Figure 7-6 to Figure 7-8 shows the meshes around the point absorber model. Based on the uniform background mesh, each cell is divided into four in both gravity and horizontal direction in the refined regions after one refinement level step. There is a buffer region of cells with an equal size between each region of refinement. The difference between the refined region and the buffer zone is one level to ensure a smooth transition between each area. The region around the point absorber has the finest mesh refinement level, and 10-20 layers are generated from the surface with an expansion ratio 1.2, see Figure 7-5.

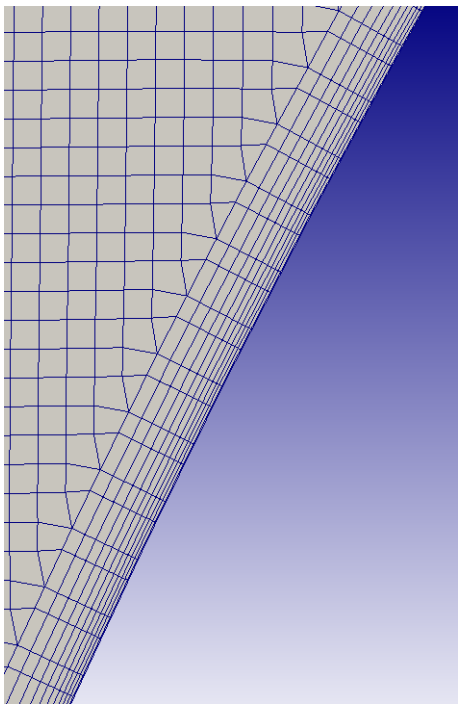

Figure 7-5 Boundary layer at point absorber surface

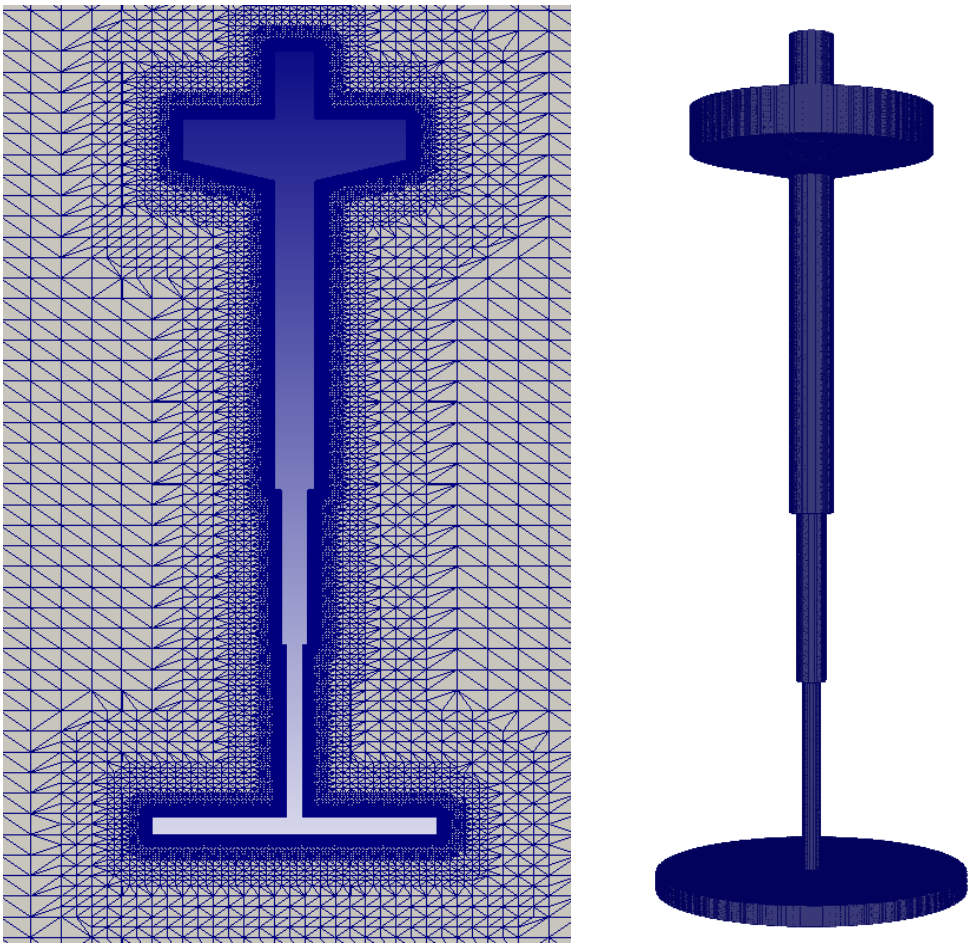

Figure 7-6 Mesh around the two-body point absorber

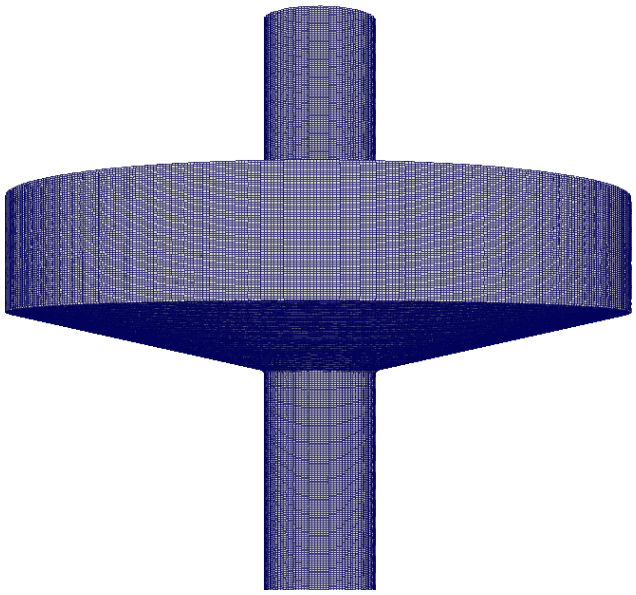

Figure 7-7 Floater on the top of two-body point absorber

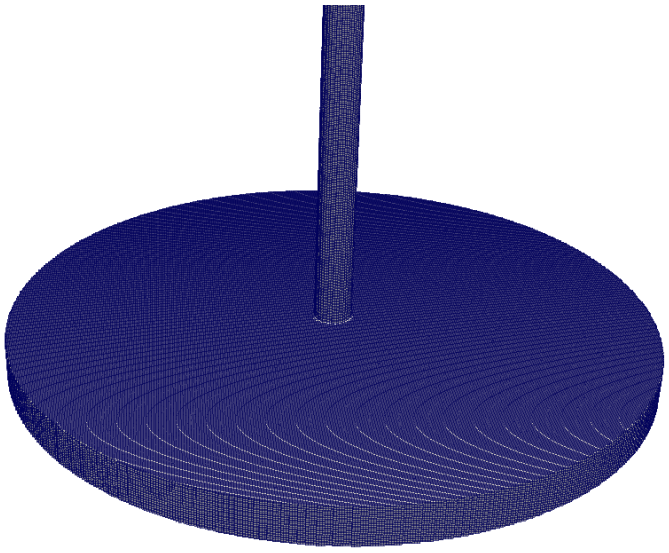

Figure 7-8 Reactor plater at the bottom of two-body point absorber

A higher mesh cell resolution in the free surface region is needed to accurately represent the surface waves. The resolution has been found to be in the order of 30-50 cells per wave length and around 30 cells per wave height (Vaz et al., 2009) which depends on the wave slope and steepness since a steeper wave requires a higher resolution in the gravity direction. Yu and Li (2013) adopted 80 cells per wave length and 20 cells per wave height as a finer region at the free surface. Because the results from the reference were drawn from a different solver algorithm, a mesh sensitive study was carried out on the wave height during wave propagation. The density of the mesh in the free surface region varied in the vertical and horizontal directions. The generated wave amplitude of 5m with wave period of 17.5s was recorded at a distance of 2.5 wave length away from the inlet. Figure *7-9* shows the results of grid independence study for 15-55 cells in each direction.

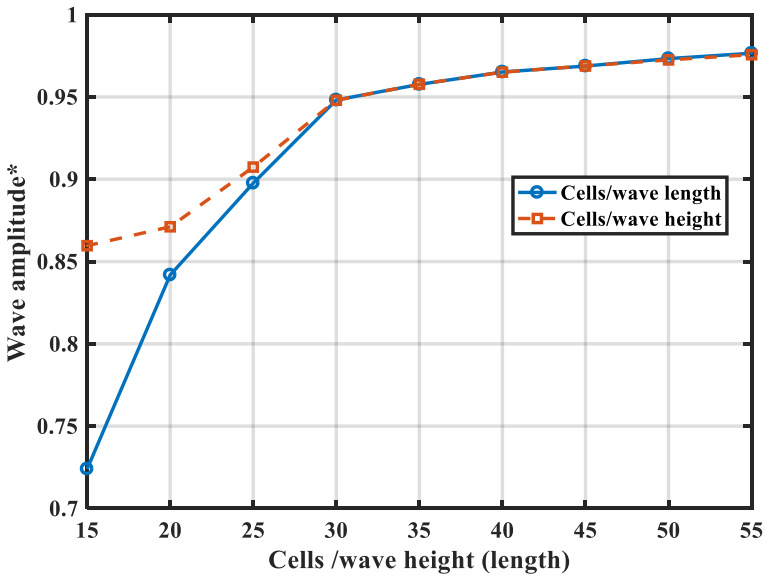

Figure 7-9 The effect of grid resolution on non-dimensional wave amplitude during wave propagation

These results indicated that at least 30 cells per wave length and height should be used throughout the calculations. It can be noticed that even at 55 cells per wave length and height, there is still a 2.5% loss of the total wave amplitude. This can be explained by the dissipation in the physical world due to viscosity. The energy of a gravity wave dissipates during propagation. An alternative way, other than mesh refinement, is to generate waves with a slightly higher amplitude at the inlet boundary to ensure the waves have the correct amplitude before they encounter the point absorber. For longer domains, for example when studying multiple point absorbers in an array, the numerical dissipation will present and it may affect the result. Thus, the number of cells in the density has to be increased to achieve the same accuracy on the wave amplitude.

Table 7-1 Mesh independence study for two-body point absorber

Mesh	*Coarse*	*Medium*	*Fine*
No. of cells	3.1M	5.3M	6.2M
y^+ *average*	1.08	1.05	1.01
Predicted force against finest mesh	-3%	1%	0

The mesh independent study is summarized in Table 7-1. Based on these settings, the meshes used in this study should be suitable to capture the hydrodynamic behaviour of the point absorber. It should be noted that the average quantities can be predicted with good accuracy, while the local variables may be sensitive to the grid resolution. Thus, the simulations with more complex point absorber geometry should be carried out with a systematic approach to verify the mesh independence of the solution.

7.1.2 Turbulent model

The turbulence model is designed to simulate the complex flow in the near wall region. The SST k-omega model was chosen to model the flow inside the boundary layer. The wave tank inlet has a small fixed value, 3%, of turbulence intensity to represent the initial turbulence in the wave tank. The non-dimensional wall distance, y+, of the first cell should be less than 1 to solve the turbulent flow in the boundary layer. But it is found that the SST k-omega could handle more coarse mesh with an enhanced wall treatment. The thickness of the boundary layer mesh in this study is set to 10-20 cells with an expansion ratio of 1.2 to achieve y+ value of 1. The boundary layers have been added to the structure surface except the right angles at the floater and reactor corners. This is because the added layers may impair the quality of the results due to highly skewed faces and affect the non-orthogonality of the mesh.

7.1.3 Numerical scheme

As mentioned before, the hydrodynamic behaviour of the point absorber relies on accurate wave simulation. Thus, the numerical scheme that impairs the wave amplitude has been further discussed here. Take the upwind scheme as an example; numerical diffusion may occur and lead to non-physical damping effect of the surface waves (Zhou et al., 2008). Ismail et al. (2010) indicated that the choice of the convection scheme and turbulence model had a great impact on the integral of forces and moments and flow features in the wave. A recommended solution to this problem was to use a limited

Total Variation Diminishing (TVD) scheme (Winden et al., 2014). In general, TVD is a scheme employed to capture sharper shock predictions without any misleading oscillations when the variable is discontinuous. The limited TVD schemes combine a second order central differencing and a first order upwind scheme based on the local flux. The flux on a certain face thus can be described (Jasak, 1996):

$$\phi_f = \phi_f^{UW} + \alpha(\phi_f^C - \phi_f^{UW}) \tag{7-1}$$

Where ϕ_f^C is the face flux calculated by central differencing scheme, ϕ_f^{UW} is the face flux calculated by upwind scheme and α is the weighting function which can be calculated based on the flux gradient:

$$\alpha = \frac{\phi_{Local} - \phi_{Upstream}}{\phi_{Downstream} - \phi_{Local}} \tag{7-2}$$

Where the ϕ with subscripts are the flux from the local cell, the upstream cell and downstream cell respectively. Moreover, in the implementation of OpenFOAM, the weight function is modified from the original TVD condition:

$$r = \frac{2\alpha}{\beta} \tag{7-3}$$

The face flux is now calculated from the central and upwind scheme by changing the value of β. r=1 is for full central differencing scheme and r=0 is for full upwind scheme.

To find the influence of the numerical scheme on the results of wave propagation, three different schemes have been tested and it is important to found confidence in wave energy research. The tested schemes that have been built in the OpenFOAM are the central differencing scheme, upwind scheme, and limited TVD schemes. The results are shown in Table 7-2. The schemes mentioned above are adopted to interpolate the deviation of velocity, turbulent kinetic energy and turbulent dissipation.

Table 7-2 Courant number requirement for each numerical scheme and their corresponding clock time for each step

Test	*Scheme*	*β*	*Maxi-courant number*	*Time per step*
1	Upwind	n/a	1-2	15s
2	2nd Upwind	n/a	0.5-0.6	17s
3	TVD	1	1-2	16s
4	TVD	0.5	0.9	16s
5	TVD	0.1	0.2	16s
6	2nd Central differencing	n/a	0.1	19s

Computer cluster have been used for each scheme. It has two nodes with dual 2.6 GHz processors and each node has 16 CPUs. It can be seen that the central differencing scheme requires a very small time step and it needs more iterations for each step before reaching convergence. The clock time for each step is shown for the computational domain with about 5.2M cells. The 1e-6 residual control is set up for velocity, turbulent kinetic energy and dissipation and 1e-7 residual for pressure correction. The velocity and pressure are coupled in the PIMPLE loop.

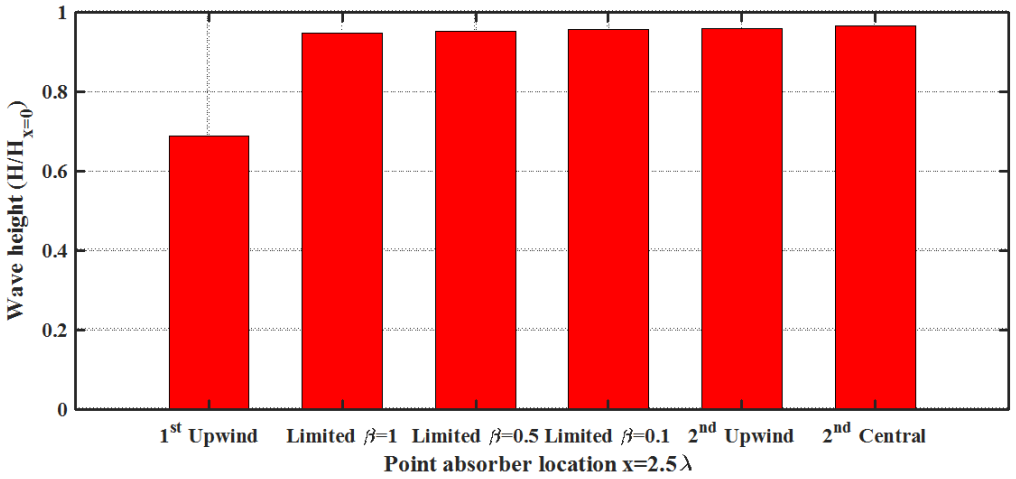

Figure 7-10 Normalized wave height measured at point absorber location by different numerical scheme

For tests in relation to regular waves, at least 20 encountered waves are ensured for the tests in accordance with ITTC recommended procedures (ITTC, 2011). The ITTC also recommends a period

of 20-30 minutes at full scale for tests in irregular waves (ITTC, 2011). Thus, the mean normalized amplitude of ten wave cycles shown in the figures are measured after twenty wave periods. The effect of the numerical scheme on the normalized wave amplitude is shown in Figure 7-10. It can be seen that the result of 1st upwind scheme is not acceptable due to the poor prediction of wave height after propagating a 2.5 wave length. The results by the limited TVD and second order upwind and central schemes have a similar order of accuracy. In terms of wave induced force, Figure 7-11 shows the average wave induced force for the different schemes. The solutions using different schemes do not vary much.

It can be concluded that the 2nd order central scheme has the best results but it requires a huge demand on the computational resources in practice. The limited TVD scheme and 2nd order upwind perform similar results with a reasonable computational source and they are much more stable than the central differencing scheme due to the usage of a higher concurrent number.

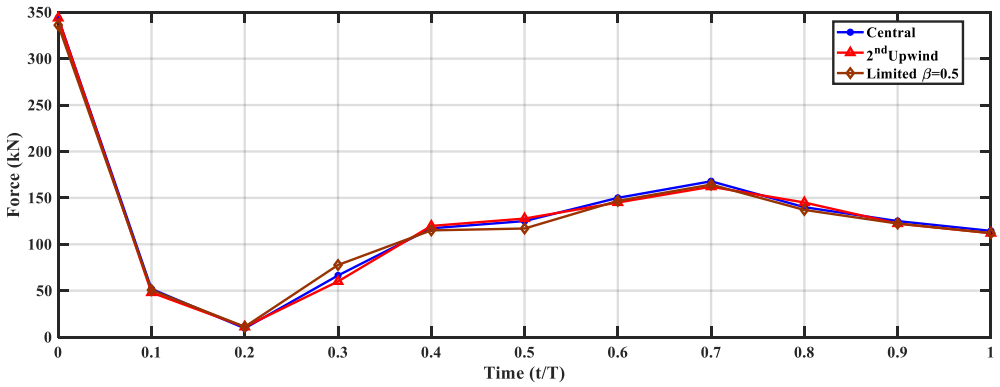

Figure 7-11 Wave induced force on the point absorber for different numerical scheme

Based on the investigation of the different schemes in this section, the limited TVD and 2nd order upwind convection scheme have been proven to be the best choice in terms of speed, accuracy and stability. Thus, they have been used throughout the study in the following sections.

7.2 Results

After presenting the numerical scheme and numerical wave tank setup, a series of computational simulations about the two-body point absorber were conducted to investigate the hydrodynamic behaviour and the results were validated against previous work. In this study, a heave decay test was first conducted to validate the numerical model. Then the behaviour of the point absorber was verified without considering the PTO mechanism. Finally, the performance of the point absorber model was examined.

7.2.1 Heave decay test

The numerical model was validated against the experimental test that was achieved in the UC Berkeley wave tank with a 1/100-scaled model, see Figure 7-3.

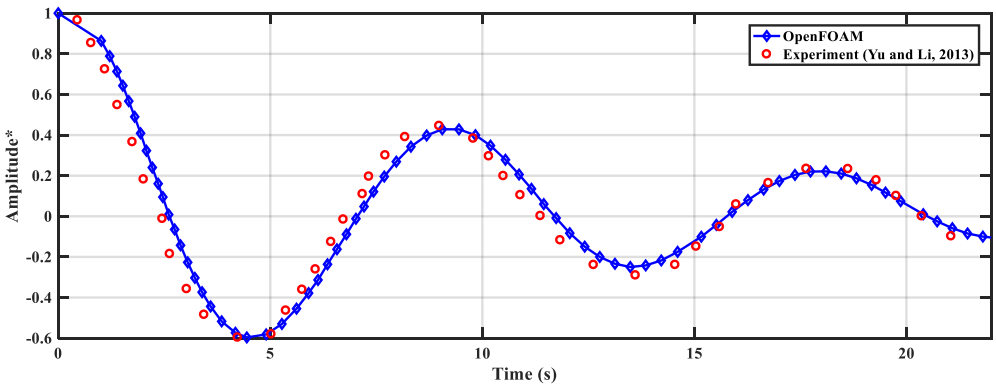

Figure 7-12 Heave decay test for 1/100-scaled point absorber model

Initially, the point absorber was lifted by 0.2m in a gravity-effected direction to test the nature period of the point absorber model. Figure 7-12 shows the comparison of the non-dimensional amplitude (divided by 0.2m) history calculated by numerical simulations and the experimental measurements. There is an error of 2% in nature period which shows good agreement. The decay test study further indicates that the mesh and specified numerical scheme, as mentioned in the previous section, are capable of modelling the point absorber in the following studies.

7.2.2 Regular wave test

The heave responses of the point absorber without the PTO system under different regular waves is shown in Figure 7-13.

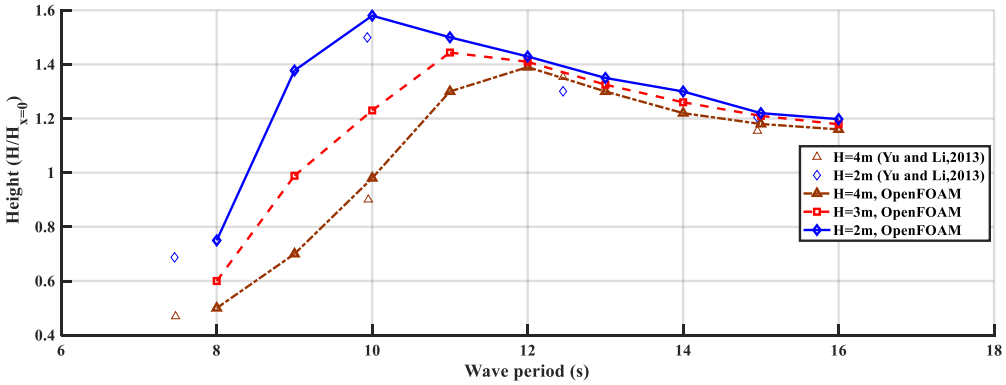

Figure 7-13 Heave response for point absorber with different wave period

The incident wave heights are 2m, 3m and 4m, respectively and the wave periods vary from 8s to 16s. Unlike the natural period shown in Figure 7-12, the resonance occurs at the wave period of 10s for the wave with the lowest wave height. The natural period of the point absorber is further shifted to a wave period of 12s by increasing the wave height. On the other hand, the optimal heave response decreases with the wave height increase. The results show that:

- For waves with a longer period, the draft of the point absorber will remain constant and finally the point absorber will follow the motion of the waves ($H/H_{x=0} = 1$).

- For a point absorber under extreme conditions, the non-linear effect cannot be neglected especially at resonance. The viscous drag force in calm waves is negligible but it increases dramatically when the waves are running high due to the shape of the reactor at the bottom. As indicated in the Chapter 6, the radiation damping force decreases with the draft thus the radiation force on the reaction plate is unimportant. The wave overtopping and water slamming can be observed in higher waves. These effects add extra terms in the original restoring force and thus change the natural period of the point absorber.

- This indicates the weaknesses of the linear potential theory-based method in predicting force and its inability to capture the non-linear interactions between the point absorber and the incoming waves.

When comparing the result with the one by Yu and Li (2013), the heave response is slightly higher than what they predicted. It can be explained by:

- The different numerical scheme in use; the numerical scheme has a great impact on wave amplitude.

- The results are not recorded after a longer simulation time. For regular waves, the wave pattern will become steady after twenty wave cycles based on the numerical wave tank length in this study. A sufficient time before the data measurements are taken is needed since the waves generated at the inlet contribute more energy than the ones in pattern, but they will dissipate as time passes and become less significant.

The hydrodynamic pressure contours and the free surface level are shown in Figure 7-14 and Figure 7-15.

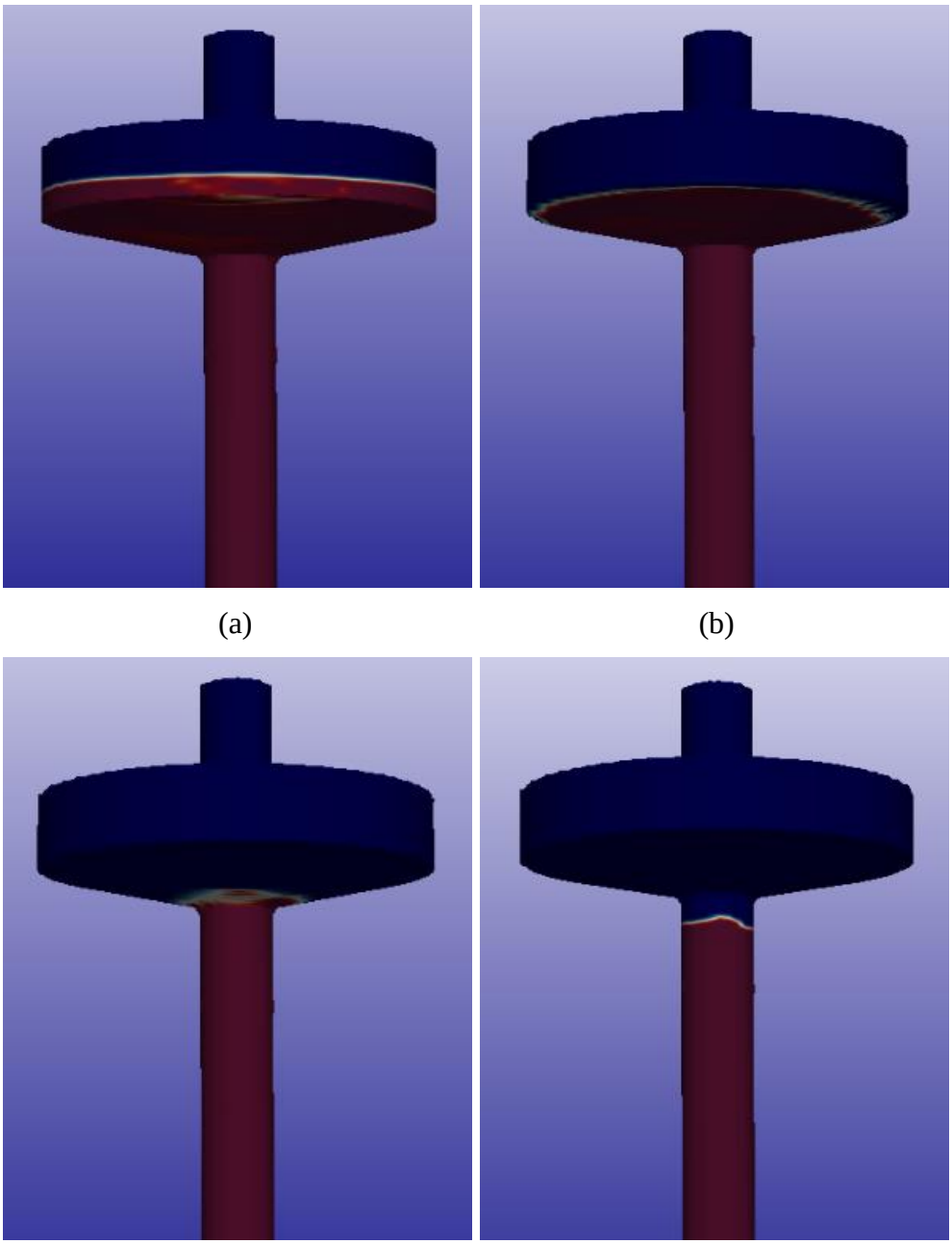

(a) (b)

(c) (d)

Figure 7-14 Hydrodynamic pressure on the point absorber for ¼ wave cycle under wave period of 10s and wave height of 2m.

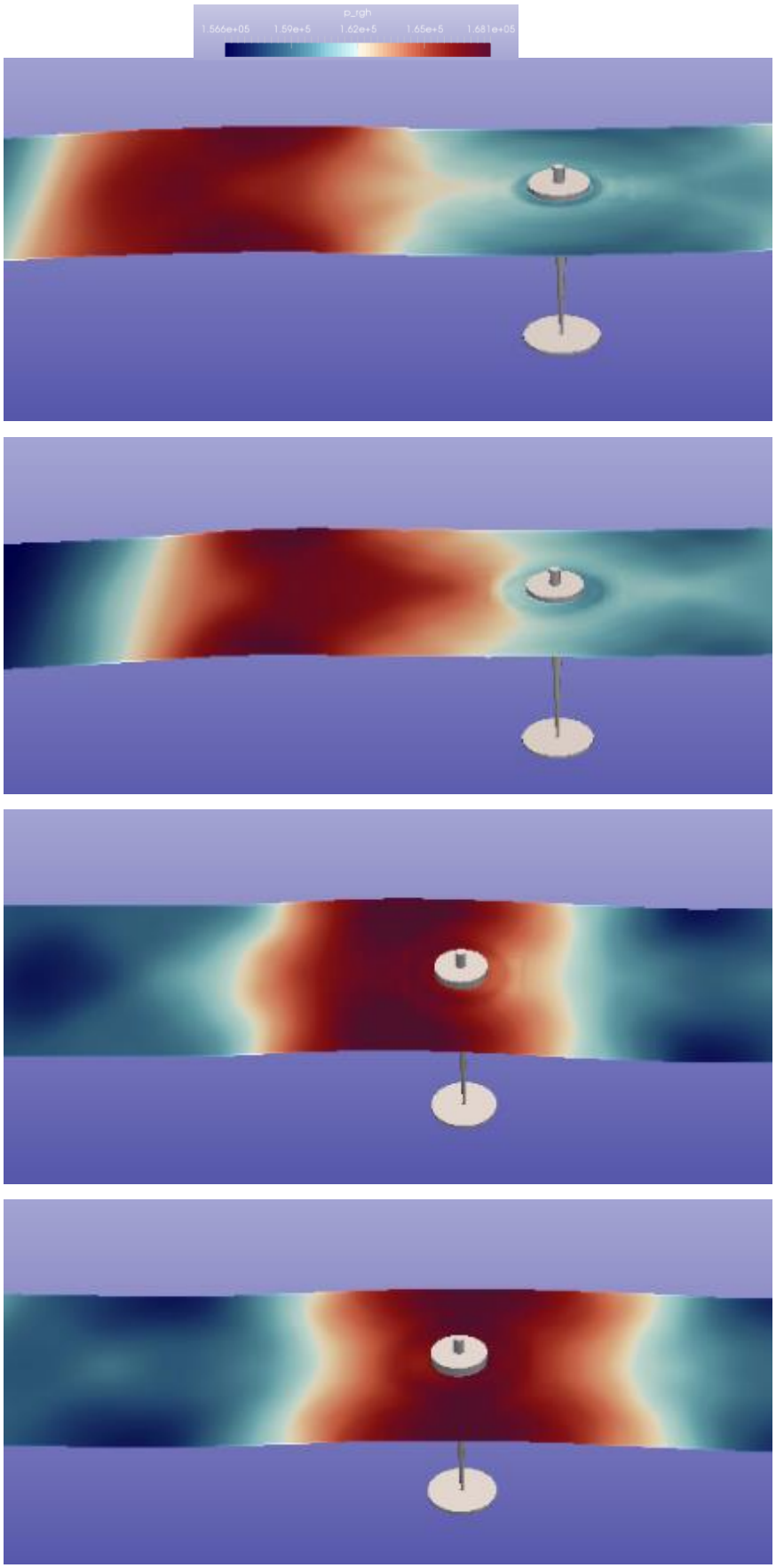

Figure 7-15 The hydrodynamic pressure on free surface for ½ wave cycle

In the next part, the power take-off system of the point absorber was considered and the power extracted from the relative motion between the float and the reaction section. The reaction plate was set to have neutral buoyancy. The mass of the upper floater and the lower reaction plate was 84500kg and 165000kg, respectively. The numerical simulations were conducted to investigate the performance of the point absorber, and the results were compared with the experimental measurement data for validation. Initially, a series of simulations were conducted to find the optimal damping coefficient for the power take-off system. It should be noted that the stiffness strength in the experimental test was kept constant (20kN/m), thus it was not optimised in this study.

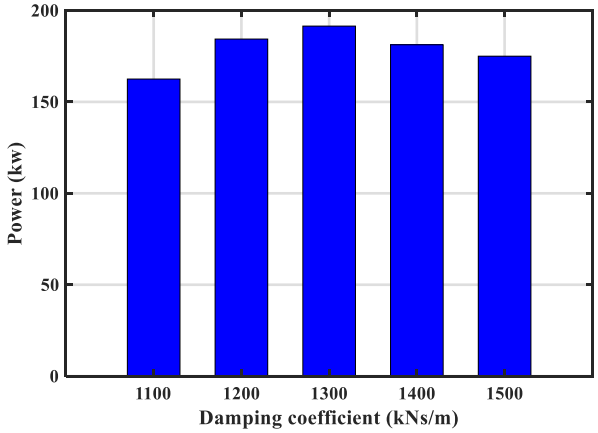

Figure 7-16 The power extraction with different damping coefficient (wave height=2.5m)

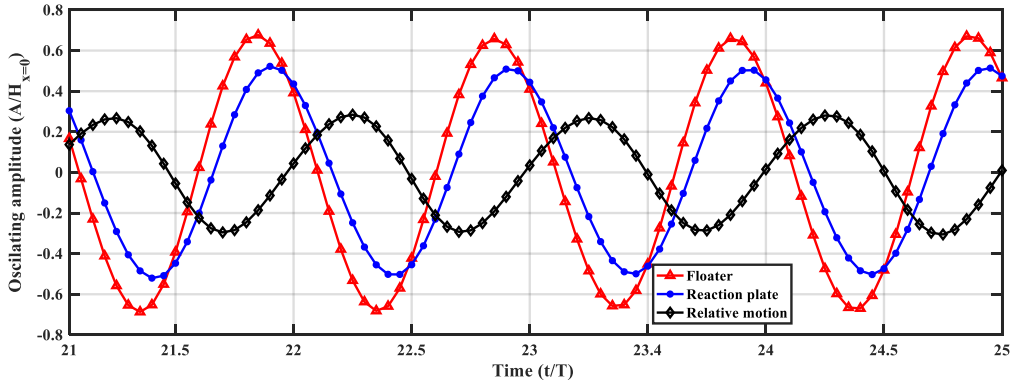

Figure 7-17 The amplitude of each section of the point absorber at wave height of 2.5m and period of 8s

The optimal damping coefficient at a wave period of 8s, which is the nature frequency of the point absorber, is shown in Figure 7-16. The optimal damping coefficient was found to be around 1300kNs/m. Figure 7-17 shows the oscillating amplitude of the upper floater and lower reaction plate and their relative motion with the optimal damping coefficient at a wave height of 2.5m with 8s wave

period. As mentioned before, wave energy is concentrated in the region that is close to the free surface, thus the upper floater suffers more wave induced force than the one on the reaction plate. There is a phase shift between the upper floater and lower reaction plate and the phase angle depends on the PTO parameter.

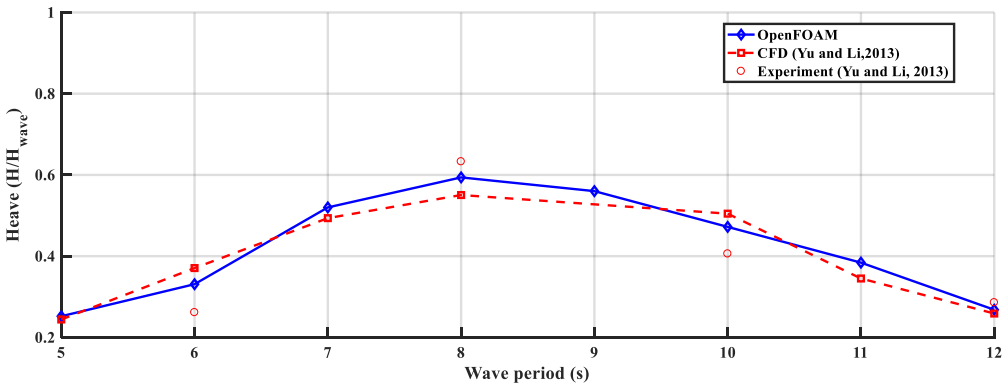

Figure 7-18 Heave response at different wave periods for wave height of 2.5m

Figure 7-18 shows the heave response with the damping coefficient of 1200 kNs/m in order to compare the results with the previous work. Both CFD simulation results agree with each other fairly well and any inconsistencies could be explained by the different numerical schemes in use and the slightly different geometry in details between them. Moreover, the difference between the numerical model and experimental model could be caused by the scaled effect. This is because it is not clear whether or not the viscous effect due to the vortex around the reaction plate is scalable.

Figure 7-21 and Figure 7-20 show the hydrodynamic pressure on the free surface and on the point absorber floater. The wave heights are 2.5m and 4m with wave period of 10s. Similarly, wave overtopping can be observed, and the floater can be completely beyond the free surface ($H/H_{x=0} > 1$).

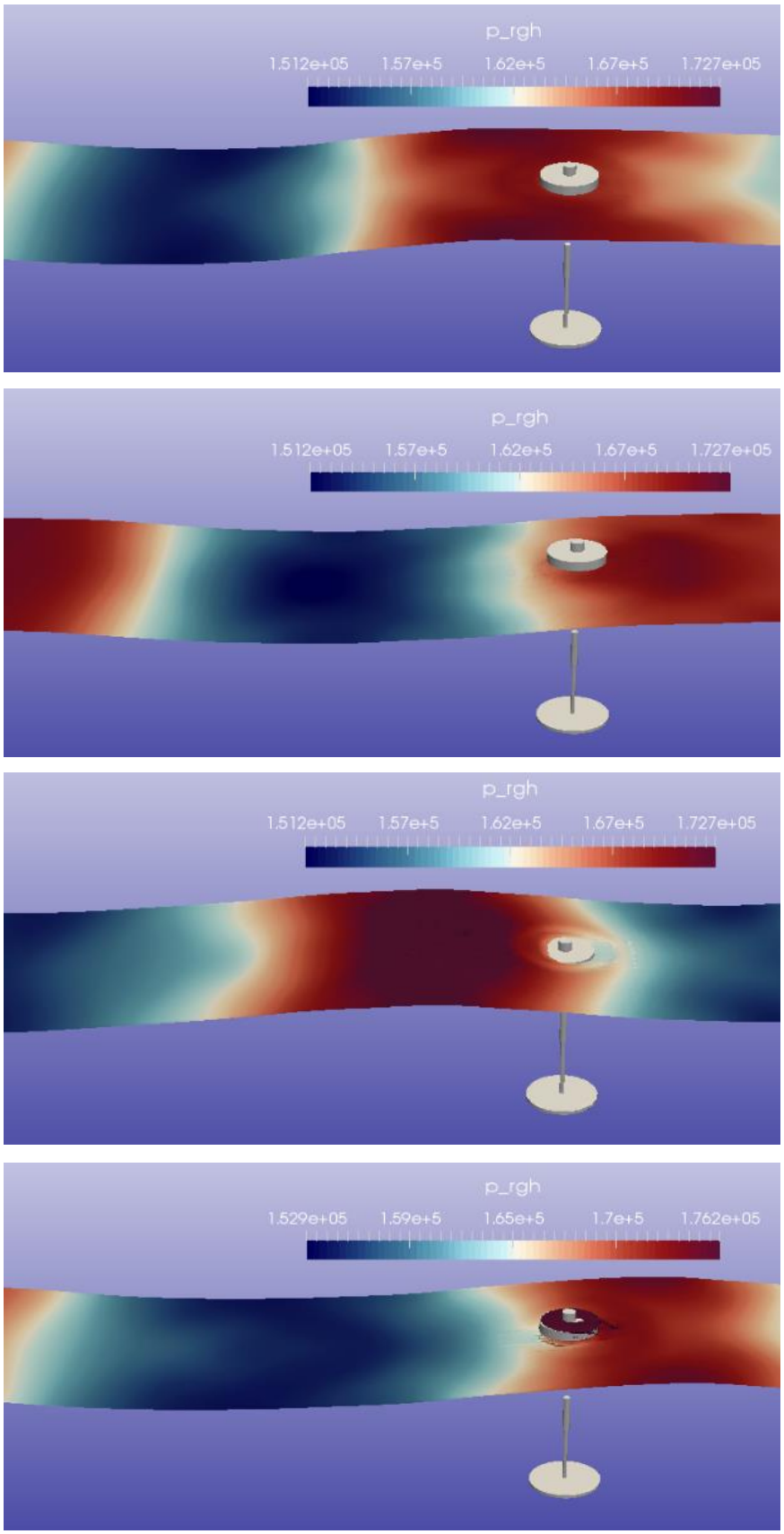

Figure 7-19 The hydrodynamic pressure on the free surface and wave overtopping phenomena under higher wave height (bottom two)

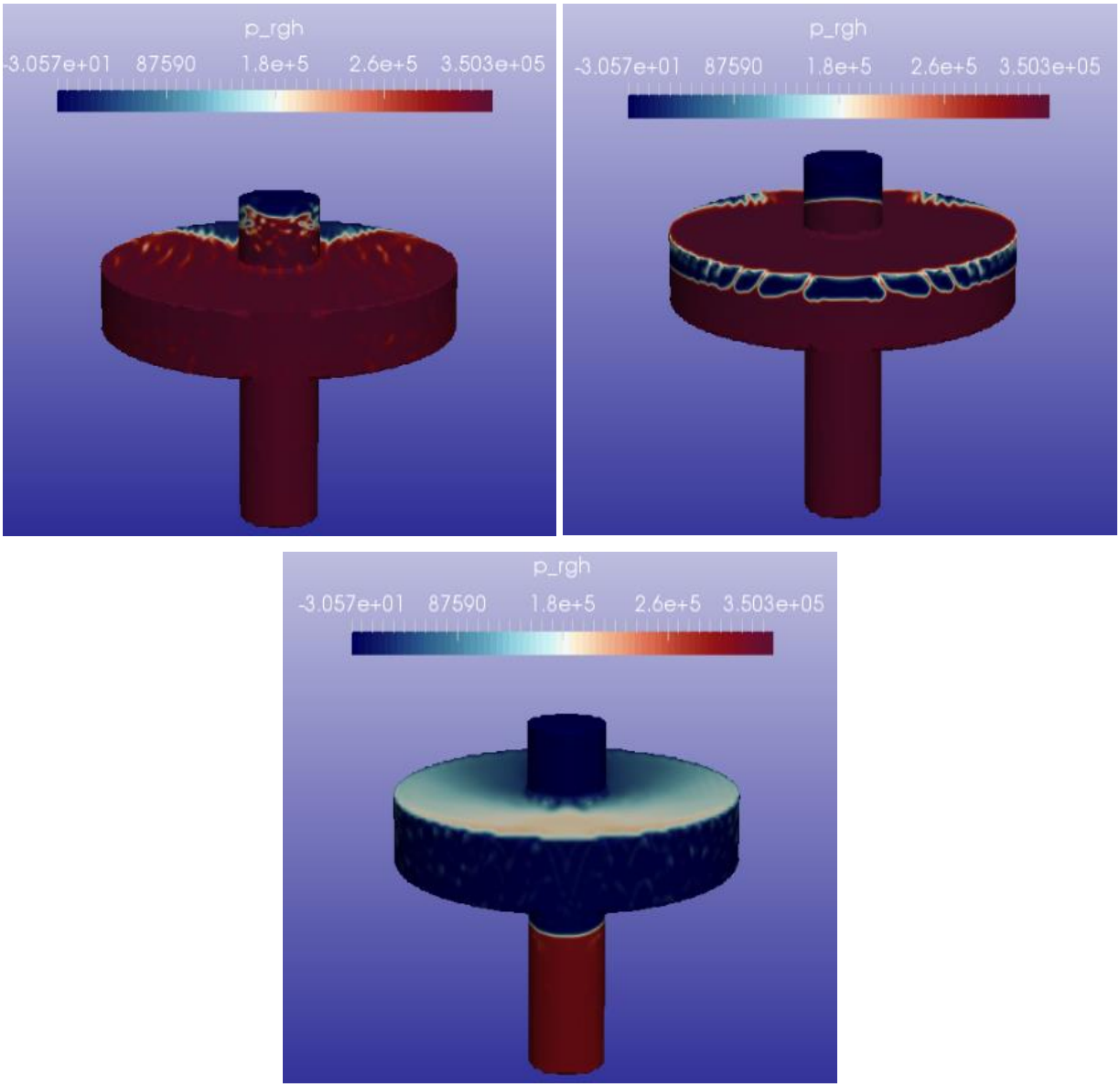

Figure 7-20 Wave overtopping effect on point absorber floater

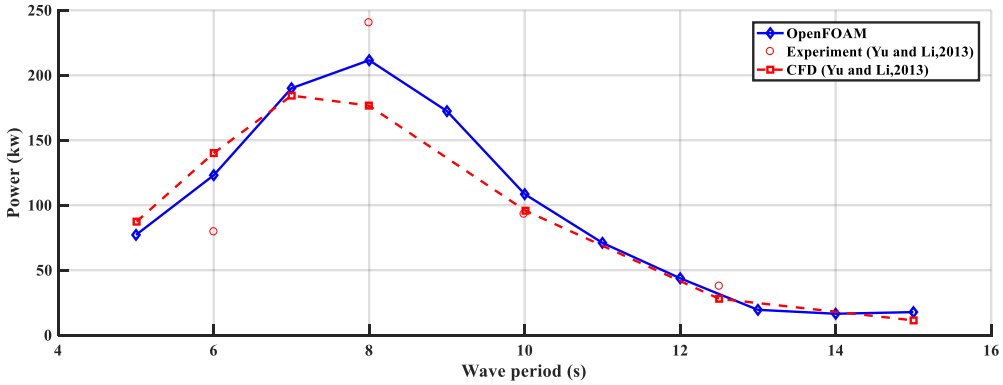

Figure 7-21 Power captured for different wave period at wave height of 2.5m

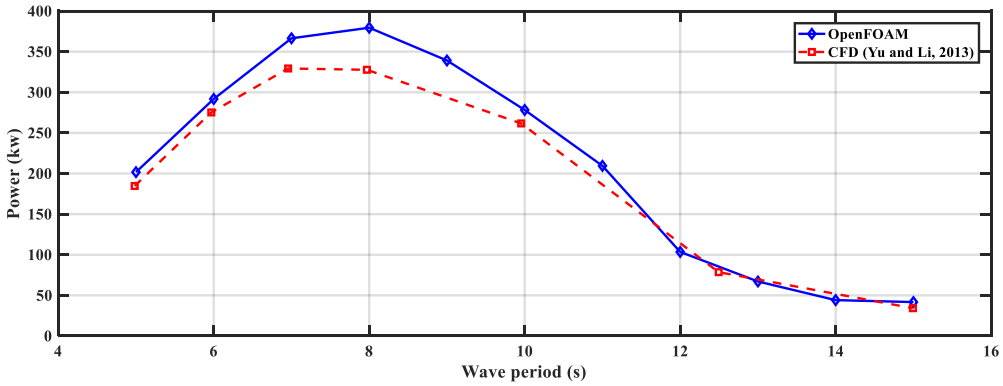

Figure 7-22 Power captured for different wave period at wave height of 4m

In terms of power extraction, Figure 7-21 and Figure 7-22 compare the performance of the two-body point absorber in both 2.5m and 4m waves with different wave period. It can be seen that the OpenFOAM results agreed well with the ones by Yu and Li (2013) except at the resonance, where the peak response occurs and a non-linear effect is essential. The difference on the power extraction is due to the heave prediction as shown in Figure 7-18. Moreover, the difference become larger when the oscillating motion of point absorber is induced by extreme waves. This indicates that the non-linear effect becomes more important in extreme wave conditions, where wave overtopping and water slamming float occur frequently during the operation of the point absorber. There is no general common effect on power capture.

7.3 Conclusion

This study demonstrates that the performance of the two-body point absorber as predicted by OpenFOAM cannot be obtained by a potential theory-based solution since the nonlinear effects, such as viscous drag and wave overtopping, have a great impact on the hydrodynamic behaviour of the point absorber. By comparing this with the work by Yu and Li (2013), it proves that the numerical model is able to model the complex nonlinear interactions between waves and point absorber with a higher order of accuracy. Some of the key findings can be summarized as:

- The 2nd order central scheme has the best results to represent the waves but it requires a huge demand on computational resource in practice. The limited TVD scheme and 2nd order upwind performs with the similar results with a reasonable computational source and they are much stable than the central differencing scheme due to the usage of higher number. Based on the investigation of the different schemes in this section, limited TVD is the best choice in terms of speed, accuracy and stability, and thus this has been used throughout the study in the following sections.

- For regular waves, the wave pattern will become steady after twenty wave cycles based on the numerical wave tank length used in this study. It is necessary to have sufficient time before any data measurements are taken since the waves generated at the inlet contribute more energy than the ones in pattern, but they will dissipate as time passes and become less significant. For irregular waves, the wave pattern involved is not steady so the energy cannot be dissipated over time. In such a case, the 2nd order upwind or other higher order scheme is essential.

- For waves with a longer period, the draft of the point absorber will keep constant and finally the point absorber will follow the motion of the waves ($H/H_{x=0} = 1$). For a point absorber under extreme conditions, the non-linear effect cannot be neglected especially at resonance. The viscous drag force in calm waves is negligible but it increases dramatically when the waves are running high due to the shape of reactor at the bottom. The power performance of a point absorber is often predicted by solving the radiation and diffraction equation and viscous drag is normally described as a quadratic damping term in the equation of motion. However, the drag coefficient value cannot be easily selected and it may lead to uncertainty in the prediction.

- The Morison’s equation prediction is applicable when the wave is linear. But wave overtopping and water slamming can be observed in higher waves. These effects add extra terms in the original restoring force and thus change the natural behaviour of the point absorber. This indicates the weaknesses of the linear theory-based method in predicting the force and its inability to capture the non-linear interactions between the point absorber and the incoming waves.

8. Investigation of point absorbers in array

The deployment of wave farms is very important for the operation of most designed wave energy power plants. Within a wave farm, multiple devices are put together in a specific configuration to make a great contribution of electricity to the power grid and also to smooth out the power output. In this situation, each isolated device is subject to waves that have been radiated or diffracted from other converters, in addition to incident waves. The effect of the array interactions on the energy absorption may be either constructive or destructive, depending on whether the averaged energy of each unit in the array is higher or lower than the energy of the isolated units. In this chapter, there has been an investigation about the interaction between waves and multiple devices.

8.1 Interaction factor

In this study, multiple point absorbers will be used as the wave energy extraction models to further study wave interaction problems. A linear power take-off system was taken into consideration. The instant power captured by each device was calculated from the damping coefficient, C, and average velocity, V:

$$Pi = C \cdot \boldsymbol{V}^2 \tag{8-1}$$

The aim of this section is to investigate the effects by array layout, the distance L between the isolated devices, and the wave′s approaching angle. The performance of the multiple wave energy devices in terms of power production is usually measured by the q factor, which is defined as the ratio between the average power absorbed from the device array and the power absorbed by an isolated device.

$$q = \frac{\sum_{i=1}^{n} P_i}{n \times P_{isolated}} \tag{8-2}$$

Where n is the number of devices. The overall power output will benefit from the interactions if averaged power production of the array is larger than the power production of an isolated device (q>1).

8.2 Environmental set-up

In the investigated hydrodynamic parameter of four different floater shapes in the previous chapter, the cone shape floater is expected to be the best choice. Thus the point absorber model used here is a floater with a 90° cone shape bottom, see Figure 8-1. The model is used here because the cone shape has a larger added damping coefficient and a broader resonance range than the floater with a flat bottom. The wetted area at the free surface is larger than in the other shapes, which leads to a higher wave induced force. A larger bandwidth is also crucial for the wave energy device under irregular conditions since the waves are highly random and it is hard to achieve its optimal working condition. The geometry of the floater is shown in Figure 8-1. It has the diameter of 6m and the centre of the gravity is located below the free surface.

In this study, the simulation of the WECs array with 2-4 units is carried out to quantify the constructive or destructive effect due to the interaction between the WECs.

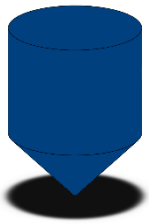

Figure 8-1 Point absorber with 90° cone shape bottom

The numerical wave tank was set to be 480m in length and 70m in depth. The widths of 70m, 95m and 100m were used for the array in tandem, with triangle and square configurations respectively when the separation distance was the half wave length. The width will change accordingly to keep the distance between the floater and its nearest boundary at least ten times the buoy diameter.

In this section, the boundary condition and numerical scheme are the same ones as in chapter 7. At the inlet boundary, the irregular waves are generated based on the sea states that are dominated by a 1.25m significant wave height with a peak period ranging from 5.5s to 9.5s which represents the most probable characteristics at the Billia Croo Wave Site (Location: $59{,}00°N; 3{,}66°W$). The parameters are collected by the European Marine Energy Centre based on the British island in question. Falnes (1980) demonstrated that the power absorbed should be proportional to the wave height squared as shown in Figure 8-2.

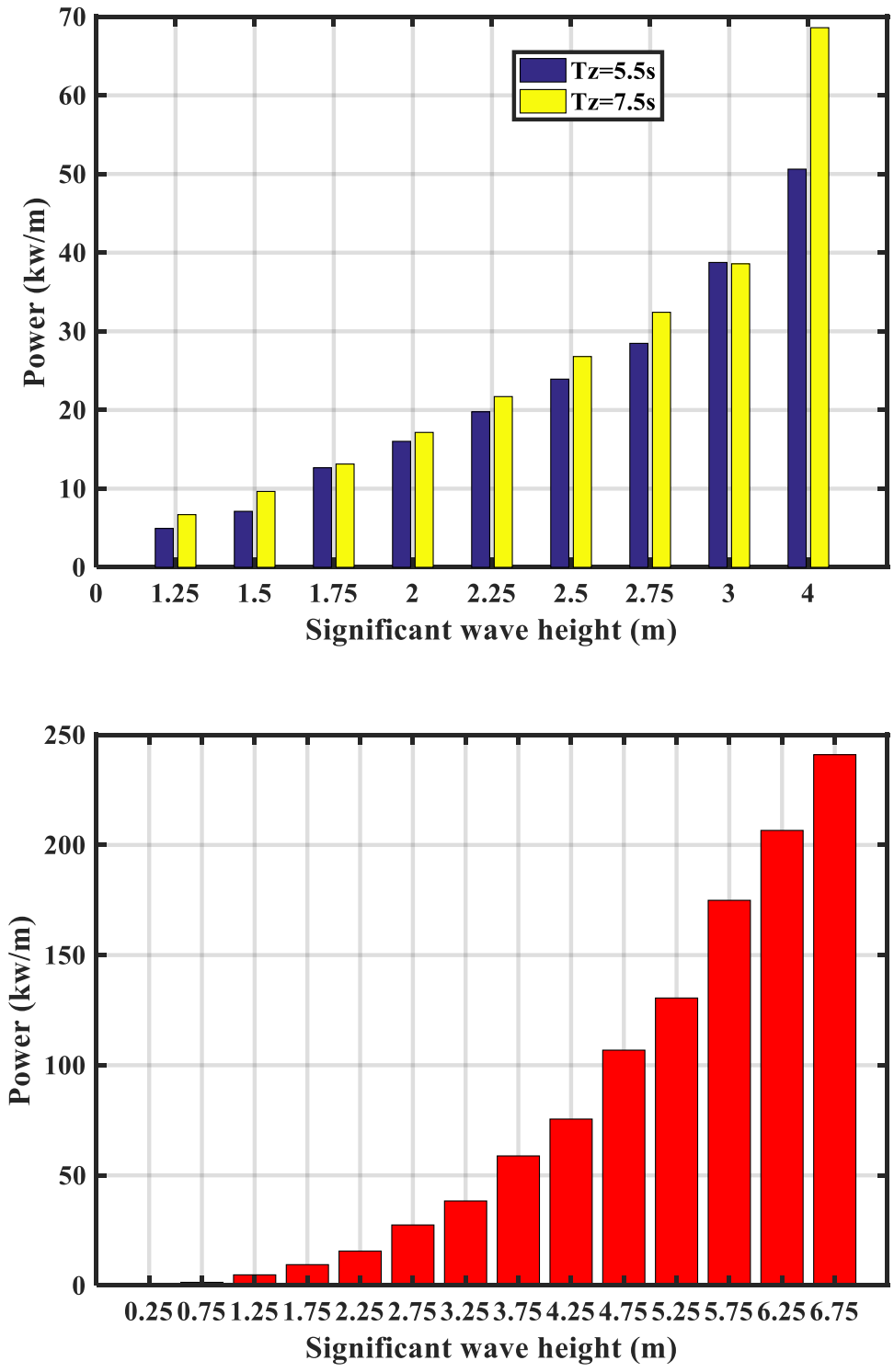

Figure 8-2 Power with different wave heights with Tz=5.5s and 7.5s (top); and Power with different heights and their corresponding period (highest occurrence) at Billia Croo Wave Site (bottom)

This figure shows a parabolic relationship between the optimal powers absorbed by the point absorber and the wave height. Thus at the beginning, only the wave farm configuration (including wave direction) and wave period are considered as key parameters that affects the performance of the array.

The irregular wave condition is described in Figure 8-3 based on the JONSWAP spectrum when the peak enhancement factor (γ) equals up to 3.3.

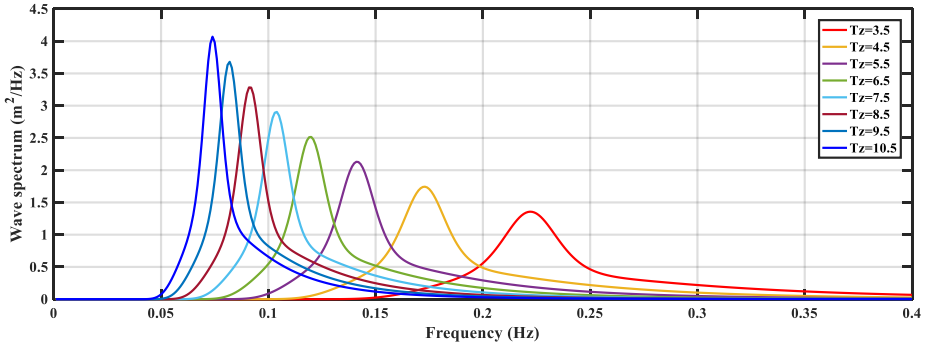

Figure 8-3 Wave spectrum generated by RANS solver for 8 scenarios, $\Delta f = 0.01Hz$

It is assumed that the wave conditions above stand for the whole year's wave climate. Thus the yearly wave condition can be calculated by taking the probability of occurrences into consideration and the result is shown in Figure 8-4.

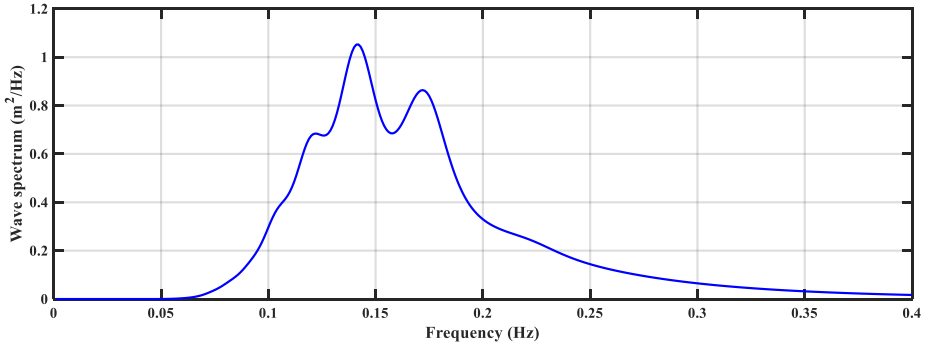

Figure 8-4 Yearly wave spectrum at Billia Croo Wave Site, $H_{1/3}$ =1.207m

In the each of following simulations, the PTO damping coefficient C is initially calculated to maximum the power production for the given sea state. The optimal damping coefficient is decided by tuning the PTO damping coefficient to match the hydrodynamic damping factor at the frequency with largest probability of occurrence. For multiple buoys, the oscillating period of each body is measured accordingly thus the optimal damping coefficient for each point absorber is different. The harvest broadband of the oscillating body is shifted to cover most of the energy spectrum as shown in Figure 8-4, instead of coinciding with the peak frequency in each wave scenario.

The layout of each configuration is shown in Figure 8-5 to Figure 8-9. The parameters focused on in this section are the separating distance and the wave direction. Figure 8-5 shows the first configuration for the wave point absorber array test, where θ is the incident wave direction. The

system has two heaving bodies with a separation distance represented by L, Configuration II and IV are the array configuration with 3 and 4 point absorbers in tandem respectively. Configurations III and V are a star and square configuration of 3 and 4 point absorbers in array, respectively.

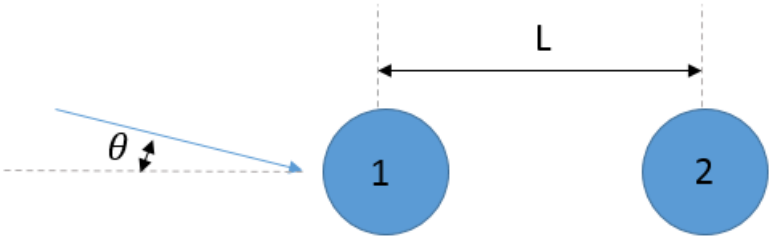

Figure 8-5 Array configuration I with two buoys in tandem

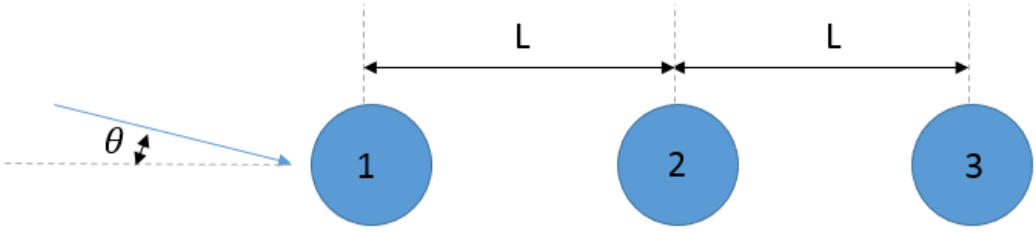

Figure 8-6 Array configuration II with three buoys in tandem

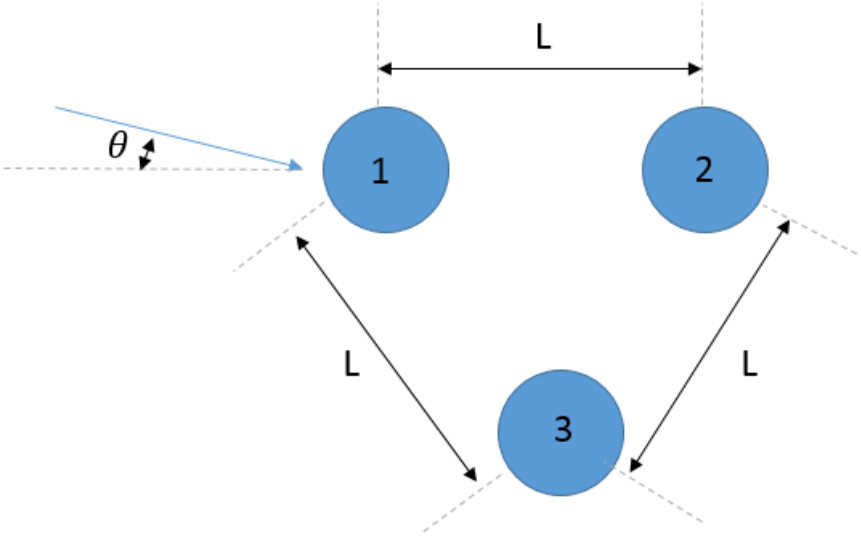

Figure 8-7 Array configuration III with three buoys in star

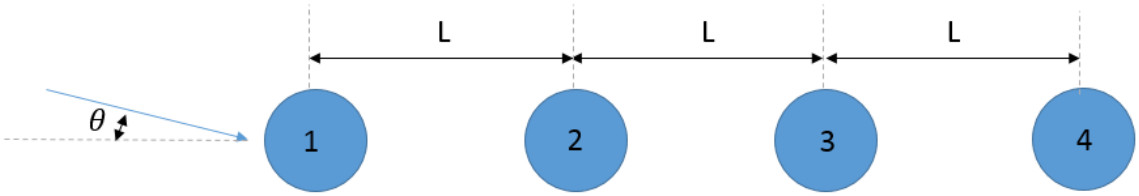

Figure 8-8 Array configuration IV with four buoys in tandem

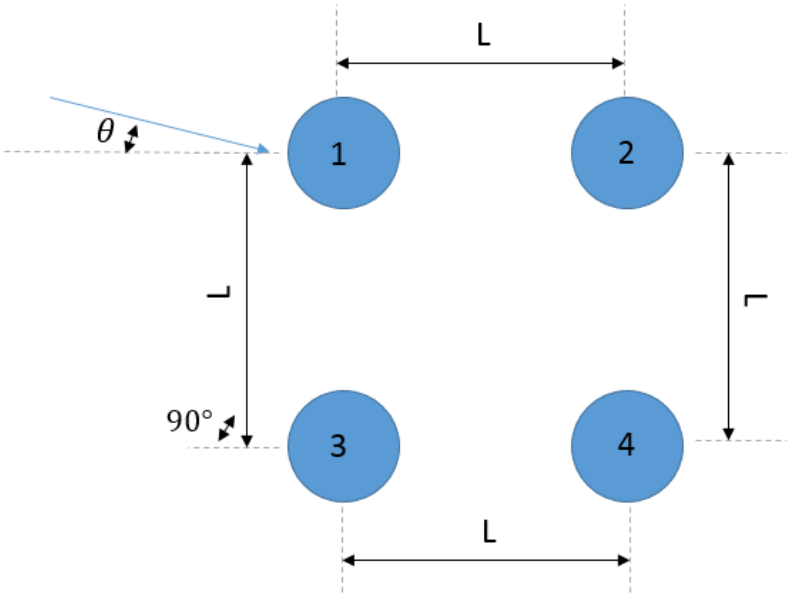

Figure 8-9 Array configuration V with four buoys in square

Now the numerical wave tanks with 2-4 WECs in different configurations have been built up. The aim of this study is to quantify the effects of the array layout, wave direction and the distance between the WECs on the performance of the wave energy farm at the given sea site. In the next section, the results of each configuration will be introduced.

8.3 Effect by separation distance

In the current study, experience is drawn from the regular waves interacting with the fixed structures, where the separation distance is normalised by the incident wave length. It is found that wave length has a great impact on the hydrodynamic force on the structures within a given separation distance. Thus the distance between each point absorber in this study is described by their corresponding wave length. For the tests under irregular wave conditions, the significant wave length has been used instead

of the incident wave length. The significant wave length for the wave climate used in this study is 78.8m.

The following simulations have been conducted with wave approaching angle= 0° for each configuration to investigate the influence by separation distance. As an example, the results for configuration I are presented to describe the q factor as the function of the separation distance. In Figure 8-10, the whole system at the beginning has a destructive effect due to the closely placed point absorbers. The maximum q factor is about 0.85 when the separation distance (L) is 0.4 of the incident wavelength (λ). There is no second peak in the curve of q factor before the distance reaches 1 wavelength. The q factor starts to increase after the L=1.3 λ and it can be imagined that the q factor will reach to 1 eventually when the separation distance is much longer than the wavelength.

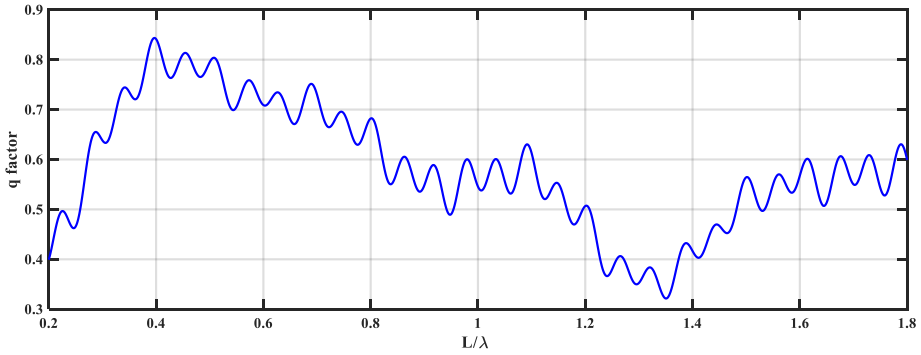

Figure 8-10 q factor for configuration I with 0° wave approaching angle, L=0.25$\lambda_{1/3}$

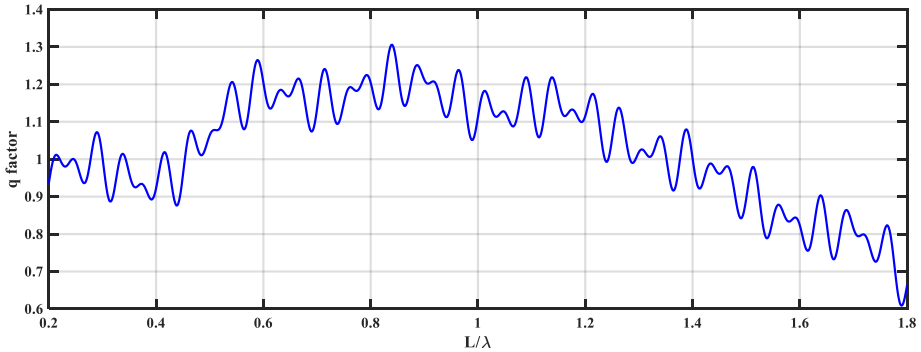

Figure 8-11 q factor for configuration I with 0° wave approaching angle, L=0.5$\lambda_{1/3}$

In Figure 8-11, the separation distance is increased to 0.5 of the significant wavelength. In this case, there is a dramatic improvement in terms of q factor. It reaches 1.3 when the L/λ is about 0.85. The peak q factor and its whole range shifts to a larger ratio of L/λ by 0.4, thus there is no trough before L/λ=1.8 when compared with the previous result. From Figure 8-10 and Figure 8-11, it can be seen

that for cases in irregular waves, whose wavelength is highly random, the q factor fluctuates a lot and it is very sensitive to the L/λ ratio. Unlike the point absorbers in regular waves, it is not clear whether the ratio has a positive or negative effect on the power production by each wave component. It can be concluded that the q factor has a nonlinear relationship with the separation distance and the performance of the whole system cannot be simply estimated by the location alone.

Thus, this investigation focuses on the overall power production and the results are represented by average q factor calculated from each wave component. Figure 8-12, Figure 8-13 and Figure 8-14 show the simulations that point absorbers are aligned in tandem and there is a similar trend that the q factor reaches its highest value around L/$\lambda_{1/3}$=0.5 to L/$\lambda_{1/3}$=0.625.

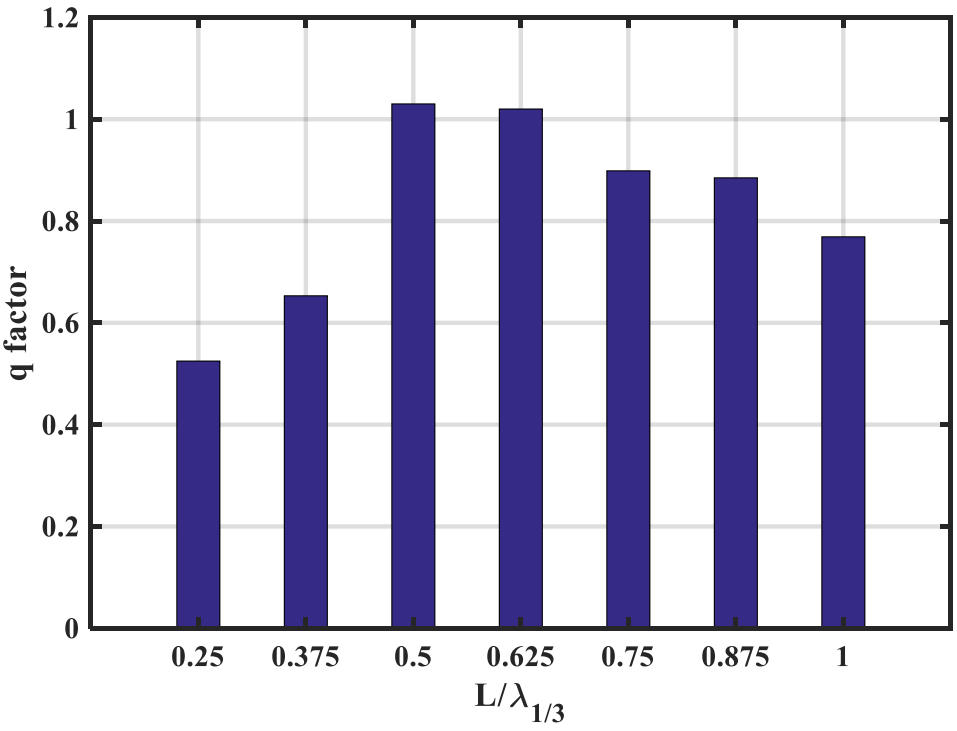

Figure 8-12 q factor for configuration I with 0˚wave approaching angle

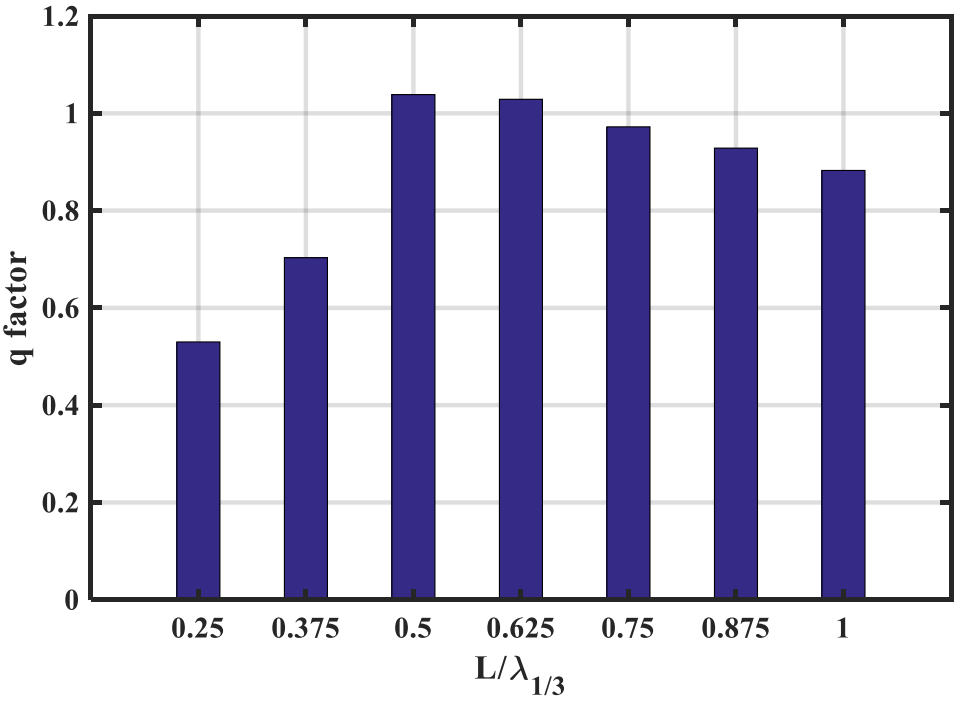

Figure 8-13 q factor for configuration II with 0˚wave approaching angle

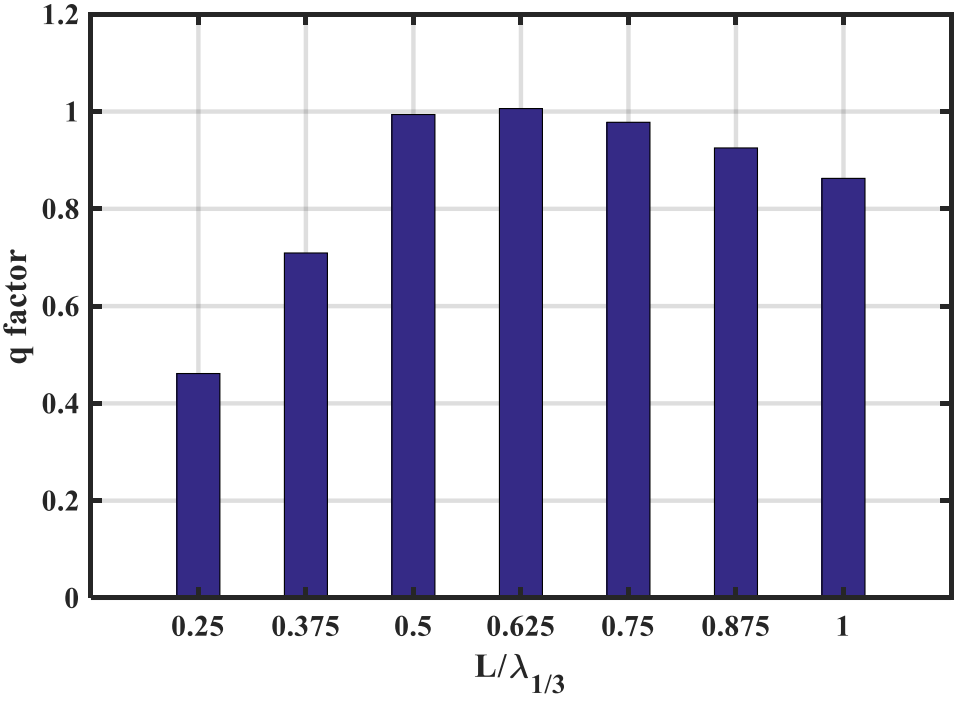

Figure 8-14 q factor for configuration IV with 0˚ approaching angle

The configuration II has a slightly better power output at the separating distance L=0.5$\lambda_{1/3}$ than configuration I. This is caused by the point absorber in the middle received radiated waves from both the front and back buoys. The superposition of incident and radiant waves results in a higher oscillating amplitude, which is more noticeable at the second buoy. It brings a positive effect on the buoy oscillating speed thus its power extraction is higher than the others.

An example of the difference in hydrodynamic pressure between configuration I and II is shown in Figure 8-15 and Figure 8-16. In the area marked by white, it can been seen that the hydrodynamic pressure on the windward buoy in the two buoy array is smaller than the one in the three buoy array. The additional buoy in configuration III at leeward position has a positive effect on the hydrodynamic force acting on the buoy at the front. A similar phenomena has also been observed in the area marked by yellow as well for the second buoy.

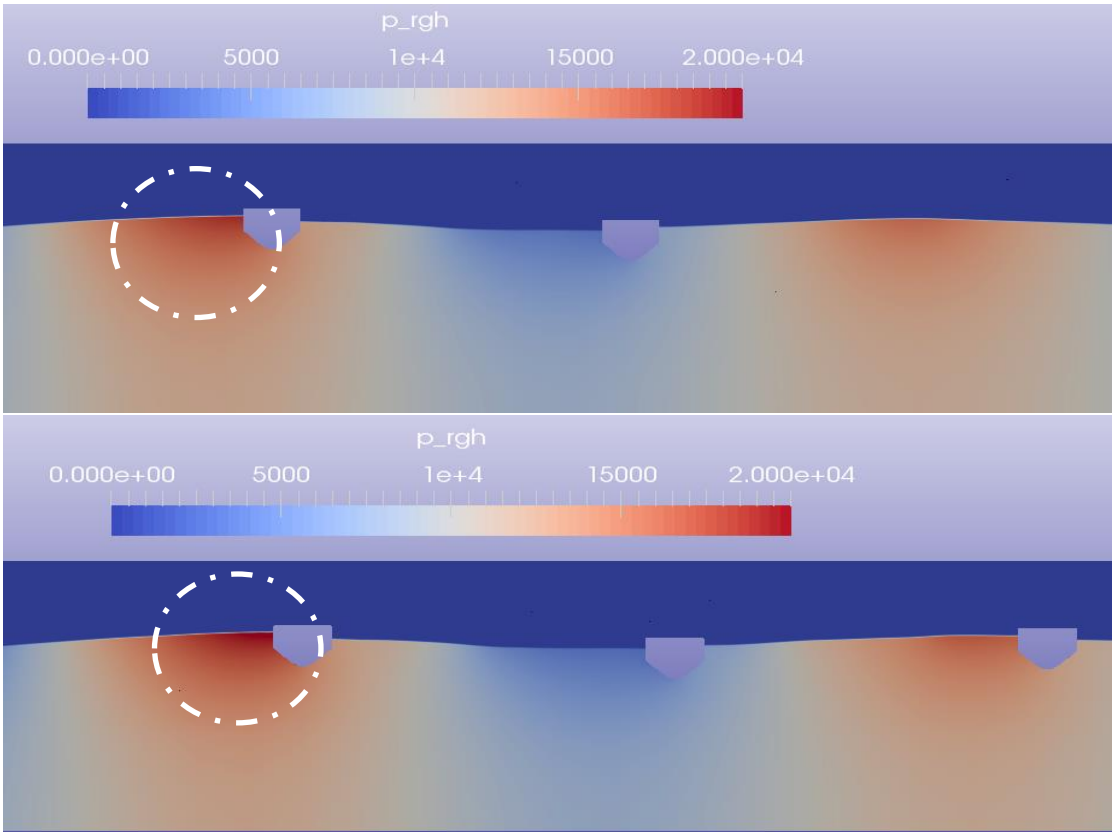

Figure 8-15 Wave crest pass first buoy in configuration I and II

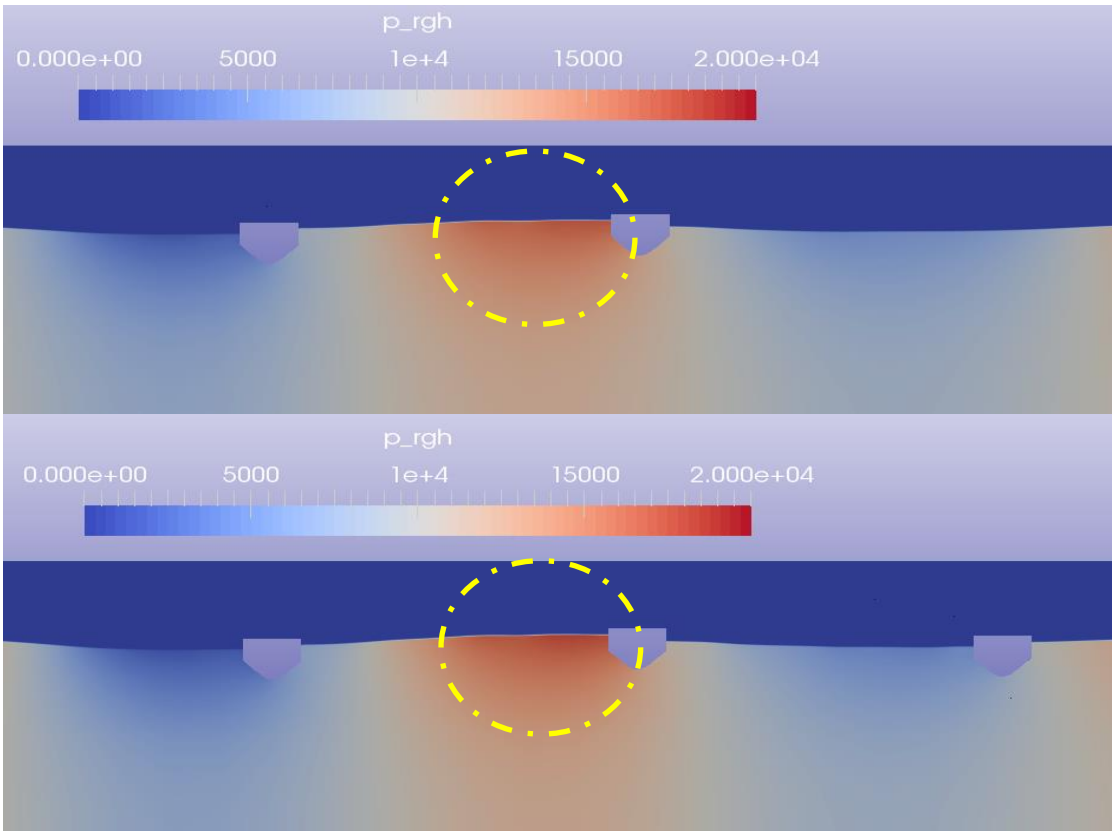

Figure 8-16 Wave crest pass second buoy in configuration I and II

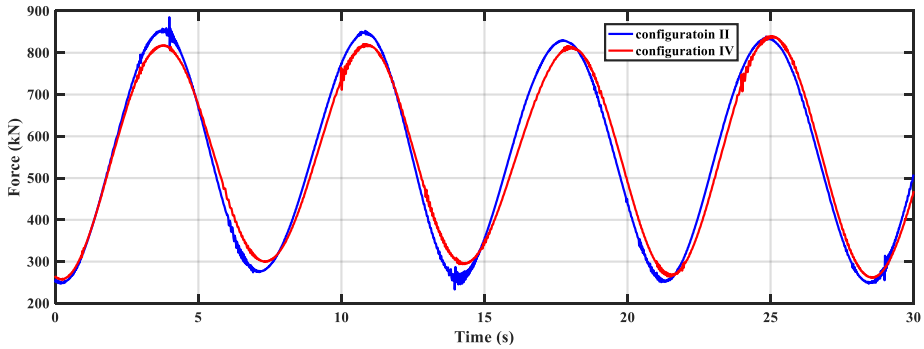

Figure 8-17 Wave induced force on the second buoy of configuration II and IV, data measured after 20T

For configuration IV, the maximum q factor value is just above 1 and its corresponding separation distance is shifted to $0.625\lambda_{1/3}$. This is because the total configuration size is $1.5\lambda_{1/3}$ so the first buoy hardly interacts with the last one when they are aligned in the wave propagation direction. It can be assumed that for long-spaced point absorbers, the total energy captured will be equal to the number of devices times the power absorbed by an isolated device (q=1). On the other hand, the last buoy brings a phase shift of the oscillating frequency away from its resonance to the two middle buoys, which results in a negative effect on the power production, see Figure 8-17.

In Figure 8-17, a simulation in regular wave conditions with $H=H_{1/3}$ and T=Tp was conducted in order to show the difference in wave-induced force in configuration II and configuration IV clearly. It indicates that the force in configuration IV is smaller than the one in configuration II and that a slight phase shift was observed. Some nonlinear phenomena occurred at the first peak and in the second trough of wave induced force of configuration II.

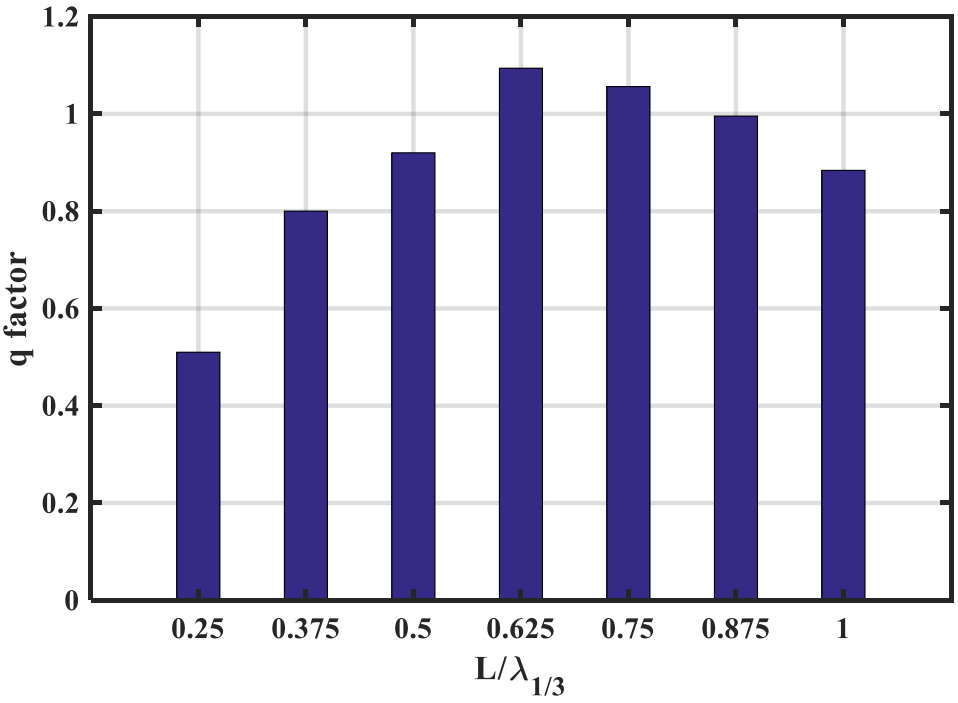

Figure 8-18 q factor for configuration III with 0° wave approaching angle

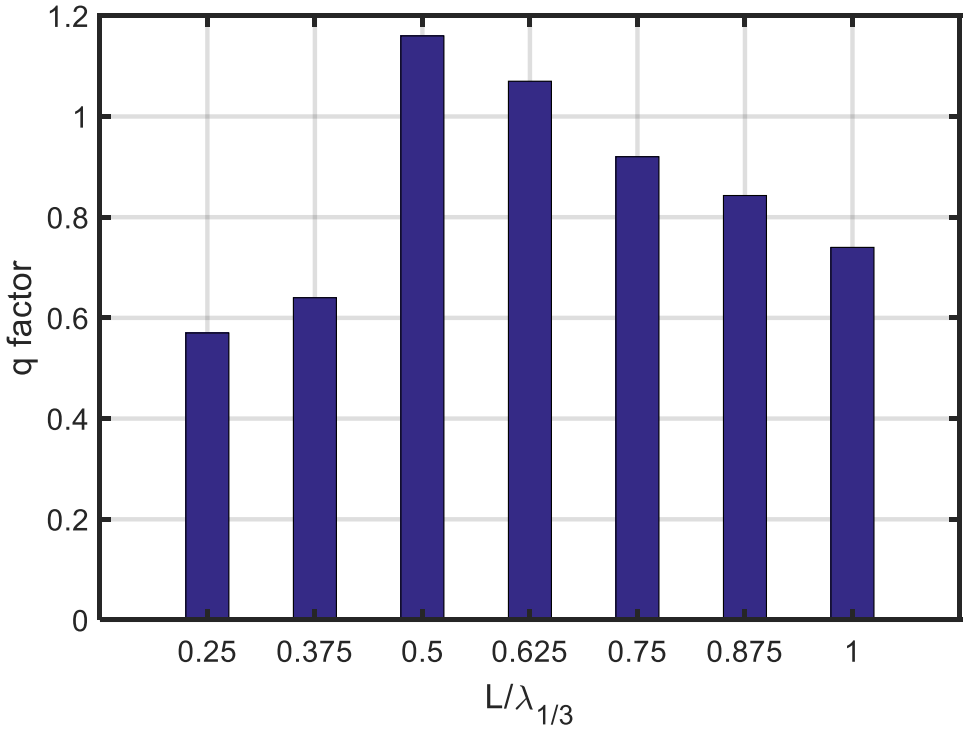

Figure 8-19 q factor for configuration V with 0° approaching angle

The performance for star (III) and square (V) configuration, see Figure 8-18 and Figure 8-19, has a similar trend to the tandem configurations in terms of separation distance. For the star configuration, the maximum power extraction occurs at L=0.625 $\lambda_{1/3}$ instead of L=0.5 $\lambda_{1/3}$. An example for configuration III is shown here for a q factor of less than one. The incident wave amplitude and radiated wave do not coincide with each other, see Figure *8-20*, with L=0.5λ. In such a case, the point absorber array has a negative effect on the average wave amplitude at each point absorber location.

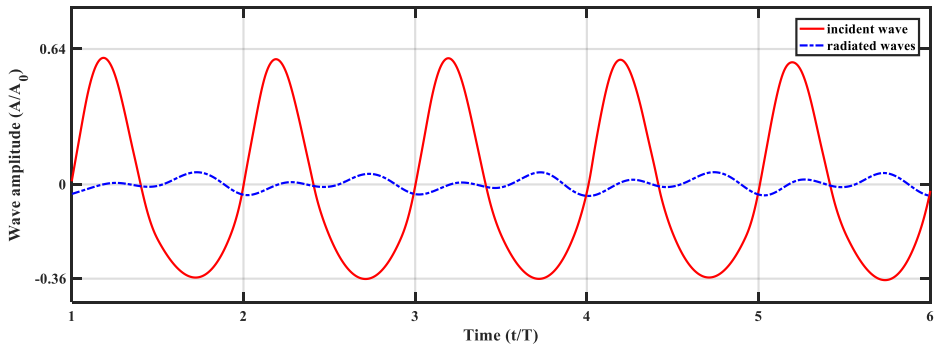

Figure 8-20 Wave amplitude in configuration III for L=0.5λ

It can be seen that the performance of these two configurations are better than the performance of the tandem configurations. The q factor for square configuration is nearly 1.2 at its optimal separation

distance and thus it has the highest energy extraction efficiency amongst all five configurations. This can be explained by the buoys are not only placed in the wake of windward devices, but also being parallel with them. The motion of the 2nd buoys was induced by the same incident waves as the 1st buoy and they also have a positive effect on the 3rd and 4th buoys by interacting with each other.

From the results shown above, it can be concluded that:

- When the separation distance is 0.5, 0.625 for configuration III and IV, of the wavelength, the radiation waves are in phase with the incident waves. They reinforce the amplitude of each other, instead of cancelling out. This results in a larger amplitude of the buoy's motion that brings a positive effect on power production.

- For wave direction is 0°, the square configuration is the best option for an array due to its symmetric layout. The performance of the four buoys in a tandem configuration is less effective than that of the other layouts. By increasing the number of buoys, the waveform becomes asymmetric and the radiation effects are much stronger. The most complex interaction zone is found to be in the middle of the array. The windward buoy always experiences the highest wave force and this wave force increases with the number of buoys. The leeward buoy, in contrast, always experiences the lowest wave induced force.

8.4 Effect by the wave direction

Other than the separation distance, the performance also relies on the wave propagation direction. A series of simulations of different wave direction separation distance are conducted. It should be noted that the effect by the separation distance at each wave propagation direction case has the same trend as the one with 0° wave direction. Thus only the results with the optimal separation distance have been shown here.

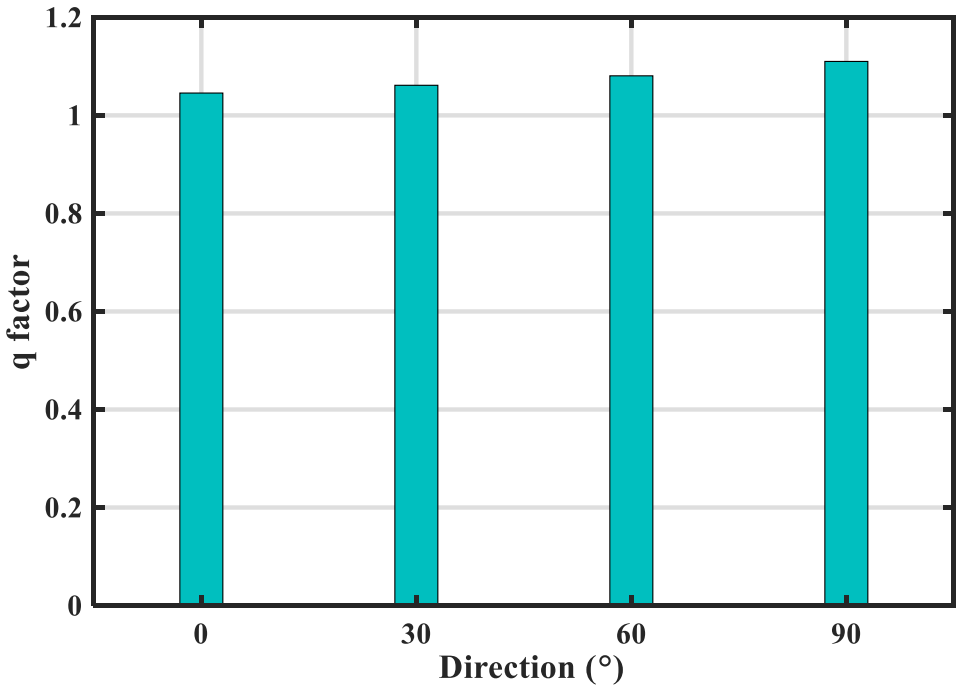

Figure 8-21 q factor for configuration I with different approaching angle, L=0.5$\lambda_{1/3}$

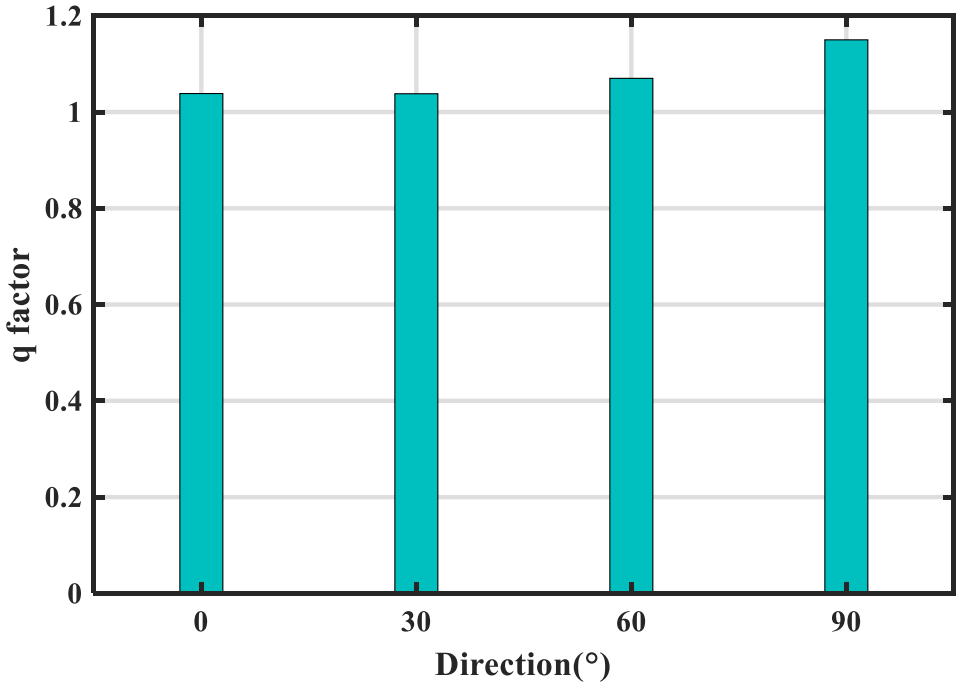

Figure 8-22 q factor for configuration II with different approaching angle, L=0.5$\lambda_{1/3}$

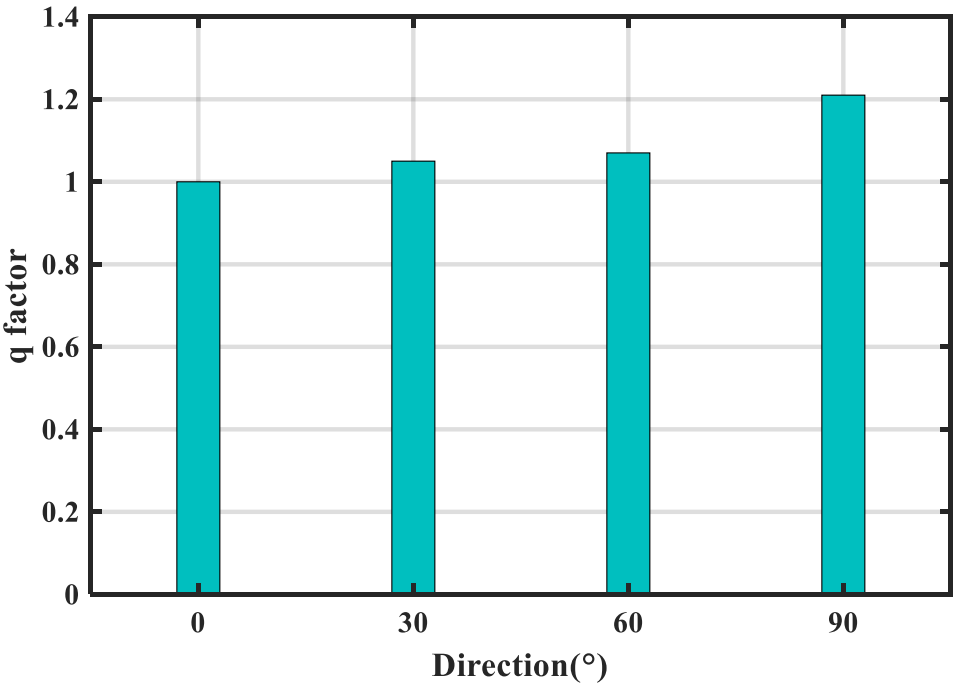

Figure 8-23 q factor for configuration IV with different approaching angle, L=0.625$\lambda_{1/3}$

The results about the point absorbers in tandem configuration with different wave approaching angle are in Figure 8-21, Figure 8-22 and Figure 8-23. The effects generated by the wave direction has a similar trend in the three configurations. The q factor is quite sensitive to the wave's approaching angle and the value of the q factor is increased by up 20% when the wave approaching is 90°. The wave farm with a tandem layout has the largest energy output when the point absorbers are aligned perpendicular to the wave direction. Each of the point absorber impacts with the incident waves at the same time and extracts the same amount of wave energy. Other than the results of the tandem configurations under 0° wave direction, configuration IV has the highest efficiency under 90° wave direction among all three tandem configurations. This can be explained by the radiated waves by each buoy has a constructive effect on its neighbours and this positive effect increases with the number of buoys in use.

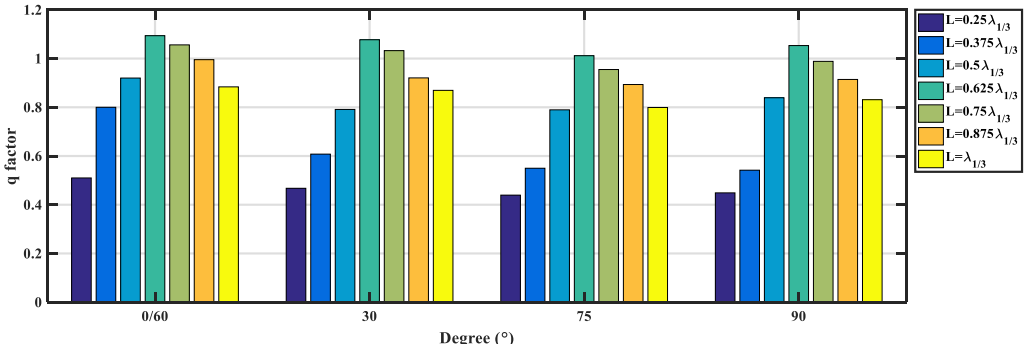

Figure 8-24 q factor for configuration III with different wave angle and separation distance

The q factor for star configuration is slightly different than the others. The maximum power extraction occurs at L=0.625$\lambda_{1/3}$ instead of L=*0.5*$\lambda_{1/3}$.Figure 8-24 shows the results of the star configuration under a different wave approaching angle and separation distance. The results for 0° and 60° are the same due to symmetry. An example of hydrodynamic pressure at the free surface for the configuration III has been shown Figure 8-25 and wave overtopping effect is observed in Figure 8-26.

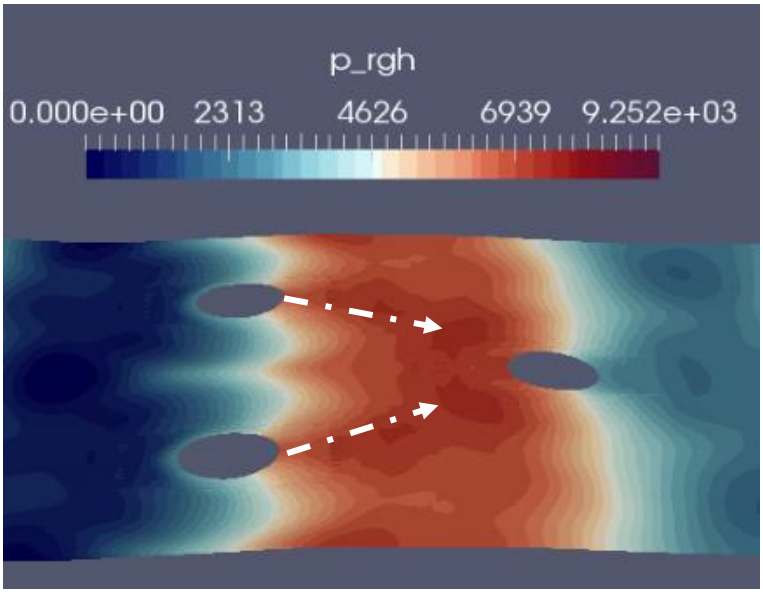

Figure 8-25 Hydrodynamic pressure at the free surface for configuration III with 90° wave direction

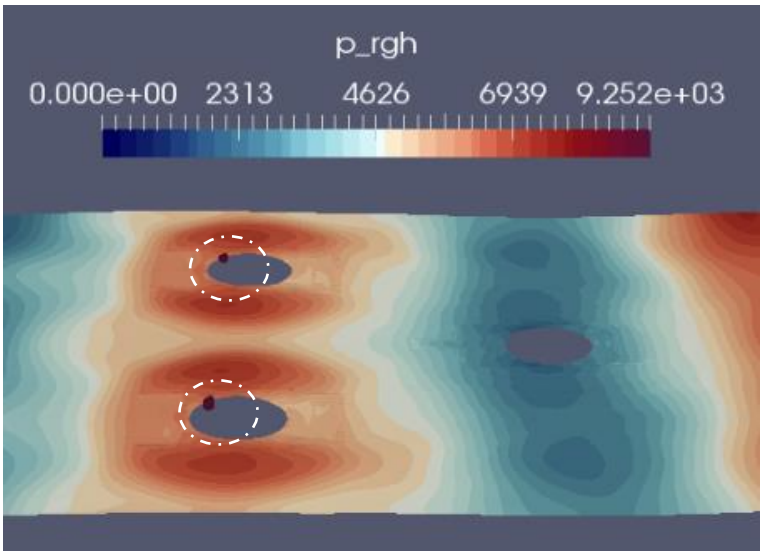

Figure 8-26 Wave overtopping on the 1st and 2nd buoys

It can be seen that the star configuration is less sensitive to the wave direction. For wave approaching angle within $\pm$ 60°. The q factor is almost the same for this layout with optimal separation distance. Even at the sub-optimal separation distance, the performance of star configuration under each wave approaching angle was alike. It indicates that the star configuration-based wave energy farm is more suitable for operation in a realistic sea site since the wave direction changes all year around. The most efficient layout is to align the whole system with a $0(60)°$ to the wave propagation direction. In such case, the third point absorber benefits from the interaction with both first and second devices. It should be also noted that the star configuration has the most compact size among all of the five configurations at their corresponding optimal separation distance.

For the square configuration (Figure 8-27), the effects on the wave approaching angle at the optimal separated distance is more sensitive when compared with the star configuration. The optimal wave direction is $45°$ and its corresponding q factor is the largest out of all five configurations.

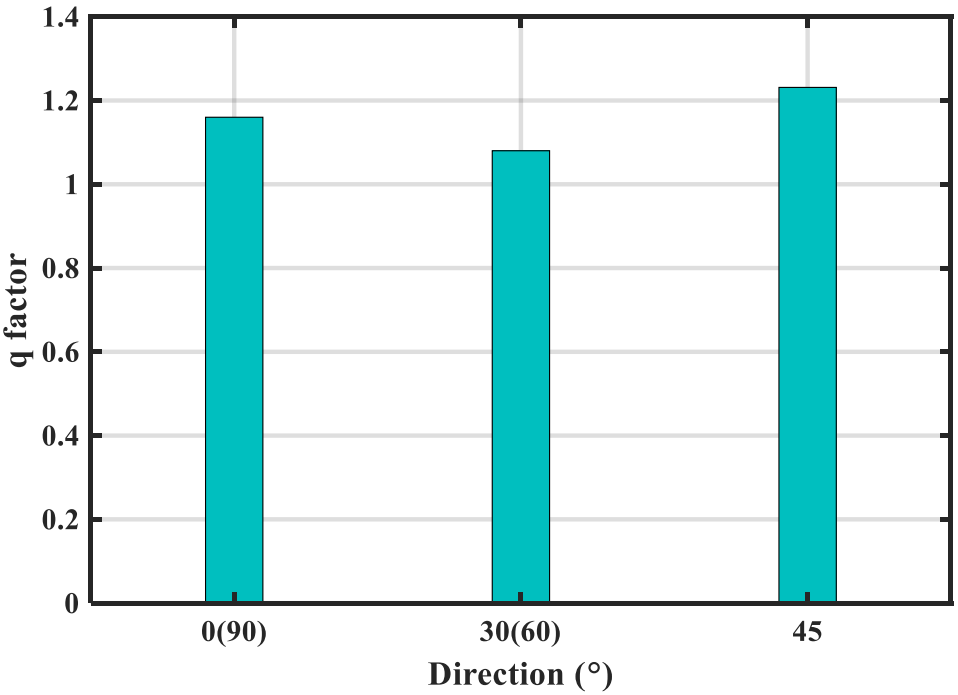

Figure 8-27 q factor for configuration V with different wave approaching angle, L=0.5$\lambda_{1/3}$

An example of the constructive effect with a wave approaching angle of 90° is shown in Figure 8-28. It can be seen that the superposition of the interactive waves increases the hydrodynamic pressure at the wave crest, as well as in the wake of the buoys in the first row, which brings a benefit to the overall amplitude of the wave induced force.

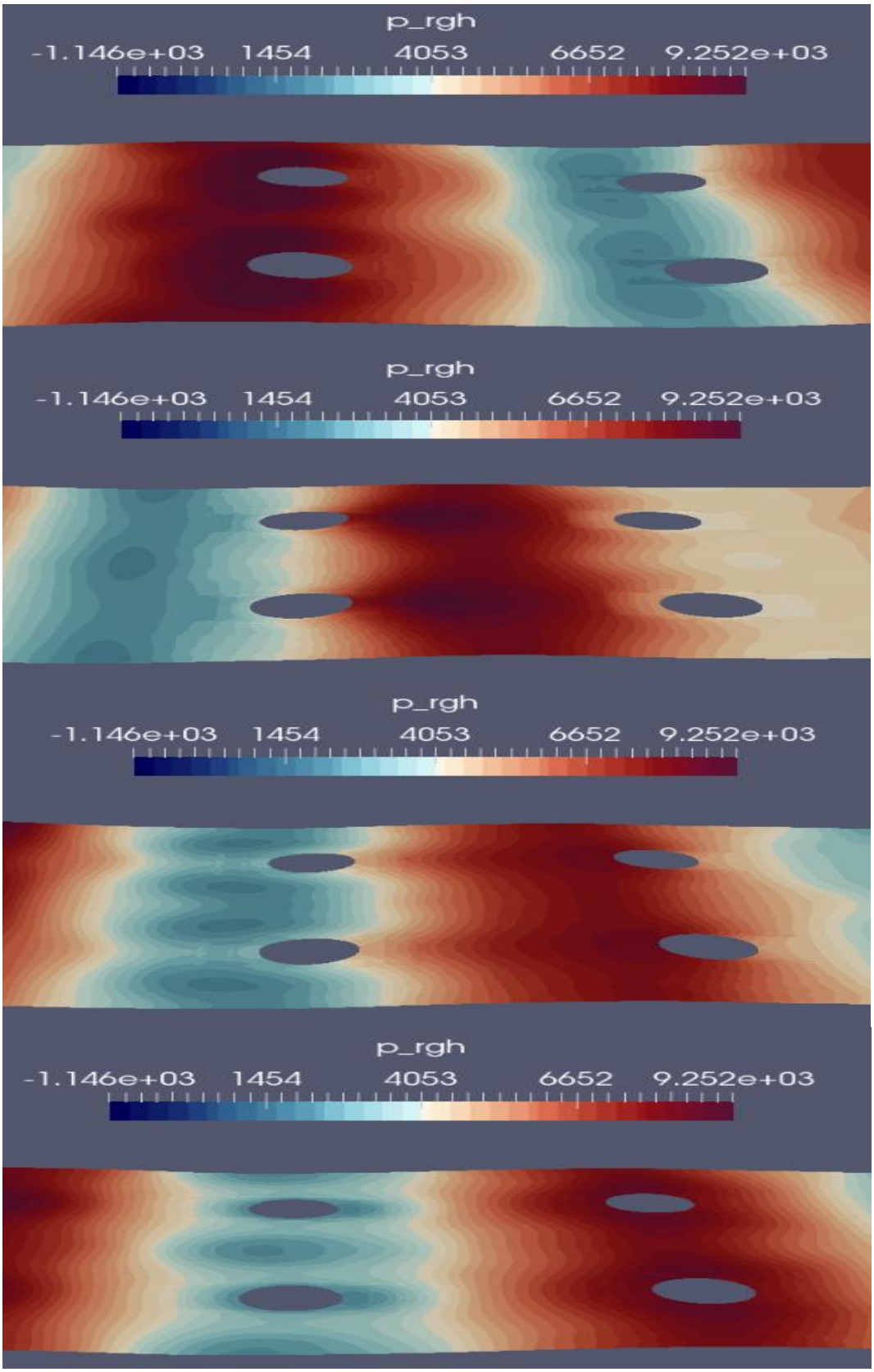

Figure 8-28 Hydrodynamic pressure at the free surface for a wave crest pass the point absorbers in configuration V

8.5 Performance in different wave height

In order to quantify the effect by wave height, the calculations are performed for the same sea state as described in Chapter 7. The average absorber power by the floaters in the tandem, star and square layouts, is shown in Figure 8-29. It can be seen that the star layout performs stably for all the sea states. The square configuration performs better in the wave condition with an approaching angle of 0 and 30 degrees. The tandem layout has the largest energy output when the wave's approaching angle is at 90 degrees.

It should be noted that the power extraction should be in parabolic relationship with the wave height if the mechanism of each individual within the array is ideally optimized. The results show that for a smaller wave height, the power extraction that follows is in proportion to the wave height square. But for a higher wave height, there is a linear relationship between the wave height and power absorption. The power extraction efficiency is lower than the ones in smaller wave height conditions. This can be explained by the fact that the nonlinear effect is crucial in higher wave height conditions. On the other hand, the bandwidth of the wave climate becomes wider when wave height is taken into consideration. This is such that the tuned harvest range cannot cover most of the wave spectrum.

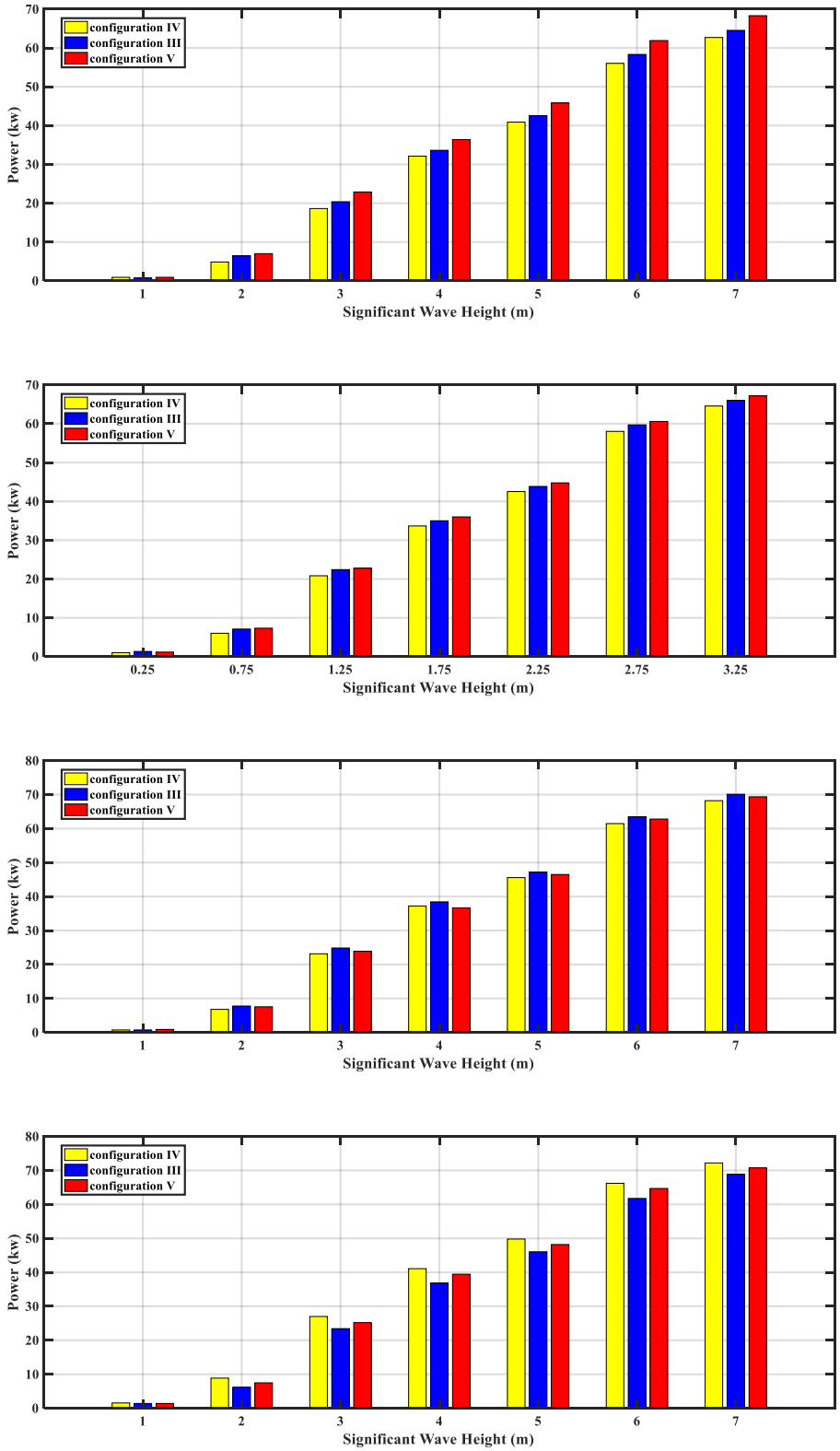

Figure 8-29 Average power capture by point absorber under wave approaching angle of 0, 30, 60 and 90 degree (from top to bottom)

8.6 Optimization in star and square configuration

In this section, two investigations were conducted in order to further increase the power production in the array of point absorbers. The layouts chosen here are the star and square configuration since they have a better overall performance than the tandem one.

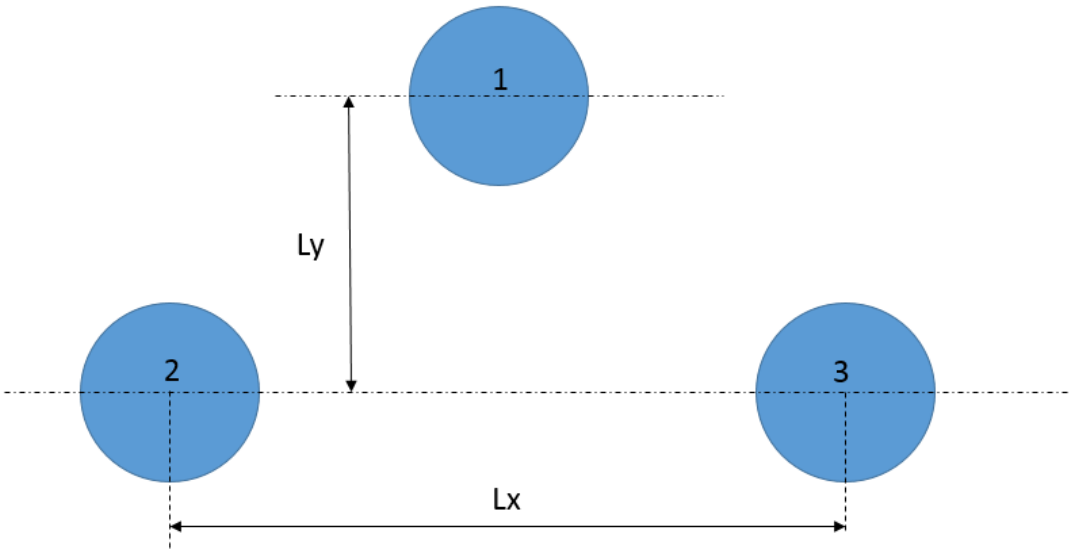

Figure 8-30 Two parameters for star configuration

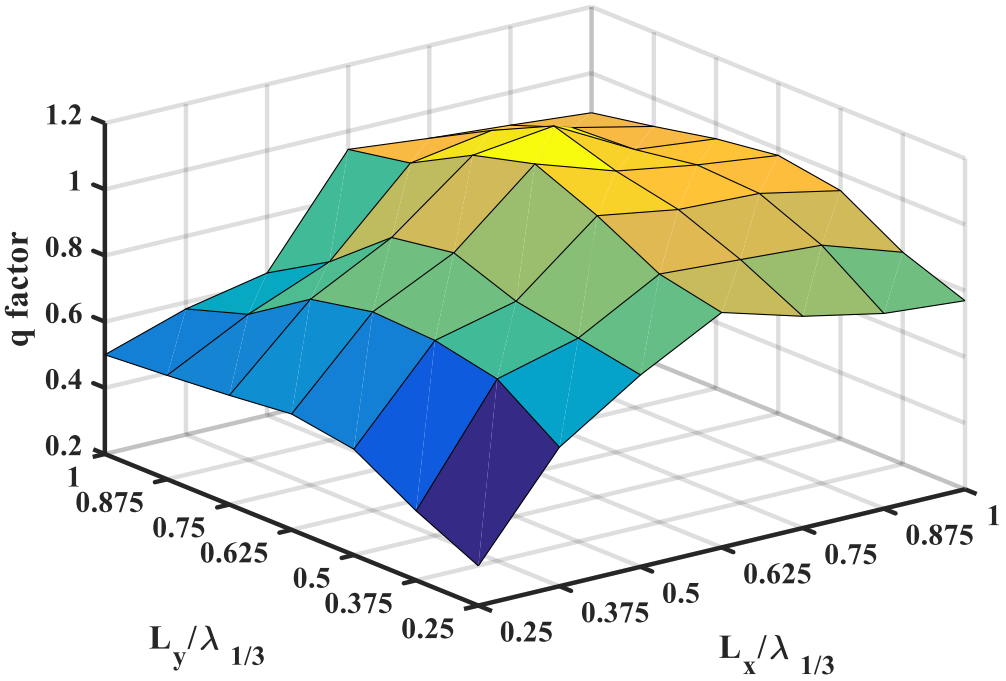

Figure 8-31 q factor for star configuration with two parameters

For star configuration, an additional parameter was used to quantify the power extraction efficiency affect by separation distance as shown in Figure 8-30. The wave approaching angle was set to be 0 degree since it shows the largest q factor in the previous sections. The results for the two parameters optimization is shown in Figure 8-31. A surprising result was that the star array with an equilateral triangle shape has the largest energy output. An example of the star configuration defined by two parameters are shown in Figure 8-32. In the first contour plot of Figure 8-32, the wave is approaching the 3rd buoy with an enhanced wave amplitude. The 3rd buoy benefits from the interaction between incident and radiated waves. The Figure 8-32 also shows the hydrodynamic pressure at the free surface during the wave approaching front two point absorbers. However, the 1st and 2nd buoy are induced by the wave with reduced amplitude, in such that the benefit in 3rd buoy cannot overcome the energy reduction in buoys one and two due to the destructive effect.

From the results above, it can be concluded that the configuration III with an equivalent separation distance is proven to be the most efficiency design for the point absorber array.

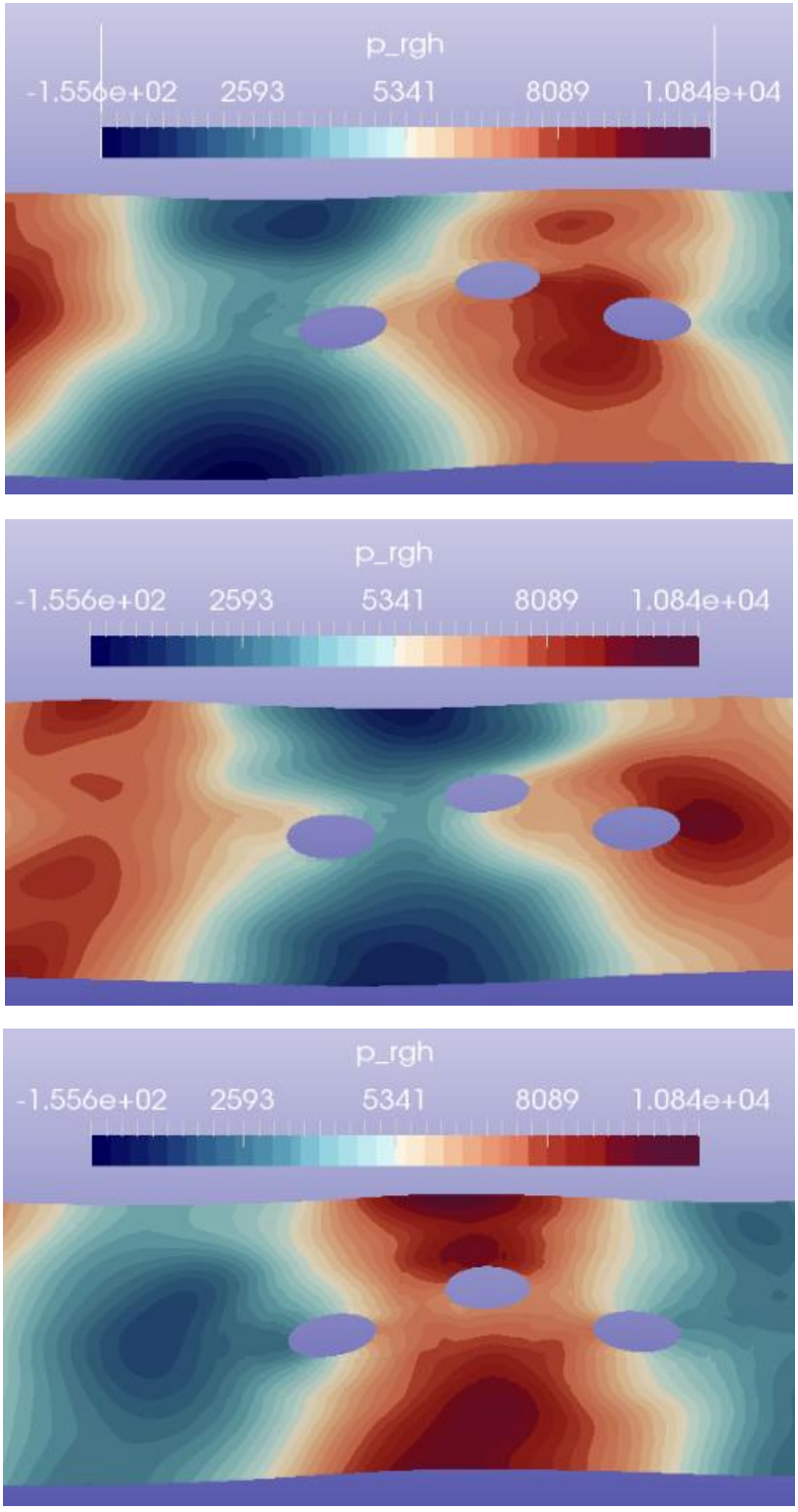

Figure 8-32 Hydrodynamic pressure at the free surface for star configuration, Ly=0.25

The square configuration is a common layout for point absorbers connected to a fixed platform such as at Wavestar. The capture bodies are located around the platform and move against it. In such a design, the platform has four fixed pillars to support the whole unit.

Figure 8-33 Wavestar model, picture from http://wavestarenergy.com/

As seen in Figure 8-33, the four piles are placed in water so that they will also have a constructive or deconstructive effect onto the wave field.

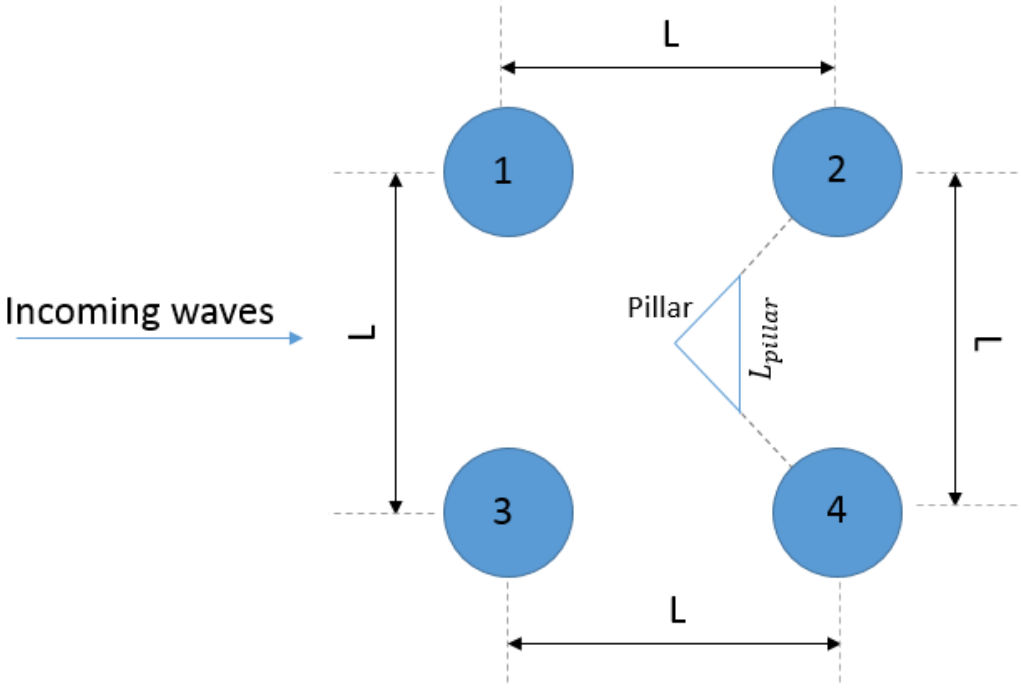

Figure 8-34 Square layout with fixed pillar in the middle

The idea here is to change the pillar into a column with a triangle transverse cross-section, which will increase the wave amplitude at the leeward point absorbers by trapping the waves. The new square layout is shown in Figure 8-34. The wave approaching angle is set to be constant (0°). In this case, the experience can be drawn from star configuration by placing a column with triangle shape whose two equilateral legs pointing towards the centres of leeward point absorbers.

As seen in Figure 8-36, the incident, radiated, as well as any diffraction waves will be directed and the hydrodynamic pressure at the particular location will be higher. By changing the (L_{pillar}) and location of the column (apex angle), the positive effect on the leeward point absorbers will become noticeable, see Figure 8-36.

In this case, experience can be drawn from the star configuration by placing a column with an equilateral triangle shape whose two legs point towards the centres of the leeward point absorbers. In this study, the platform with the size of $0.25\lambda_{1/3}$ and apex angle of 90° is found to have the largest constructive effect on the whole system, in which the q factor is increased by 10%. The column with 120° apex angle has a constructive effect on the leeward point absorbers, but it also reduces the performance of the point absorbers in the front. Thus its net benefit is less than the one with 90° apex angle.

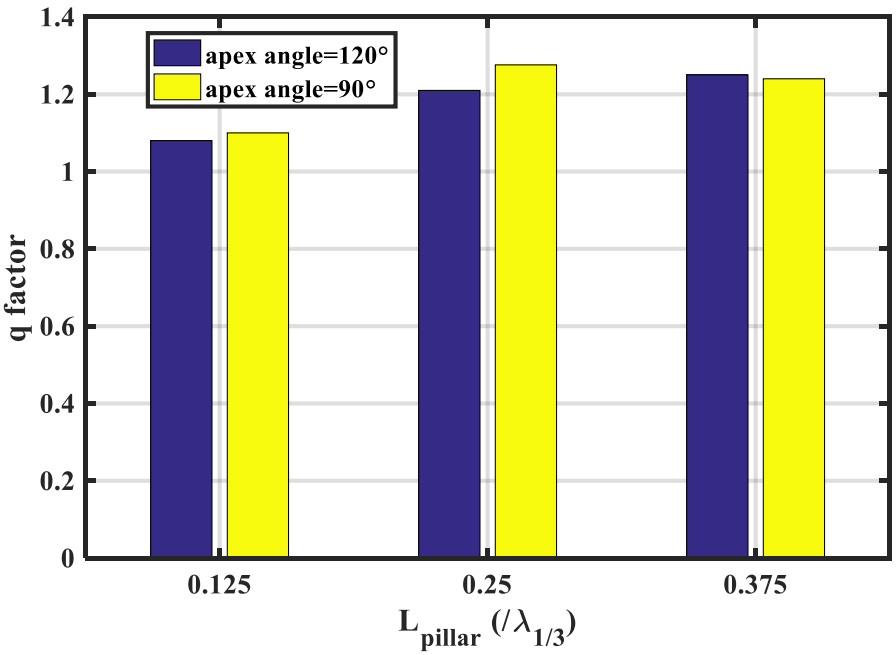

Figure 8-35 q factor for square configuration with different size of the column

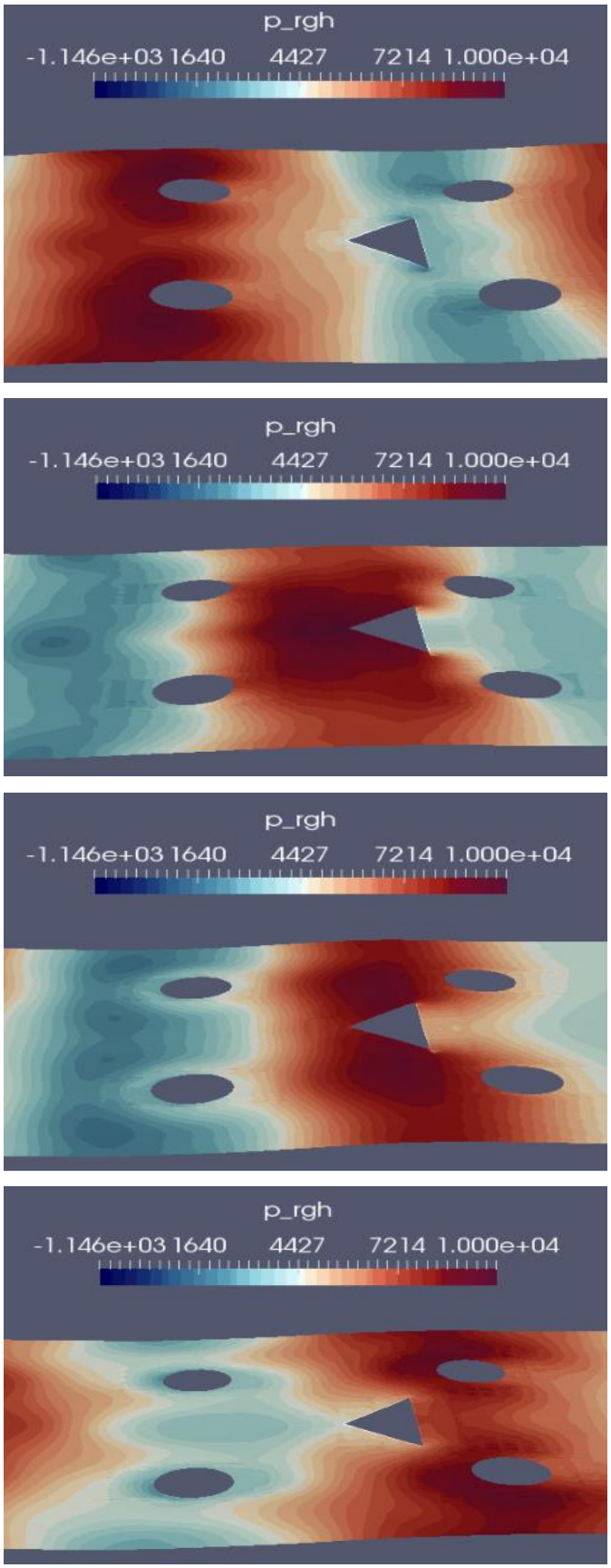

Figure 8-36 Hydrodynamic pressure at the free surface for configuration V with triangle shape column

In Figure 8-36, a time series of hydrodynamic pressure at the free surface for wave propagating through the whole system is shown. It can be seen that wave amplitude is enhanced due to the interaction within the system at the windward location. The waves continue moving without too much energy loss and are separated by the fixed column with triangle transverse cross section. In such that, the wave excited force on the leeward buoys are improved due to the existence of the fixed column.

8.7 Conclusions

In this section, the point absorber array with five configurations was investigated in terms of separation distance and wave direction to quantify the performance in power extraction. The presented numerical approach was based on the RANS equation with consideration taken regarding the fully nonlinear effect. The separation distance between the devices was found to be a key factor for the optimization of the device array. About half of the wavelength was found to be the optimum distance between devices. The wave period is less important in irregular waves compared with regular wave conditions. It can be seen that the tandem configuration has the worst performance when the converters are spread along the wave travel direction. The star and square configurations are more efficient in a multi-directional ocean wave site, and the most efficient way to capture wave energy is to align the squared based layout system at an angle of 45° to incoming waves.

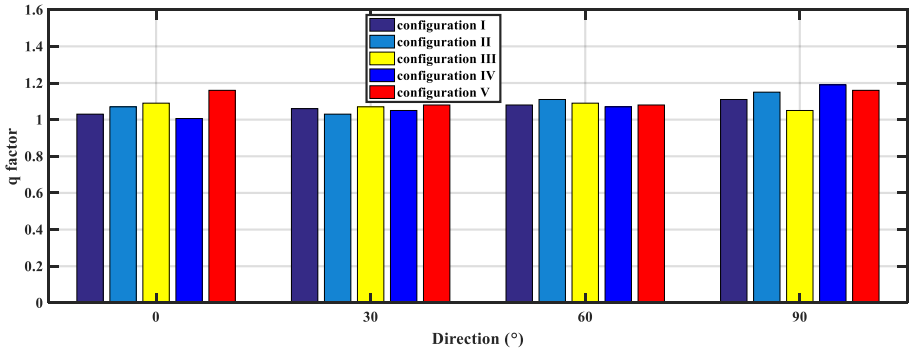

Figure 8-37 comparison between different configurations with their optimal separation distance

From the results above, it can be summarized that:

- The optimal damping coefficient is decided by tuning the PTO damping coefficient to match the hydrodynamic damping factor at the frequency with largest probability of occurrence. For multiple buoys, the oscillating period of each body is measured accordingly thus the optimal damping coefficient for each point absorber is different. The harvest broadband of the oscillating body is shifted to cover most of the energy spectrum

- When the separation distance is 0.5, 0.625 for configuration III and IV, of the wavelength, the radiation waves are in phase with the incident waves. They reinforce the amplitude of each other, instead of cancelling out. This results in a larger amplitude of the buoy motion that brings a positive effect on power production.

- For tandem configurations, the q factor is quite sensitive to the wave's approaching angle and the value of q factor can be increased by up 20% when the wave approaching is 90°. By increasing the number of buoys, the waveform becomes asymmetric and the radiation effects are much stronger. The most complex interaction zone is found to be in the middle of the array. The windward buoy always experiences the highest wave force and the wave force increases with the number of buoys. The leeward buoy, in contrast, always experiences the lowest wave induced force. The radiated waves by each buoy with optimal separation distance has a constructive effect on its neighbours and this positive effect increases with the number of buoys in use.

- For the star configuration, the equivalent separation distance is found to be the most efficient design. The q factor is less sensitive to the wave approaching angle. The performance is similar in each wave direction and it can achieve its optimal power extract efficiency with $\pm 60^{\circ}$ wave approaching angle. Thus, the star layout has a wide range of applications for operating in offshore area, where the wave direction is non-uniform.

- For the square configuration, it has the largest q factor when the wave direction is 45°. The waves travel along the diagonal line of the square layout with the least energy loss caused by a blockage effect. The performance of the square configuration can be further improved 10% by interacting with a fixed pillar with a triangular transverse cross-section.

- The local wave climate should be considered preferentially since it is crucial for power extraction efficiency. The bandwidth of the system is tuned to cover most of the local wave periods. In this study, only the probability of occurrence and wave period was taken into consideration, and the wave directions have been kept constant. Further research should also consider the wave direction.

9. Final conclusions

The wave energy converters have been developed to extract energy from the renewable ocean resource. The point absorber is a simple but robust wave energy device. A point absorber can be equipped with a direct drive power take-off (PTO) system which is designed for a long wave length and periodic ocean waves. The scope of this PhD study was to develop a numerical model to investigate the hydrodynamic interaction between the point absorber buoy(s) and the irregular ocean waves. The point absorber in this study was coupled with a linear power take-off unit, and this model was then used to quantify the maximum power extraction under different wave conditions. Moreover, several verifications of the numerical tool against experimental and analytical results were conducted to provide a greater overall confidence in this study.

This thesis is divided into a number of chapters. Chapter 2 firstly presented the background of the point absorber. It introduced the development of point absorber concepts, the working principles and their corresponding mooring systems. Then, the recent literature about point absorber wave energy converters has been reviewed. The primary approaches adopted in the mentioned work includes the analytical method, the frequency and time domain boundary element method (BEM) and the Navier-stokes (NS) based computational fluid dynamic (CFD) method. For a different research emphasis, each method has its own advantages and drawbacks

In Chapter 3, the procedures to solve the wave-structure interaction problem was introduced. The implementation that adopted in OpenFOAM was presented in order to solve the RANS equation. Three different turbulent models were provided to close the NS equation. The VoF method with MULES scheme was used to capture the sharp free surface. The spatial and transient discretisation approach was then introduced and the focuses are on the 2^{nd} order scheme to achieve the results with a higher order of accuracy. The brief introduction about the boundary condition and pressure-velocity coupling method has also been provided. Moreover, the dynamic mesh strategy that was used to simulate the point absorber motion under waves has been discussed and the results show that the moving mesh with a quadratic inverse distance scheme is the most robust strategy. This chapter also indicated four types of error may occur during the process of OpenFOAM simulation, which is discretization error, initial input, such as the geometry of the structure and flow behaviour, modelling error including turbulent model adopted, free surface resolution, etc. and the numerical error caused by the convergecey

There are two main approaches to improve the power extraction of a wave energy device; by improving the energy capture efficiency or the power take-off efficiency. In this study, the author focused on the energy capture efficiency. A validation of hydrodynamic parameters against experimental and analytical results was firstly introduced in chapter 5. It could be proven that the hydrodynamic coefficient can be calculated accurately by RANS model and that the influence of viscosity is not negligible. The approach of estimating hydrodynamic behaviour in a full viscous solver in time domain proved to be successful and some key findings can be summarized as:

- The differences in the hydrodynamic parameter predicted by the RANS model can be significant and vary considerably depending on the draft, frequency and amplitude of the oscillation motion. The nonlinear profile of the free surface around the oscillating body will lead to a variation in the added mass coefficient. The hydrostatic force is poorly addressed by the linear assumption. The free surface in the higher frequency cases are nonlinear thus the hydrostatic part in the total force will remain in the hydrodynamic force. As a result, the added mass calculated by the linear theory and RANS model will be different due to the discrepancy in the wetted surface area prediction. It also suggests that the added mass is becoming frequency independent (as well as frequency increasing) and the increase in the damping from the Fourier transmission produces the best match to the nonlinear hydrodynamic force.

- Moreover, the viscous eddies will form along the body surface and dissipate in the wake of any motion. The viscous force is an unsteady component of the total force which will affect the hydrodynamic coefficients since the damping coefficient is related to the dissipation of energy. The viscous eddies can be observed. The flow separation at the sharp edges leads to an energy loss because of the formation of eddies. The strength of the eddies will increase with the frequency and amplitude of the oscillating motion. The nonlinearity has a great effect on the whole system when the draft is lower and the frequency and amplitude of motion is higher. The method used by many previous literatures using constant coefficients is not suitable and may lead to discrepancies. It can be surmised that the RANS model can handle the free surface distribution, eddy formation and diffusion much better than the potential flow solutions, especially at high frequency amplitudes of motion.

- The submerged depth for the heaving motion is a crucial parameter. It is shown that a smaller draft is associated with a large force, and a larger added mass and hydrodynamic damping coefficient are then observed. This suggests that a smaller draft will result in a larger power

absorption from the wave energy device. The submerged depth also proves to be a crucial parameter that affects the hydrodynamic behaviours in sway mode and the amplitude has less of an impact on the results.

- The hydrodynamic damping coefficient for the cone shape appear to be slightly larger than the other two shapes. Therefore, it is expected that the triangle-cylinder will be a better wave energy absorber. The results also indicate that eddy formation has less of an impact on the pressure distribution around the body since the added mass in all three modes has been predicted well. It proves that the added mass-related sinusoidal component of the force is accurately calculated, which is crucial to estimate the hydrodynamic loads on an offshore structure occurring in all wave conditions.

Later on, a parametric study about the heaving point absorber was carried out to investigate the wave energy potential that can be captured at a given sea site. It can be found that the wave energy has a great potential and this amount of wave energy can be extracted by employing proper wave energy converters. In this study, the hydrodynamic behaviour of four different heaving point absorbers together with PTO system has been examined in irregular wave conditions by way of the CFD method. For validating the model, free vibrations in various non-dimensional damping ratios and free decay tests of a heaving subject on the free surface have been firstly simulated. The numerical results have then been compared with those from the experiments and analytics where a good agreement was observed. The effects by buoy draft, size, shape and PTO parameters on the performance of a point absorber at different sea conditions was investigated and can be concluded as follows:

- The power take-off (PTO) system should co-operate with an extra control mechanism to adjust the natural frequency of the device to match the frequency of the incoming waves. This results in a resonance phenomenon where the oscillating motion is so large so that the interaction between waves and PTO device cannot be accurately estimated by the potential solution. Additionally, the capture width ratio (CWR) relies on the PTO damping coefficient and the incident wave period. For an irregular sea state, the PTO parameter, including the stiffness strength of the control mechanism, should be tuned for the largest overall power production.

- The capture device with the 90° cone shape at the bottom has the best performance in the investigated harvest range, especially in the one with a large wave height. This can be explained by the relatively large hydrodynamic parameters when compared with the other shapes and wider resonance range.

- The draft of the capture device has a dramatic effect on the power production. A lower draft results in a large hydrodynamic force, which will increase the power absorption potentially. The lower draft, on the other hand, changes the capture device's harvest range and shifts the optimal PTO damping coefficient to suit the sea site with a higher wave frequency. The investigation about draft also indicates that the wave energy is highly concentrated in the region close to the free surface. Similarly, the size of capture device also has a great influence on the power absorption. The performance of each buoy in terms of power absorption is improved by using a larger capture device. While the larger size of point absorber WEC buoy results in a deeper draft for the devices made from the same material, the balance between buoy size and draft should be taken into consideration.

In Chapter 7, a particular two-body PowerBuoy model has been chosen as the test model. The numerical simulation was carried out to compare the results with the ones from the experimental measurements to demonstrate that the CFD model is able to represent the energy harvest processes accurately. This study demonstrates that the performance of the two-body point absorber as predicted by OpenFOAM cannot be obtained by a potential theory-based solution since the nonlinear effects, such as viscous drag and wave overtopping, have a great impact on the hydrodynamic behaviour of the point absorber. The study proves that the numerical model is able to model the complex nonlinear interactions between waves and point absorber with a higher order of accuracy. Some of the key findings can be summarized as:

- At least 30 cells per wave length and height should be used throughout the simulation. For longer domains, as studying multiple point absorbers in an array, the numerical dissipation will present and it may affect the result. Thus, the number of cells in the density has to be increased to achieve the same accuracy on the wave amplitude.

- The 2^{nd} order central scheme has the best results to represent the waves but it requires a huge demand on computational resource in practice. The limited TVD scheme and 2^{nd} order upwind performs with the similar results with a reasonable computational source and they are much stable than the central differencing scheme due to the usage of higher number. Based on the investigation of the different schemes in this section, limited TVD is the best choice in terms of speed, accuracy and stability, and thus this has been used throughout the study for regular waves. For regular waves, the wave pattern will become steady after twenty wave cycles based on the numerical wave tank length used in this study. It is necessary to have sufficient time

before any data measurements are taken since the waves generated at the inlet contribute more energy than the ones in pattern, but they will dissipate as time passes and become less significant. For irregular waves, the wave pattern involved is not steady so the energy cannot be dissipated over time. In such a case, the 2nd order upwind or other higher order scheme is essential.

- For waves with a longer period, the draft of the point absorber will keep constant and finally the point absorber will follow the motion of the waves ($H/H_{x=0} = 1$). For a point absorber under extreme conditions, the non-linear effect cannot be neglected especially at resonance. The viscous drag force in calm waves is negligible but it increases dramatically when the waves are running high due to the shape of reactor at the bottom. The power performance of a point absorber is often predicted by solving the radiation and diffraction equation and viscous drag is normally described as a quadratic damping term in the equation of motion. However, the drag coefficient value cannot be easily selected and it may lead to uncertainty in the prediction.

- The Morison's equation prediction is applicable when the wave is linear. But wave overtopping and water slamming can be observed in higher waves. These effects add extra terms in the original restoring force and thus change the natural behaviour of the point absorber. This indicates the weaknesses of the linear theory-based method in predicting the force and its inability to capture the non-linear interactions between the point absorber and the incoming waves.

In the last chapter, the point absorber array with five configurations is investigated in terms of separation distance and wave climate to quantify the performance in power extraction efficiency. The presented numerical approach is based on the RANS equation with the consideration of the fully nonlinear effect. The separation distance between devices is found to be a key factor for optimization of device array. About half the wavelength is found to be the optimum distance among devices. The wave period is less important in irregular waves compared with regular wave condition. It can be seen that the tandem configuration has the worst performance when the converters are spread along the wave travel direction. Star and square configurations are more efficient in multi-directional ocean wave site, and the most efficient way to capture wave energy is to align the squared based layout system an angle between 45° to income waves. The key findings can be summarized as:

- For star configuration, the equivalent separation distance is found to be the most efficient design. The q factor is less sensitive to the wave approaching angle. The performance is similar in each wave direction and it can achieve its optimal power extract efficiency with $\pm 60^{\circ}$ wave approaching angle. Thus, the star layout has a wide range of application for operating in offshore area, where the wave direction is non-uniform.

- For square configuration, it has the largest q factor when the wave direction is $45°$. The waves travel along the diagonal line of the square layout with the least energy loss caused by blockage effect. The performance of the square configuration can be further improved 10% by interacting with a fixed pillar with triangle transverse cross section.

- The local wave climate should be considered preferentially since it is crucial for the power extraction efficiency. The bandwidth of the system is tuned to cover most of the local wave periods. In this study, only the probability of occurrence and wave period are taken into consideration, and the wave direction are kept constant. Further research should also consider the wave direction.

There are several suggestions for the further work:

- In practice, the device motion is normally restricted and, for this purpose, an optimal control strategy will be needed in order to improve the WEC performance. The control system can also, based on the motion of the buoy, determine the right control actions to avoid damage to the system. For the modelling of this type of control actions, the nonlinear functions of constraint force can be included in the governing equations or different dynamic motion module can be applied. The motion amplitude of each degree of freedom can be constrained according to the incoming waves, and this may result in an improvement of overall efficiency when considering devices array.

- In this thesis, the PTO system consists of a spring and a damper system and an optimal fixed damping coefficient are selected for each sea state. Hence, the optimal power absorbed in irregular waves is under estimated. It is expected to achieve an optimal power absorption if the varied damping system based on the incident wave period is adopted. Additionally, the PTO system can be further developed. The realistic nonlinear power take-off system of the device, such as hydraulic pump used by some attenuator WECs, should be modelled. In such

case, a more physically accurate model could be validated with experimental results, and this comparison would be more valuable.

- To save computational cost during the optimization, while the wave approaches the structure, the CFD models could be coupled with Boundary Element Methods or potential flow solvers, and where there are nonlinear effects, such as wave breaking and overtopping, the use of the method in this study is required.

By combining the efficient and practical considerations of the above, the applicability of the numerical WEC model can be enhanced.

A. Appendix A Example code

An example code implemented in the interFoam solver is given below

```
#include "fvCFD.H"
#include "MULES.H"//adopt MULES scheme
#include "subCycle.H"// call sub timestep
#include "interfaceProperties.H"//call the definition related to surface tension term
#include "incompressibleTwoPhaseMixture.H"//alpha equation
#include "turbulenceModel.H"// turbulence model
#include "pimpleControl.H"//PIMPLE algorithm
#include "fvIOoptionList.H"//source term

// * * * * * * * * * * * * * * * * * * * * * * * * * * * * * * * * * * * * *

int main(int argc, char *argv[])
{
  #include "setRootCase.H"//case location
  #include "createTime.H"
  #include "createMesh.H"

   pimpleControl pimple(mesh);//PIMPLE control

  #include "initContinuityErrs.H"//continuity errors
  #include "createFields.H"



   Info<< "Reading transportProperties\n" << endl;
   incompressibleTwoPhaseMixture twoPhaseProperties(U, phi);

   volScalarField& alpha1(twoPhaseProperties.alpha1());//states alpha 1(water)
   volScalarField& alpha2(twoPhaseProperties.alpha2());//states alpha 2(air)

   const dimensionedScalar& rho1 = twoPhaseProperties.rho1();//rho1 quotation
   const dimensionedScalar& rho2 = twoPhaseProperties.rho2();//rho2 quotation


   // Need to store rho for ddt(rho, U)
   volScalarField rho
   (
      IOobject
      (
         "rho",
         runTime.timeName(),
         mesh,
         IOobject::READ_IF_PRESENT
      ),
      alpha1*rho1 + alpha2*rho2, //ρ=α1ρ1+(1−α1)ρ2
      alpha1.boundaryField().types()//rho and alpha has the same boundary condition
   );
   rho.oldTime();//save old rho value


   // Construct interface from alpha1 distribution
   interfaceProperties interface(alpha1, U, twoPhaseProperties);

   // Construct incompressible turbulence model
```

```
    autoPtr<incompressible::turbulenceModel> turbulence
    (
        incompressible::turbulenceModel::New(U, phi, twoPhaseProperties)
    );//build up turbulence model

    #include "readGravitationalAcceleration.H"//build up gravity field


    #include "readTimeControls.H"//read time control
    #include "correctPhi.H"
    #include "CourantNo.H"//courant number
    #include "setInitialDeltaT.H"//set timesetp


    // * * * * * * * * * * * * * * * * * * * * * * * * * * * * * * * * * * * * * * * * //

    Info<< "\nStarting time loop\n" << endl;

    while (runTime.run())
    {
        #include "readTimeControls.H"
        #include "CourantNo.H"
        #include "alphaCourantNo.H"
        #include "setDeltaT.H"

        runTime++;

        Info<< "Time = " << runTime.timeName() << nl << endl;

        twoPhaseProperties.correct();
```

The two phase properties are corrected by:

```
//- Calculate and return the laminar viscosity
void Foam::incompressibleTwoPhaseMixture::calcNu()
{
    nuModel1_->correct();//update phase1 viscosity
    nuModel2_->correct();//update phase2 viscosity

    const volScalarField //limitedAlpha1
    (
        "limitedAlpha1",
        min(max(alpha1_, scalar(0)), scalar(1))
    );//alpha within (0 1)

    // Average kinematic viscosity calculated from dynamic viscosity
    nu_ = mu()/(limitedAlpha1*rho1_ + (scalar(1) - limitedAlpha1)*rho2_);// v = μ/(α1ρ1+α2ρ2)
}
```

In the interfaceProperties. C:

```
void Foam::interfaceProperties::calculateK()
{
    const fvMesh& mesh = alpha1_.mesh();
    const surfaceVectorField& Sf = mesh.Sf();//surface normal vector
```

```
// Cell gradient of alpha
    const volVectorField gradAlpha(fvc::grad(alpha1_));//∇α1

// Interpolated face-gradient of alpha
    surfaceVectorField gradAlphaf(fvc::interpolate(gradAlpha));//∇α1,f∇α1,f

// Face unit interface normal
surfaceVectorField nHatfv(gradAlphaf/(mag(gradAlphaf) + deltaN_));//n=∇α/|∇α|
 correctContactAngle(nHatfv.boundaryField(), gradAlphaf.boundaryField());

// Face unit interface normal flux
    nHatf_ = nHatfv & Sf;//change vector n to scalar n
// Simple expression for curvature
    K_ = -fvc::div(nHatf_);//k=-∇·n
```

In velocity equation:

```
// momentum equation: ∂ρU/∂t + ∇·(ρUU) − ∇·τ = Ck∇α − gh∇ρ − ∇p_rgh
    fvVectorMatrix UEqn
    (
        fvm::ddt(rho, U) //∂ρU/∂t
      + fvm::div(rhoPhi, U)//∇·(ρUU)
      + turbulence->divDevRhoReff(rho, U)//−∇·τ
    );

    UEqn.relax();

    if (pimple.momentumPredictor())
    {
        solve
        (
            UEqn
         ==
            fvc::reconstruct
            (
                (
                    fvc::interpolate(interface.sigmaK())*fvc::snGrad(alpha1)//
Ck∇α
                  - ghf*fvc::snGrad(rho)// gh∇ρ
                  - fvc::snGrad(p_rgh)//∇p_rgh
                ) * mesh.magSf()
            )
        );
    }
```

Then the calculation goes into pressure stage, which is be discussed Pressure-velocity coupling section.

An example of PIMPLE code implemented in the two-phase RANS solver is given below

```
#include "fvCFD.H"
#include "dynamicFvMesh.H"//required by dynamic mesh
#include "singlePhaseTransportModel.H"
```

```
#include "turbulentTransportModel.H"
#include "pimpleControl.H"//pimple control
#include "CorrectPhi.H"//required by dynamic mesh solver
#include "fvOptions.H"

// * * * * * * * * * * * * * * * * * * * * * * * * * * * * * * * * * * * * * * * * * * * * //

int main(int argc, char *argv[])
{
  #include "setRootCase.H"
  #include "createTime.H"
  #include "createDynamicFvMesh.H"//required by dynamic mesh
  #include "initContinuityErrs.H"

   pimpleControl pimple(mesh);

  #include "createFields.H"
  #include "createUf.H"//Calculated surface velocity from volume central
  #include "createMRF.H"
  #include "createFvOptions.H"
  #include "createControls.H"
  #include "CourantNo.H"
  #include "setInitialDeltaT.H"

   turbulence->validate();

   // * * * * * * * * * * * * * * * * * * * * * * * * * * * * * * * * * * * * * * * * * * * * //

   Info<< "\nStarting time loop\n" << endl;

   while (runTime.run())
   {
     #include "readControls.H" // PIMPLE control
     #include "CourantNo.H" // courant number

     #include "setDeltaT.H" //set time step length

       runTime++; //time marching

       Info<< "Time = " << runTime.timeName() << nl << endl;

       mesh.update(); //calculate mesh motion such as slide, rotation, deform and 6DoF motion. ,


       phi = mesh.Sf() & Uf; // Calculate absolute flux from the mapped surface velocity

       if (mesh.changing() && correctPhi)
       {
         #include "correctPhi.H"//space conservative law: ∂/∂t − ∇ · U_b = 0, U_b=0 for static mesh.
       }


       fvc::makeRelative(phi, U);//transform to relative flux

       if (mesh.changing() && checkMeshCourantNo)
       {
         #include "meshCourantNo.H"
```

```
        }

        // --- Pressure-velocity PIMPLE corrector loop
        while (pimple.loop())
        {
            #include "UEqn.H"//∂U/∂t + ∇ · (U(U − U_b)) = −∇p/ρ + ∇ · (∇U)
            // --- Pressure corrector loop
            while (pimple.correct())
            {
                #include "pEqn.H"
            }

            if (pimple.turbCorr())
            {
                turbulence->correct();
            }
        }
.............
while (pimple.correctNonOrthogonal())//get into pressure equation
{
    fvScalarMatrix pEqn
    (
        fvm::laplacian(rAtU(), p) == fvc::div(phiHbyA)
    ); //∇ · U = 0

    pEqn.setReference(pRefCell, pRefValue);

    pEqn.solve(mesh.solver(p.select(pimple.finalInnerIter())));

    if (pimple.finalNonOrthogonalIter())
    {
        phi = phiHbyA - pEqn.flux(); //phi switch to absolute flux
    }
}

#include "continuityErrs.H"

// Explicitly relax pressure for momentum corrector
p.relax();

U = HbyA - rAtU*fvc::grad(p);//update velocity
U.correctBoundaryConditions();
fvOptions.correct(U);

{
    Uf = fvc::interpolate(U);
    surfaceVectorField n(mesh.Sf()/mesh.magSf());
    Uf += n*(phi/mesh.magSf() - (n & Uf));
}

fvc::makeRelative(phi, U); // Make the fluxes relative to the mesh motion
```

B. Appendix B Turbulence models

Turbulence Model	Short Description
Spalart-Allmaras (Spalart and Allmaras, 1992)	Suitable for external aerodynamics, such as airplane and wing flows, turbomachinery and high speed flows around ships. It is good for mildly complex external and internal flows and boundary layer flows under pressure gradient, but it is not suitable for free shear flows and flows with strong separation
Standard k-epsilon (Launder and Spalding, 1974)	It is a robust turbulence model with less computational cost and widely used except for the known limitations of the model. It is good for initial iterations and parametric design. It is not suitable for complex flows including severe pressure gradient, separation, and strong streamline curvature.
Realizable k-epsilon (Shih et al., 1995)	It is an improvement over the standard k−ε model. Suitable for complex shear flows involving rapid strain, moderate swirl, vortices, and locally transitional flows (e.g. boundary layer separation and massive separation). It overcome the limitations of the standard k-epsilon model.
Standard k–omega (Wilcox, 1998)	It has a more accurate near wall treatment than models from the k-epsilon. It is good for wall-bounded boundary layer, free shear, and low Reynolds number formulation. But it needs higher resolution near the wall boundary.
SSt k-omega (Menter, 1994)	It has the similar benefits as standard k–omega. Not overly sensitive to inlet boundary conditions like the standard k–omega. It combines the k-omega with k-epsilon model to treat area away from wall boundary by using a blending function. It has a more accurate estimation of flow separation than other standard k-omega model.

C. Appendix C Piston type wave maker

The most straightforward technique to replicate physical experiments is to reproduce the motion of a piston/flap wave generator. This is achieved by simulating an oscillating wall type boundary within the dynamic mesh. One of the benefit of physical wave generation method is that it has a better reproduction with the wave in physical wave tank. Initially, a piston-type wave maker is configured as a moving boundary in the numerical wave tank. A sketch of the numerical model compared with physical wave tank is shown in Figure C-1. The wave maker is at the left inlet side of the numerical flume, which is 35m long, and at its right side the wave damping zone is set to absorb the wave reflected from right boundary. The computational domain is filled with water in the lower part and air above; and a solid wall boundary is imposed on the bottom boundary. Wave probes will be set in the middle of the flume to record the free surface height in the simulation.

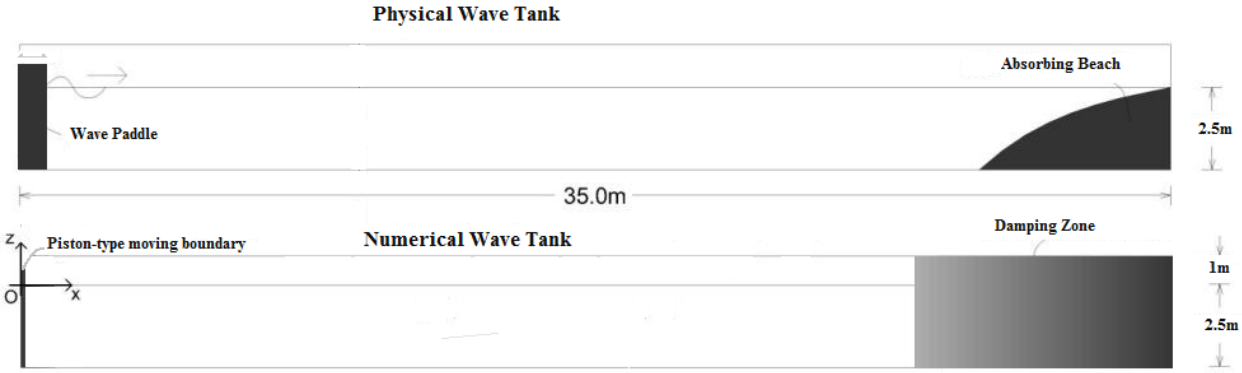

Figure C-1 Sketch of physical and numerical wave tank

In this section, implementation based on linear wave maker theory is developed. Firstly, the numerical waves are generated through a piston-type wave maker. Then, results for the nonlinear stokes wave generation, and irregular wave generation are described. Finally some conclusions are drawn.

According to Dean and Dalrymple (1984), the motion pattern of the piston-type boundary should be set to satisfy the following conditions to generate a linear (1st order stokes) wave:

$$\eta = \frac{H}{2} sin(kx - \omega t) \tag{C-1}$$

$$X_t = \frac{S}{2}\cos(\omega t) = \frac{\omega\eta(2kd + \sinh(2kd))}{4\sinh^2(kd)} \tag{C-2}$$

Where X_t is the position of the moving boundary, x represents the distance along longitudinal direction, S is the stroke length of piston type wave maker, ω is the angular wave frequency, η is the wave elevation, k is the wave number, and d is the still water depth. There are two assumptions for linear wave: there are no energy losses due to friction, turbulence and so on; the wave height is much smaller than the wave length.

In order to absorb the wave reflected from outlet boundary, the damping zone approach is applied to represent far field of the computational domain instead of slope beach. In this method, an artificial source term D is added into the governing equation for wave damping closed to the outlet boundary.

$$\rho(U_t + U \cdot \nabla U) = \nabla \cdot \mu \nabla U - \nabla p + F_b + f_\sigma + \underline{D} \tag{C-3}$$

$$D = \begin{cases} \alpha \left(\frac{x - x_0}{x_1 - x_0}\right)^2 \rho U, & x_0 \le x \le x_1 \\ 0, & x < x_0 \end{cases} \tag{C-4}$$

Where α is the wave damping coefficient, which can be determined from Romate (1992), and $x \in [x_0, x_1]$ denotes the wave damping zone, which is normally longer than two wave length.

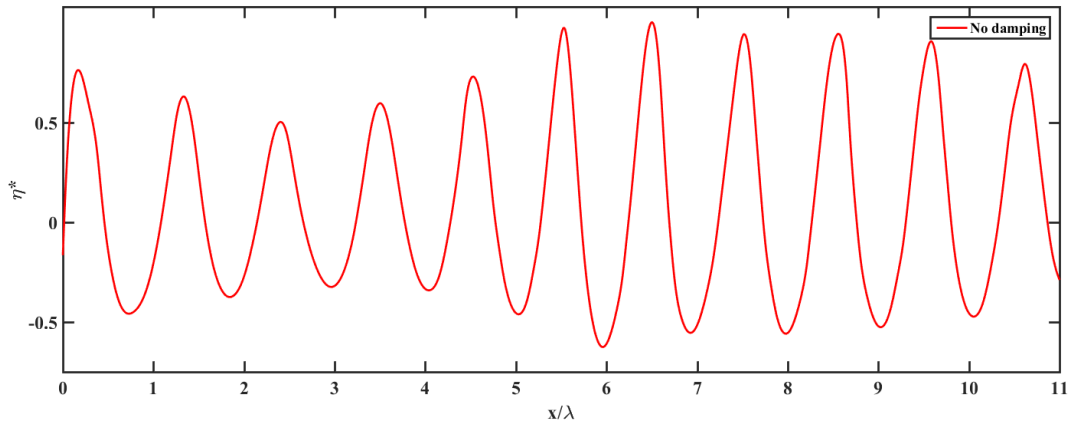

(a)

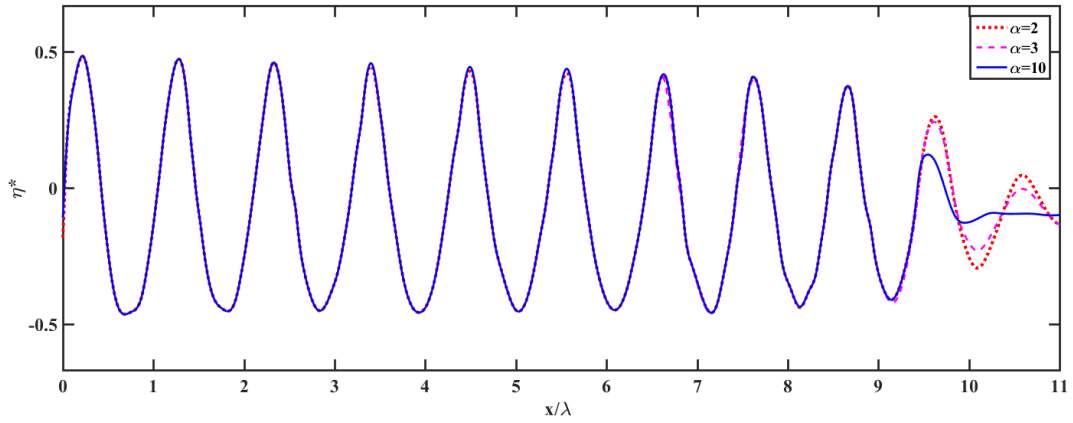

(b)

Figure C-2 Wave Profile along the wave tank after 10 wave period

The numerical wave tank is set to be 35m long including damping zone. At the beginning, the damping coefficient is 0 and it can be seen that the wave profile is asymmetry due to reflection from the downstream boundary. By increasing the damping coefficient, the wave profile is improved by gradually dissipating wave energy in the damping zone. The key benefit of this method is that the computational cost can be reduced because of short the wave tank. Figure C-2 and Figure C-3 show the parameter study on the effect of the damping coefficient and the size of damping zone on the dissipating performance of this method. Two separate comparisons were made. In the Figure C-2b, the damping coefficient equals 2, and 3 to 10 with an L=2λ (λ is wavelength) for the damping zone; and in the Figure C-3, the length of the damping zone varies from 1λ to 3λ with the damping coefficient equals 2. It should be note that the longer dissipation zone increases the length of domain, which will increase computational cost and may cause brings unstable simulation.

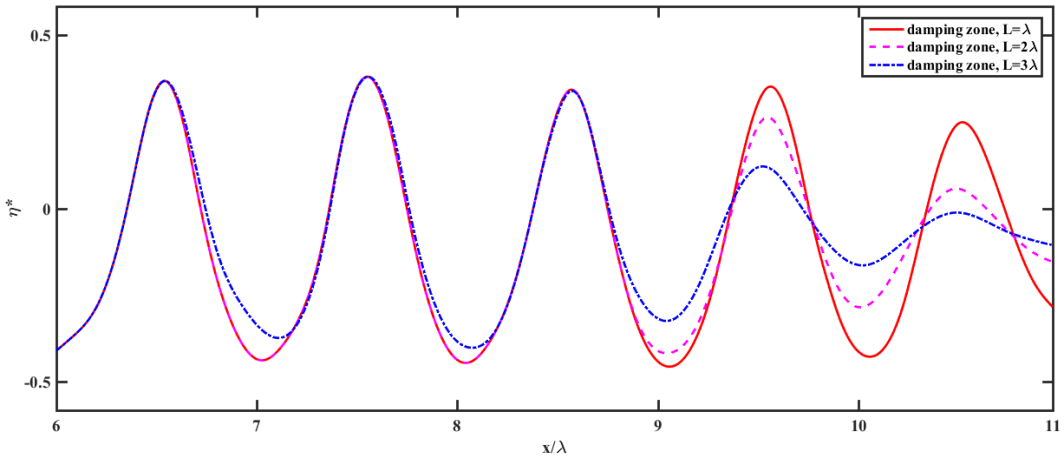

Figure C-3 Wave profile at the output with different damping zone length

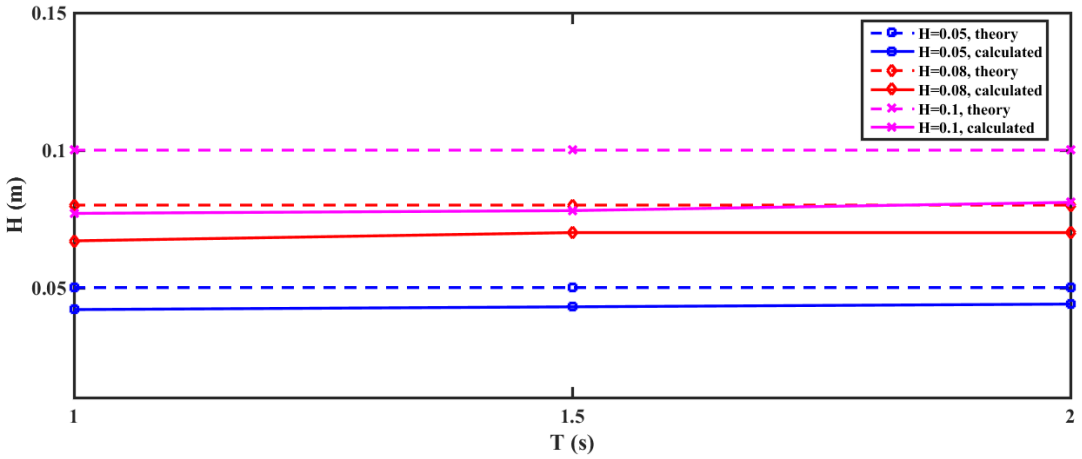

Figure C-4 Linear wave validation, d=0.25m

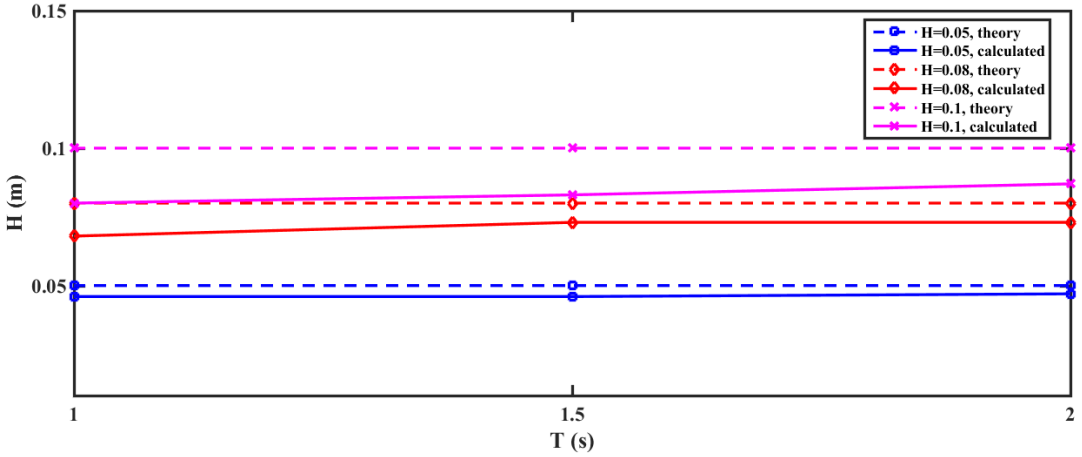

Figure C-5 Linear wave validation, d=0.4m

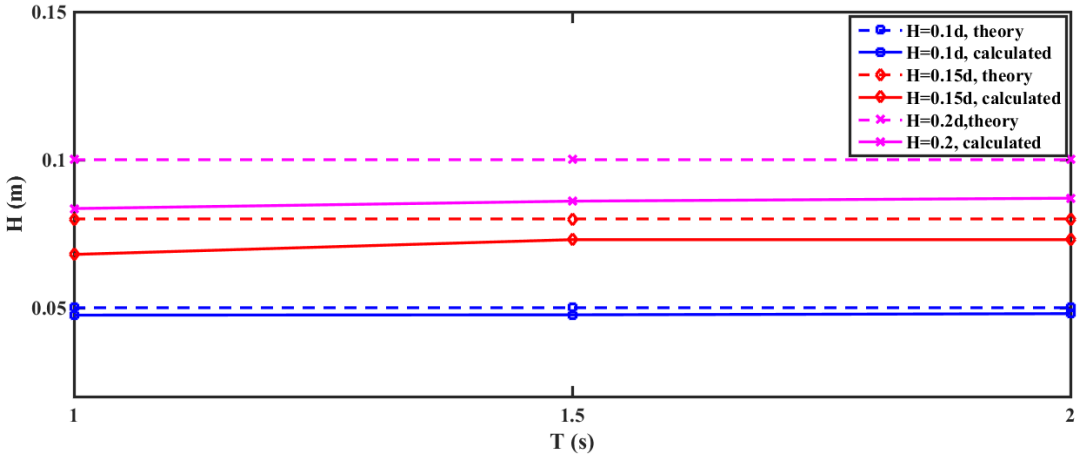

Figure C-6 Linear wave validation, d=0.5m

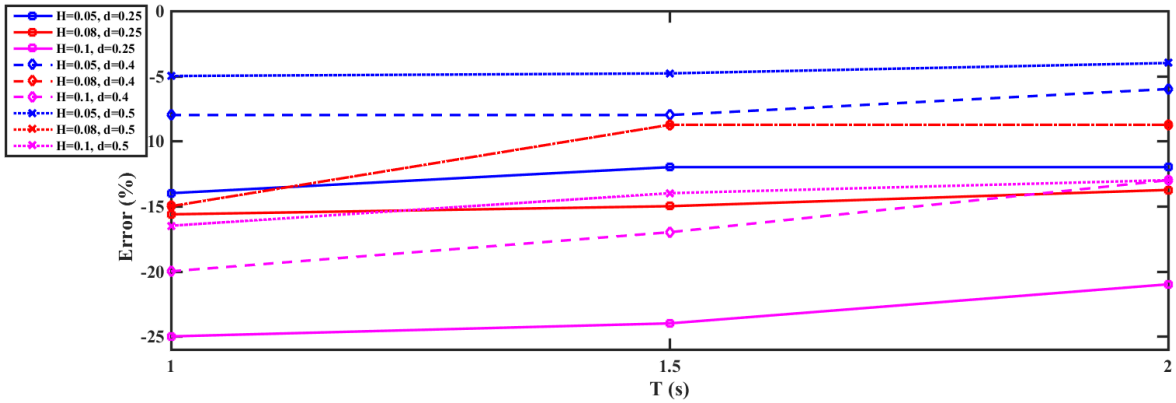

Figure C-7 Linear wave error analysis at different wave depth and height

Figure C-4-Figure C-6 illustrate that all the calculated wave heights are lower than their corresponding wave height input at the flume entry, especially at shallower water depth, longer wave period and higher wave height (Figure C-7). The main reason for this error is caused by the larger wave maker stroke. The solution assume small wave market motion and so have limitation to deal with more extreme wave conditions. The nonlinear effect generates unwanted free surface waves; and this is the motivation that the development of highly non-linear wave theory is required to generate wave travelling longer. Overall, the calculated results show good agreement and the linear wave theory is suitable for deep water waves with small wave height and long wave period.

The application of the linear wave theory is restricted to the small amplitude assumed in the governing equations. When considering larger ratio of wave height and water depth, and wave steepness, the wave becomes unstable and linear wave marker theory is not accurate enough to describe wave pattern. According to Madsen (1971), the wave generated by linear wave maker theory contains 2nd order free wave pattern, which leads to unstable wave profiles due to the phase shift and frequency difference between free wave and dominant wave. Nonlinear wave theories are generally described by higher order Stokes waves. Dynamic and kinematic free surface boundary conditions are different from linear theory. The accuracy of the theory depends on the number of terms contained in the equation. Take 2nd order Stokes wave as an example, it improves the accuracy by adding a correction into 1st order Stokes wave:

$$\eta = \frac{H}{2}\cos(kx - \omega t) + \frac{3H^2}{16k^2\, d^3}\cos[2(kx - \omega t)] \tag{C-5}$$

$$X_{t,\,2^{nd}\,order} = \frac{H\left(1 + \frac{2kd}{\sinh(2kd)}\right)}{4\tanh(kd)}\Bigg[\cos(\omega t) + \frac{H}{4d\left(\frac{1}{2}\left(1 + \frac{2kd}{\sinh(2kd)}\right)\right)}\left(\frac{3}{4\sinh^2(kd)} - \frac{1}{4}\left(1 + \frac{2kd}{\sinh(2kd)}\right)\right)\sin(2\omega t)\Bigg] \tag{C-6}$$

where $X_{t,\,2^{nd}\,order}$ is the position of the new moving boundary for 2nd order wave, λ is wave length and g represents acceleration due to gravity. In the following researches, fifth-order Stokes wave theory (Fenton, 1985) is used to simulate more realistic wave propagation in the computational domain. The fifth-order Stokes wave theory has a higher order of accuracy and can describe larger finite amplitude wave.

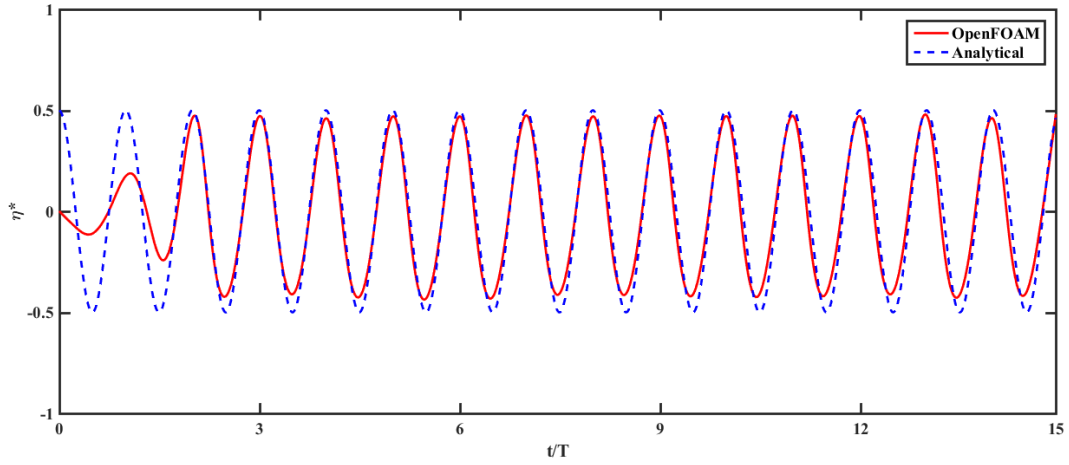

Figure C-8 2nd order wave generated by piston type wave maker

The time series of wave profile at gauge 1 compared with analytical solution is shown in Figure C-8. The results shows good agreement.

The realistic waves are highly variable. The surface waves are composed of random waves of various lengths and periods. The concept of the spectrum of ocean waves is used to describe the surface with some simplifications. The spectrum gives the distribution of wave energy among different wave frequencies of wave-lengths on the sea surface. There are several types of energy spectra available in the literatures and the most widely used spectrums are the Pierson-Moskowitz spectrum and JONSWAP spectrum. The Pierson-Moskowitz spectrum is used to describe the fully developed sea state for the irregular waves (Pierson and Moskowitz, 1964). Hasselmann et al. (1973) after analyzing data collected during the Joint North Sea Wave Observation Project (JONSWAP) suggested the following form to represent a developing ocean wave improved from Pierson-Moskowitz spectrum by an underlined extra term:

$$S(\omega) = 0.219 H_{1/3}^2 T_p^{-4} \omega^{-5} exp\left[-\frac{5}{4}\left(\frac{\omega_p}{\omega}\right)^4\right] \underline{\gamma^{\exp\left[-\frac{(\omega-\omega_p)^2}{2\sigma^2\omega_p^2}\right]}} \tag{C-7}$$

$$T_p = \frac{T_{1/3}}{1 - 0.132(\gamma + 0.2)^{-0.559}} \tag{C-8}$$

$$\sigma = \begin{cases} 0.07, & \omega \leq \omega_p \\ 0.09, & \omega > \omega_p \end{cases} \tag{C-9}$$

$$H_{1/3} = \frac{1}{\frac{N}{3}} \sum_{i=1}^{\frac{N}{3}} H_i \tag{C-10}$$

The elevation of each irregular wave component thus can be expressed as:

$$\eta_i = \sqrt{2S(\omega_i)\Delta\omega} \tag{C-11}$$

where ω_i is a random frequency and $\Delta\omega$ is the interval between frequency components. Each wave component can be generated by the wave maker as a regular wave. In this numerical model, irregular waves are generated by superposition of the regular wave components.

The numerical simulations are carried out with the same wave tank settings as the previous section. The numerical results are compared with the theoretical wave energy spectrum. The wave profile at $x = 3\lambda$ along the period of 120T, where T is the mean wave period, is shown below. The Figure C-9 and Figure C-10 demonstrate that the numerical results for the wave energy at $x = 3\lambda$ match reasonably well with the theory; while the numerical results with high frequencies are greater than the theoretical ones for the wave at the remote location. It should be noted that wave energy spectrum is maintained at different location. However, the peak value changes slightly during the wave propagation. This means that the numerical simulation has a wider energy spectrum range. The phenomenon may be caused by energy dissipation due to wave breaking.

To verify the effect of the interval between frequency components on the generated wave spectrum at $x = 3\lambda$ and $x = 9\lambda$ in the wave tank, another set of simulation is carried out by decreasing integral $\Delta\omega$ as shown in Figure C-11 and Figure C-12.

The results from numerical simulation with smaller $\Delta\omega$ is smaller than those from theory when approaching peak wave spectrum density. The simulated wave spectrum density has a slightly better agreement with the estimated values at the location close to wave outlet boundary but the improvement compared with the numerical results with larger Δf is not noticeable. Less

energy fluctuation is observed but the density curve is still not smooth due to energy dissipation caused by wave breaking. This may also be caused by the initial wave condition, the geometry of the wave tank or the numerical error in the discretization of wave spectrum. Another factor that should be kept in mind is that duration of simulation should be sufficient to let the propagation waves fully develop. So 120T is used after several sets of simulation.

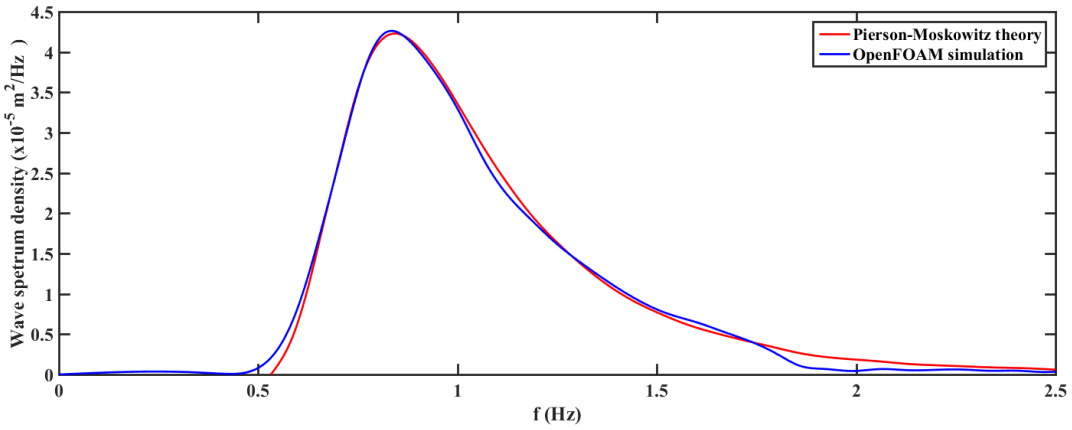

Figure C-9 Wave energy spectrum at $x = 3\lambda$ with $\Delta f = 0.01Hz$

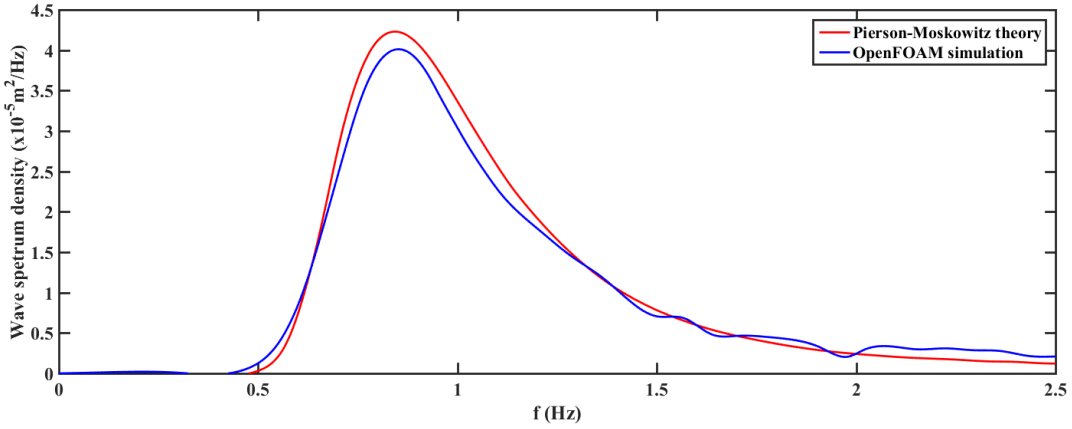

Figure C-10 Wave energy spectrum at $x = 9\lambda$ with $\Delta f = 0.01Hz$

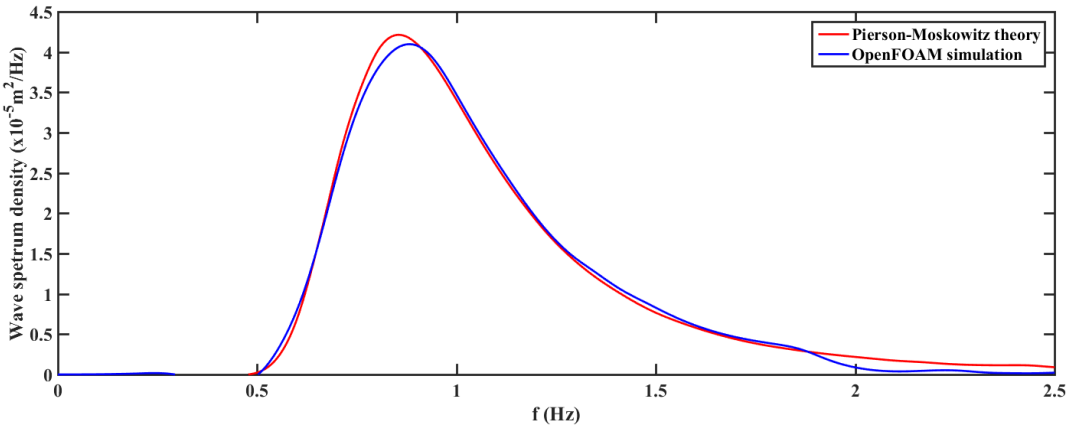

Figure C-11 Wave energy spectrum at $x = 3\lambda$ with $\Delta f = 0.005Hz$

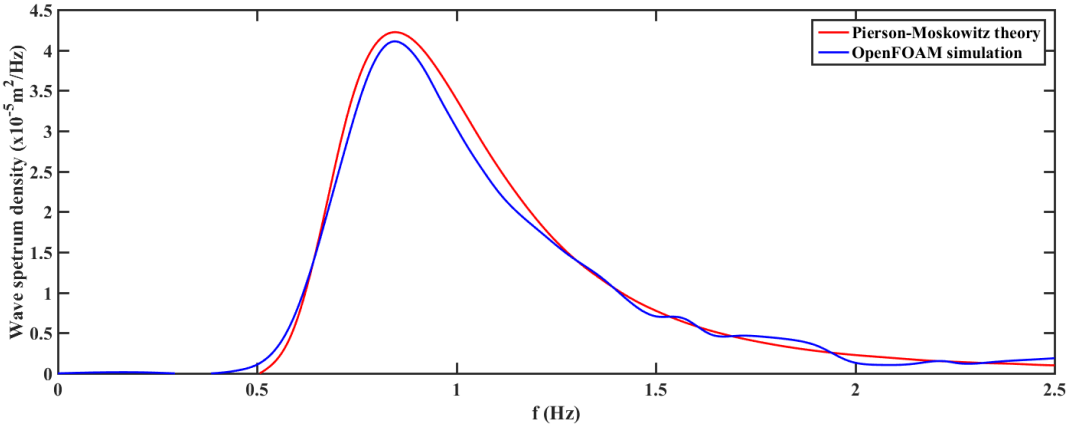

Figure C-12 Wave energy spectrum at $x = 9\lambda$ with $\Delta f = 0.005Hz$

D. Appendix D Steep wave propagation test Results

These are additional test results showing the longer and steeper waves than the case in Chapter 4. These represent a more violent wave-structure interaction and a more non-linear wave. Due to the wave breaking, the results of wave height is shown in frequency domain. The wave parameters used are: wave period of 3.571s, wave height of 0.058m, and wave steepness of 0.0059.

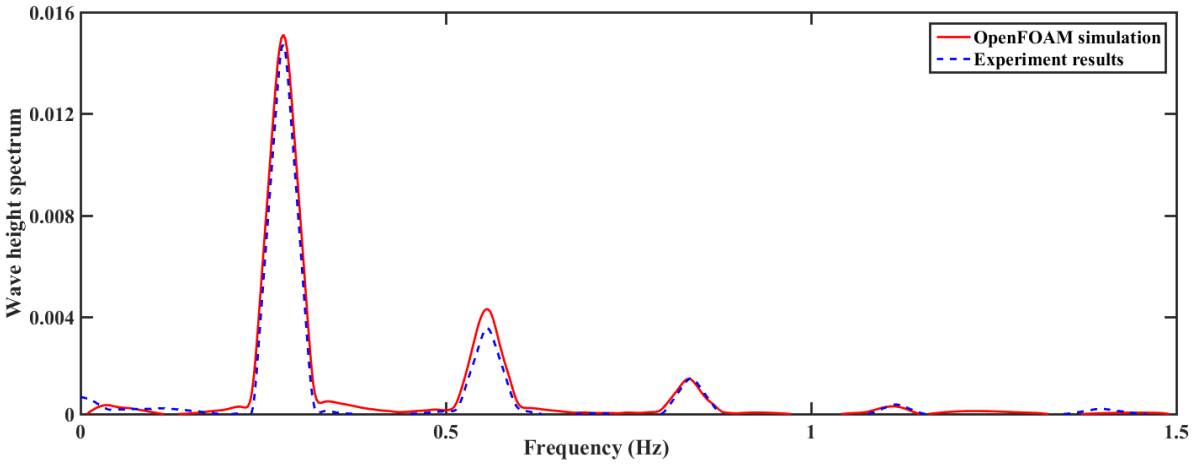

Figure D-1 Wave height validation between experimental data and OpenFOAM results at gauge 1, H/L=0.059

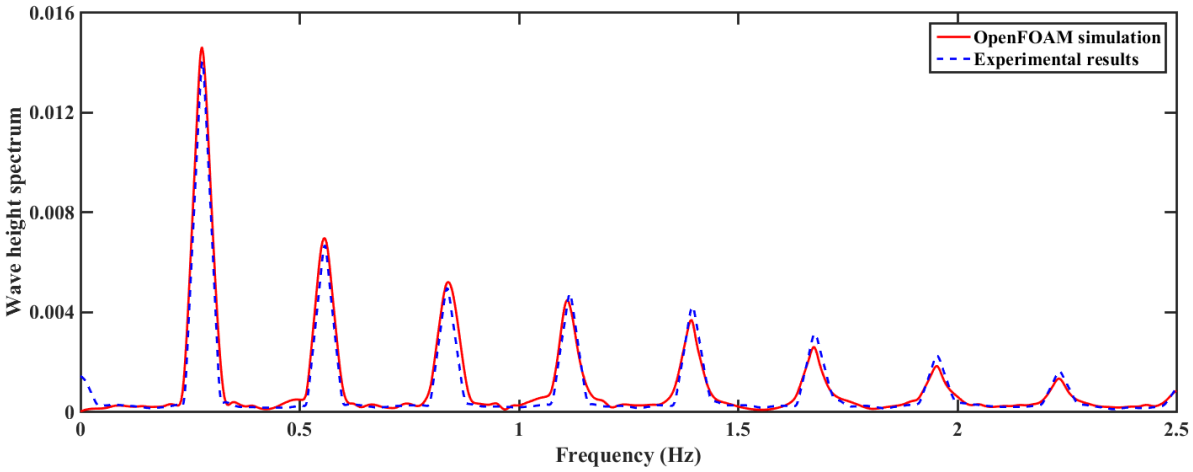

Figure D-2 Wave height validation between experimental data and OpenFOAM results at gauge 2, H/L=0.059

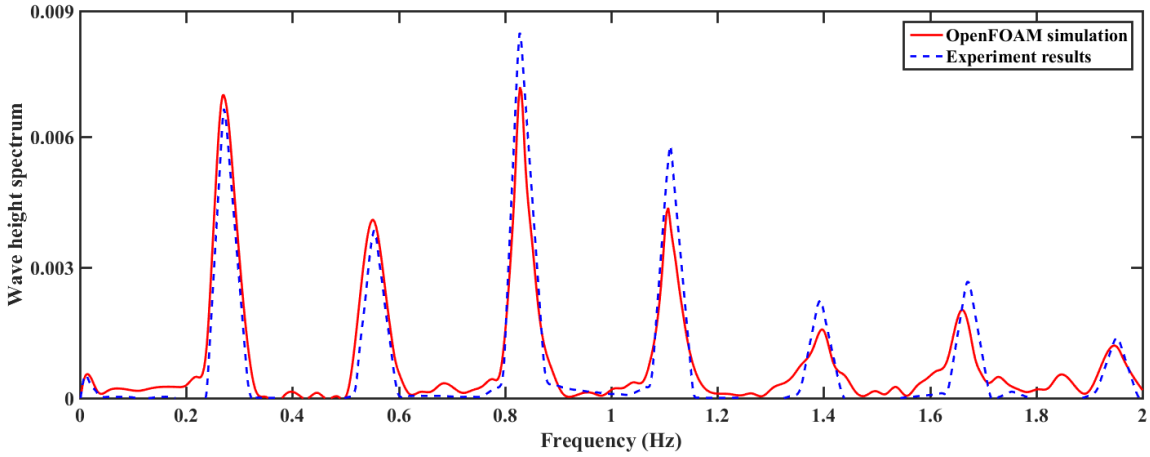

Figure D-3 Wave height validation between experimental data and OpenFOAM results at gauge 3, H/L=0.059

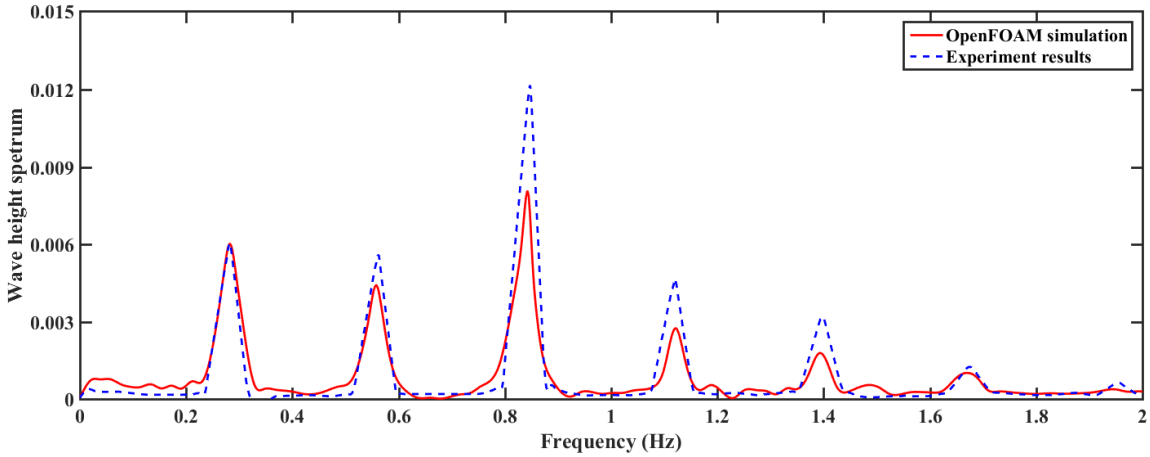

Figure D-4 Wave height validation between experimental data and OpenFOAM results at gauge 4, H/L=0.059

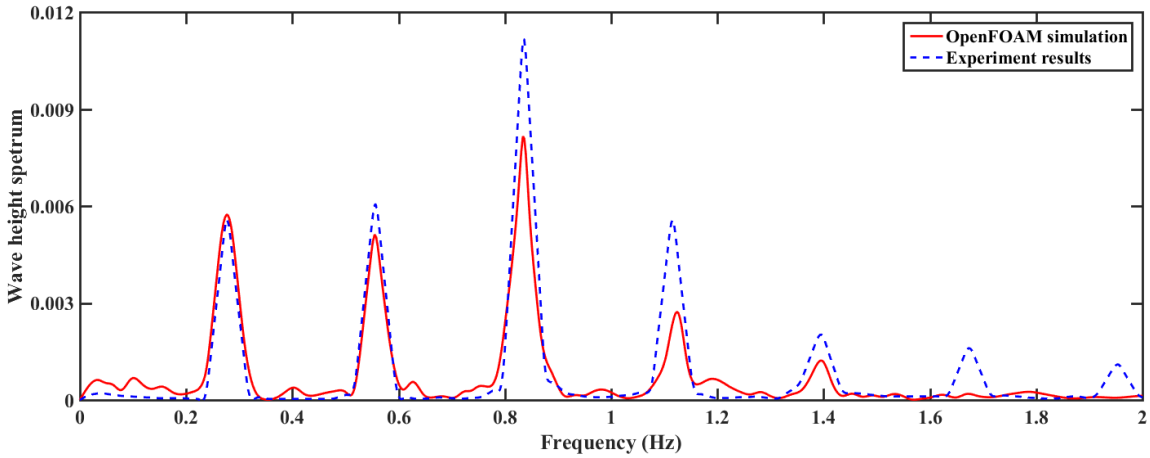

Figure D-5 Wave height validation between experimental data and OpenFOAM results at gauge 5, H/L=0.059

The wave parameters used below are: wave period of 1.438s, wave height of 0.082m, and wave steepness: 0.027.

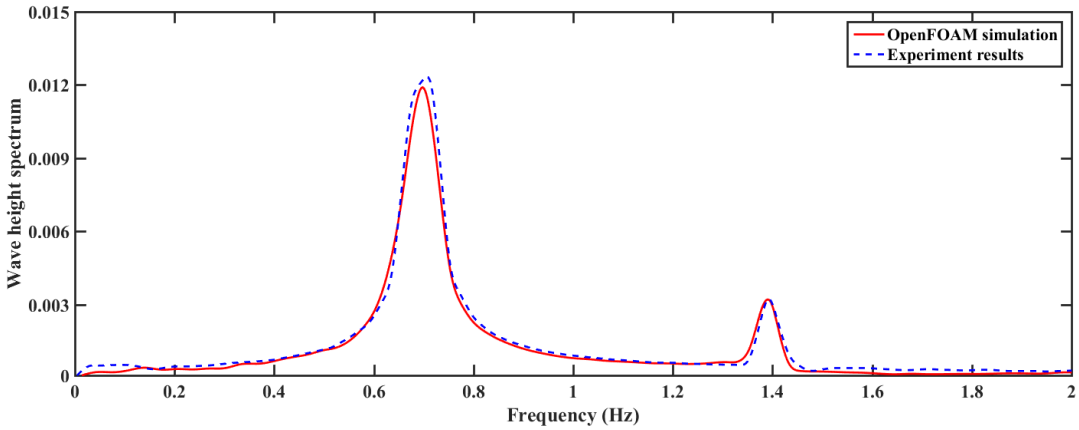

Figure D-6 Wave height validation between experimental data and OpenFOAM results at gauge 1, H/L=0.027

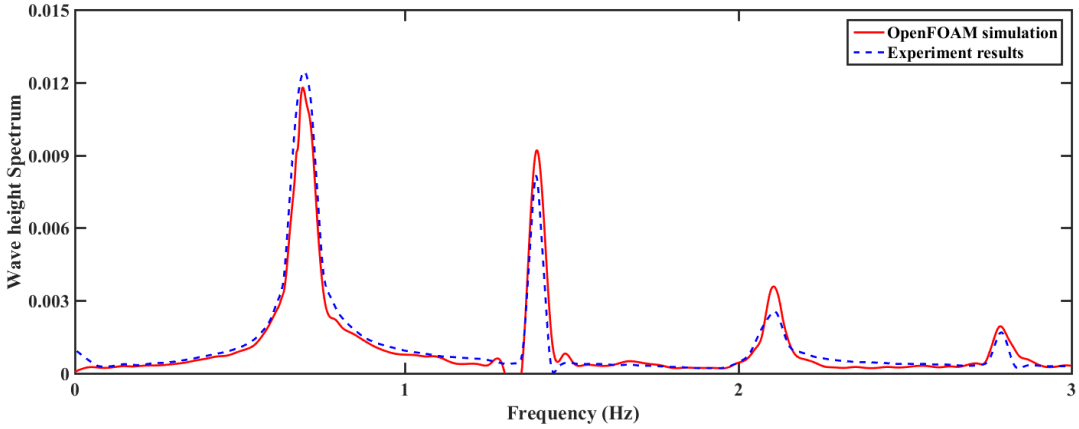

Figure D-7 Wave height validation between experimental data and OpenFOAM results at gauge 2, H/L=0.027

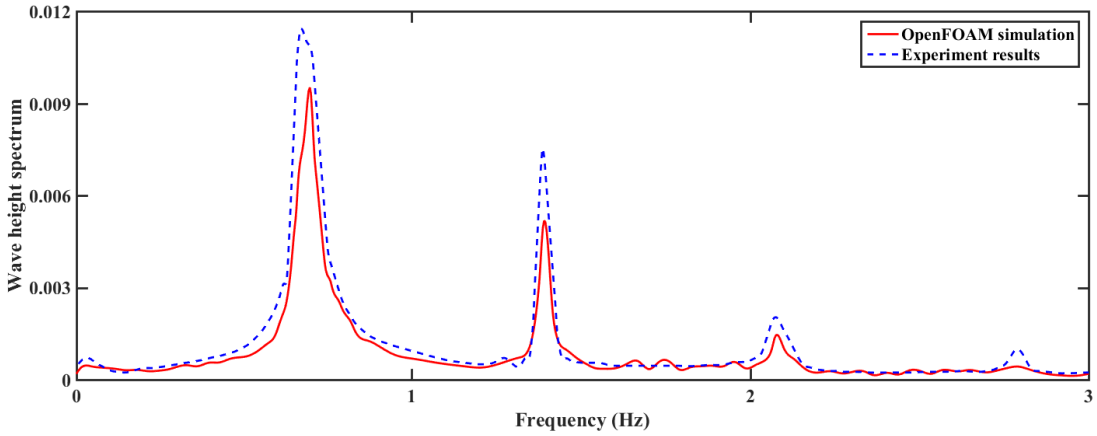

Figure D-8 Wave height validation between experimental data and OpenFOAM results at gauge 3, H/L=0.027

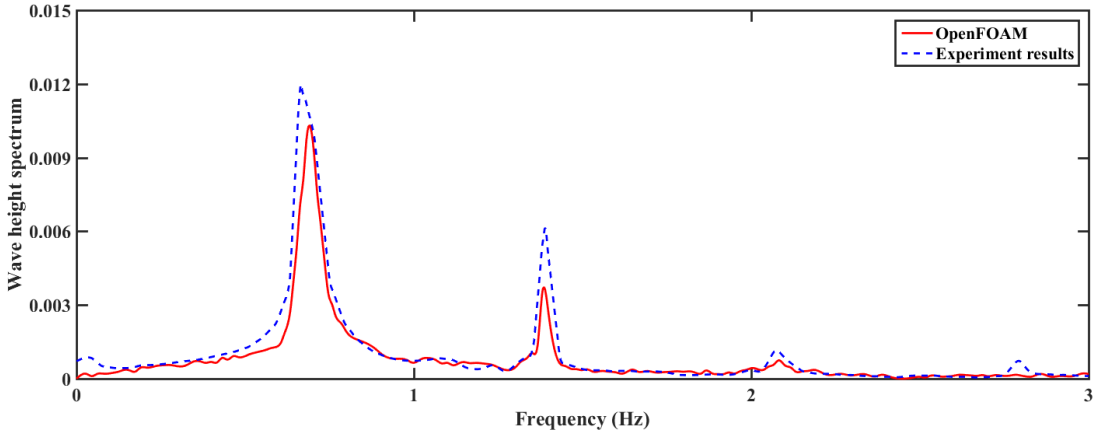

Figure D-9 Wave height validation between experimental data and OpenFOAM results at gauge 4, H/L=0.027

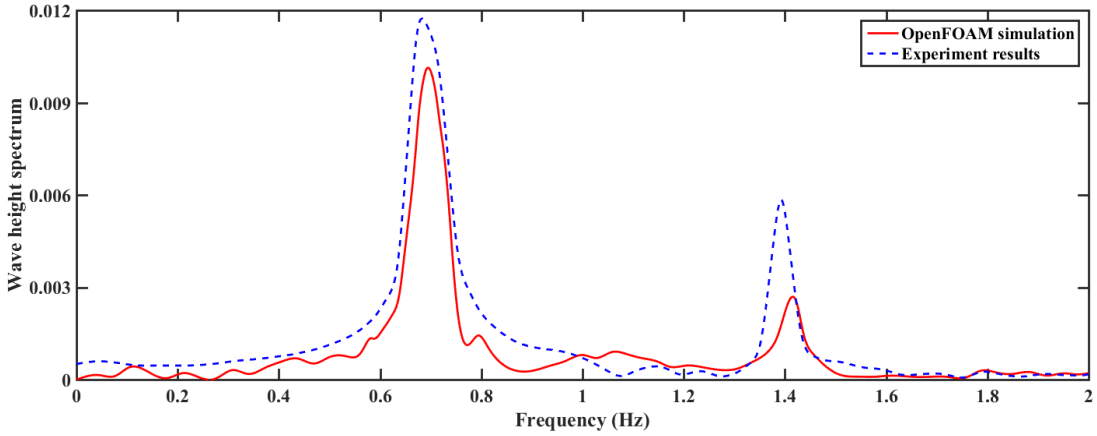

Figure D-10 Wave height validation between experimental data and OpenFOAM results at gauge 5, H/L=0.027

E. Appendix E 5th order stokes wave parameters

5th order stokes wave parameters:

$S = 1/\cosh(2k\cdot d);$

$a_{11} = 1/\sinh(k\cdot d);$

$a_{22} = 3\cdot S^2/(2(1 - S)^2);$

$a_{31} = (-4 - 20\cdot S + 10\cdot S^2 - 13\cdot S^3) / (8\cdot\sinh(k\cdot d)\cdot(1 - S)^3);$

$a_{33} = (-2\cdot S^2 + 11\cdot S^3) / (8\cdot\sinh(k\cdot d)\cdot(1 - S)^3);$

$a_{42} = (12\cdot S - 14\cdot S^2 - 264\cdot S^3 - 45\cdot S^4 - 13\cdot S^5)/(24\cdot(1 - S)^5);$

$a_{44} = (10\cdot S^3 - 174\cdot S^4 + 291\cdot S^5 + 278\cdot S^6)/(48\cdot(3 + 2\cdot S)\cdot(1 - S)^5);$

$a_{51} = (-1184 + 32\cdot S + 13232\cdot S^2 + 21712\cdot S^3 + 20940\cdot S^4 + 12554\cdot S^5 - 500\cdot S^6 - 3341\cdot S^7 - 670\cdot S^8)/(64\cdot\sinh(k\cdot d)\cdot(3 + 2\cdot S)\cdot(4 + S)\cdot(1 - S)^6);$

$a_{53} = (4\cdot S + 105\cdot S^2 + 198\cdot S^3 - 1376\cdot S^4 - 1302\cdot S^5 - 117\cdot S^6 + 58\cdot S^7)/(32\cdot\sinh(k\cdot d)\cdot(3 + 2\cdot S)\cdot(1 - S)^6);$

$a_{55} = (-6\cdot S^3 + 272\cdot S^4 - 1552\cdot S^5 + 852\cdot S^6 + 2029\cdot S^7 + 430\cdot S^8)/(64\cdot\sinh(k\cdot d)\cdot(3 + 2\cdot S)\cdot(4 + S)\cdot(1 - S)^6);$

$b_{22} = ((\cosh(k\cdot d)/\sinh(k\cdot d))\cdot(1 + 2\cdot S))/(2\cdot(1 - S));$

$b_{31} = (-3\cdot(1 + 3\cdot S + 3\cdot S^2 + 2\cdot S^3))/(8\cdot(1 - S)^3);$

$b_{42} = ((\cosh(k\cdot d)/\sinh(k\cdot d))\cdot(6 - 26\cdot S - 182\cdot S^2 - 204\cdot S^3 - 25\cdot S^4 + 26\cdot S^5))/(6\cdot(3 + 2\cdot S)*(1 - S)^4)$;

$b_{44} = ((\cosh(k\cdot d)/\sinh(k\cdot d))\cdot(24 + 92\cdot S + 122\cdot S^2 + 66\cdot S^3 + 67\cdot S^4 + 34\cdot S^5))/(24\cdot(3 + 2\cdot S)\cdot(1 - S)^4)$;

$b_{53} = (9\cdot(132 + 17\cdot S - 2216\cdot S^2 - 5897\cdot S^3 - 6292\cdot S^4 - 2687\cdot S^5 + 194\cdot S^6 + 467\cdot S^7 + 82\cdot S^8))/(128\cdot(3 + 2\cdot S)\cdot(4 + S)\cdot(1 - S)^6)$;

$b_{55} = (5\cdot(300 + 1579\cdot S + 3176\cdot S^2 + 2949\cdot S^3 + 1188\cdot S^4 + 675\cdot S^5 + 1326\cdot S^6 + 827\cdot S^7 + 130\cdot S^8))/(384\cdot(3.0 + 2.0\cdot S)\cdot(4.0 + S)\cdot(1 - S)^6)$;

$c_0 = (\tanh(k\cdot d))^{0.5}$;

$c_2 = c_0\cdot(2 + 7\cdot S^2)/(4\cdot(1 - S)^2)$;

$c_4 = (c_0\cdot(4 + 32\cdot S - 116\cdot S^2 - 400\cdot S^3 - 71\cdot S^4 + 146\cdot S^5))/(32\cdot(1 - S)^5)$;

$e_2 = (\tanh(k\cdot d)\cdot(2 + 2\cdot S + 5\cdot S^2))/(4\cdot(1 - S)^2)$;

$e_4 = (\tanh(k\cdot d)\cdot(8 + 12\cdot S - 152\cdot S^2 - 308\cdot S^3 - 42\cdot S^4 + 77\cdot S^5))/(32\cdot(1 - S)^5)$;

5th order stokes horizontal wave velocity:

$$
\begin{aligned}
Ux = {} & c_0 \cdot \mathrm{sqrt}(9.81/k) \\
& \cdot ((\mathrm{eps} \cdot a_{11} + \mathrm{pow}(\mathrm{eps},3) \cdot a_{31} + \mathrm{pow}(\mathrm{eps},5) \cdot a_{51}) \cdot \cosh(k \cdot (d+z)) \cdot \cos(kx\text{-}wt\text{-}phi) \\
& + 2 \cdot (\mathrm{pow}(\mathrm{eps},2) \cdot a_{22} + \mathrm{pow}(\mathrm{eps},4) \cdot a_{42}) \cdot \cosh(2 \cdot k \cdot (d+z)) \cdot \cos(2 \cdot (kx\text{-}wt\text{-}phi)) \\
& + 3 \cdot (\mathrm{pow}(\mathrm{eps},3) \cdot a_{33} + \mathrm{pow}(\mathrm{eps},5) \cdot a_{53}) \cdot \cosh(3 \cdot k \cdot (d+z)) \cdot \cos(3 \cdot (kx\text{-}wt\text{-}phi)) \\
& + 4 \cdot \mathrm{pow}(\mathrm{eps},4) \cdot a_{44} \cdot \cosh(4 \cdot k \cdot (d+z)) \cdot \cos(4 \cdot (kx\text{-}wt\text{-}phi)) \\
& + 5 \cdot \mathrm{pow}(\mathrm{eps},5) \cdot a_{55} \cdot \cosh(5 \cdot k \cdot (d+z)) \cdot \cos(5 \cdot (kx\text{-}wt\text{-}phi))
\end{aligned}
$$

5th order stokes vertical wave velocity:

$$
\begin{aligned}
Uy = {} & c_0 \cdot \mathrm{sqrt}(9.81/k) \\
& \cdot ((\mathrm{eps} \cdot a_{11} + \mathrm{pow}(\mathrm{eps},3) \cdot a_{31} + \mathrm{pow}(\mathrm{eps},5) \cdot a_{51}) \cdot \sinh(k \cdot (d+z)) \cdot \sin((kx\text{-}wt\text{-}phi)) \\
& + 2 \cdot (\mathrm{pow}(\mathrm{eps},2) \cdot a_{22} + \mathrm{pow}(\mathrm{eps},4) \cdot a_{42}) \cdot \sinh(2 \cdot k \cdot (d+z)) \cdot \sin(2 \cdot (kx\text{-}wt\text{-}phi)) \\
& + 3 \cdot (\mathrm{pow}(\mathrm{eps},3) \cdot a_{33} + \mathrm{pow}(\mathrm{eps},5) \cdot a_{53}) \cdot \sinh(3 \cdot k \cdot (d+z)) \cdot \sin(3 \cdot (kx\text{-}wt\text{-}phi)) \\
& + 4 \cdot \mathrm{pow}(\mathrm{eps},4) \cdot a_{44} \cdot \sinh(4 \cdot k \cdot (d+z)) \cdot \sin(4 \cdot (kx\text{-}wt\text{-}phi)) \\
& + 5 \cdot \mathrm{pow}(\mathrm{eps},5) \cdot a_{55} \cdot \sinh(5 \cdot k \cdot (d+z)) \cdot \sin(5 \cdot (kx\text{-}wt\text{-}phi));
\end{aligned}
$$

F. Appendix F-1 Results from rectangular cylinder in heave

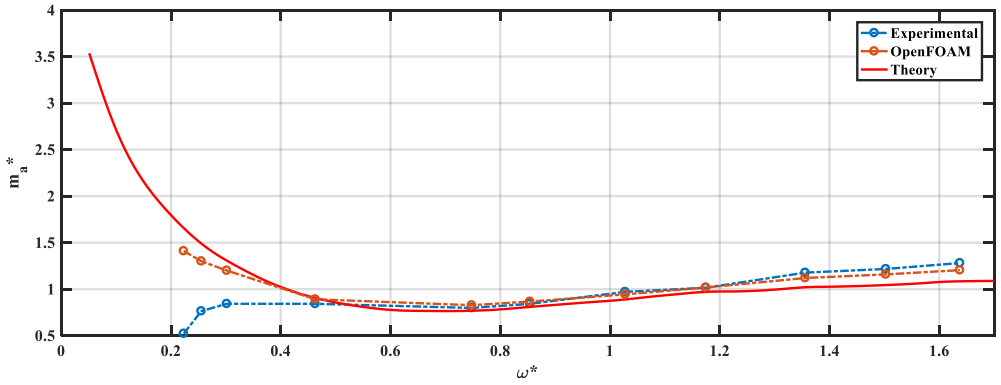

Figure F-1 Non-dimensional added mass coefficients vs non-dimensional frequency under heave motion, Draft =0.5 cylinder height, Amplitude =0.01m

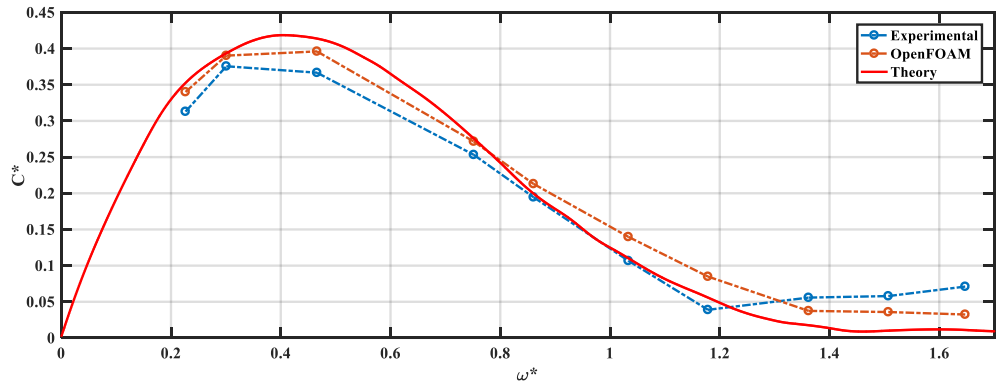

Figure F-2 Non-dimensional damping vs non-dimensional frequency under heave motion, Draft =0.5 cylinder height, Amplitude =0.01m

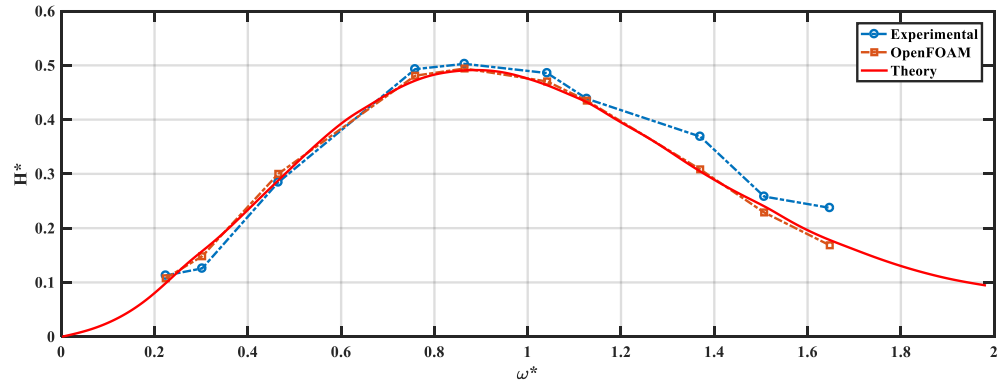

Figure F-3 Non-dimensional wave height vs non-dimensional frequency under heave motion, Draft =0.5 cylinder height, Amplitude =0.01m

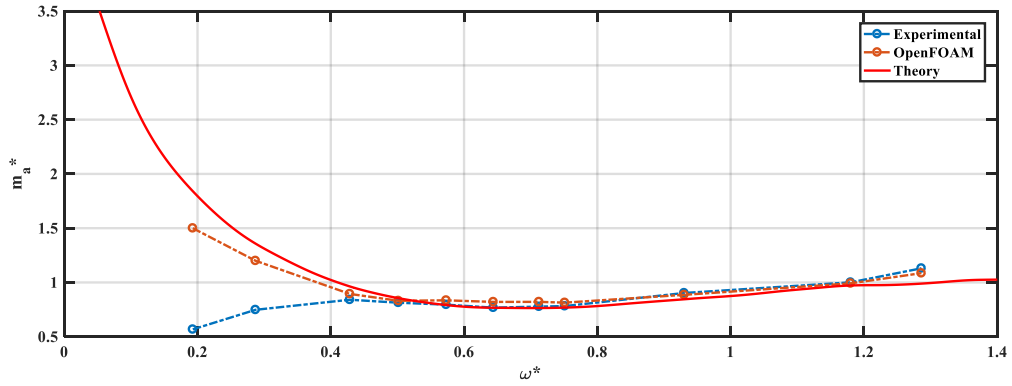

Figure F-4 Non-dimensional added mass vs non-dimensional frequency under heave motion, Draft =0.5 cylinder height, Amplitude =0.02m

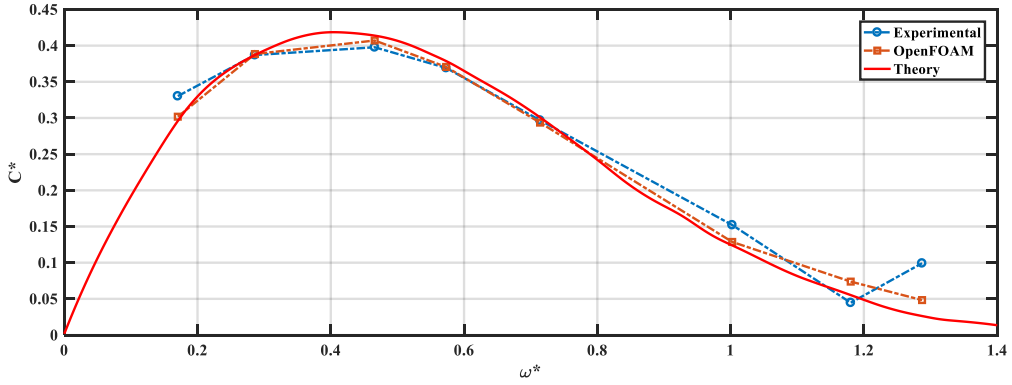

Figure F-5 Non-dimensional damping vs non-dimensional frequency under heave motion, Draft =0.5 cylinder height, Amplitude =0.02m

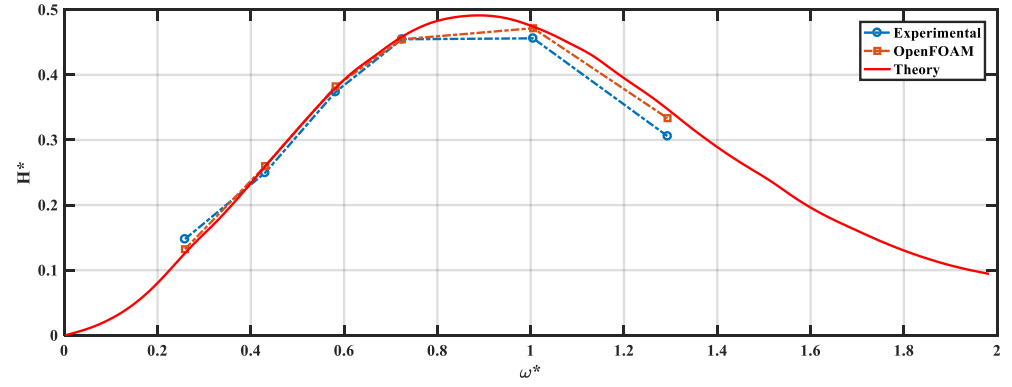

Figure F-6 Non-dimensional wave height vs non-dimensional frequency under heave motion, Draft =0.5 cylinder height, Amplitude =0.02m

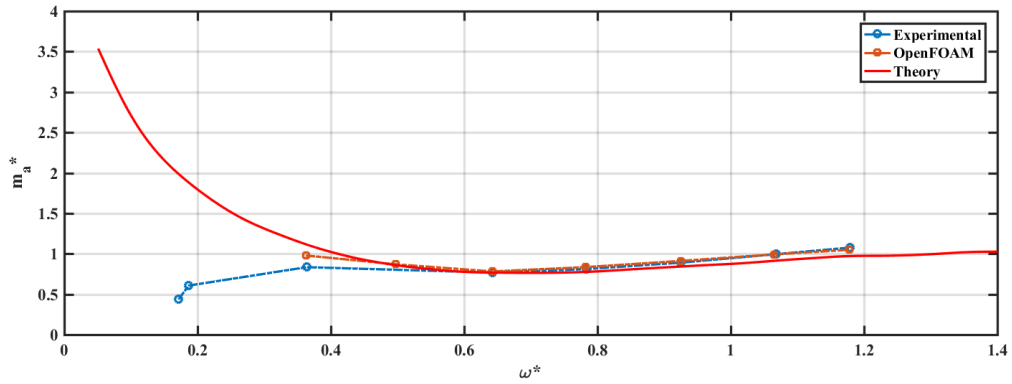

Figure F-7 Non-dimensional added mass vs non-dimensional frequency under heave motion, Draft =0.5 cylinder height, Amplitude =0.03m

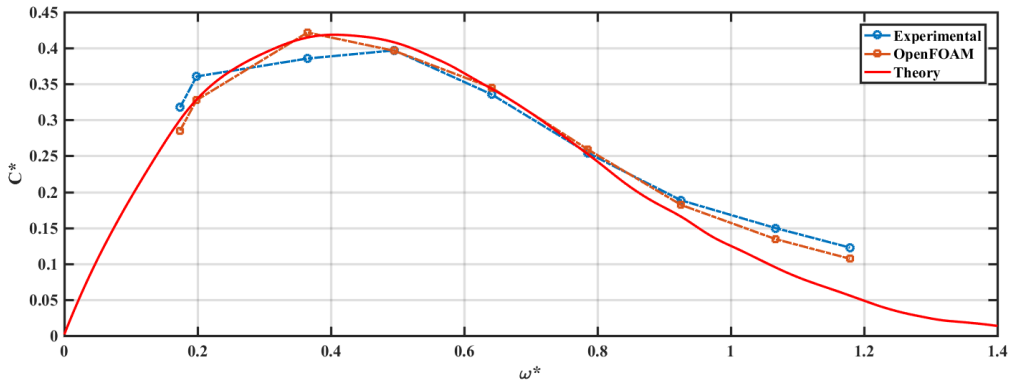

Figure F-8 Non-dimensional damping vs non-dimensional frequency under heave motion, Draft =0.5 cylinder height, Amplitude =0.03m

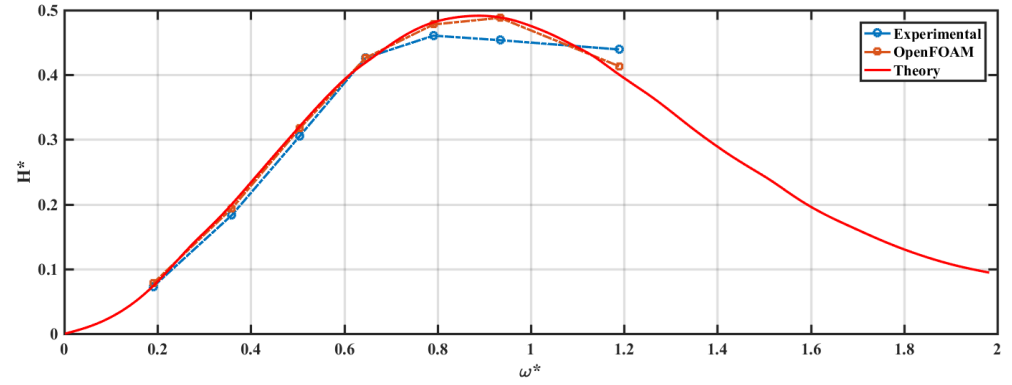

Figure F-9 Non-dimensional wave height vs non-dimensional frequency under heave motion, Draft =0.5 cylinder height, Amplitude =0.03m

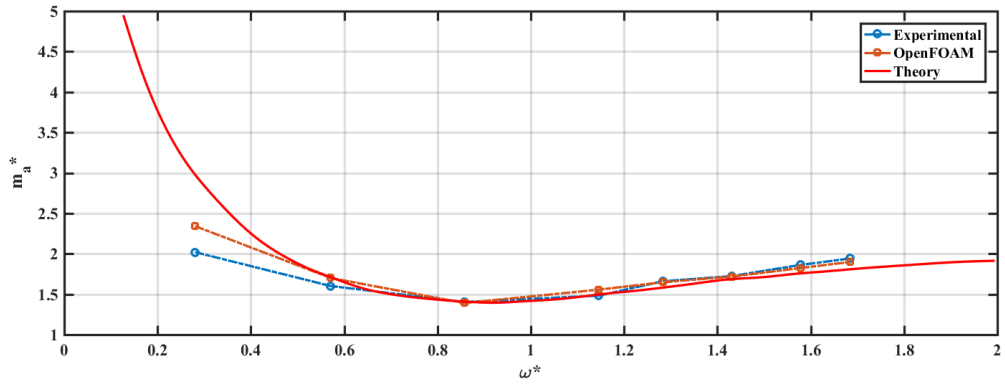

Figure F-10 Non-dimensional added mass vs non-dimensional frequency under heave motion, Draft =0.25 cylinder height, Amplitude =0.01m

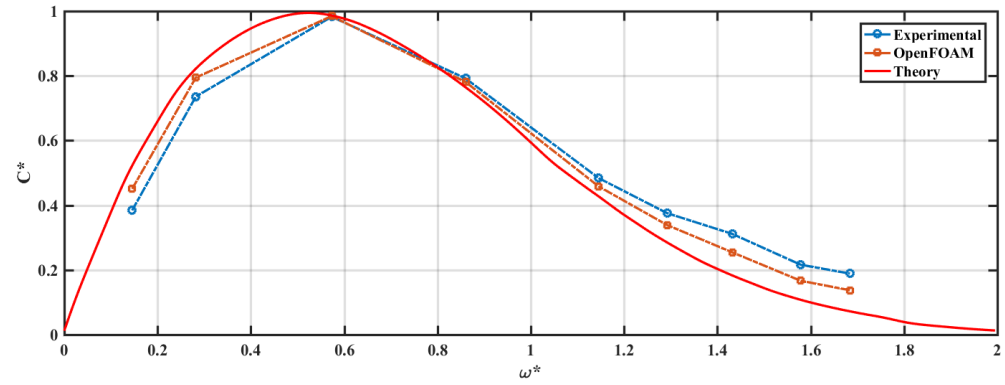

Figure F-11 Non-dimensional damping vs non-dimensional frequency under heave motion, Draft =0.25 cylinder height, Amplitude =0.01m

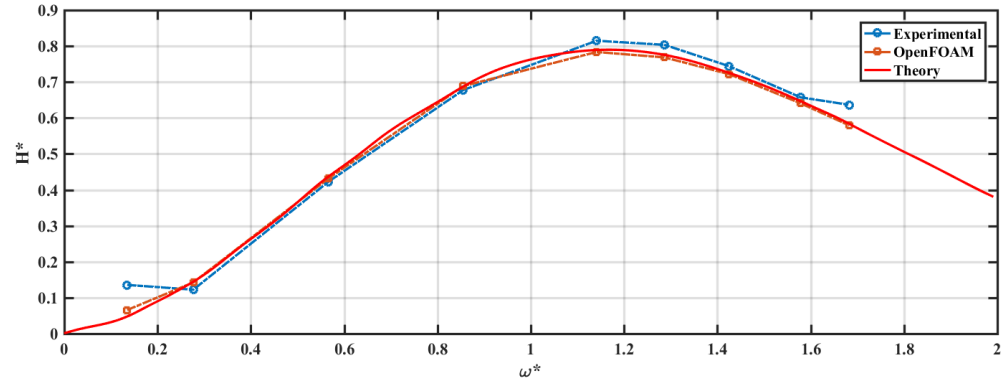

Figure F-12 Non-dimensional wave height vs non-dimensional frequency under heave motion, Draft =0.25 cylinder height, Amplitude =0.01m

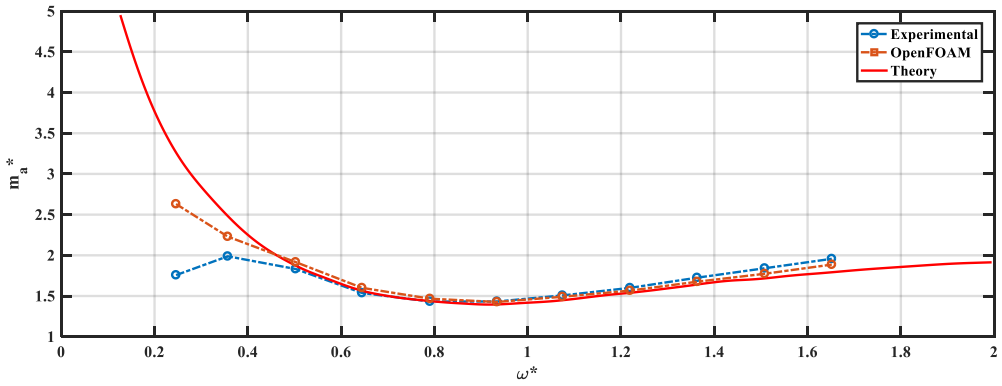

Figure F-13 Non-dimensional added mass vs non-dimensional frequency under heave motion,

Draft =0.25 cylinder height, Amplitude =0.02m

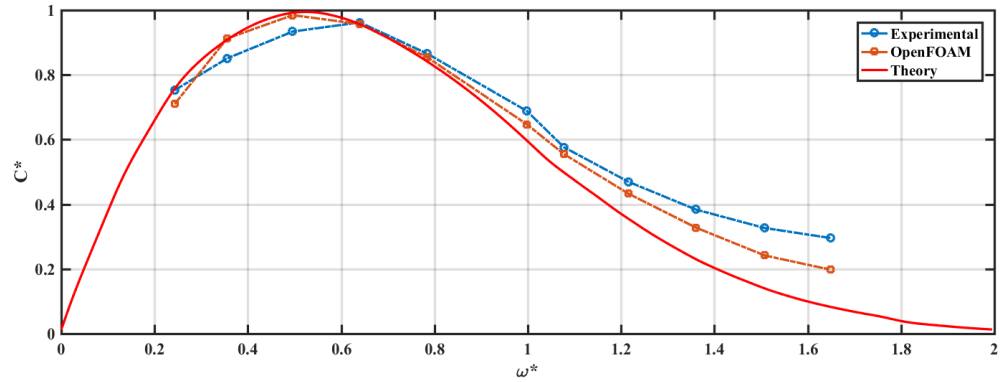

Figure F-14 Non-dimensional damping vs non-dimensional frequency under heave motion,

Draft =0.25 cylinder height, Amplitude =0.02m

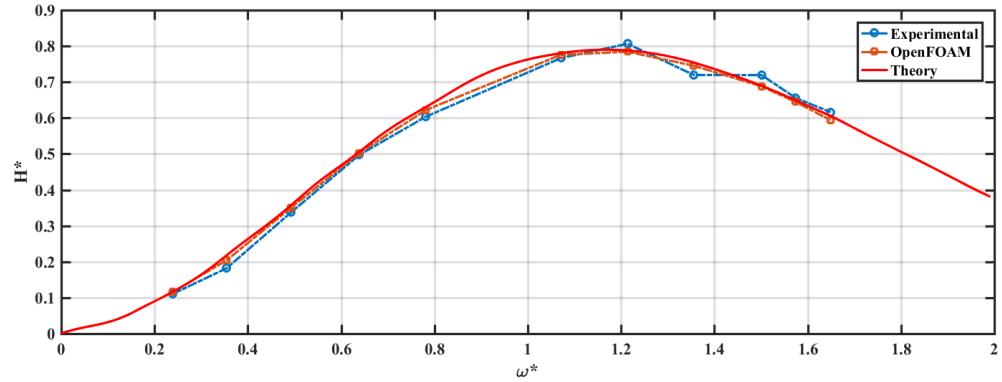

Figure F-15 Non-dimensional wave height vs non-dimensional frequency under heave motion, Draft =0.25 cylinder height, Amplitude =0.02m

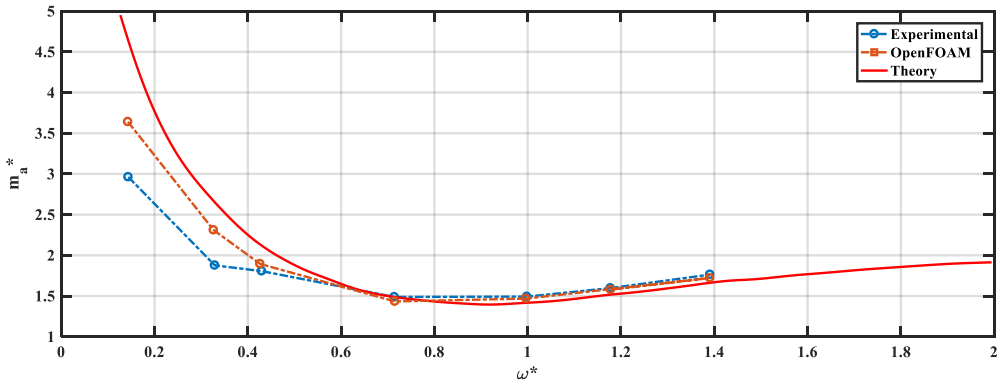

Figure F-16 Non-dimensional added mass vs non-dimensional frequency under heave motion, Draft =0.25 cylinder height, Amplitude =0.03m

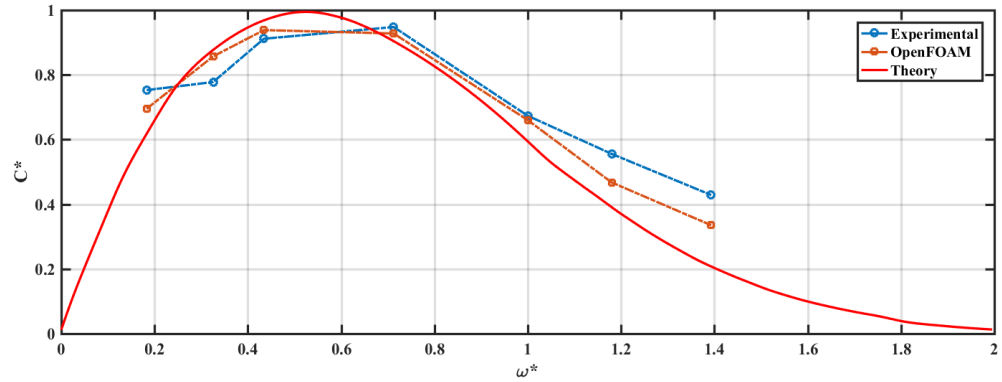

Figure F-17 Non-dimensional damping vs non-dimensional frequency under heave motion, Draft =0.25 cylinder height, Amplitude =0.03m

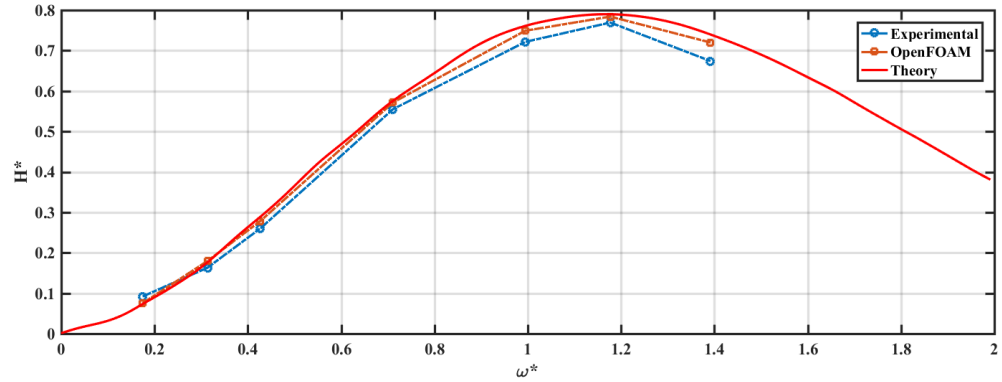

Figure F-18 Non-dimensional wave height vs non-dimensional frequency under heave motion, Draft =0.25 cylinder height, Amplitude =0.03m

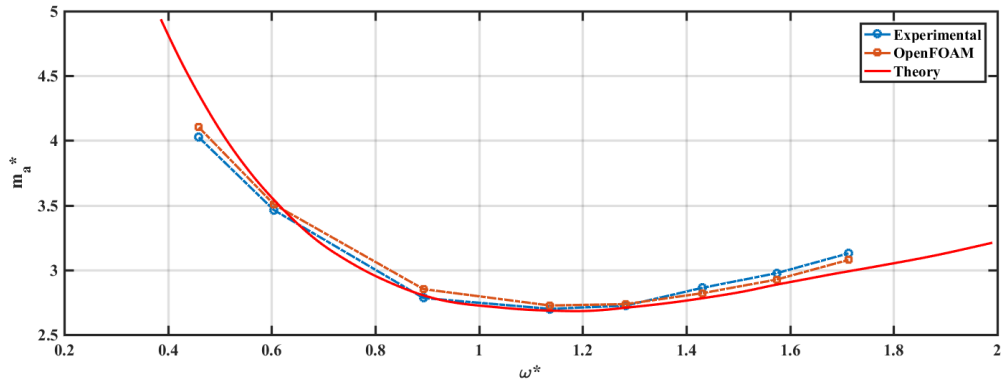

Figure F-19 Non-dimensional added mass vs non-dimensional frequency under heave motion,

Draft =1/8 cylinder height, Amplitude =0.01m

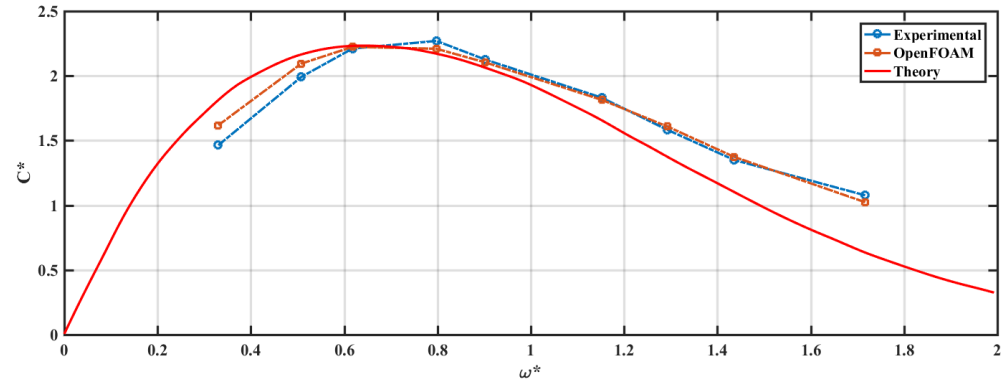

Figure F-20 Non-dimensional damping vs non-dimensional frequency under heave motion,

Draft =1/8 cylinder height, Amplitude =0.01m

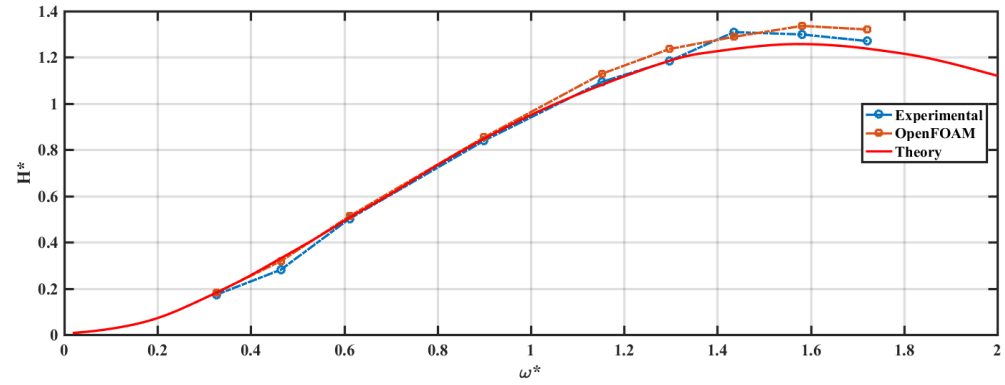

Figure F-21 Non-dimensional height vs non-dimensional frequency under heave motion,

Draft =1/8 cylinder height, Amplitude =0.01m

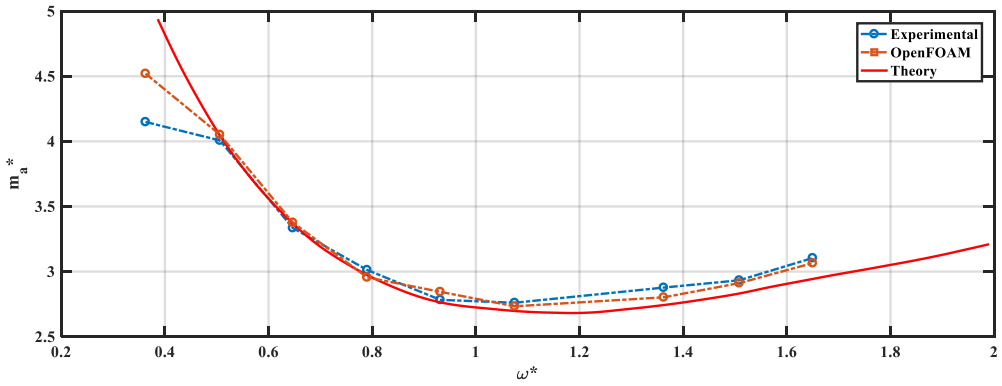

Figure F-22 Non-dimensional added mass vs non-dimensional frequency under heave motion, Draft =1/8 cylinder height, Amplitude =0.02m

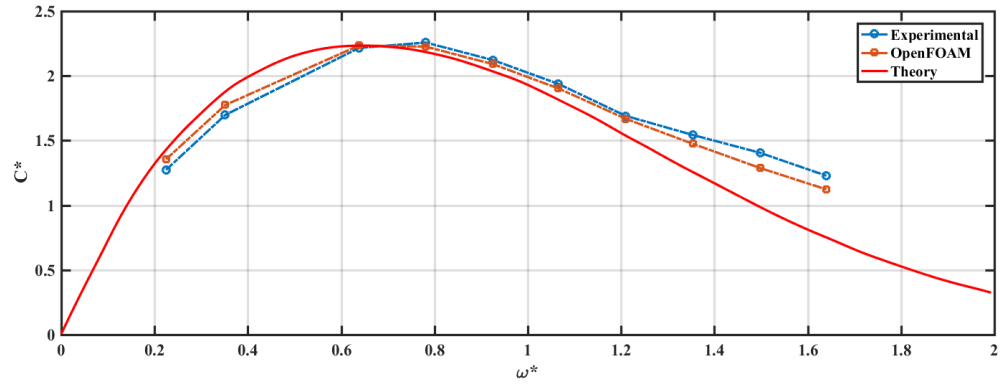

Figure F-23 Non-dimensional damping vs non-dimensional frequency under heave motion, Draft =1/8 cylinder height, Amplitude =0.02m

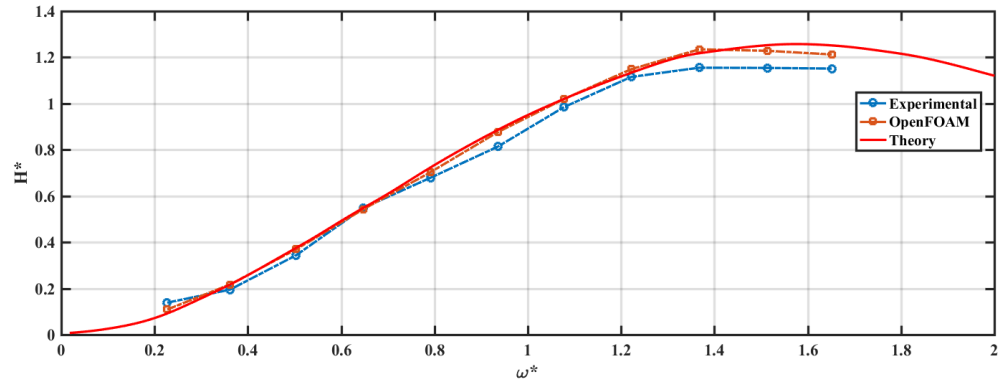

Figure F-24 Non-dimensional wave height vs non-dimensional frequency under heave motion, Draft =1/8 cylinder height, Amplitude =0.02m

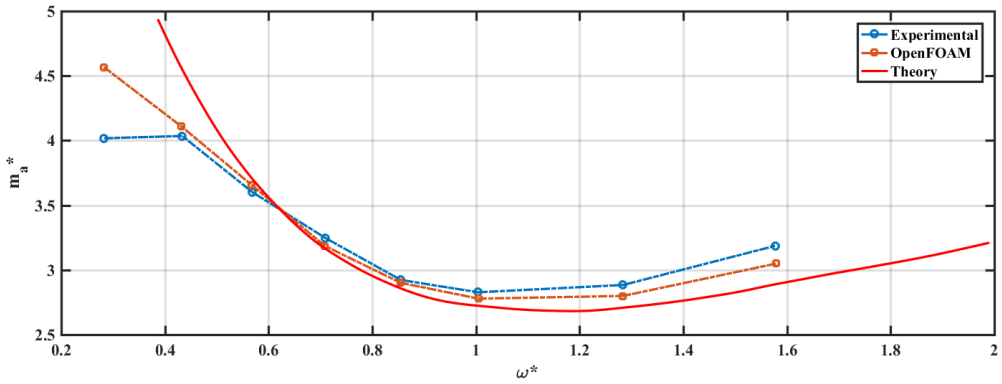

Figure F-25 Non-dimensional added mass vs non-dimensional frequency under heave motion, Draft =1/8 cylinder height, Amplitude =0.03m

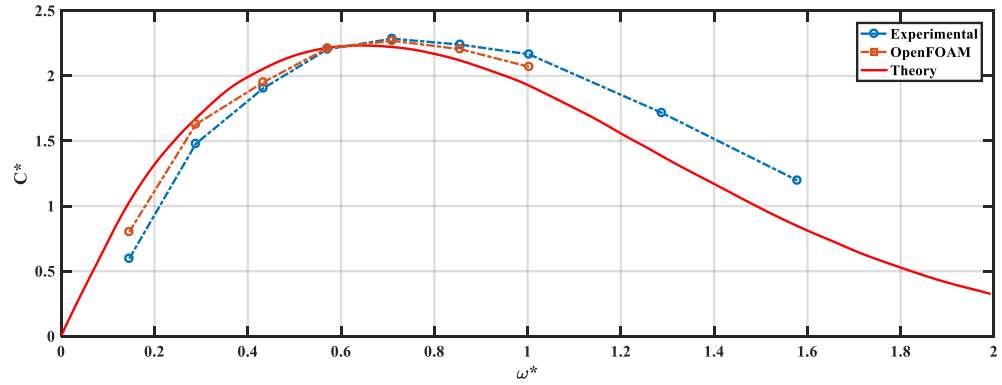

Figure F-26 Non-dimensional damping vs non-dimensional frequency under heave motion, Draft =1/8 cylinder height, Amplitude =0.03m

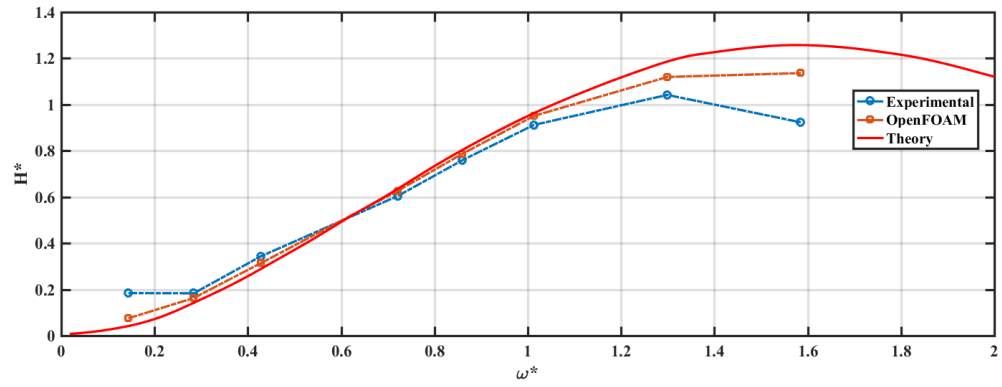

Figure F-27 Non-dimensional wave height vs non-dimensional frequency under heave motion, Draft =1/8 cylinder height, Amplitude =0.03m

Appendix F-2 Results from rectangular cylinder in sway

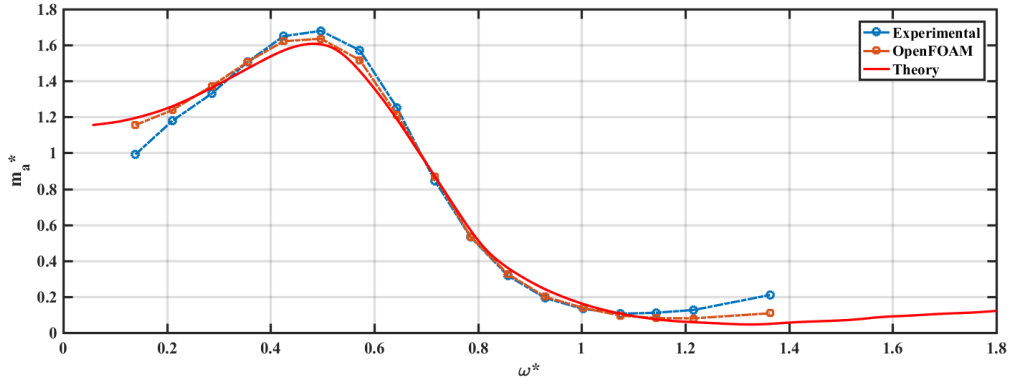

Figure F-28 Non-dimensional added mass vs non-dimensional frequency under sway motion,

Draft =1/2 cylinder height, Amplitude =0.01m

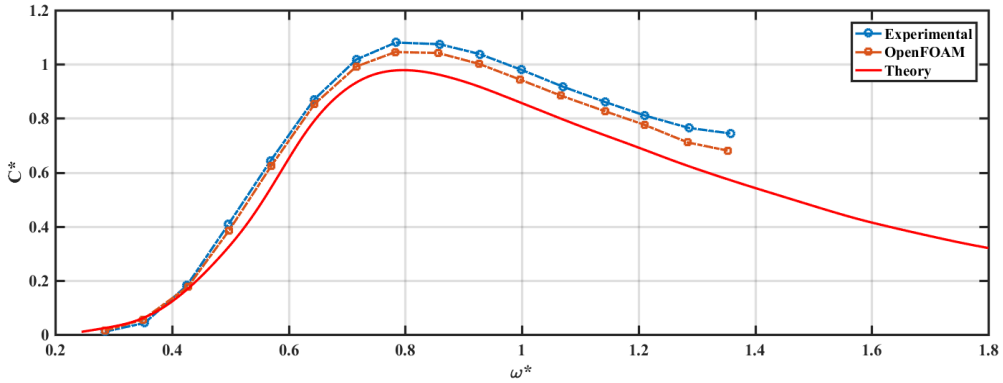

Figure F-29 Non-dimensional damping vs non-dimensional frequency under sway motion,

Draft =1/2 cylinder height, Amplitude =0.01m

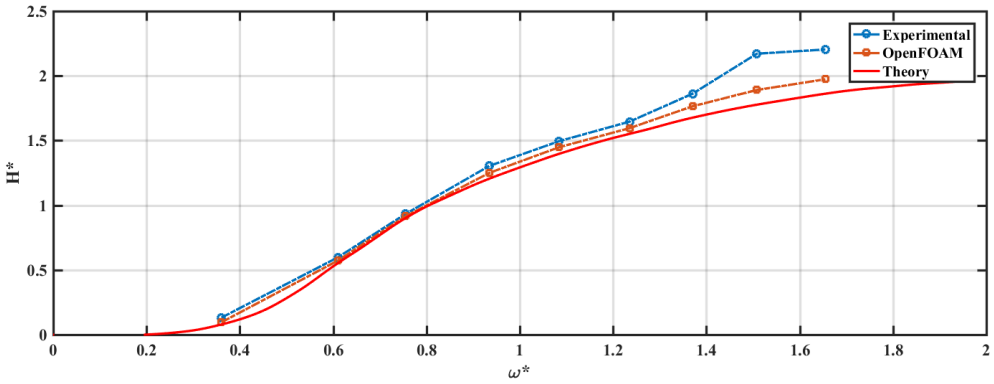

Figure F-30 Non-dimensional wave height vs non-dimensional frequency under sway motion, Draft =1/2 cylinder height, Amplitude =0.01m

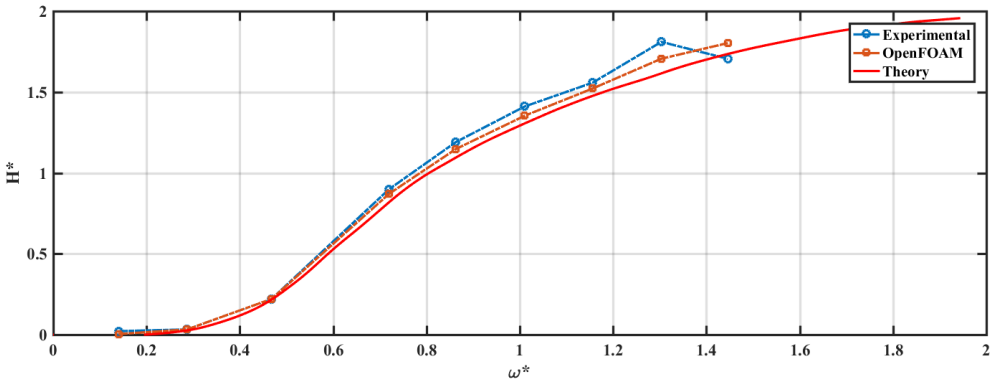

Figure F-31 Non-dimensional wave height vs non-dimensional frequency under sway motion, Draft =1/2 cylinder height, Amplitude =0.02m

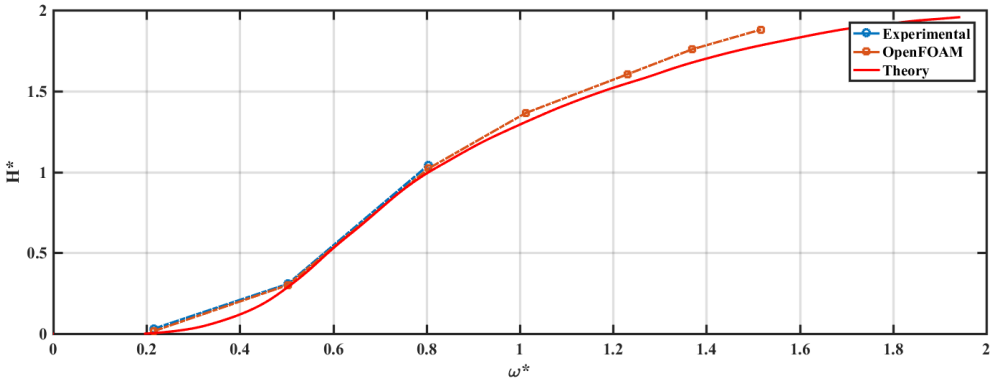

Figure F-32 Non-dimensional wave height vs non-dimensional frequency under sway motion, Draft =1/2 cylinder height, Amplitude =0.03m

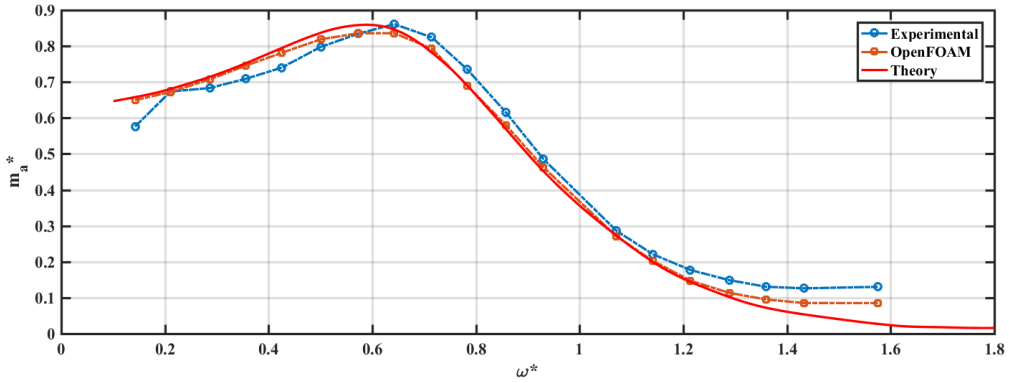

Figure F-33 Non-dimensional added mass vs non-dimensional frequency under sway motion, Draft =1/4 cylinder height, Amplitude =0.01m

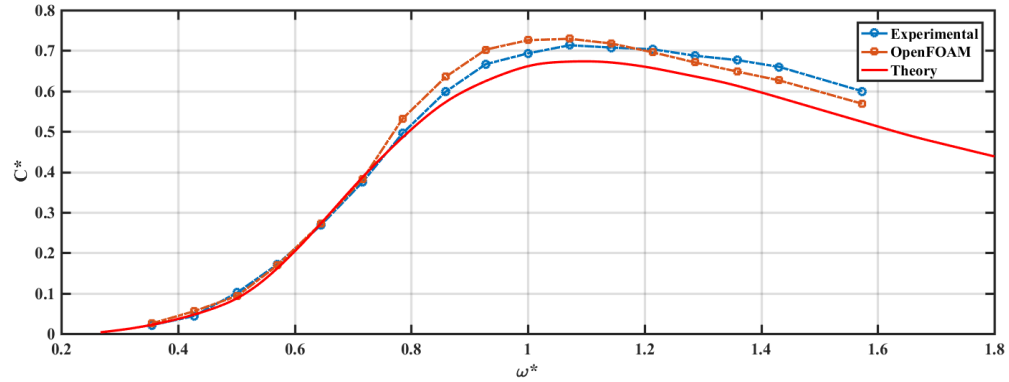

Figure F-34 Non-dimensional damping vs non-dimensional frequency under sway motion, Draft =1/4 cylinder height, Amplitude =0.01m

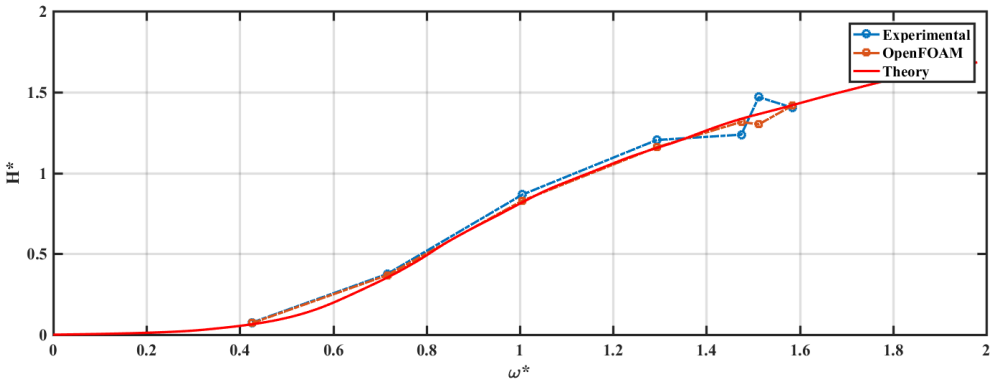

Figure F-35 Non-dimensional wave height vs non-dimensional frequency under sway motion, Draft =1/4 cylinder height, Amplitude =0.01m

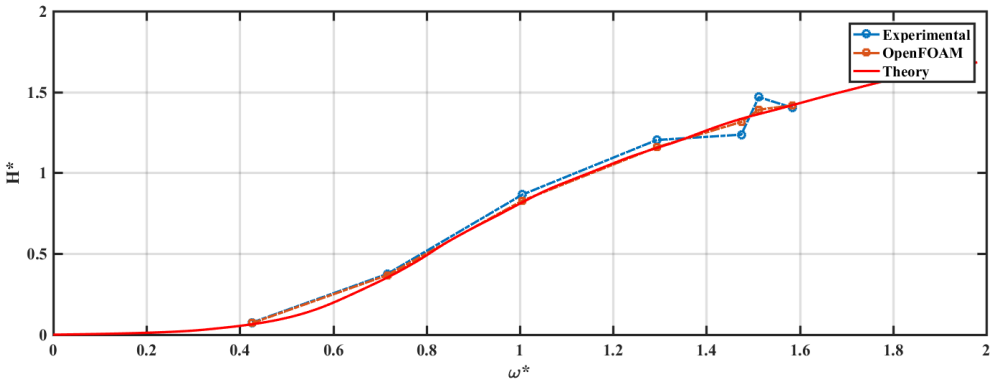

Figure F-36 Non-dimensional wave height vs non-dimensional frequency under sway motion, Draft =1/4 cylinder height, Amplitude =0.02m

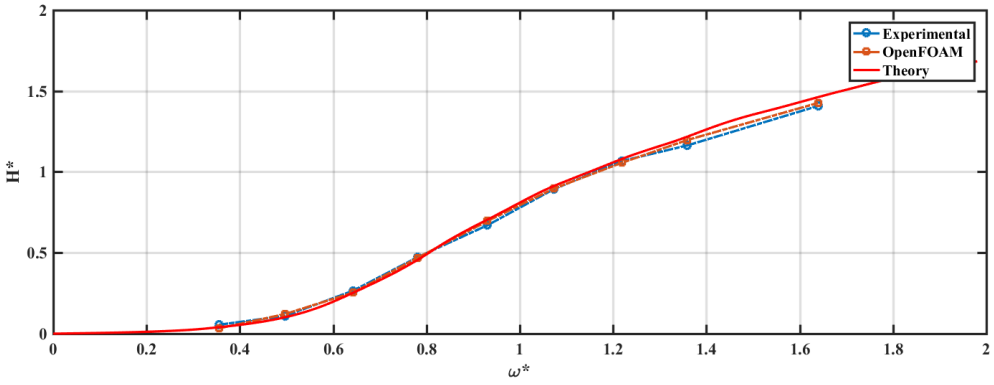

Figure F-37 Non-dimensional wave height vs non-dimensional frequency under sway motion, Draft =1/4 cylinder height, Amplitude =0.03m

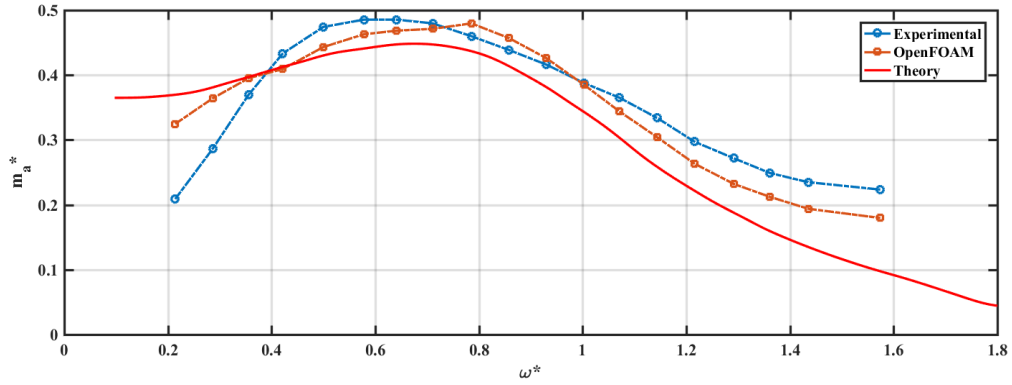

Figure F-38 Non-dimensional added mass vs non-dimensional frequency under sway motion,

Draft =1/8 cylinder height, Amplitude =0.01m

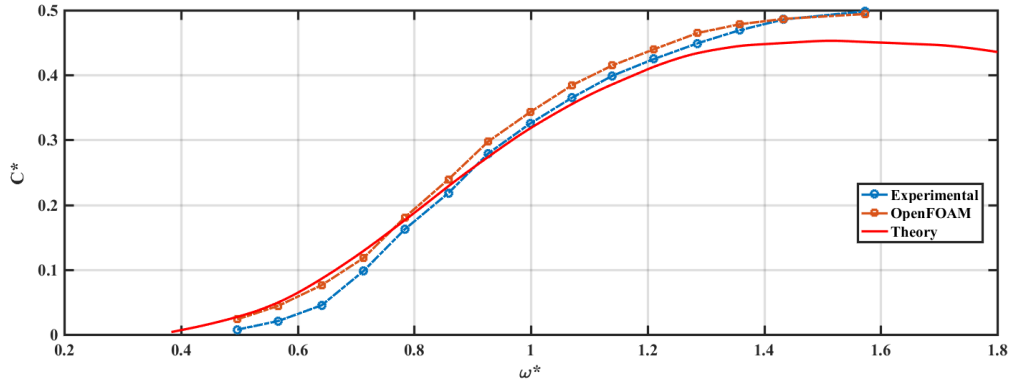

Figure F-39 Non-dimensional damping vs non-dimensional frequency under sway motion,

Draft =1/8 cylinder height, Amplitude =0.01m

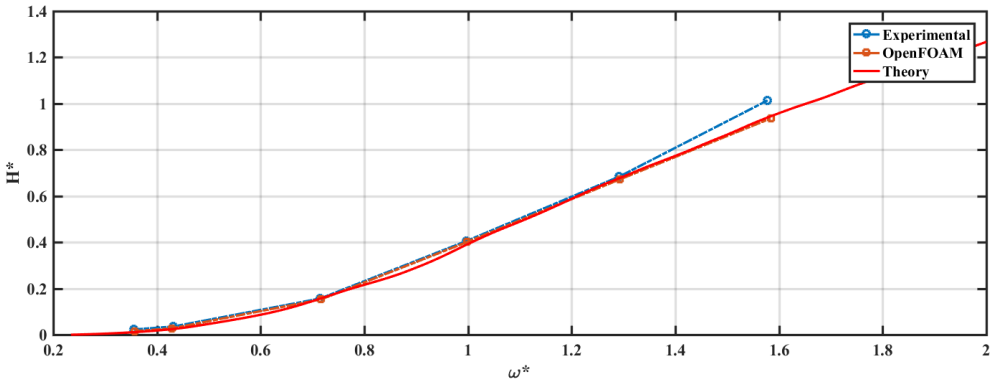

Figure F-40 Non-dimensional wave height vs non-dimensional frequency under sway motion, Draft =1/8 cylinder height, Amplitude =0.01m

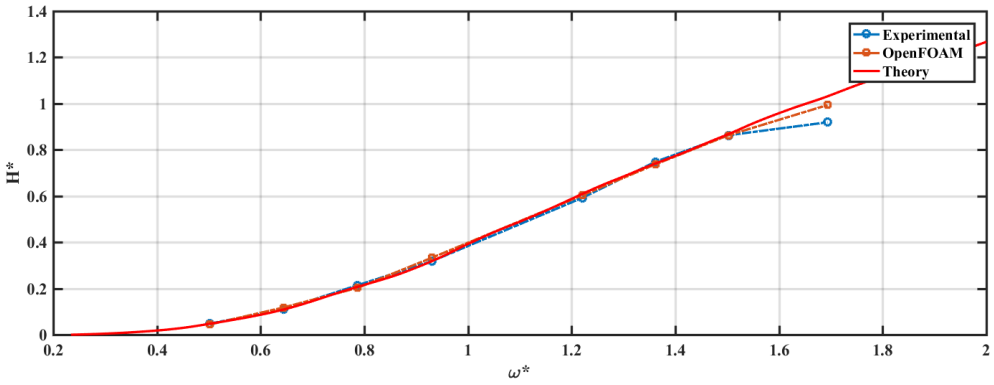

Figure F-41 Non-dimensional wave height vs non-dimensional frequency under sway motion, Draft =1/8 cylinder height, Amplitude =0.02m

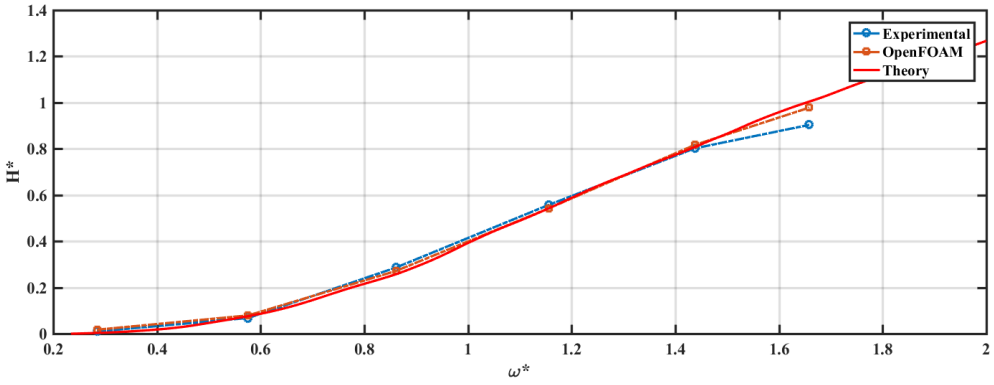

Figure F-42 Non-dimensional wave height vs non-dimensional frequency under sway motion, Draft =1/8 cylinder height, Amplitude =0.03m

Appendix F-3 Results from rectangular cylinder in roll

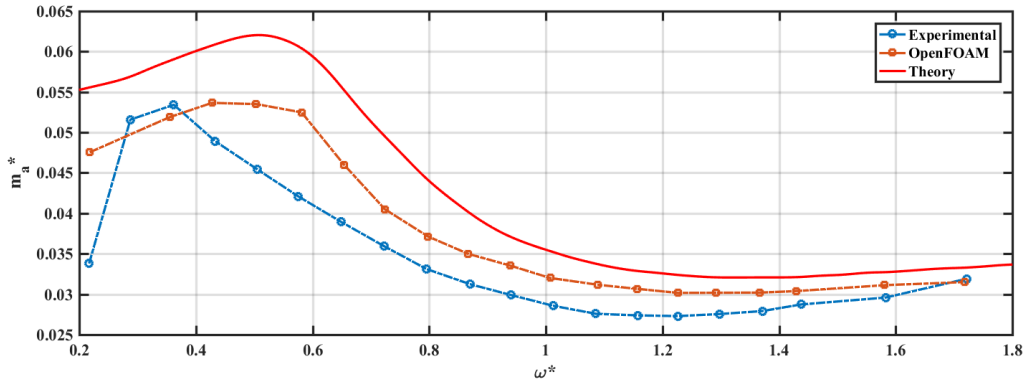

Figure F-43 Non-dimensional added mass vs non-dimensional frequency under roll motion,

Draft =1/2 cylinder height, Amplitude =0.05 rads

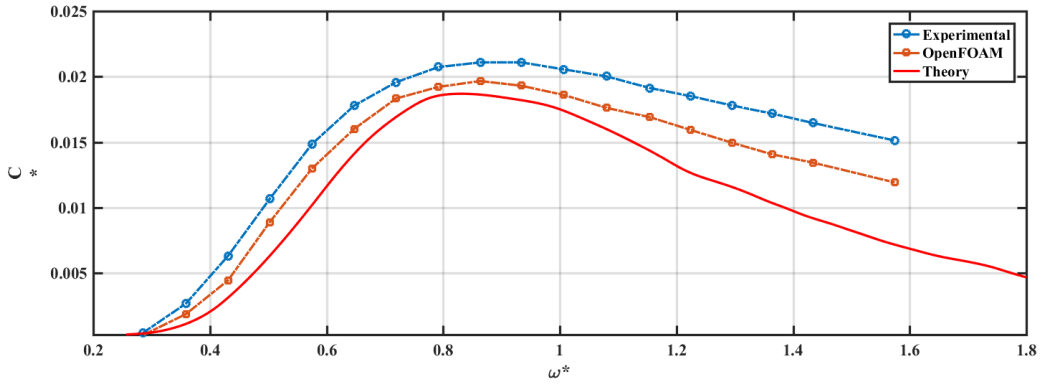

Figure F-44 Non-dimensional damping vs non-dimensional frequency under roll motion,

Draft =1/2 cylinder height, Amplitude =0.05 rads

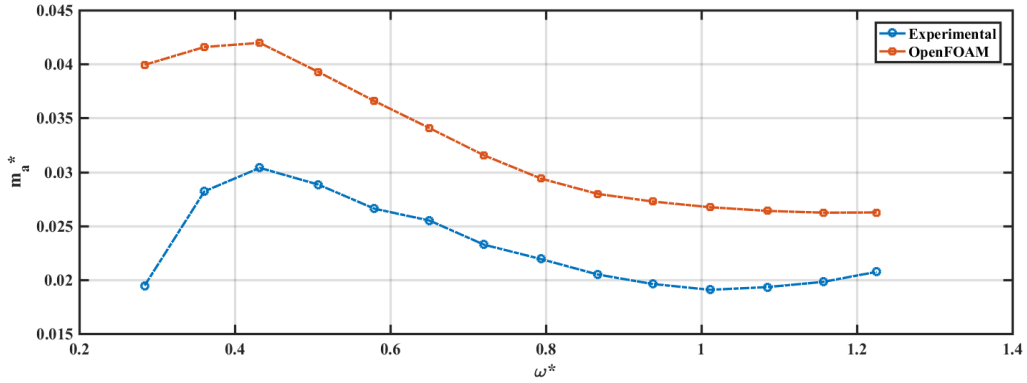

Figure F-45 Non-dimensional added mass vs non-dimensional frequency under roll motion, Draft =1/2 cylinder height, Amplitude =0.2 rads

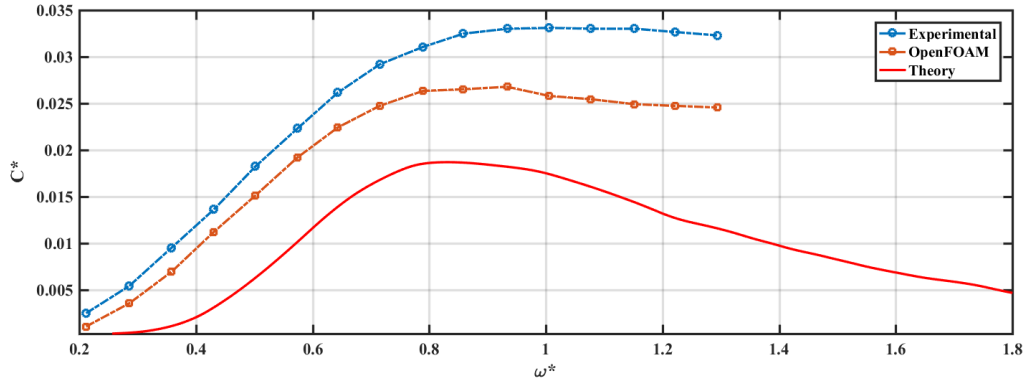

Figure F-46 Non-dimensional damping vs non-dimensional frequency under roll motion, Draft =1/2 cylinder height, Amplitude =0.2 rads

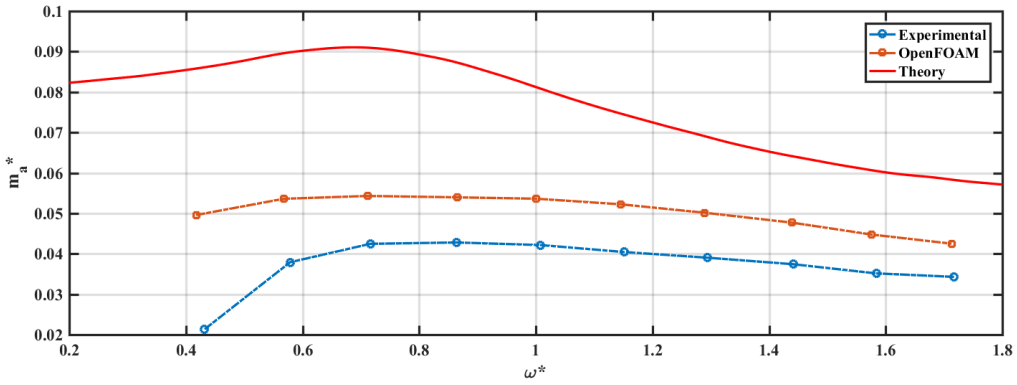

Figure F-47 Non-dimensional added mass vs non-dimensional frequency under roll motion,

Draft =1/4 cylinder height, Amplitude =0.05 rads

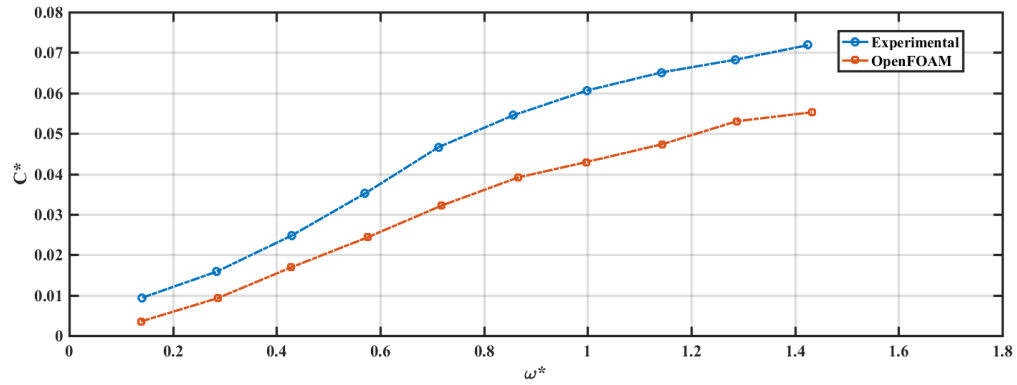

Figure F-48 Non-dimensional damping vs non-dimensional frequency under roll motion,

Draft =1/4 cylinder height, Amplitude =0.05 rads

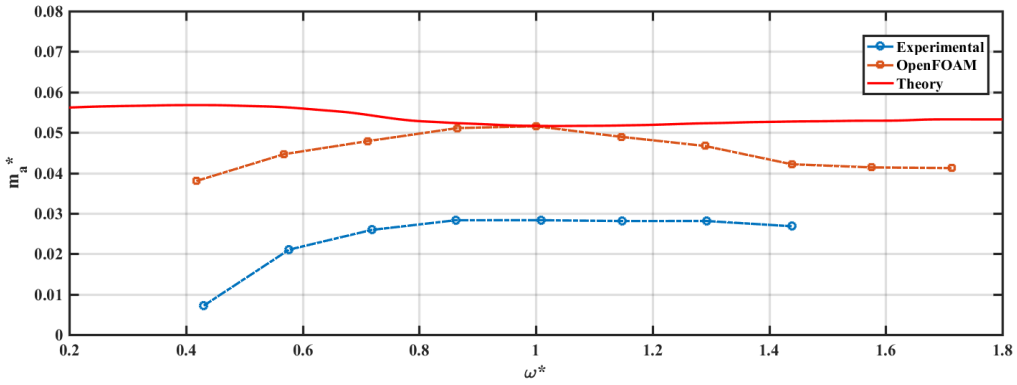

Figure F-49 Non-dimensional added mass vs non-dimensional frequency under roll motion, Draft =1/4 cylinder height, Amplitude =0.2 rads

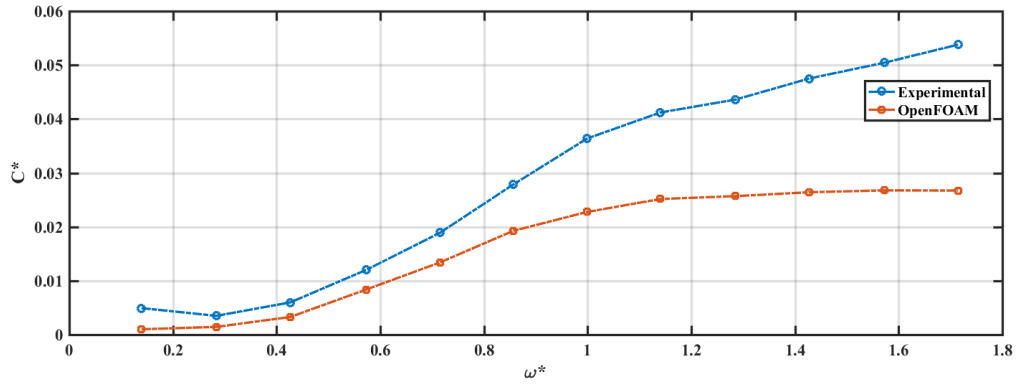

Figure F-50 Non-dimensional damping vs non-dimensional frequency under roll motion, Draft =1/4 cylinder height, Amplitude =0.2 rads

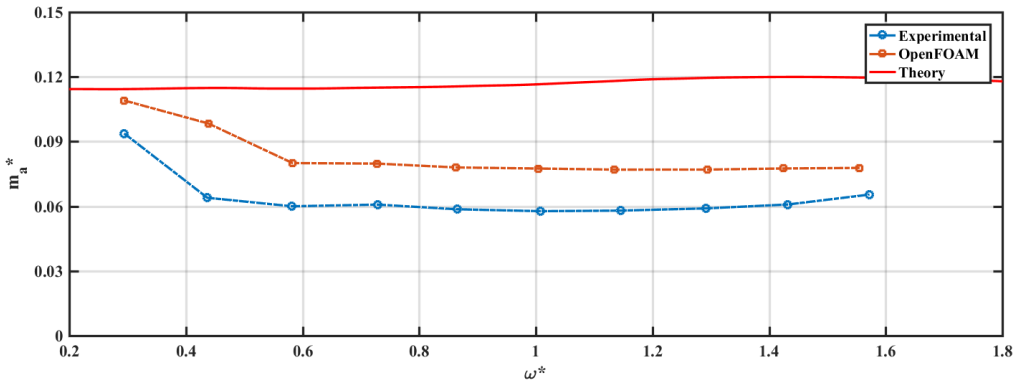

Figure F-51 Non-dimensional added mass vs non-dimensional frequency under roll motion,

Draft =1/8 cylinder height, Amplitude =0.05 rads

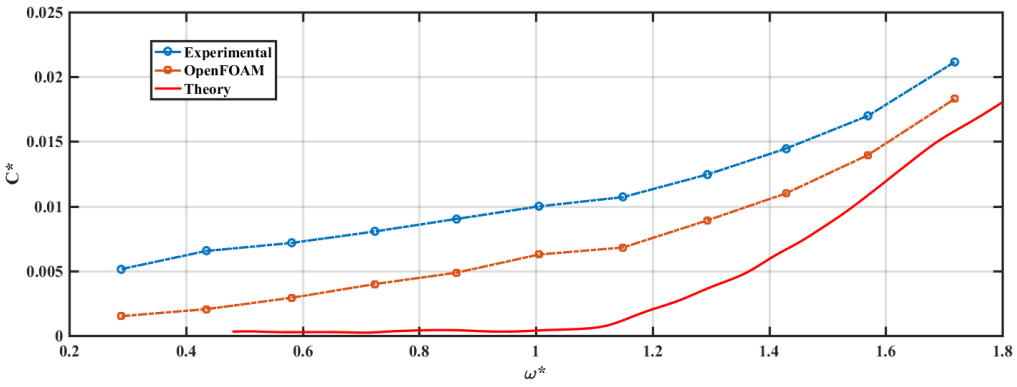

Figure F-52 Non-dimensional damping vs non-dimensional frequency under roll motion,

Draft =1/8 cylinder height, Amplitude =0.05 rads

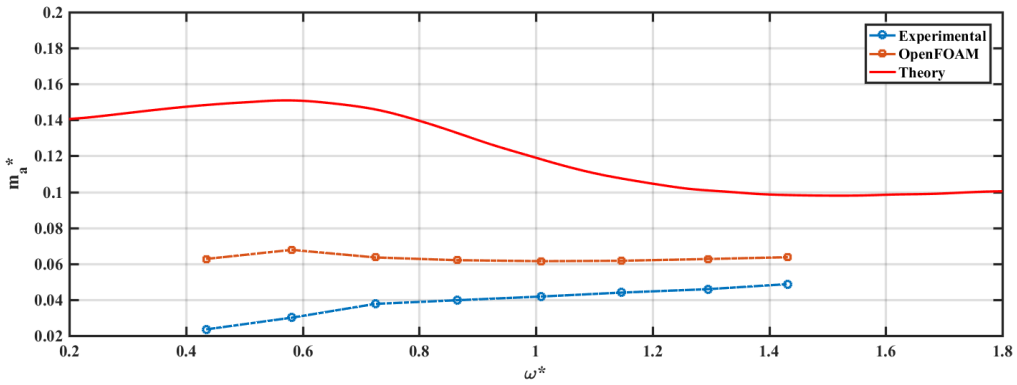

Figure F-53 Non-dimensional added mass vs non-dimensional frequency under roll motion, Draft =1/8 cylinder height, Amplitude =0.2 rads

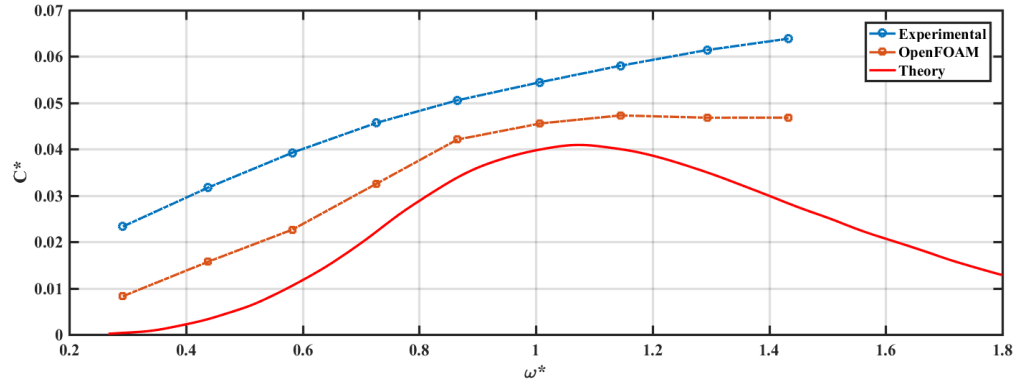

Figure F-54 Non-dimensional damping vs non-dimensional frequency under roll motion, Draft =1/8 cylinder height, Amplitude =0.2 rads

G. Appendix G-1 Results from hemisphere cylinder in heave

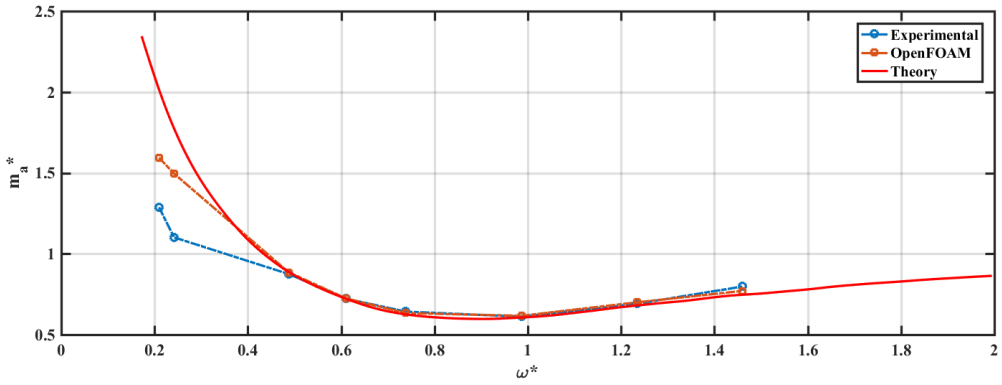

Figure G-1 Non-dimensional added mass vs non-dimensional frequency under heave motion,

Amplitude =0.01m

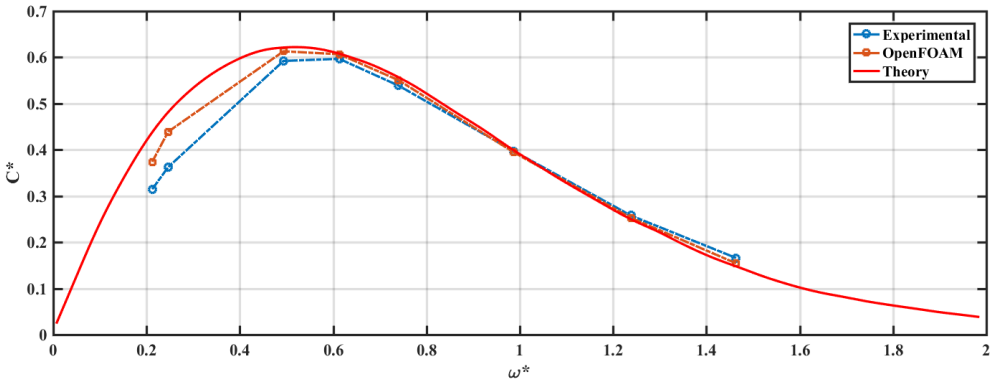

Figure G-2 Non-dimensional damping vs non-dimensional frequency under heave motion,

Amplitude =0.01m

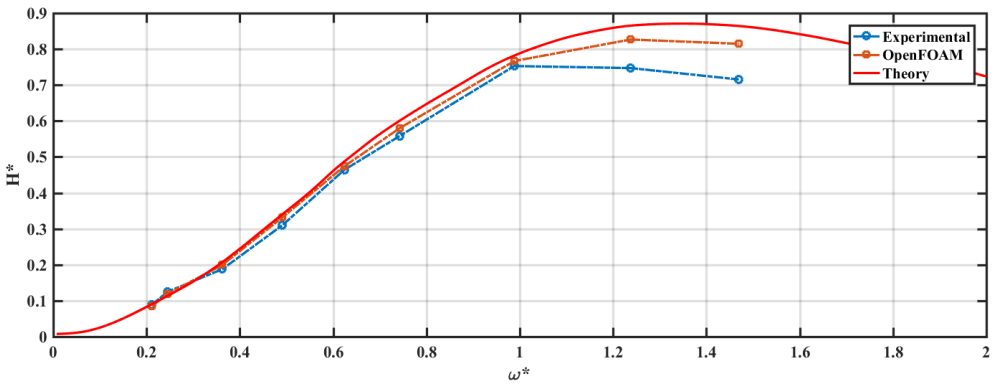

Figure G-3 Non-dimensional wave height vs non-dimensional frequency under heave motion,

Amplitude =0.01m

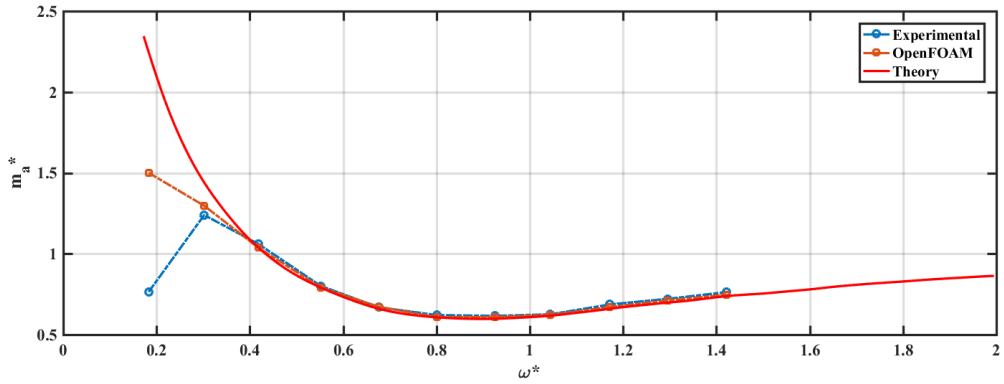

Figure G-4 Non-dimensional added mass vs non-dimensional frequency under heave motion, Amplitude =0.02m

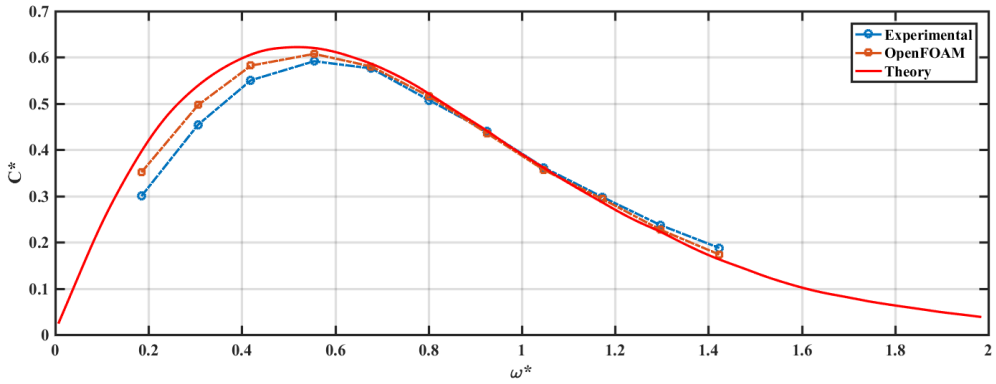

Figure G-5 Non-dimensional damping vs non-dimensional frequency under heave motion, Amplitude =0.02m

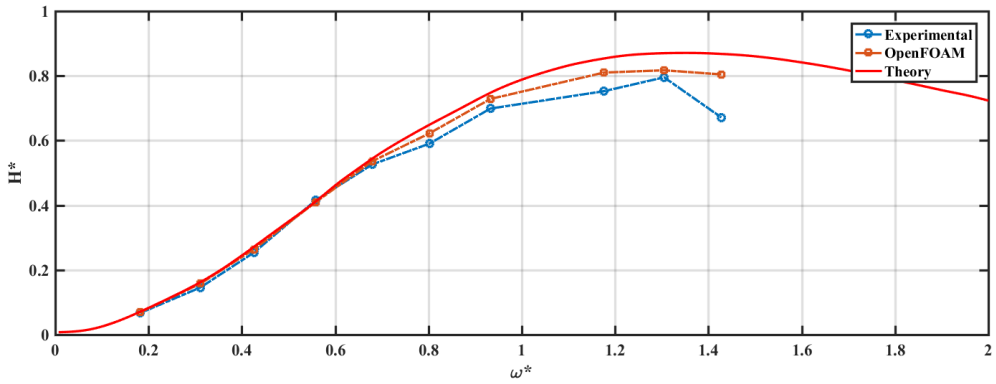

Figure G-6 Non-dimensional wave height vs non-dimensional frequency under heave motion, Amplitude =0.02m

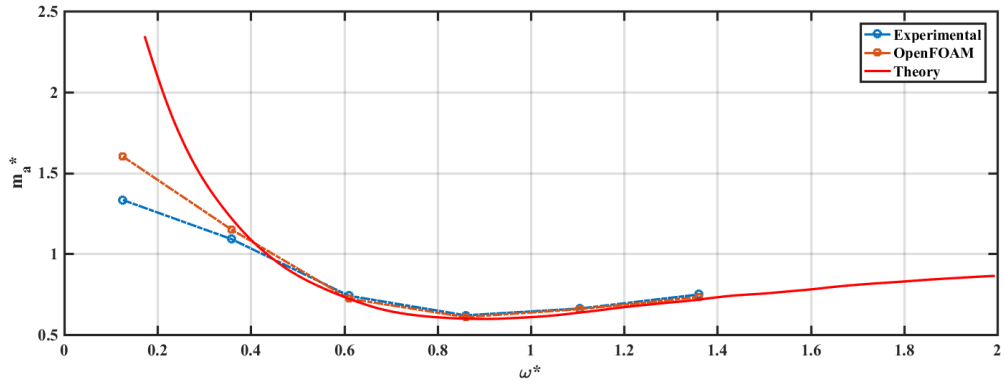

Figure G-7 Non-dimensional added mass vs non-dimensional frequency under heave motion, Amplitude =0.03m

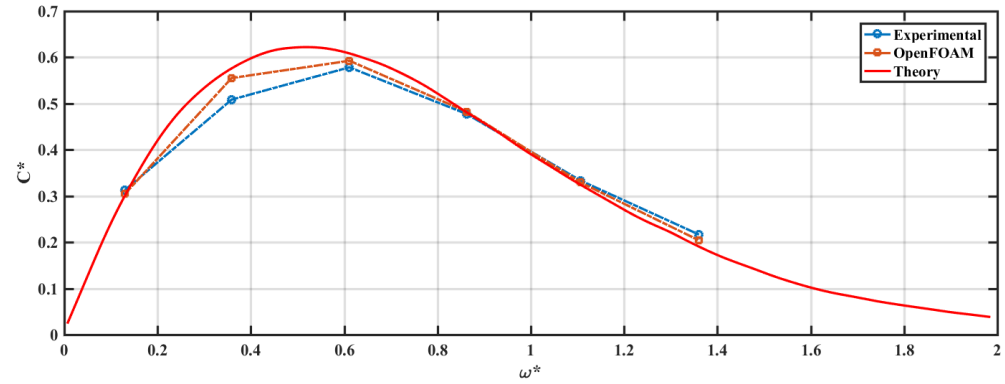

Figure G-8 Non-dimensional damping vs non-dimensional frequency under heave motion, Amplitude =0.03m

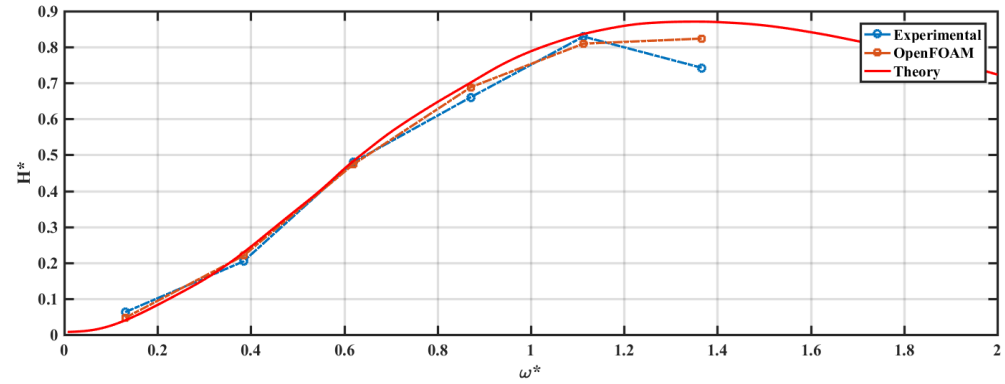

Figure G-9 Non-dimensional wave height vs non-dimensional frequency under heave motion, Amplitude =0.03m

Appendix G-2 Results from hemisphere cylinder in sway

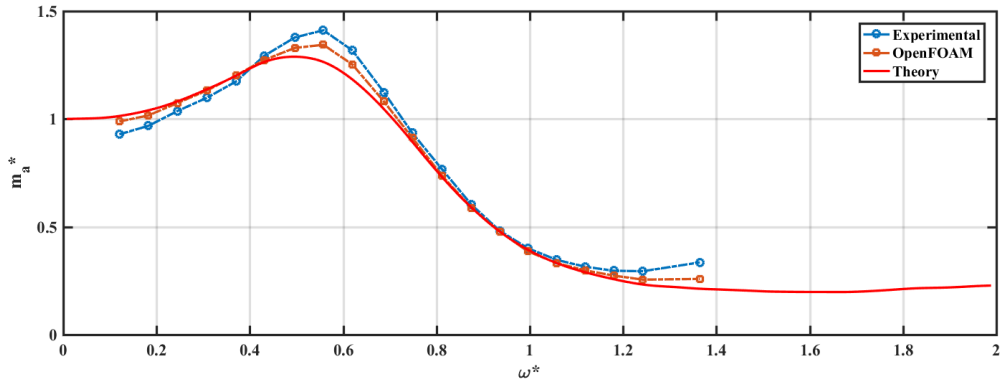

Figure G-10 Non-dimensional added mass vs non-dimensional frequency under sway motion, Amplitude =0.02m

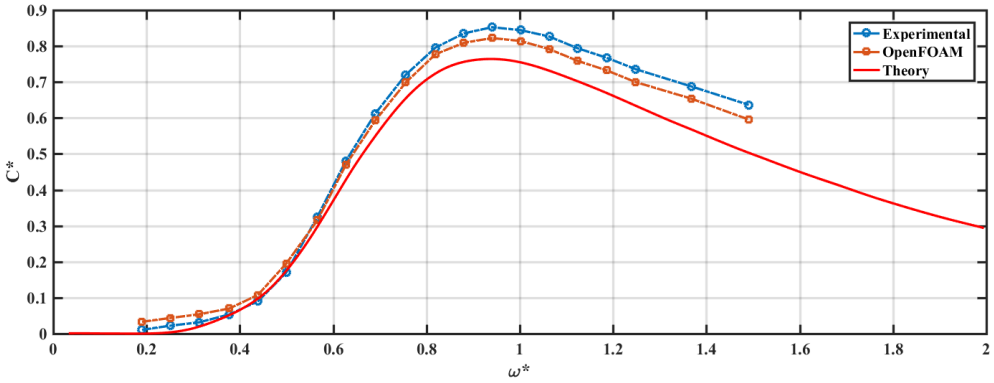

Figure G-11 Non-dimensional damping vs non-dimensional frequency under sway motion, Amplitude =0.02m

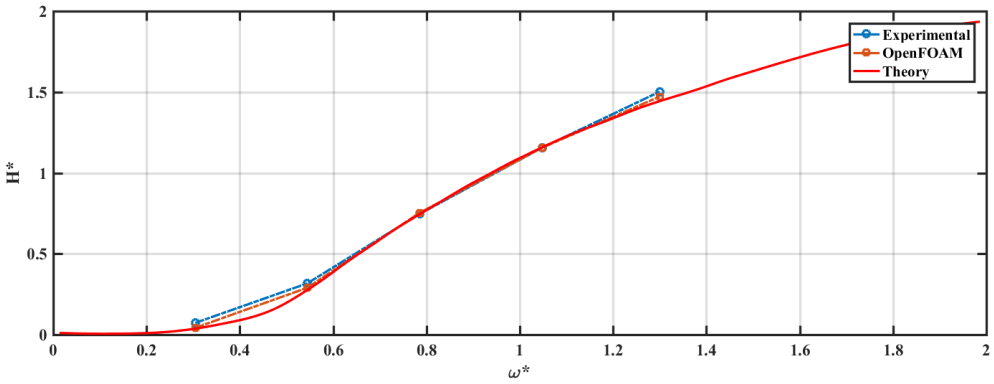

Figure G-12 Non-dimensional wave height vs non-dimensional frequency under sway motion, Amplitude =0.01m

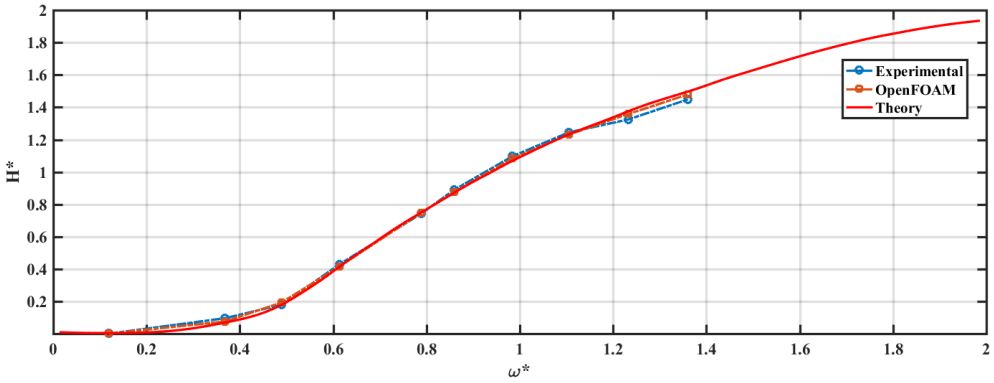

Figure G-13 Non-dimensional wave height vs non-dimensional frequency under sway motion, Amplitude =0.02m

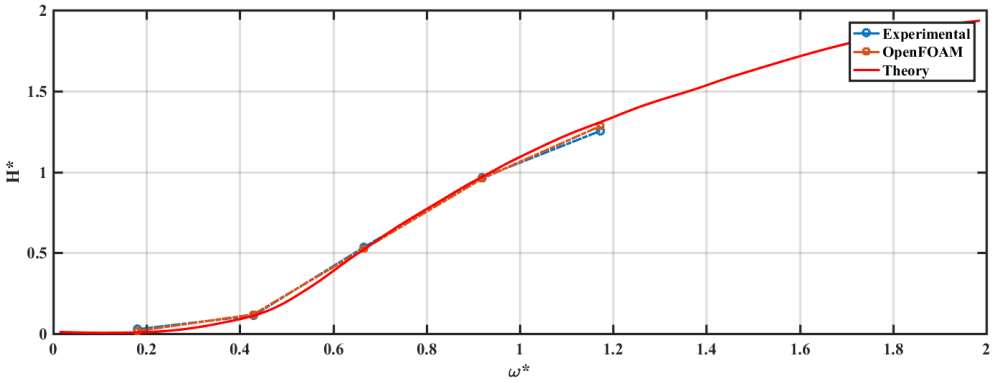

Figure G-14 Non-dimensional wave height vs non-dimensional frequency under sway motion, Amplitude =0.03m

Appendix G-3 Results from hemisphere cylinder in roll

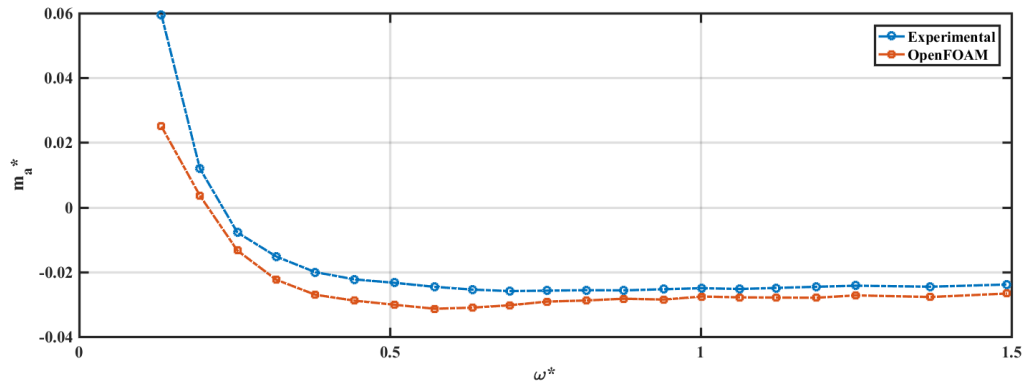

Figure G-15 Non-dimensional added mass vs non-dimensional frequency under roll motion, Amplitude =0.1rads

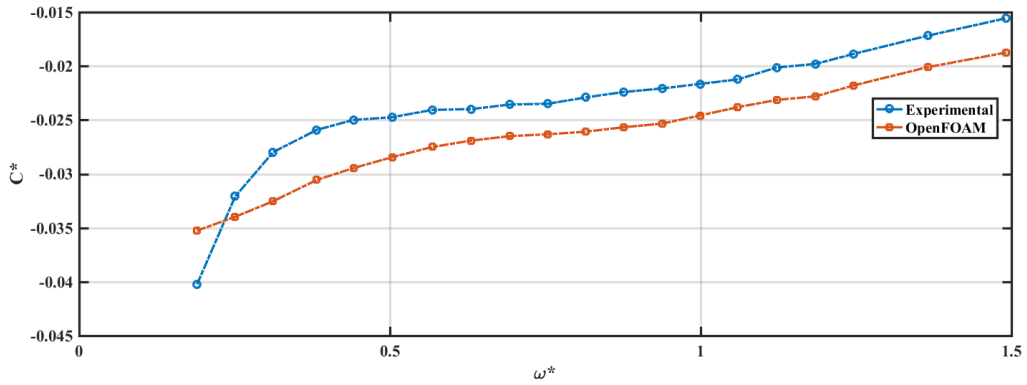

Figure G-16 Non-dimensional damping vs non-dimensional frequency under roll motion, Amplitude =0.1rads

H. Appendix H-1 Results from triangular cylinder in heave

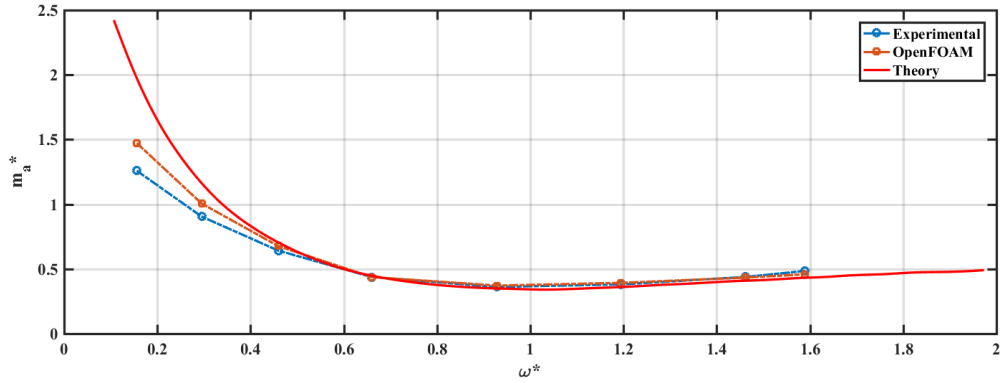

Figure H-1 Non-dimensional added mass vs non-dimensional frequency under heave motion,

Amplitude =0.01m

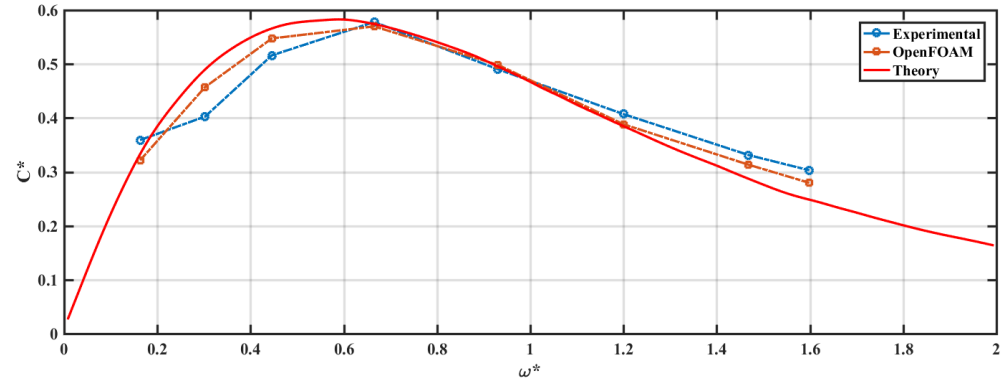

Figure H-2 Non-dimensional damping vs non-dimensional frequency under heave motion,

Amplitude =0.01m

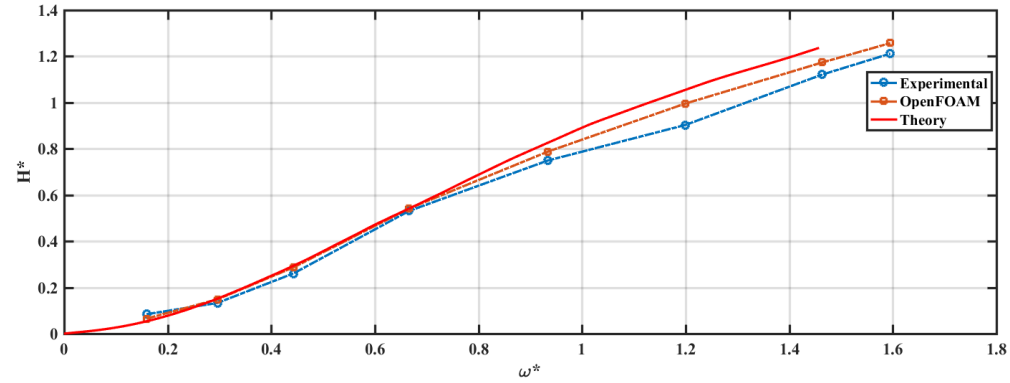

Figure H-3 Non-dimensional wave height vs non-dimensional frequency under heave motion,

Amplitude =0.01m

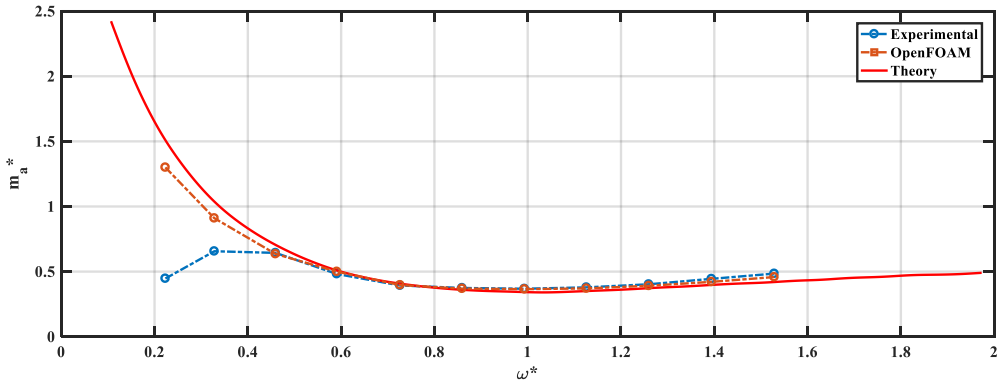

Figure H-4 Non-dimensional added mass vs non-dimensional frequency under heave motion, Amplitude =0.02m

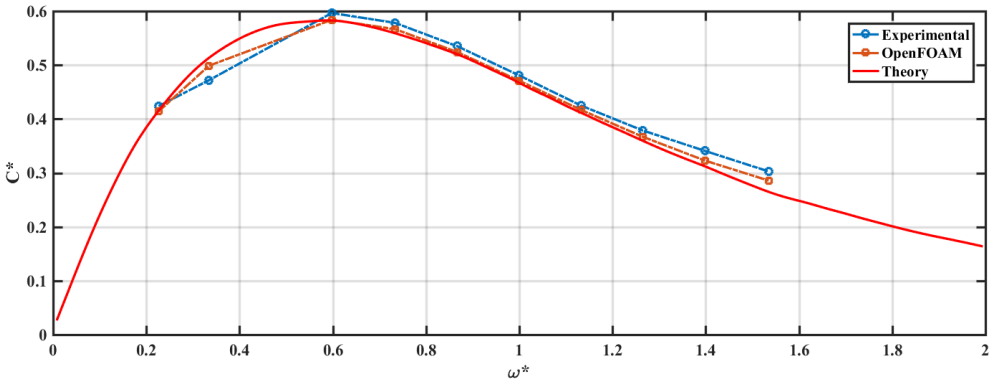

Figure H-5 Non-dimensional damping vs non-dimensional frequency under heave motion, Amplitude =0.02m

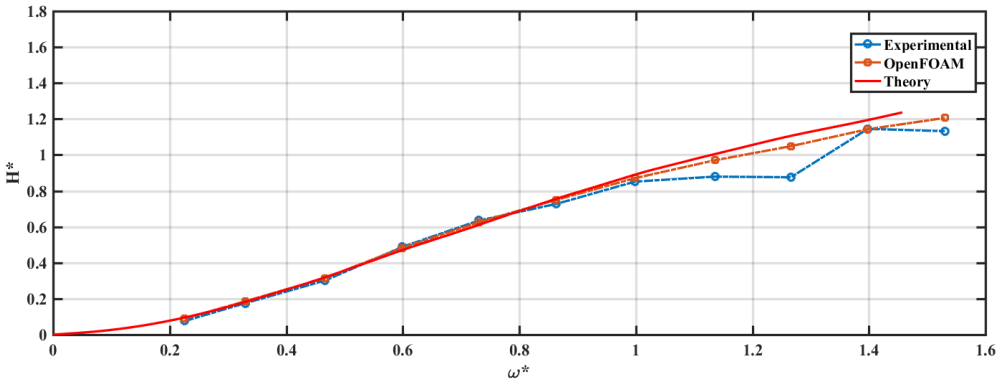

Figure H-6 Non-dimensional wave height vs non-dimensional frequency under heave motion, Amplitude =0.02m

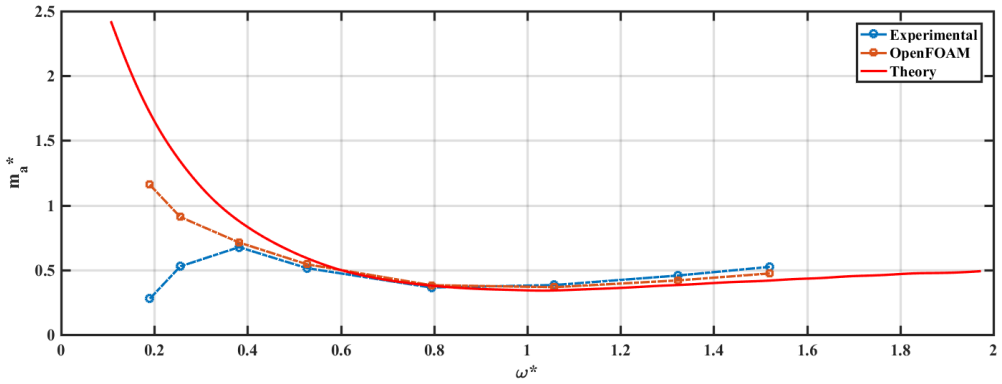

Figure H-7 Non-dimensional added mass vs non-dimensional frequency under heave motion, Amplitude =0.03m

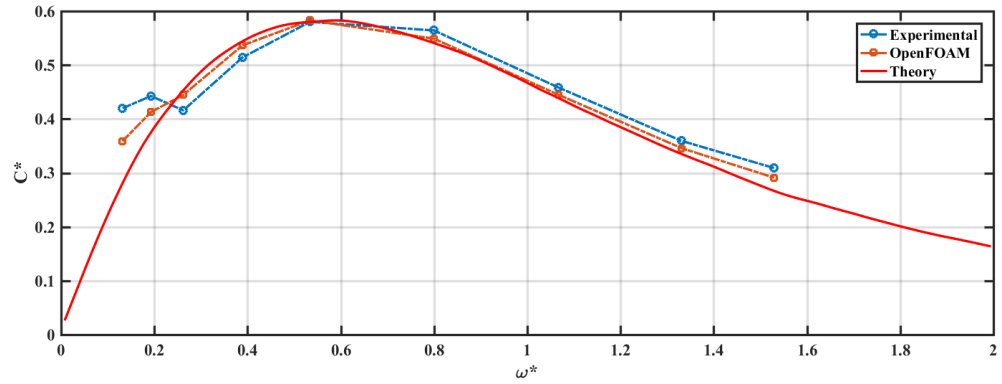

Figure H-8 Non-dimensional damping vs non-dimensional frequency under heave motion, Amplitude =0.03m

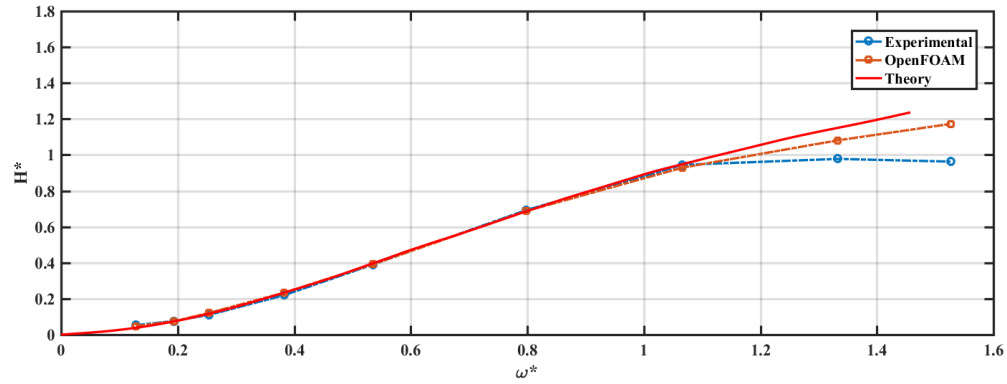

Figure H-9 Non-dimensional wave height vs non-dimensional frequency under heave motion, Amplitude =0.03m

Appendix H-2 Results from triangular cylinder in sway

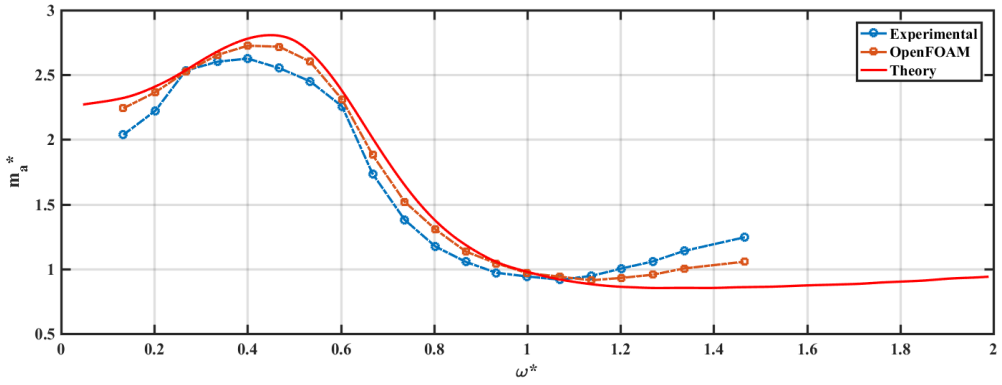

Figure H-10 Non-dimensional added mass vs non-dimensional frequency under sway motion,

Amplitude =0.02m

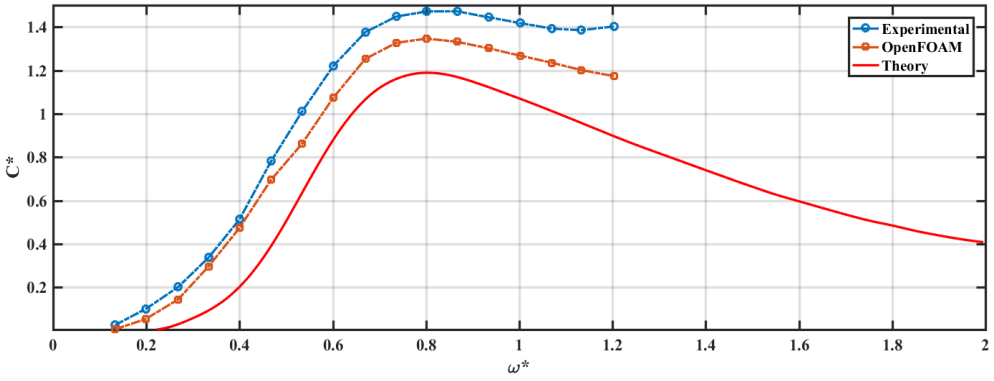

Figure H-11 Non-dimensional damping vs non-dimensional frequency under sway motion,

Amplitude =0.02m

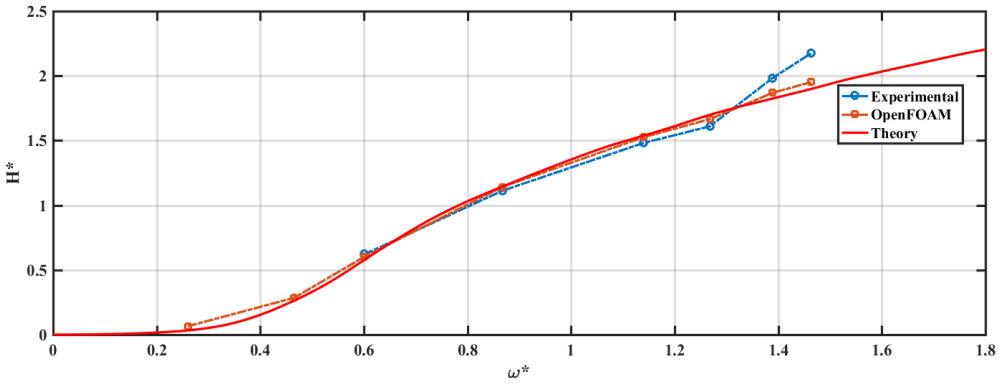

Figure H-12 Non-dimensional wave height vs non-dimensional frequency under sway motion,

Amplitude =0.01m

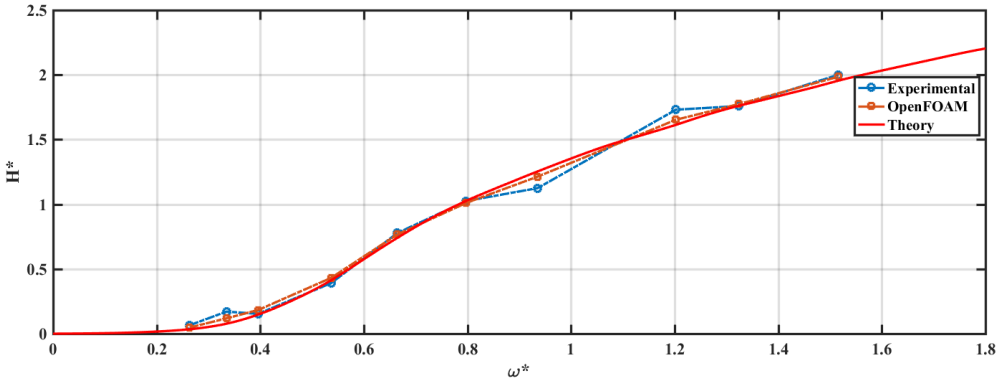

Figure H-13 Non-dimensional wave height vs non-dimensional frequency under sway motion,

Amplitude =0.02m

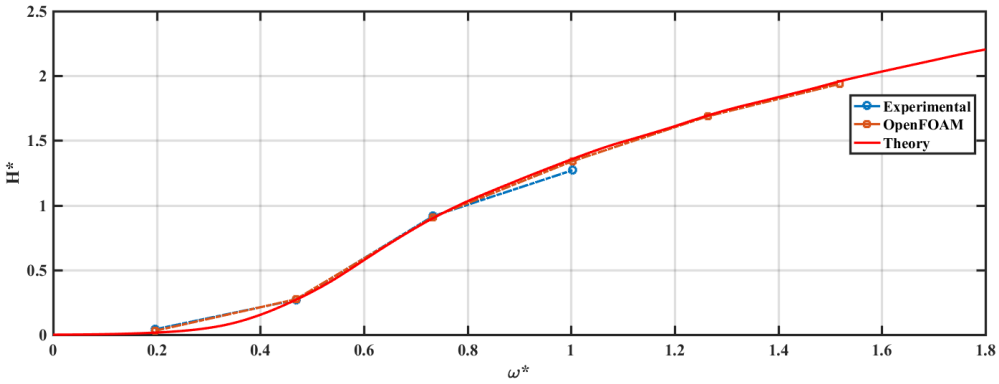

Figure H-14 Non-dimensional wave height vs non-dimensional frequency under sway motion,

Amplitude =0.03m

Appendix H-3 Results from triangular cylinder in roll

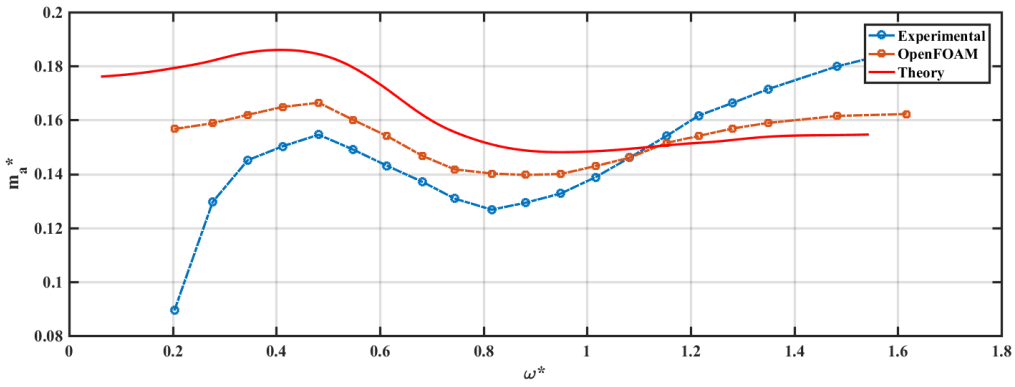

Figure H-15 Non-dimensional added mass vs non-dimensional frequency under roll motion,

Amplitude =0.1rads

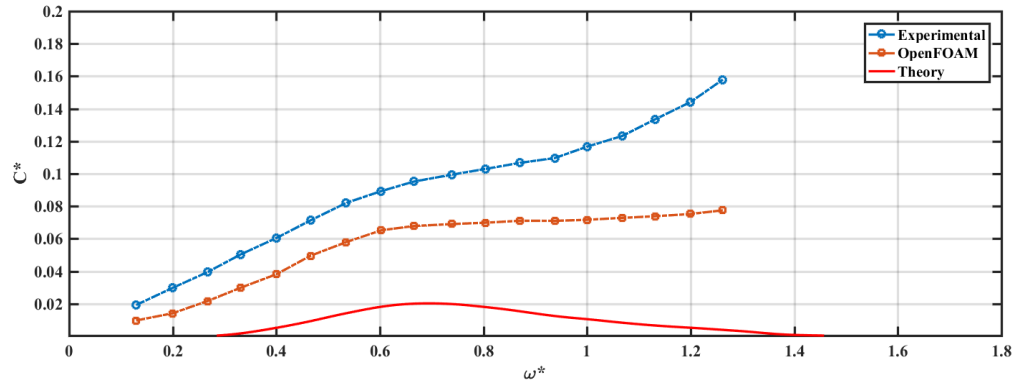

Figure H-16 Non-dimensional damping vs non-dimensional frequency under roll motion,

Amplitude =0.1rads

I. Appendix I Wave interaction with multiple cylinders

In this section, the configuration of two cylinder columns placed inline in the direction of the wave propagation is firstly used to study the wave – multiple structures interaction problem. Two cylinders with the same diameter (D) are separated with distance (L) in the wave tank ($30D \times 5D \times 16D$), which is shown in Figure I-1. The first cylinder is placed three wavelength away from wave inlet boundary in order to let the wave fully develop and avoid reflected wave from the cylinders contaminating wave inlet. The still water level (d) is 8D and a damping zone is set to be two wavelength from the outlet boundary.

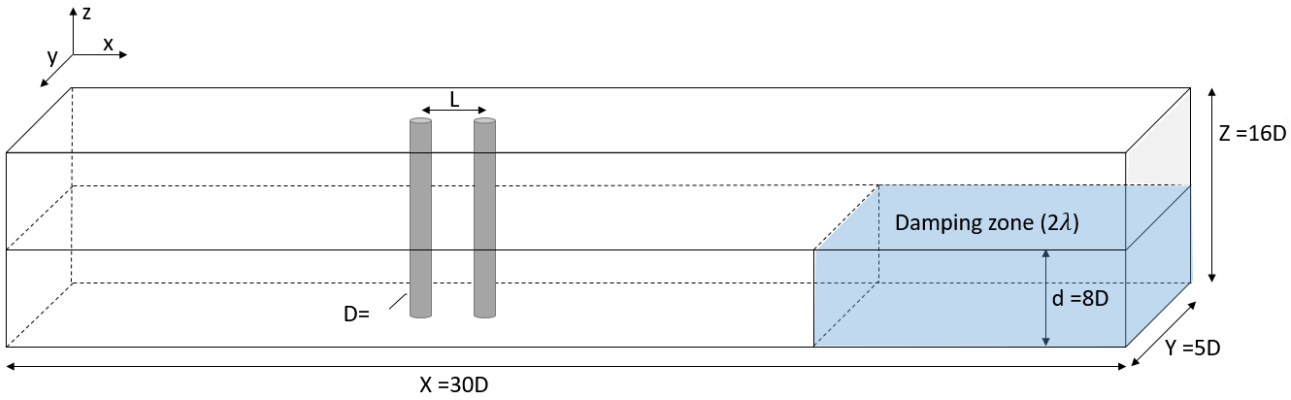

Figure I-1Layout of numerical wave tank with two vertical cylinders

Boundary conditions on front and back walls are set to be free slip-type, which is zero fixed value when the velocity are normal to the boundary and zero gradient if it is parallel to the wall . The outlet was set to a Neumann type boundary condition (zero gradient) for the velocity if the velocity vector points into the domain and a Dirichlet type (with a fixed value on the flux representative of the freestream) if the velocity vector points out of the domain. This was done to increase the stability of the outlet. The wave induced force on single cylinder is validated in the previous section and it shows a good agreement. The mesh density from previous sections is used to calculate the hydrodynamic behaviors in this study; and it is also suitable for the k –omega two equation turbulence model with wall function.

Firstly, 25 simulations are carried out to investigate the effect of separation distance between two cylinders. The results show that the wave force on leeside cylinder is nearly unchanged; and the force has a noticeable fluctuation on the front cylinder. The largest wave force on the

front cylinder occurs at the L=4D, which is the same as wavelength, and it is also the distance for the largest total force (Figure I-2). It is observed that the effect of reflection and diffraction has positive influence on the system. The total force is more than two times the one of isolated cylinder. If the second cylinder is placed far away (larger than 15D) from the front cylinder, the wave forces on both of them are nearly the same which means the wave diffraction effect has no influence between them. With separation distance L=4D, the wave forces under different wave height is further investigated. It can be seen that the changes of wave forces on both of the cylinders, especially upstream cylinder, remain a positive effect. It can be conclude that by increasing the wave height under the breaking limit, the effect of interaction is not that noticeable as the one caused by separation distance.

Figure I-4 shows the induced force against time with the separation space L=4D. It can be seen from Figure I-5 and Figure I-6 that the wave profiles are changed due to wave-structures interaction. The wave profiles at both of the cylinders have narrow but higher wave crests and broad but shallower wave troughs. The complex wave reflection and radiation zone between two cylinders results in an increase in wave run-up and a phase shift at leeside, which is more noticeable at the second cylinder. The superposition of incident and diffraction waves at the windward side of the second cylinder brings positive effect on wave elevation but a negative effect on elevation for the leeside. Together with leeside phase shift, the relative wave run-up between windward and leeward sides of the second cylinder is smaller than the one of the first cylinder. Therefore, for a pressure force dominated case, the first cylinder experiences more pressure drop between its front and back, resulting in a higher wave force.

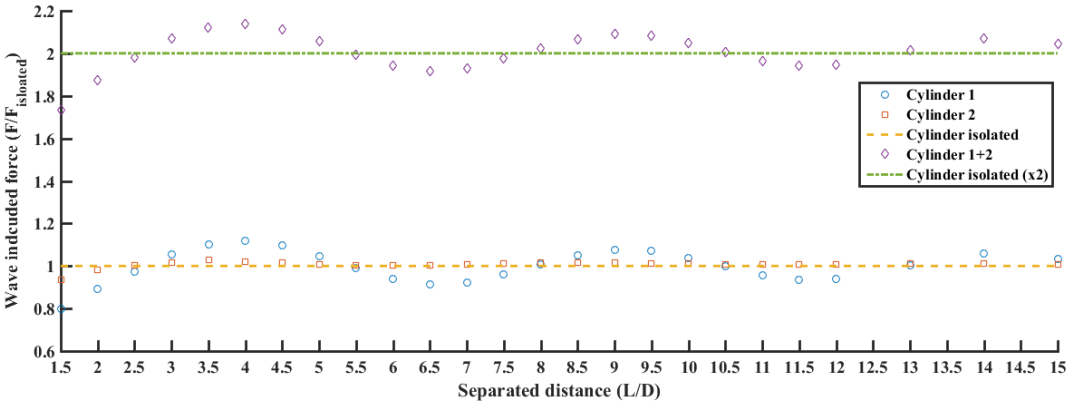

Figure I-2 Wave induced force on cylinders against separation space

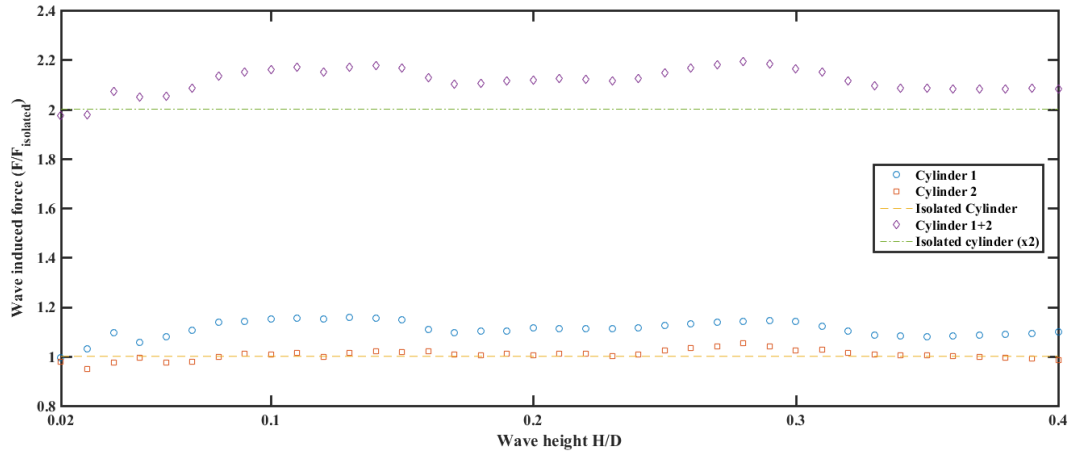

Figure I-3 Wave induced force on cylinders against different wave height with separated distance L=4D

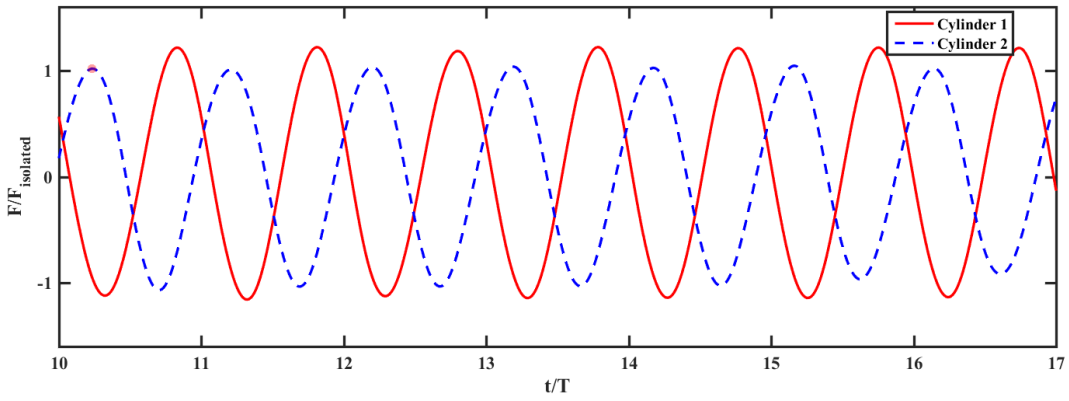

Figure I-4 Wave induced force on cylinder with separation space L=4D

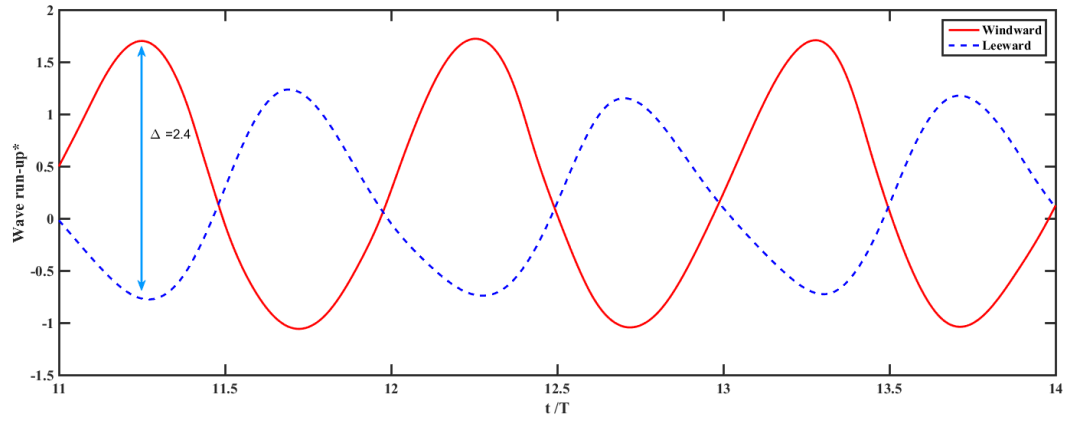

Figure I-5 Wave run-up at windward and leeward side of the front cylinder

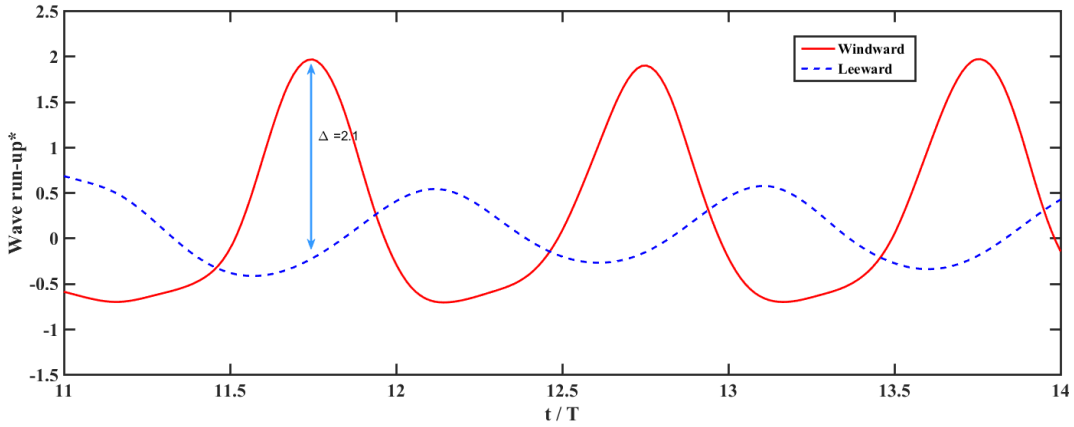

Figure I-6 Wave run-up at windward and leeward side of the second cylinder

Now, another cylinder with the same diameter is placed L=4D behind the second cylinder. The mesh density keeps the same and the layout is shown below:

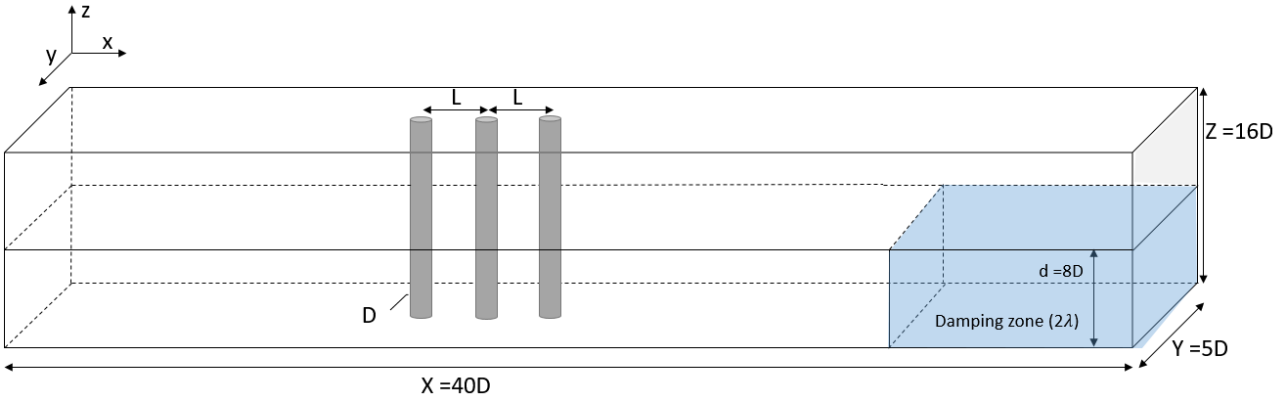

Figure I-7 Layout of numerical wave tank with three cylinders

It can be seen from the Figure I-8, both of the front two cylinders have larger wave induced force compared with two cylinder case. The cylinder in the middle experience nearly the same force amplitude as the cylinder in front; and the cylinder in the downstream, as in two cylinder case, experience the least effect on wave force. The cylinder in the middle experience wave reflection and diffraction from both upstream and downstream, resulting in higher wave elevation in the front and shallower wave trough in the back so that the wave force is increased significantly. The trend can be concluded that, with L=λ, the wave force on cylinder increases with the addition of cylinder number in the leeside; the reflected and diffracted waves travel from cylinder in the upstream, reinforced at cylinder in the back during propagation and finally they decay so that the largest relative wave run up between cylinder front and back always occur in the middle of array. The total force divided by the number of cylinders also increases from 1.1 to 1.4.

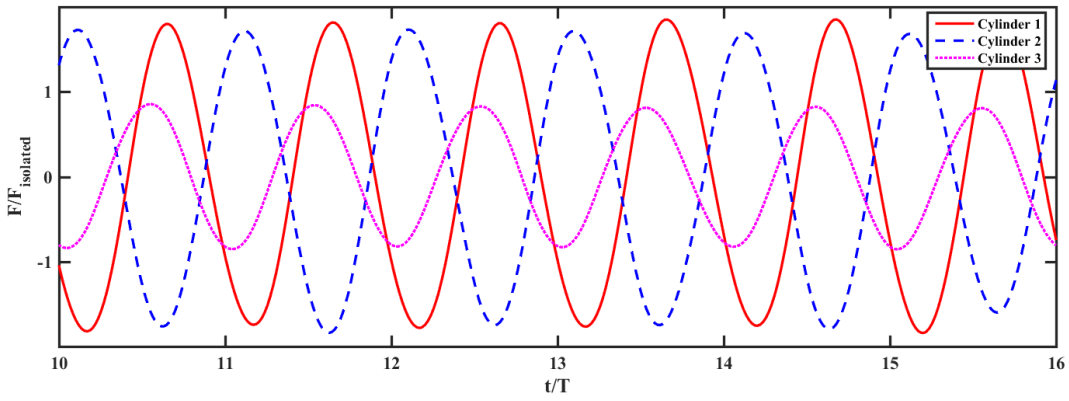

Figure I-8 Wave induced force on cylinder with H/D=0.1

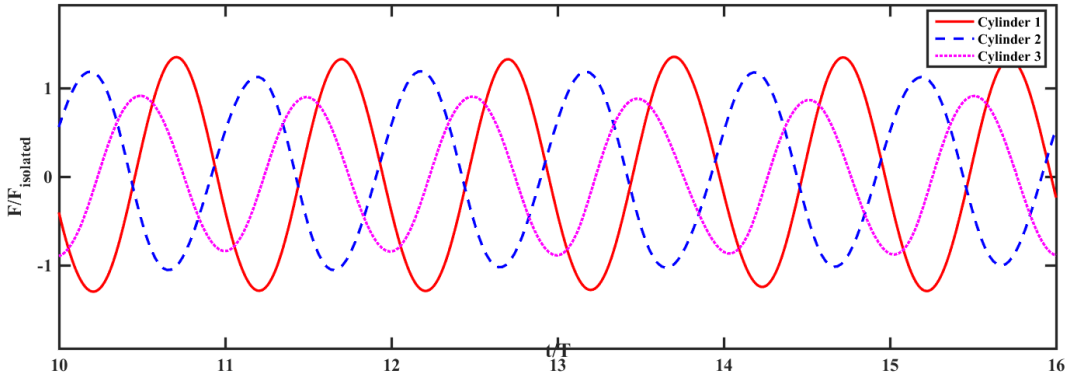

Figure I-9 Wave induced force on cylinder with H/D=0.3

By increasing the wave height, the effect on wave force is still constructive but the rate of increase is reduced. This is mainly caused by the difference between wave profiles. Higher wave height results in sharp wave crest and shallow wave trough. This means that the waveform is asymmetric and the diffraction effects are much stronger and more complex interaction zone is found in the middle of the array for the higher incident waves. The forces on the downstream cylinders are reduced significantly in comparison to the lower incident waves.

In general, for both of two and three cylinder cases, the windward cylinder always experiences the highest wave force and the wave force increases with the number of additional cylinder. The leeward cylinder, on the contrast, always experiences the lowest wave force and the wave force approximately equals to the one on single cylinder.

Bibliography

Airy, G. Tides and waves. Encyc. Metrop, 1845;192:241–396

Afshar, M. Numerical wave generation in OpenFOAM, Chalmars University of Technology. Master thesis, 2010.

Alam, M. Nonlinear analysis of an actuated seafloor-mounted carpet for a high performance wave energy extraction. Proc. R. Soc. London, Ser. A, 2012; 468:3153–3171.

Alamian, R., Shafaghat, R., Miri, S., Yazdanshenas, N., Shakeri, M. Evaluation of technologies for harvesting wave energy in Caspian Sea. Renew Sustain Energy Rev, 2014;32:468-76.

Ambühl, S., Kramer, M. and Sorensen, J. D. Reliability-based structural optimization of wave energy converters. Energies, 2014;7:8178–200.

Anbarsooz, M., Passandideh-Fard, M., Moghiman, M. Fully nonlinear viscous wave generation in numerical wave tanks. Ocean Engineering, 2013; 59:73–85

Andres de A, MacGillivray A, Roberts O, Guanche R, Jeffrey H. Beyond LCOE: A study of ocean energy technology development and deployment attractiveness. Sustainable Energy Technologies and Assessments. 2017;19:1-16.

Antonutti, R., Hearn, G.E. Optimization of point-absorber arrays. In: 9th European Wave and Tidal Energy Conference (EWTEC) 2011, Southampton, UK (5th – 9th September).

Antonio, F. Wave energy utilization: A review of the technologies. Renewable and sustainable energy reviews. 2010;14(3):899-918.

API. Recommended practice for design and analysis of station-keeping systems for floating structures. API RP- 2SK, 2005.

Arent, D.,,Wise, A., Gelman, R. The status and prospects of renewable energy for combating global warming. Energy Economy, 2011;33:584–93.

Astariz, S., Iglesias, G. The economics of wave energy: a review. Renew Sustain Energy Rev 2015;45:397–408.

AW-Energy, Waveroler project. Available from: http://aw-energy.com/

Babarit, A., Duclos, G., Clément, A. Comparison of latching control strategies for a heaving wave energy device in random sea. Applied Ocean Research, 2001;26(5):227-238.

Babarit, A., Clément, A., Gilloteaux, J. Optimization and time-domain simulation of the SEAREV wave energy converter. InASME 2005 24th International Conference on Offshore Mechanics and Arctic Engineering 2005 Jan 1 (pp. 703-712).

Babarit, A., Hals, J., On the maximum and actual capture width ratio of wave energy converters. In: 9th European Wave and Tidal Energy Conference (EWTEC), Southampton, UK, 2011, 5th–9th September.

Babarit, A., Hals, J., Muliawan, M., Kurniawan, A., Moan, Krokstad, J. Numerical benchmarking study of a selection of wave energy converters. Renewable Energy, 2012; 41:44-63.

Babarit, A. On the park effect in arrays of oscillating wave energy converters. Renewable Energy, 2013;58:68-78.

Barltrop, N. Floating structures: a guide for design and analysis,1998; 2.

Bergmann, M., Bracco, G., Gallizio, F., Giorcelli, E., Iollo, A. A two-way coupling CFD method to simulate the dynamics of a wave energy converter. OCEANS15 MTS/IEEE 2015, Genova, Italy.

Berteaux, H. Buoy engineering. John Wiley & Sons, 1976.

Borgarino, B., Babarit, A., Ferrant, P. Impact of wave interactions effects on energy absorption in large arrays of wave energy converters. Ocean Engineering, 2012;41:79-88.

Bhinder, M., Mingham, C., Causon, D, Rahmati, M., Aggidis, G., Chaplin, R. A joint numerical and experimental study of a surging point absorbing wave energy converter (WRASPA). In: 28th International conference on ocean, offshore and arctic engineering, OMAE, Honolulu, HI, United States; 2009

Bhinder, M., Babarit, A., Gentaz, L., Ferrant, P. Effect of viscous forces on the performance of a surging wave energy converter, in: Proceedings of the Twenty-second International Offshore and Polar Engineering Conference, Rhodes, Greece, 2012.

Budar, K., Falnes, J., A resonant point absorber of ocean-wave power. Nature 1975;256(5517):478-9.

Budal, K. Theory of absorption of wave power by a system of interacting bodies. Journal of Ship Research, 1977; 21:248–253

Candido, J., Modelling Justino, P. Control and Pontryagin maximum principle for a two-body wave energy device. Renew Energy 2011;36(5):1545–57.

Carballo, R., Iglesias, G. A methodology to determine the power performance of wave energy converters at a particular coastal location. Energy Convers Manag 2012;61:8-8.

Chakrabarti, S. Offshore structure modeling. World Scientific, 1994.

Chakrabarti, S. The theory and practice of hydrodynamics and vibration. World scientific, 2002.

Cordonnier, J., Gorintin, F., Cagny, A., Clément, A., Babarit, A. SEAREV: Case study of the development of a wave energy converter. Renewable Energy, 2015;80:40-52.

Cruz, J. Ocean wave energy: current status and future prespectives. Springer Science & Business Media, 2007.

Davis, J. Wave energy absorption by the Bristol cylinder-linear and non-linear effects. Proc Inst Civil Eng, 1990; 89:317–340.

Dean, R., Dalrymple, R. Water wave mechanics for engineers and scientists. World Scientific Publishing Co Inc, 1991.

DNV. Offshore Standard - Position Mooring. DNV OSE301, 2004.

Drew, B., Plummer, A., Sahinkaya, M. A review of wave energy converter technology. P I. Mech Eng A-J Pow 2009;223(8):887–902.

Eckart, C. The propagation of gravity waves from deep to shallow water. In Gravity waves 1952(p. 165).

Edinburgh Wave Power Group, http://www.homepages.ed.ac.uk/v1ewaveg/, 2009.

Eriksson, M. Modelling and experimental verification of direct drive wave energy conversion: Buoy-generator dynamics. Doctoral dissertation, Acta Universitatis Upsaliensis, 2007.

Energy without carbon, http://www.energy-without-carbon.org/WaveFarms, 2015

Emre Ozkop, Ismail H. Altas, Control, power and electrical components in wave energy conversion systems: A review of the technologies. Renewable and Sustainable Energy Reviews, 2017;67:106-115.

Erksson M, Isberg J, et al. Hydrodynamic modelling of a direct drive wave energy converter. International Journal of Engineering Science , 2005, 43(17–18):1377–1387.

Eskilsson, C., Palm, J., Ensig-Karup, A., Bosi, B. and Ricchiuto, m. Wave induced motions of point-absorbers: a hierarchical investigation of hydrodynamic models. Proc. EWTEC 2015, Nantes, France

European Ocean Energy Association. Position paper – towards European industrial leadership in Ocean Energy in 2020, 2012; pp. 14–50

EMEC: European Maring Energy Centre Ltd – Wave Energy Developers. [online]: http://www.emec.org.uk/marine-energy/wave-developers/.

Evans, D.V. Some theoretical aspects of three-dimensional wave-energy absorbers. In: Proceedings of the 1st Symposium on Ocean Wave Energy Utilization, Gothenburg, Sweeden, 1979 (30th October–1st November).

Faizal, M., Ahmed, M., Lee, Y. A design outline for floating point absorber wave energy converters. Advances in Mechanical Engineering, 2014.

Falcao, A. Stochastic modelling in wave power-equipment optimization: maximum energy production versus maximum profit. Ocean Engineering, 2004; 31(11-12):1407–1421.

Falcao, A. Modelling and control of oscillating-body wave energy converters with hydraulic power take-off and gas accumulator. Ocean Eng 2007;34(14-15):2021-32.

Falcao, A. Wave energy utilization: a review of the technologies. Renew Sustain Energy Rev 2010;14(3):899-918.

Falcao, A., Henriques, J., Candido, J. Dynamics and optimization of the OWC spar buoy wave energy converter. Renewable Energy, 2012a; 48:369–381

Falcao, A, Candido, J., Justino, P., Henriques, J. Hydrodynamics of the IPS buoy wave energy converter including the effect of non-uniform acceleration tube cross section. Renew Energ 2012b;41:105–14.

Falnes, J., Lillebekken, P. Budal's latching-controlled-buoy type wavepower plant. Institute for Fysikk, Noregsteknisk-naturvitskaplegeuniversitet (NTNU). Trondheim Norway. 2003.

Falnes, J., Hals, J. Heaving buoys, point absorbers and arrays. Philosophical Transactions of the Royal Society of London A: Mathematical, Physical and Engineering Sciences. 2012;370(1959):246-77.

Farley, F.J.M., Rainey, R.C.T., Chaplin, J.R. Rubber tubes in the sea Proc. Philos. Trans. R. Soc. Ser. A 2011; 370: 381–402.

Farley J. Far-field theory of wave power capture by oscillating systems. Philosophical Transactions of the Royal Society of London A: Mathematical, Physical and Engineering Sciences. 2012;370(1959):278-87.

Fenton, J. A fifth-order Stokes theory for steady waves. Journal of waterway, port, coastal, and ocean engineering. 1985;111(2):216-34.

Flick, R., Guza, R. Paddle generated waves in laboratory channels. Journal of Waterway, port,coastal and ocean engineering, American society of civil engineers, 1980 106(1): 79-97.

Folley, M., Babarit, A., Child B., Forehand, D., O'Boyle L., Silverthorne, K., Spinneken, J., Stratigaki, V., Troch, P. A review of numerical modelling of wave energy converter arrays. In: Proceedings, 31st International Conference on Offshore Mechanics and Arctic Engineering 2012, Rio de Janeiro, Brazil.

Galarraga, I., Eguino, M., Markandya, A. Handbook of sustainable energy. Edward Elgar Publishing, Inc; 2011.

Garnaud, X., Mei, C. Comparison of wave power extraction by a compact array of small buoys and by a large buoy. Iet Renew Power Gen 2010;4 (6):519–30.

Ghosh, T., Prelas, M. Energy resources and systems: volume 2: renewable resources.New York: Springer; 2011.

Göteman, M., Engström, J. Eriksson, M., Isberg, J., Leijon, M. Methods of reducing power fluctuations in wave energy parks J. Renewable Sustainable Energy, 2014; 6: 043103

Göteman, M., Engström, J., Eriksson, M., Isberg, J. Optimizing wave energy parks with over 1000 interacting point-absorbers using an approximate analytical method. International Journal of Marine Energy, 2015;10:113-126.

Guedes Soares, C., Bhattacharjee, J., Karmakar, D. Overview and prospects for offshore wave and wind energy. Brodogradnja, 2014; 65(2): 91–113.

Harris, R., Johanning, L., Wolfram, J. Mooring systems for wave energy converters: A review of design issues and choices. In3rd international conference on marine renewable energy, Blyth, UK, 2004;pp. 180-189.

Hasselmann, K. et al. Measurements of wind-wave growth and swell decay during the Joint North Sea Wave Project (JONSWAP). Ergnzungsheft zur Deutschen Hydrographischen Zeitschrift Reihe 1973;8(12): 95.

Havelock T.H. Forced surface-wave on water. Philosophical, 1929; 8(7): 569-576.

Hooft, J. Advanced dynamics of marine structures. Ocean Engineering, WILEY, NEW YORK, NY(USA). 1982:345.

Hu, K., Mingham, C., Causon, D. Numerical simulation of wave overtopping of coastal structures using the non-linear shallow water equations. Coastal engineering, 2000;41(4): 433-465.

Hudspeth, R., Sulisz, W. Stokes drift in two-dimensional wave flumes. Journal of Fluid Mechanics, 1991;230: 209–229.

Hunt, J. Direct solution of wave dispersion equation. Journal of the Waterway, Port, Coastal and Ocean Division. 1979;105(4):457-9.

Ismail, F., Carrica, P., Xing, T. and Stern, F. Evaluation of linear and nonlinear convection schemes on multidimensional non-orthogonal grids with applications to KVLCC2 tanker, International Journal for Numerical Methods in Fluids, 2010; 64:850– 886.

ISO. Petroleum and natural gas industries - Specific requirements for offshore structures - Part 7: Stationkeeping systems for floating offshore structures and mobile offshore units. ISO 19901-7, 2005.

ITTC, Recommended Procedures and Guidelines Rev. 04 7.5-02-07-02.2, Technical report, 2011.

International Energy Agency (IEA), Bioenergy: A Sustainable and Reliable Energy Source, Executive Summary, prepared by the Energy Research Centre of the Netherlands (ECN), E4tech, Chalmers University of Technology and the Copernicus Institute of the University of Utrecht (Utrecht: 2009). Available from:

http://www.ieabioenergy.com/publications/bioenergy-asustainable-and-reliable-energy-source-executive-summary/

International Energy Agency (IEA). Energy Efficiency Market Report 2015: Market Trends and Medium-Term Prospects (Paris: 2015). Available from:

https://www.iea.org/publications/freepublications/publication/MediumTermEnergyefficiencyMarketReport2015.pdf

International Energy Agency (IEA). Energy Technology Perspectives 2016: Towards Sustainable Urban Energy Systems. Available from: http://www.iea.org/

Jacobsen, N., Fuhrman, D., Fredsøe, J. A wave generation toolbox for the open-source CFD library: OpenFoam." International Journal for Numerical Methods in Fluids, 2012.

Jefferys, E. Device characterization. In: Count B, eds. Power from sea waves. London: Academic Press, 1980, 413–438.

Jeffrey, H., Jay, B, Winskel, M. Accelerating the development of marine energy: exploring the prospects, benefits and challenges. Technol Forecast Soc Change 2013;80:1306–16.

Karmakar, D., Soares, C. Scattering of gravity waves by a moored finite floating elastic plate. Applied Ocean Research. 2012;34:135-49.

Kelly, J. Hydrodynamic Optimisation of point wave-energy converter using laboratory experiments, Doctoral dissertation, 2007.

Kinsman, B. Wind waves: their generation and propagation on the ocean surface. Courier Corporation; 1965.

Lara J, Garcia N, Losada I. RANS modelling applied to random wave interaction with submerged permeable structures. Coastal Engineering, 2006, 53(5–6):395–417.

Lamont-Kane, P., Folley, M., and Whittaker, T. Investigating uncertainties in physical testing of wave energy converter arrays. In: Proceedings, 10th European Wave and Tidal Energy Conference 2013, Aalborg, Denmark.

Lawrence, J., Sedgwick, J., Jeffrey, H., Bryden, I. An overview of the UK Marine energy sector. Proc IEEE, 2013;101(4): 876–890.

Le-Ngoc, L., Gardiner, A., Stuart, R., Caughley, A., Huckerby, J. Progress in the development of a multi-mode self-reacting wave energy converter. InOCEANS 2010 IEEE-Sydney, IEEE, 2010: 1-7.

Lejerskog, E., Boström, C., Hai, L., Waters, R., Leijon, M. Experimental results on power absorption from a wave energy converter at the Lysekil wave energy research site. Renewable energy. 2015;77:9-14.

Li, W. and Williams, A. Second-order waves in a three-dimensional wave basin with perfectly reflecting sidewalls.” Journal of Fluids and Structures, 2000;14(4):575-592.

Liu, X., Garcia, M. Three-dimensional numerical model with free water surface and mesh deformation for local sediment scour. Journal of Waterway, Port, Coastal, and Ocean Engineering, 2008; 134(4).

Lopez, I., Andreu, J. Ceballos, S. Martinez de Alegria, I., Kortabarria, I. Review of wave energy technologies and the necessary power-equipment. Renew Sustain Energy Rev, 2013;27: 413–434.

Madsen, O. On the generation of long waves. Journal of Geophysical Research, 1971;76: 8672-8683.

Majid, A., Bhinder, Babarit, A. Lionel Gentaz, Pierre Ferrant, Potential time domain model with viscous correction and CFD analysis of a generic surging floating wave energy converter, International Journal of Marine Energy, Volume 10, June 2015, Pages 70-96, ISSN 2214-1669.

Mayer, S. et al. A fractional step method for unsteady free-surface flow with applications to non-linear wave dynamics." International Journal for Numerical Methods in Fluids, 1999; 28(2): 293-315.

McCormick, M. Ocean wave energy conversion. Courier Corporation; 2013

Menter, F., Kuntz, M. and Langtry, R. Ten Years of Industrial Experience with the SST Turbulence Model, in ‘Proceedings of the 4th International Symposium on Turbulence, Heat and Mass Transfer’, 2013, 625–632.

Morgan, G., Zang, J., Greaves, D., Heath, A., Whitlow, C., Young, J. Using the rasInterFoam CFD model for wave transformation and coastal modeling. Coastal Engineering Conference, Shanghai, China, 2010.

Mueller, M., Wallace, R. Enabling science and technology for marine renewable energy. Energy Policy 2008;36(12):4376–82.

Neary, V., Previsic, M., Jepsen, R., Lawson, M., Yu, Y., Copping, A. et al. Methodology for design and economic analysis of marine energy conversion (MEC) technologies. Technical report from Sandia National Laboratories (USA) SAND2014-9040, 2014

Nematbakhsh, A., Michailides, C., Gao, Z., Moen, T. Comparison of experimental data of a moored multibody wave energy device with a hybrid CFD and BIEM numerical analysis framework. Proc. OMAE 2015, St John's, Canada

Newman, J. Analysis of wave generators and absorbers in basins, Journal of Applied Ocean Research, 2010;32: 71-82.

Nielsen, P. Explicit solutions to practical wave problems. In Coastal Engineering, 1984 and 1985: 968-982.

Oh, J., Jang, J. OWC design to increase wave energy absorption efficiency in wave conversion systems. J Mech Sci Technol 2015;29(7):2987–93.

Olson, F. An explicit expression for the wavelength of a gravity wave. Journal of Physical Oceanography. 1973;3(2):238-9.

Oskamp, J. Ozkan-Haller, H. T. Power calculations for a passively tuned point absorbed wave energy converter on the Oregon Coast Renewable Energy 2012; 45:72–77.

Ottesen-Hansen, N., Sand, S., Lundgren, H., Sorensen, T., Gravesen, H. Correct reproduction of long group induced waves. Proceedings of the 17th costal engineering conference, Sydney, Australia, 1980;784-800.

Paik, J., Thayamballi, A. Ship-shaped offshore installations: design, building, and operation. Cambridge University Press; 2007.

Patel, M. Dynamics of offshore structures. Butterworth-Heinemann; 2013.

Paixão Conde, J., Didier, E., Numerical Simulation of an oscillating water column wave energy converter: comparison of two numerical codes. In: 21st International offshore (ocean) and polar engineering conference, ISOPE, Maui, Hawaii; 2011. pp. 668–74.

Payne, G., Taylor, J., Bruce, T., Parkin, P. Assessment of boundary-element method for modelling a free-floating sloped wave energy device. Part 1: Numerical modelling. Ocean Engineering. 2008a;35(3):333-41.

Payne, G., Taylor, J., Bruce, T., Parkin, P. Assessment of boundary-element method for modelling a free-floating sloped wave energy device. Part 2: Experimental validation Ocean Eng, 2008b; 35(3):342–357.

Pedro C. Vicente, António F.O. Falcão, Paulo A.P. Justino, Nonlinear dynamics of a tightly moored point-absorber wave energy converter, Ocean Engineering, 2013;59:20-36.

Pierson, W., Moskowitz, L. A proposed spectral form for fully developed wind seas based on the similarity theory of SA kitaigorodskii. Journal of Geophysical Research, 1964;69(24): 5181-5190.

Rafiee, A., Elsaesser, B., Dias, F. Numerical simulation of wave interaction with an oscillating wave surge converter. In: Proceedings of the ASME 2012 31st International Conference on Ocean, Offshore and Arctic Engineering.

Rahm, M. Ocean wave energy: underwater substation system for wave energy converters ,Doctoral dissertation, Acta Universitatis Upsaliensis, 2010.

Rahm, M, Svensson, O., Bostrom, C., Waters, R., Leijon, M. Experimental results from the operation of aggregated wave energy converters. IET Renew Power Gen 2012; 6(3):149–60.

Renzi, E. and Dias, F. Resonant behaviour of the oscillating wave surge converter in a channel J. Fluid Mech., 2012; 701: 482–510

Renzi, E. and Dias, F. Relations for a periodic array of flap-type wave energy converters, Applied Ocean Research, Volume 39, January 2013, Pages 31-39, ISSN 0141-1187

Retes, M., Merigaud, A., Gilloteaux, J., and Ringwood, J. Nonlinear Froude–Krylov force modelling for two heaving wave energy point absorbers Proc. EWTEC 2015, Nantes, France.

REN21. Renewables 2011 Global Status Report. Available from: ⟨http://www. ren21.net/Portals/0/documents/Resources/GSR2011_FINAL.pdf⟩.

REN21. Renewables 2016 Global Status Report. Available from: http://www.ren21.net/wp-content/uploads/2016/10/REN21_GSR2016_FullReport_en_11.pdf

Rodriguez, G.R., Soares, C.G. Correlation between successive wave heights and periods in mixed sea states. Ocean Eng 2001;28(8):1009–30.

Rourke, F., Boyle, F. and Reynolds, A. Marine current energy devices: current status and possible future applications in Ireland. Renew Sustain Energy Rev 2010;14(3):1026–36.

Rusu, E., Onea, F. Evaluation of the wind and wave energy along the Caspian Sea. Energy 2013;50:1-14.

Rusu, E. Evaluation of the wave energy conversion efficiency in various coastal environments. Energies 2014;7:4002–18.

Rusu L, Onea F. The performance of some state-of-the-art wave energy converters in locations with the worldwide highest wave power. Renewable and Sustainable Energy Reviews. 2017.

Saulnier, J., Clement, A., Falco, A., Pontes, T., Prevosto, M., Ricci, P. Wave groupiness and spectral bandwidth as relevant parameters for the performance assessment of wave energy converters. Ocean Eng 2011;38(1):130–47.

Seabased AB Available from: http://www.seabased.com/en/.

Sand, S. Long wave problems in laboratory models. Journal of Waterway, port,coastal and ocean engineering, 1982;108(WW4): 492- 503.

Sand, S. and Donslund, B. Influence of the wave board type on bounded long waves Journal of hydraulic research, 1985;23: 147-163.

Schaffer, H. Second-order wavemaker theory for irregular waves. Ocean engineering, 1996;23: 47-88.

Schmitt, P., Bourdier, S., Sarkar, D., Renzi, E., Dias, F., Doherty, K., Whittaker, T., van't Hoff, J. Hydrodynamic loading on a bottom hinged oscillating wave surge converter. In: Proceedings of the 22nd International Offshore and Polar Engineering Conference. International Society of Offshore and Polar Engineers (ISOPE), 2012a; pp.550–557.

Schmitt, P., Doherty, K. Clabby, D., Whittaker, T. The opportunities and limitations of using CFD in the development of wave energy converters Mar. Offshore Renew. Energy 2012b, pp. 89–97.

Schmitt, P., Elsaesser, B. On the use of OpenFOAM to model oscillating wave surge converters, Ocean Engineering, Volume 108, 1 November 2015, Pages 98-104, ISSN 0029-8018.

Sharkey K, Honer K, Conlon M, Gaughan K, Robinson E. The domestic and export market for large scale wave energy in Ireland and the economics of export transmission. Universities' Power Engineering Conference 2013, Dublin

Sheng, W., Alcorn, R., Lewis, A. On improving wave energy conversion, (part I): optimal and control technologies. Renew Energy 2015;75:922–34.

Stratigaki, V., Troch, P., Stallard, T., Forehand, D., Kofoed, J., Folley, M., Benoit, M., Babarit, A., Kirkegaard, J. Wave basin experiments with large wave energy converter arrays to study interactions between the converters and effects on other users in the sea and the coastal area. Energies, 2014; 7(2):701–734.

Taghipour, R., Moan,T. Efficient frequency-domain analysis of dynamic response for the multi-body wave energy converter in multi-directional wave. International Society of Offshore and Polar Engineers; 2008.

Tedeschi, E., Carraro, M., Molinas, M., Mattavelli, P. Effect of control strategies and power take-off efficiency on the power capture from sea waves. IEEE Trans Energy Conver 2011;26(4):1088–98.

Truong, D., Ahn, K. Wave prediction based on a modified grey model MGM (1,1) for real-time control of wave energy converters in irregular waves. Renew Energy 2012;43:242–55.

Uihlein, A., Magagna, D. Wave and tidal current energy – A review of the current state of research beyond technology. Renewable and Sustainable Energy Reviews. 2016;58:1070-81.

Ursell, F., Dean, R., and Yu, Y. Forced small-amplitude water waves: a comparison of theory and experiment. Journal of Fluid Mechanics, 1960; 7(01): 33-52.

Vates, A. Wave energy converters. Universitὰ degli studi di Firenze, Facoltὰ di Ingegneria; 2009.

Veigas, M., Lopez, M., Iglesias, G. Assessing the optimal location for a shoreline wave energy converter. Appl Energy 2014;132:404-11.

Venezian, G. Discussion of Direct Solution of Wave Dispersion Equation by John N. Hunt. Journal of the Waterway, Port, Coastal and Ocean Division. 1980;106(4):501-502.

Verduzco-Zapata, M. Ocampo-Torres, F. Study of a 6 DOF wave energy converter interacting with regular waves using 3D CFD, 2015, Proc. 11th EWTEC 2015.

Vicente, M., Alves, M., Sarmento, A. Layout optimization of wave energy point absorbers arrays, in: Proc. of the 10th EWTEC Conference, Aalborg, Denmark, 2013.

Vicinanzaa, D., Contestabilea, P., Ferrantea, V. Wave energy potential in the north-west of Sardinia (Italy). Renew Energy 2013;50:506–21.

Wang, H., Sun, Z. Experimental study of a porous floating breakwater. Ocean Engineering. 2010;37(5):520-7.

Weller, H.G., Tabor, G., Jasak, H., Fureby, C. A tensorial approach to computational continuum mechanics using object-oriented techniques Comput. Phys., 1998; 12(6): 620–631.

Westphalen, J., Greaves, D., Hunt-Raby, A., Williams, C., Taylor, P., Hu, Z., et al. Numerical simulation of wave energy converters using Eulerian and Lagrangian CFD methods. In: 20th international offshore (Ocean) and polar engineering conference, ISOPE, Beijing, China; 2010.

Winden, B., Turnock, S. and Hudson, D. A RANS modelling approach for predicting powering performance of ships in waves, International Journal of Naval Architecture and Ocean Engineering 2014, 6(2).

Wu, C., Thornton, E. Wave numbers of linear progressive waves. Journal of Waterway, Port, Coastal, and Ocean Engineering. 1986;112(4):536-40.

Yavuz, H., Mistikoglu, S., Stallard, T. Processing irregular wave measurements to enhance point absorber power capture performance. Ocean Eng 2011;38 (4):684–98.

Yu, Y. Li, Y. Reynolds-Averaged Navier–Stokes simulation of the heave performance of a two-body floating-point absorber wave energy system, Computers & Fluids, 2013;73:104-114.

Weller, H., Tabor, G., Jasak, H. and Fureby, C. A tensorial approach to CFD using object orientated techniques. Computers in Physics, 1998; 12:620-631.

Zabihian, F., Fung, A. Review of marine renewable energies: case study of Iran. Renew Sustain Energy Rev 2011;15(5):2461-74.

Zhang, H. A deterministic combination of numerical and physical models for coastal waves," PhD thesis, Department of mechanical engineering, Technical university of Denmark, 2005.

Zhou, Y., Yan, C. and Kang, H.-l. Numerical Dissipation Effect Analysis of Upwind Schemes, in ‘46th AIAA Aerospace Sciences Meeting and Exhibit, AIAA 2008-759’, 2008.